Time-resolved Imaging of Secondary Gamma Ray Emissions for *in vivo* Monitoring of Proton Therapy:

Methodological and Experimental Feasibility Studies

Patrícia Cambraia Lopes

TIME-RESOLVED IMAGING OF SECONDARY GAMMA RAY EMISSIONS FOR *IN VIVO* MONITORING OF PROTON THERAPY: METHODOLOGICAL AND EXPERIMENTAL FEASIBILITY STUDIES

Proefschrift

ter verkrijging van de graad van doctor
aan de Technische Universiteit Delft,
op gezag van de Rector Magnificus prof. ir. K. C. A. M. Luyben
voorzitter van het College voor Promoties,
in het openbaar te verdedigen op maandag 16 oktober 2017 om 10:00 uur

door

Patrícia CAMBRAIA LOPES FERREIRA DA SILVA

Master of Science in Medical Physics
Universidade do Porto,
geboren te Figueira da Foz, Portugal

This dissertation has been approved by the
promotors: Prof. dr. ir. H. van der Graaf and Prof. dr. rer. nat. K. Parodi
copromotors: Dr. ir. D.R. Schaart and Dr. rer. nat. P.A. Vieira Crespo

Composition of the doctoral committee:

Rector Magnificus	chairman
Prof. dr. ir. H. van der Graaf	Delft University of Technology, promotor
Prof. dr. rer. nat. K. Parodi	Ludwig Maximillans Universität München, Germany, promotor
Dr. ir. D.R. Schaart	Delft University of Technology, copromotor
Dr. rer. nat. P.A. Vieira Crespo	Universidade de Coimbra, Portugal, copromotor

Independent members:

Prof. dr. ir. C.W.E. van Eijk	Delft University of Technology
Prof. dr. S. Brandenburg	University of Groningen
Prof. dr. ir. F. Verhaegen	Maastricht University
Prof. dr. M. van Vulpen	HollandPTC Proton Therapy Centre
Prof. dr. H. Th. Wolterbeek	Delft University of Technology, reserve member

The research presented in this thesis was performed at the Medical Physics & Technology (MP&T) section of the department of Radiation Science and Technology, Faculty of Applied Sciences, Delft University of Technology, The Netherlands.
Visiting Address: Mekelweg 15, 2629 JB, Delft, The Netherlands.

Part of this research was performed at the Laboratório de Instrumentação e Física Experimental de Partículas, Coimbra, Portugal, and at the Heidelberg Ion-Beam Therapy Center, Heidelberg University Clinic, Heidelberg, Germany.

This research was funded by FCT – Fundação para a Ciência e a Tecnologia, Lisbon, Portugal, co-funded by the European Social Fund and by POPH – Programa Operacional Potencial Humano, through the individual doctoral grant no. SFRH/BD/73705/2010; and by the foundation for Fundamental Research on Matter (FOM), The Netherlands, through the grant no. 09NIG18.

Cover: Reactor Institute Delft. Design by Ben Blumensheid and idea by José Buurman.

Printed in The Netherlands by Rijnja Repro.

ISBN: 978-94-6186-850-3

An electronic version of this dissertation is available at
`https://repository.tudelft.nl/`

Para ti, Mãezinha
e
Para ti, Avô Lopinhos

To you, Mommy
and
To you, Grandpa Lopinhos

Contents

Chapter 1

Introduction

1.1 Proton (radio)therapy

Radiotherapy (or radiation therapy, RT) is a commonly-used, effective modality for the treatment of cancer. Proton therapy is an advanced form of external beam radiotherapy that uses proton beams to destroy solid tumors. It is included under the general term of particle therapy (PT) or hadron therapy. This term additionally refers to the therapeutic use of positively-charged heavy[1] ions - such as the clinically established carbon ions and potentially novel species under investigation (e.g., helium, lithium, oxygen) - as well as neutrons and sub-atomic particles (e.g., pions). Proton therapy is the second most accessible form of external RT after conventional photon RT. The first patient was treated with protons at the Lawrence Berkeley Laboratory in California in 1955, and over the past 2-3 decades proton therapy has been rapidly growing. By 2009 about 25 facilities were treating patients wordwide (Smith 2009) and this number has more than doubled by the end of 2013, when already 62 centers have been reported by PTCOG 2014 (Newhauser and Zhang 2015). Thanks to the superior dose conformity in comparison to photon RT (section 1.1.1), it is especially suited for the treatment of deep-seated, sometimes inoperable tumors, in particular those occurring in children and/or located in the vicinity of radiosensitive organs-at-risk (OARs).

However, the technology is not yet fully mature. There is a need for a number of technological and methodological improvements, in treatment planning, treatment delivery, and very importantly, in *in vivo* image- and dose-guidance, before the full potential of proton therapy can be translated into clinical benefits, improving its cost/benefit ratio and making it competitive to state-of-the-art photon RT for a wide spectrum of cancers (Engelsman *et al* 2013). In the following, the main principles and challenges of proton therapy are summarized. Photon and carbon RT will be briefly addressed in comparative terms.

1.1.1 Rationale

The general challenge in external beam RT is to permanently damage a tumor while sparing the surrounding healthy tissues and OARs as much as possible (i.e. to maximize the therapeutic ratio). To this aim, modern techniques approach the tumor with various beams from multiple directions/angles (so-called irradiation fields) that overlap in the tumor volume, at the same time optimizing the geometrical shape and intensity pattern of each field

[1] 'Heavy' in the radiobiological sense (Kraft 2000)

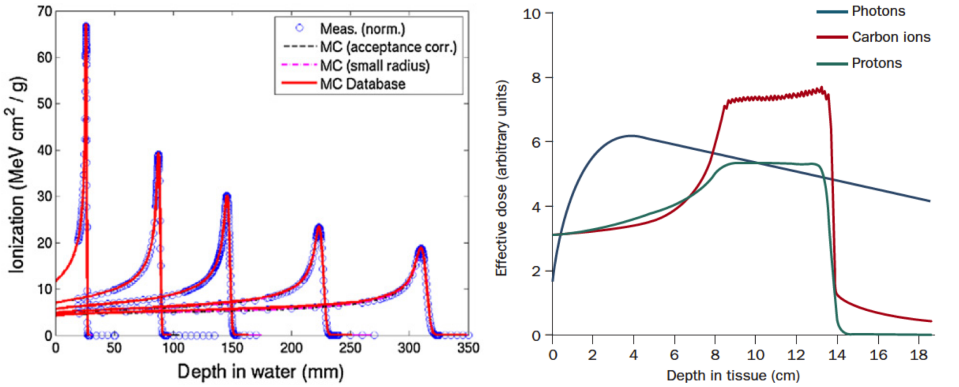

Figure 1.1: *Left*: Measured and simulated (Monte Carlo, MC) depth-dose distributions (pristine Bragg peaks) generated in water by individual mono-energetic proton pencil beams with representative energies in the entire therapeutic range, from (Parodi *et al* 2012b). *Right*: Schematic comparison of effective depth-dose distributions in tissue of single-field irradiations for photons, protons and carbon ions, from (Durante and Loeffler 2010).

(intensity-modulated radiation therapy, IMRT). By these means, the high-dose region can be conformed to the generally irregular shape of the tumor (Cheung 2006, Bortfeld 2006). Another strategy in RT is to fractionate the treatment into multiple, typically daily sessions, in order to enable gradual recovery of normal tissue from radiation damage, taking advantage of its improved repair mechanisms compared to the tumor cells.

Robert R. Wilson was the first to propose the use of fast protons (H^+) to treat localized cancer, highlighting their favorable depth-dose[2] distribution (Wilson 1946). Protons and heavy ions release a large amount of their energy in a highly localized region, just before they stop in the tissue. The dose peak is called the Bragg peak (BP) and its position in depth can be tuned by changing the initial energy of the projectile (higher energy results in a higher endpoint, figure 1.1-left). By properly overlapping ion beams with different energies, it is possible to create a uniform dose distribution in the tumor region, as illustrated in figure 1.1-right for a single field. Also shown in figure 1.1-right is that the dose deposited by therapeutic photon beams (X-rays or γ-rays) decreases with depth, in contrast with ions, and that some dose is always deposited beyond the target (section 1.1.2.1).

In practice, this means that proton (and heavy-ion) therapy can deliver high and tumor-conformal doses with less overall dose to healthy tissues and using a lower number of fields (Kosaki *et al* 2012), in comparison to photon RT. Such advantages are very important to spare critical organs-at-risk and to reduce the side effects of irradiation (van de Water *et al* 2011, van der Laan *et al* 2013), in particular, to reduce late radiation effects for pediatric patients (e.g., development of secondary malignancies). The integral dose with protons has been estimated to be about 2 times lower than that with photon IMRT (recently, also denoted as IMXT) (Lomax *et al* 1999). In fact, this may be an underestimation considering more sophisticated techniques such as inverse treatment planning and intensity-modulated proton therapy (IMPT) (DeLaney 2011).

The choice of RT beam should take into account the advantages and disadvantages of each for the particular treatment case, based on their physical properties (section 1.1.2),

[2] *Dose (D)* is a measure of absorbed ionizing-radiaton energy locally. It is defined in SI units of gray (*Gy*) or one joule of energy per one kilogram of matter (J/kg).

but also on radiobiological considerations, and on its robustness to treatment uncertainties (section 1.1.4). Excluding the latter, figure 1.1-right shows that the dose after the BP is reduced to a minimum (nearly no exit dose) for protons with respect to carbon ions. In comparison to protons, carbon ions may deposit an overall lower dose outside the tumor region, at the expense of a higher exit dose (dose tail distal to the beam, section 1.1.2 has details). In comparison to photons and protons, carbon ions may be the best choice in situations where increased biological effectiveness[3] is of utmost importance, e.g., for treating hypoxic and radioresistant tumors. In addition, the reduced lateral straggling of carbon ions with respect to protons allows beams tangent to OARs to provide optimum tumor-to-healthy tissue dose profiles (Schardt *et al* 2010).

It should be noted, however, that the increased precision offered by heavy-ion therapy comes at the cost of much higher complexity and vulnerability to treatment uncertainties, thus requiring extreme care and a specific approach which is beyond the scope of the present dissertation. Only a small number of research-driven PT sites worldwide meet the technological demands for carbon therapy, which is about three times more expensive than proton therapy. Examples are the world's first clinical center at the National Institute of Radiological Sciences (NIRS) in Chiba, Japan (Okada *et al* 2010), and the Heidelberg Ion-Therapy Center (HIT), in Germany (Combs *et al* 2010), with the world's only heavy-ion gantry, set up after the clinical experience gained at the Gesellschaft für Schwerionenforschung (GSI) pilot project in Darmstadt.

1.1.2 Mechanisms of interaction and physical properties

The way charged particles interact with matter determines the dose distribution[4]. In proton therapy, beams of protons with energies between ~50 MeV and ~220 MeV are typically used, which correspond to endpoints (ranges) in water of about 2 cm to 30 cm (Parodi *et al* 2012b). With these energies, protons can experience Coulomb interactions with the atomic electrons (section 1.1.2.1) or the atomic nucleus (section 1.1.2.2), as well as nuclear interactions (section 1.1.2.3) in the medium. Radiative energy losses via Bremsstrahlung (inelastic collisions with the nucleus) are negligible.

1.1.2.1 Electronic energy loss and range

Protons and other charged particles in the therapeutic energy range lose their energy primarily by frequent inelastic Coulomb interactions with the orbital electrons in the traversed medium, causing ionization and excitation of the atoms. Although protons are 1836 times heavier than electrons, with the consequence that proton trajectories are nearly straight, multiple Coulomb scattering with target nuclei results in considerable beam lateral straggling (section 1.1.2.2). A good approximation of proton energy loss rate can be described by the linear stopping power ($-dE/dx$), defined as the mean amount of energy E released per unit path length x in the medium.

This is well described by a quantum-mechanical and relativistic[5] formalism known as the Bethe-Bloch equation, including corrections at low proton energies (i.e. comparable

[3] The same physical dose may result in different cell killing, depending on the type and energy of ionizing radiation. The *relative biological effectiveness* (RBE) is a multiplicative factor used in radiobiology to normalize the physical dose (D) to the dose that would be necessary to achieve the same cell killing effect using X-rays, the *equivalent dose* (D_{eq}) (RBE = 1 for photons). RBE is typically ~1.1 for clinical protons while for carbons it increases considerably with decreasing ion energy (Weyrather and Debus 2003).

[4] For a more complete review, the interested reader may refer to (Boon 1998) and (Newhauser and Zhang 2015).

[5] Irrelevant for the energies of interest in RT.

to the ionization energy), such as the Barkas correction and shell corrections (Bethe 1930, Bloch 1933, Bethe and Ashkin 1953, ICRU 1993). Briefly, the mean energy loss rate for a given particle depends most strongly on the material density (it is directly proportional) and the ion velocity (approximately inversely proportional to the square of the velocity). The density can vary considerably: ~ 3 orders of magnitude between air in the lungs and rib bone. Furthermore, the stopping power is directly proportional to the ratio between the atomic number and the nuclear number (Z/A) and to the square of the ion charge (equal to 1 for protons). It also depends on the mean excitation potential I of the material (specifically, on the logarithm of I^{-1}). The physical dose D (footnote *2 on page 2*) imparted to a medium with mass density ρ by a parallel beam of particles with fluence Φ, can be expressed as follows:

$$D(x) = -\frac{dE}{\rho dx}(x) \cdot \Phi(x) \tag{1.1}$$

where $-dE/\rho dx$ is the mass stopping power.

The increase in energy loss with decreasing energy dictates that the dose is peaked (Bragg peak) at the end of the track. The Bragg peak position, or the (mean) range, is defined as the penetration depth at which half of the protons have stopped. A good approximation for the range can be derived by integrating the inverse of the stopping power with respect to the particle energy, from zero to the initial particle energy. Range is a statistical quantity that is defined for a beam of particles, whereas individual proton path lengths vary stochastically (approx. Gaussian distribution), causing a broadening of the BP, denoted as range or energy straggling. Energy straggling is lower for massive projectiles (e.g., carbon ions versus protons) and for lower initial projectile energy (figure 1.1-left). In clinical practice, the range is usually defined as the penetration depth at which the distal dose falloff reaches a fraction of the dose profile maximum (typically 80%) for proton pencil beams (i.e. narrow beams). Tables of stopping powers and ranges are accessible for the most common compounds and elements (ICRU 1993).

For completeness, it is noted that contrarily to protons, heavier projectiles lead to some exit dose in the form of a tail beyond the BP (figure 1.1-right for carbon). This is due to fragmentation of a certain fraction of the projectiles (section 1.1.2.3) into lower-charge particles, which have lower stopping power, thus longer ranges, compared to the original projectile.

Unlike charged particles, photons can traverse a material without interacting (also valid for other neutral particles, e.g., a neutron). Photons can also interact with the orbital electrons, losing all/part of their energy in a small number of interactions (Compton scattering), or losing all their energy in one interaction (photoelectric effect). Compton scattering is the dominant interaction at the energies of interest in RT. Due to the stochastic nature of these interactions, the intensity of the photon beam decreases exponentially with the material depth. The energy deposition profile also falls exponentially, with the exception of a dose build-up in the entrance region (figure 1.1-right), which takes place before electronic equilibrium is reached. This build-up occurs because the ejected electrons are directed forward such that they deposit their energy into the target at depths (~ a few cm) beyond the location of primary ionization.

In particle therapy, some of the secondary electrons (so-called δ-*electrons*) can possess enough energy to create secondary ionizations while they dissipate their energy along a so-called spur track ($\leq$ than a few mm for protons) that is different from the beam path. However, this is mainly relevant in microdosimetry or near material interfaces. Since energy loss is not necessarily the same as energy deposition, in radiobiology the term stopping

power is replaced by linear energy transfer (LET[6]). Ions heavier than protons generate a comparatively higher density of primary and secondary ionizations (high-LET) around the end of their track (Krämer and Kraft 1994, Kraft *et al* 1999), thus inducing more damage by direct ionization of the DNA molecule in repect to lighter ions. Contrarily, sparsely ionizing radiation (low-LET), like photons and protons, induce most of the DNA damage indirectly, i.e. mediated by free radicals.

1.1.2.2 Multiple Coulomb scattering

Multiple Coulomb scattering (MCS) refers to the accumulation of many, mostly small-angle, deflections of the particle trajectory due to repulsive elastic interactions with the electric field of the target nuclei. The angular distribution was well described by Molière (1948) (Gottschalk *et al* 1993) and for small scatter angles it is approximately Gaussian. MCS results in lateral broadening (penumbra) of the beam, and hence in lateral spreading of the dose distribution. The relatively broad lateral penumbra of protons is not advantageous compared to heavier ions and even to photons, for sparing OARs in the vicinity of the target (Weyrather and Debus 2003, Lu and Flanz 2011).

1.1.2.3 Non-elastic nuclear interactions

When the impact parameter, i.e. the distance between the trajectories of the centers of two colliding nuclei, is much lower than the atomic radius, and the projectile energy is high enough to overcome the nuclear Coulomb barrier, non-elastic nuclear interactions may occur. In such proton-induced reactions, it is possible that the proton grazes the nucleus, leaving it intact but in an excited energy state. The resulting excited nucleus typically decays within less than a nanosecond resulting in the emission of gamma rays, so-called prompt gammas-rays (PGs), with energies up to ~15 MeV. Proton capture and fragmentation of the target nucleus may also occur, accompanied most-likely by the emission of protons and neutrons, but also by for e.g., deuterons, tritons, and alpha particles. Fragments can be left in an excited state resulting in the emission of PGs, but they can also give rise to delayed radiation.

In the case of delayed radiation, of interest to proton therapy are radioisotopes that have a deficit of neutrons and may decay through positron emission. One example is the formation of ^{15}O through the reaction channel ^{16}O(p,pn)^{15}O, which eventually decays to ^{15}N as is illustrated in figure 1.2-top. As the emitted positron comes to rest it will annihilate with an electron, giving rise to a pair of 511 keV annihilation quanta. Figure 1.2-bottom depicts an example of characteristic PG emission (6 MeV) from deexcitation of ^{16}O after an inelastic collision with a proton, ^{16}O(p,p)^{16}O*. The detection of both prompt and delayed gamma radiation are active fields of research in the context of *in vivo* monitoring of proton therapy (section 1.2).

Although non-elastic proton-nuclear interactions are less frequent than the electromagnetic interactions (24% probability of non-elastic interaction for a 209 MeV proton), they have an impact on the spatial dose distribution by (1) reducing the primary beam fluence (equation 1.1), and (2) giving rise to (mostly) secondary protons that increase the dose deposition upstream the BP, due to their lower energies and larger angles with the beam axis compared to primary protons (Gottschalk 2012). In addition, the emitted neutrons and gamma rays contribute to background dose (Newhauser and Zhang 2015). The probability

[6]LET is a measure of energy dissipated locally into a medium by all the electrons excited/ejected by the primary radiation, and it is defined for both charged and neutral radiations.

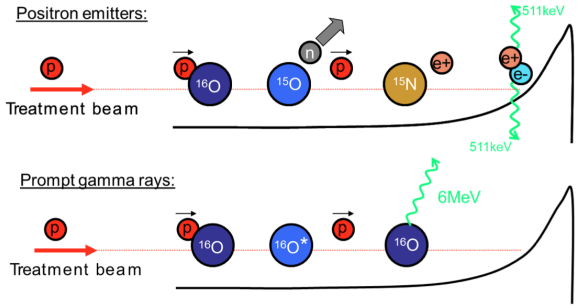

Figure 1.2: Schematic illustration of two non-elastic collisions between protons and oxygen nuclei, giving rise to the emission of 'prompt' (bottom) or 'delayed' (top) gamma radiation.

of non-elastic interactions is nearly constant in the span of therapeutic proton energies, except in the last few cm of their range where it almost doubles before the cut-off from the Coulomb barrier (Paganetti 2012), peaking at energy values of a few 10 MeV (Newhauser and Zhang 2015). PG emission from main tissue elemental constituents also show a maximum in that energy range (Polf *et al* 2009a). The energy threshold for nuclear fragmentation is somewhat higher than for nuclear excitation.

1.1.3 Beam delivery

Clinical proton beams are typically produced in particle accelerators like cyclotrons and synchrotrons (Schippers 2009). In most institutes cyclotrons are used to accelerate proton beams to one or a few fixed energies (usually the highest therapeutic energy) and the energy selection is done by using a degrader. Compared to synchrotrons, clinical cyclotrons are conveniently more compact and less complex in operation. However, synchrotrons are more flexible in that they can accelerate various ion species and that the particle energy selection can be done by the accelerator (e.g., Ondreka and Weinrich 2008).

Proton beams are transported from the accelerator via a beam line with magnetic steering, and brought to the treatment nozzle where they are shaped (section 1.1.3.2) and finally delivered. The beam nozzle can be preceded by a rotating gantry with magnetic bending of the beam such that it can enter the treatment site from multiple directions, allowing for the highest flexibility in angles of incidence of the treatment fields. A typical fractionated proton-RT regimen consists of 30-35 total irradiations (fractions) administered on a daily basis, with a daily dose of about 2 Gy delivered to the tumor. The treatment plan is usually split into a few irradiation fields that can last up to few minutes (Durante and Loeffler 2010, Min *et al* 2013).

1.1.3.1 Time structure

The time structure of clinical proton beams can differ substantially depending on the particle accelerator, namely a synchrotron or a cyclotron. In general terms, ions are accelerated in bunches while they travel in circular motion, by means of oscillating electromagnetic fields that are synchronized with the orbital frequency of the ions and are driven by a radiofrequency (RF) power source (accelerator RF). Synchrotrons operate in cycles comprising essentially the following steps: particle injection into the ring, particle acceleration to

a specified energy, and particle extraction into the beam line. Therefore, the beam is delivered in a periodic macro-structure of particle extraction or spills (beam on) intercalated with pauses (beam off). During each spill, an iso-energy-layer of tissue can be irradiated. The spill and pause durations are of the order of seconds, while variable duty cycles (viz. spill duration divided by the cycle period) can be achieved. Within a spill there is a periodic beam micro-structure, such that particle bunches are delivered with arrival times that are correlated to the accelerator RF signal (Parodi *et al* 2005a). The time-spread/uncertainty in arrival times of protons within one RF period is called the bunch width. Both the bunch width and the RF-period depend on the energy of the particle, among other accelerator-specific factors. The bunch width has been measured for carbon ions and can be of the order of a few to several tens of nanoseconds (full width at half maximum, FWHM) (Parodi *et al* 2005a), and the RF-period can be one order of magnitude higher (Crespo *et al* 2005). Cyclotrons operate in continuous-wave mode, delivering beam pulses at a repetition rate given by the RF cycle. The RF period is typically in the range of a few tens of nanoseconds, and the bunch width can be of the order of a nanosecond or lower (Crespo 2005).

1.1.3.2 Beam shaping

Beam shaping refers to the manipulation of the properties of the beam, i.e. its size, energy and intensity distribution over space and time, in order to achieve (ideally) a uniform tumor-conform dose deposition. Although hybrid techniques exist (Smith 2009, Engelsman *et al* 2013), the two most distinct forms of beam shaping are: (1) the conventional form of passive beam shaping; and (2) the more advanced form of pencil-beam scanning (PBS).

In passive beam shaping, the particle beam is shaped through a set of mechanical attenuators and scatterers. The (narrow) pencil beam from the accelerator is laterally broadened by a scattering system and passes through a range modulation wheel[7] or ridge filter to create a spread-out Bragg peak (SOBP), i.e. an overlay of several Bragg peaks that cover the tumor span in depth. In addition, the use of a patient- and field-specific collimator and range compensator assures the lateral and distal-surface conformity of the dose to the irregular shape of the target, respectively (Kraft 2000). The main disadvantages of this approach are (a) the lack of conformity of the high-dose region to the proximal surface of the tumor, since the energy modulation width is fixed throughout the field; and (b) the generation of background radiation due to the amount of material in the beam path (section 1.1.2.3).

For the active scanning or PBS technique (Haberer *et al* 1993), the pencil beam is steered horizontally and vertically by two pairs of dipole magnets, in order to bring the BP at different positions, voxel-by-voxel, within the tumor. For each beam energy, an iso-energy-slice can be 'painted' in the target volume by either step-and-shoot or raster-scan approaches, while the beam intensity / scan speed and beam size can be dynamically adjusted to achieve high dose conformality in both distal and proximal tumor surfaces. Both adaptive and intensity-modulated particle therapy (IMPT) can only be achieved by means of PBS techniques (Engelsman *et al* 2013). IMPT requires simultaneous optimization of all Bragg peaks from all fields with or without additional dose constraints to OARs (Smith 2009). On the other hand, PBS is not yet as robust as passive scattering techniques in the treatment of moving targets. The former technique faces additional difficulties since the spot position may vary in space and time (being limited by the speed capabilities from e.g. the accelerator) at a different rate with respect to the anatomic/density changes in the beam path due to the organ motion (Phillips *et al* 1992, Engelsman *et al* 2013), resulting in so-called 'interplay' effects.

[7] A modulation wheel is a rotating absorber material composed of several steps with different thicknesses.

1.1.4 Dose uncertainties

There are several sources of uncertainty in proton-dose delivery in a patient (sections 1.1.4.1 and 1.1.4.2). Such errors can impact the spatial distribution of the high-dose region (thus the level of conformity to the target volume) and the level of homogeneity within that region, thus possibly impacting the level of tumor control and/or healthy tissue sparing. In particular, knowing the exact position of the proton range within the body is of primary importance in proton therapy. This is the case since, for example, the occurrence of shifts in the distal-most Bragg peak position resulting from an unexpected over-dense (or hypodense) tissue in the beam path, may lead to tumor underdosage (or healthy-tissue/OAR overdosage). This is a distinguishing factor between proton RT and photon RT. The latter is more robust to tissue density variations in the beam path due to the absence of sharp depth-dose gradients (Müller *et al* 2015).

As a consequence of dose uncertainties, full exploitation of the physical advantages of the sharp distal dose falloff from proton beams is not yet possible in clinical practice, as it rarely is the case that the distal falloff is used to spare nearby (i.e. $<$ 1-2 cm) OARs downstream of the beam (Engelsman *et al* 2013, Knopf and Lomax 2013). The reduction of such uncertainties constitutes the main motivation for the development and implementation of techniques for imaging guidance and adaptive proton therapy (section 1.1.4.3).

1.1.4.1 Range uncertainties

Range uncertainties *per se* typically refer to uncertainties in predicting the proton range within the patient at the stage of the treatment planning. Those uncertainties have been extensively reviewed by Paganetti (2012). In treatment planning, analytical dose calculation algorithms are typically used, which incorporate X-ray computed tomography (CT) imaging data to define the patient geometry and to derive relative tissue stopping powers.

Range uncertainties arise from the CT imaging itself (due to e.g., noise, spatial resolution, calibration) and from the conversion of the CT numbers (in Hounsfield units), which essentially measures electron density, to proton interaction data, dependent on the mixture of different nuclei present in the tissue (Schaffner and Pedroni 1998, Lomax 2008a, Yang *et al* 2012). In addition, the uncertainty in the mean excitation energy (I-value (ICRU 1993)) contributes substantially to the stopping power uncertainty, thus the range uncertainty (Paganetti 2012). Other possible uncertainties are related to variations in the RBE at the distal end of the proton range, as well as to the presence of complex heterogeneities in the beam path due to limitations of analytical dose-calculation algorithms to model MCS.

The common approach to deal with such range uncertainties is to avoid dosimetrically-challenging beam directions (such as those in the presence of inhomogeneities lateral to the beam path) and to add range margins to the prescribed range. Despite the lack of a generic margin recipe since range uncertainties are tissue specific and thus beam-direction specific (Yang *et al* 2012), Paganetti (2012) estimated a range uncertainty of 2.7% of the prescribed range plus a fixed 1.2 mm margin due to factors that are independent on the dose calculation algorithm, such as beam-, hardware- and patient-setup-related factors. In addition, Paganetti (2012) estimated that, even in the presence of lateral inhomogeneities, the former margin could be reduced to about 2.4% by employing Monte Carlo (MC) calculations of the dose distribution, mainly due to the improved modeling of MCS with respect to analytical algorithms.

Other sources of range uncertainties may further complicate the treatment planning, such as the presence of CT artefacts due to metal implants in the patient. Improved algorithms have been proposed that correct for effects from beam hardening and/or from missing projections, as shown by Verburg and Seco (2012).

1.1.4.2 Dose-changing phenomena

Additional sources of uncertainty in the delivered dose result from local changes in both the composition and density of the traversed tissues, with respect to the planning CT, occurring throughout the course of the fractionated therapy (typically lasting several weeks). In fact, Kraan *et al* (2013) have shown that the combined effect of anatomical, range, and setup errors on the simulated delivered dose in the specific case of IMPT for oropharyngeal cancer patients, was larger than the sum of the effects separately.

Interfractional changes in patient anatomy may occur due to, for example, weight gain/loss and tumor progression/regression, as well as due to physiological mechanisms such as the filling of internal cavities (e.g., bladder, bowel, nasal cavities). In addition, biological mechanisms occurring in response to radiotherapeutic injury (Denham and Hauer-Jensen 2002) may also contribute to changes in tissue density and composition (e.g., due to edema or formation of scar tissue). Such anatomical/tissue changes can drastically affect the dose distribution if not adequately dealt with. In fact, they may yield tumor underdosage (Müller *et al* 2015) and/or healthy-tissue overdosage (Nishio *et al* 2006). An example of OAR overdosage due to tumor regression is shown in figure 1.3. Some examples of interfractional dose changes will be further addressed in chapter 6.

Interfractional and intrafractional variations can also occur due to motion (Lomax 2008b). Intrafractional variations are mostly attributed to organ motion (e.g., respiratory and involuntary bowel movements). Some strategies to minimize motion effects and their limitations have been reviewed by e.g. Engelsman *et al* (2013). Finally, there can be setup errors. Although these are typically minimized by online alignment of the bone anatomy prior to irradiation (based on X-ray radiography), the existence of possible inaccuracies combined with effects such as intrafractional patient motion might induce considerable patient-to-beam alignment errors.

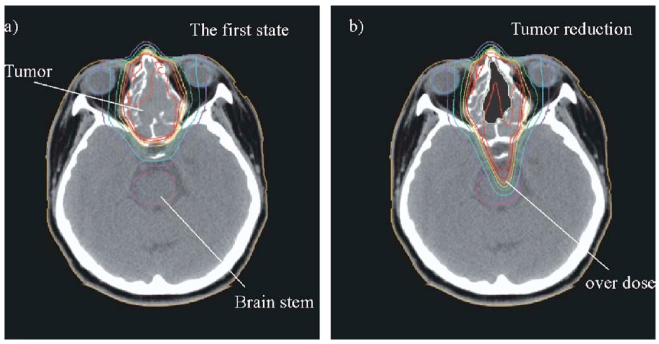

Figure 1.3: Example of a proton dose distribution for a tumor of the paranasal sinuses. *Left:* dose distribution at the beginning of the treatment. *Right:* dose distribution after several fractions. The reduction of the tumor volume gives rise to harmful overdosing of the radiation-sensitive brainstem. From (Nishio *et al* 2006).

1.1.4.3 Dose-delivery uncertainty reduction by imaging and adaptive therapy

It is the desire of any radio-oncologist to be able to detect and quantify range uncertainties and dose-changing phenomena such as those described in the previous sections. This would allow the improvement of PT clinical outcomes by continuously supporting physicians in their decision to: (1) stop and re-plan a treatment that has evolved to a situation that does no

longer fulfill the initial dose requirements (adaptive therapy), or (2) proceed the treatment with reassured quality (an important variable for both the RT team and the patient). So-called image-guided radiation therapy (IGRT) constitutes the state-of-the-art technology aiming at this task.

In adaptive proton therapy, treatment re-planning (dose recalculation) may be applied when justified, based on repeated imaging of the patient anatomy, ideally realized immediately before treatment delivery in order to minimize anatomical errors (online adaptive therapy). For this purpose, recent and upcoming proton therapy centers are putting efforts towards the implementation of *in-situ* anatomical imaging by means of e.g., an in-room CT on rails that shares its couch with the treatment equipment. While adaptive therapy is an effective way to mitigate most of the interfractional sources of dose errors, the optimal adaptive strategy, including the frequency of volumetric imaging, is yet an open question (Kraan *et al* 2013) due to for e.g. the added dose intrinsic to such imaging, and possible compromise of patient throughput.

Proton therapy monitoring by means of imaging secondary γ rays emitted from the patient (section 1.2) may be a valuable tool to provide an end check of treatment delivery for every fraction. Compared to prior-to-treatment volumetric imaging, it has the potential advantage of enabling the detection of intrafractional dose variations and unpredicted/not-accounted-for errors in treatment delivery in general (arising from the whole treatment chain), while at the same time not constituting any additional dose to the patient. In addition, it may aid adaptive proton therapy by, for example, triggering the necessity for a repeat CT scan and dose recalculation should a deviation from the treatment plan be detected (section 1.2.3), in case CT scans are not taken prior to every fraction. Proton therapy monitoring techniques could ultimately enable intrafractional online adaptive therapy, should (1) the adaptation of treatment planning by re-optimization algorithms be made fast enough (i.e. within the time frame of the treatment fraction) and (2) treatment-delivery monitoring be possible in real time, including necessary image processing for the detection of dose deviations.

For completeness, it should be mentioned that further improvements in CT imaging are expected to reduce the CT-related range uncertainties in treatment planning. In particular, dual-energy CT and spectral CT may provide more accurate estimations of relative proton stopping powers, especially for soft tissues with approximately the same CT number but different elemental compositions (Yang *et al* 2010, 2012). A promising approach to measure the proton range directly, which is currently under development, is the proton radiograph (2D projection imaging) or proton CT (volumetric imaging). In this approach, beams of protons with energies above therapeutic range are applied to the patient, such that they exit the patient, and the proton stopping power in the tissues can be derived by measuring the beam residual range. Proton CT may eventually replace conventional X-ray CT in proton therapy, as it has the potential advantage of reducing the imaging dose exposure as well as further reducing CT-related range uncertainties (Schneider and Pedroni 1995). A more complete review of these and other *in vivo* proton range verification modalities has been reported by Knopf and Lomax (2013).

1.2 *In vivo* proton therapy monitoring by imaging secondary γ-rays

In the case of PT, there is no primary radiation emerging from the target as the therapeutic beam is stopped inside the patient. Although direct dose measurements are possible through implantation of dosimeters, they provide only local information and constitute an invasive

method that has limited applicability (Knopf and Lomax 2013). This work focusses on *in vivo* proton therapy monitoring by measuring secondary gamma (γ) radiation emitted by the patient, as a result of nuclear interactions between the projectiles and the nuclei of the irradiated medium (section 1.1.2.3). Such techniques are mainly divided into two categories, according to the type of secondary γ rays probed: (1) positron emission tomography (PET), which makes use of delayed emission, namely pairs of 511 keV annihilation photons, resulting from projectile (heavy-ion RT) and/or target-induced (proton and heavy-ion RT) radioactivity; and (2) prompt gamma (PG) imaging, which makes use of the emission of single photons typically on a sub-nanosecond timescale. A brief overview of the fundamental concepts underlying these techniques will be given in the following sections.

1.2.1 Positron emission tomography (PET)

As the name indicates, PET is a technique used to image the spatial distribution of positron (β^+) emitters, or more precisely, of the positions of positron-electron annihilation events following β^+-radioactive decay. PET scanners with incorporated CT are well-established tools that are widely used for diagnostic purposes in the context of nuclear medicine, to image the distribution of radiotracers that are injected in the body and that bind to particular sites such as a tumor. PET in particle therapy (PT PET) was first proposed by Maccabee *et al* (1969) and implemented in clinical routine by Enghardt *et al* (1999, 2004). Although it is a readily available technique in nuclear medicine, the particular needs and constraints in PT impose technological demands and further customization beyond typical clinical PET/CT scanners.

1.2.1.1 Basic principles of PET and Time-Of-Flight PET

Since positron annihilation events give rise to the emission of two gamma rays in nearly opposite directions, each with an energy equivalent to the rest mass of the electron/positron (511 keV), spatial discrimination of the position of emission in PET relies on the coincidence detection of the two annihilation quanta, typically using rings of detectors (figure 1.4). The line connecting the two detection points that occur in the same coincidence interval window is called line of response (LOR). In practice, however, one has to deal with tubes or volumes of response due to the finite size of the detector elements. If fast detectors are used, i.e. capable of resolving the time difference between the arrival of the two gamma rays (viz. $t_2 - t_1$ in figure 1.4), the time-of-flight (TOF) information can be used to confine the event to the most probable section within the LOR (TOF PET). The width $\triangle x$ of this section, i.e. the uncertainty in spatial positioning, depends directly on the accuracy to resolve the time difference (i.e. the coincidence resolving time, CRT), with $\triangle x = c \cdot \mathrm{CRT}/2$, and c being the speed of light. Currently, clinical TOF-PET scanners typically have a CRT of about 550 ps FWHM, corresponding to $\triangle x = 8.2$ cm FWHM (Lois *et al* 2010). It must be stated for completeness that commercial PET systems exist with a CRT as low as 325 ps and < 400 ps FWHM, based on digital (Vereos PET/CT (Philips-Healthcare 2015)) and analog (SIGNA PET/MR (GE Healthcare 2016)) silicon photomultipliers, respectively (section 1.3.2). Considerable improvements are further expected in the near future (Schaart *et al* 2010, Seifert *et al* 2012b, van Dam *et al* 2013, Schaart *et al* 2016).

In PET imaging, image reconstruction techniques are necessary to estimate the spatial distribution of the activity from the finite set of detected coincidences. A primitive but elucidative way of image reconstruction consists of backprojecting all the detected LORs, such that the intensity value for a given image voxel is obtained by summing the contribution from all LORs that cross that voxel. All the image voxels along any LOR may be

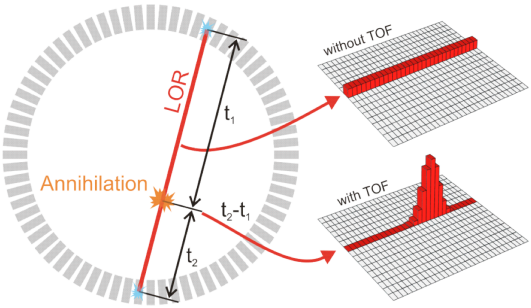

Figure 1.4: Principle of time-of-flight positron emission tomography (TOF PET). In TOF PET, the difference in the arrival times of the gamma quanta is used to localize the position of annihilation with approximately centimeter resolution along a line-of-response (LOR).

assigned equal weights or different weights in the case TOF information can be used (figure 1.4). In order to reduce the inevitable blurring present in such images (i.e. the spreadout of the apparent activity outside the true location), the projection (detected) profiles are convoluted with a 'ramp' filter before they are backprojected to the image space, a method called filtered backprojection. Despite the fact that this method is typically outperformed in terms of image quality by more complex, modern iterative reconstruction methods, it still remains as a standard check of image quality.

Iterative reconstruction methods rely on accurate mathematical models that can incorporate corrections associated with physics processes, such as correction for the attenuation and scattering of gamma rays within the patient. Gamma attenuation increases with the object size and, if not corrected, gives rise to e.g. higher intensity at the edges. Compton-scattered gamma rays lose directional information, thus they constitute background and contribute to image noise. These are partially rejected by selecting events that deposit about 511 keV energy in the detector, the extent of which depends on the detector energy resolution. Another source of background are the so-called random coincidences, i.e. the detection of two gamma rays that arise from different annihilation points. The rate of random coincidences is proportional to the square of the singles count rate and to the size of the coincidence window (Lewellen and Karp 2004). Based on the above simple considerations, it becomes clear that the use of TOF information improves the signal-to-noise ratio (SNR), hence the image quality. In fact, the use of TOF information enables the confinement of the position estimation of the annihilation point within a LOR (figure 1.4), and allows a reduction of the size of the coincidence window to about the size of the patient/object being imaged, hence the amount of random coincidences.

1.2.1.2 PT PET

The initial clinical experience in PT PET was in the context of carbon-ion RT (Enghardt *et al* 2004), where activity densities of ~200 $BqGy^{-1}cm^{-3}$ after considering biological washout were created, with typical fields having a physical dose of ~0.5 Gy (Crespo 2005). The feasibility of PET monitoring in proton therapy was first supported from simulation studies by Parodi and Enghardt (2000) and subsequent experimental investigations (Parodi *et al* 2002, Parodi *et al* 2005b). A comparison with carbon-induced activation showed the proton-induced activation to be about three times larger at the same range and applied physical dose (Parodi *et al* 2002). This ratio should further increase considering (1) that the RBE of

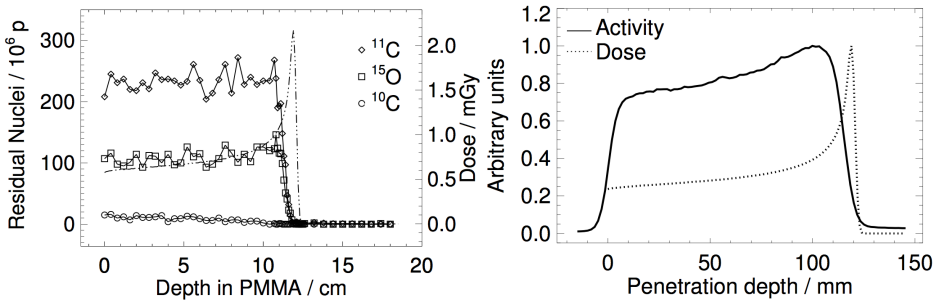

Figure 1.5: Simulated depth distribution of positron emitters, using FLUKA Monte-Carlo code (left), and exemplary measured activity distribution (right), produced in PMMA upon irradiation with a 140 MeV proton beam. The calculated depth-dose distributions are shown by the dashed curves. Left figure from (Parodi and Enghardt 2000) and right figure from (Parodi *et al* 2005b).

carbon ions is higher than that of protons and (2) the observed higher ^{15}O to ^{11}C production-rate ratio for protons in comparison to carbon ions (Parodi *et al* 2002).

Figure 1.5 shows the spatial correlation existing between the depth-dose profile created by a proton beam and the most prominent β^+-emitting radioisotopes produced in PMMA (left), as well as the PET signal (right) measured with a double-head PET scanner. The lack of induced activity due to the decreased nuclear cross section for the production of β^+-emitting nuclei in the last part of the proton track can be seen. Reviews of threshold energies and reaction cross sections can be found in the literature (Beebe-Wang *et al* 2003, Fiedler *et al* 2012, Seravalli *et al* 2012, Sarrut *et al* 2014, de Napoli *et al* 2014).

In table 1.1 the most relevant positron emitters that can be produced by protons on the most abundant nuclei in human tissue are listed. Although ^{15}O is one of the most relevant radionuclides produced, it can be seen that its half-life makes it useful mostly if the PET signal is acquired during the irradiation (in-beam PET, e.g. Enghardt *et al* 2004). Carbon-11, the most produced β^+-emitting radioisotopes in human tissue, is the main component of the PET signal in so-called offline PT PET (Parodi *et al* 2007b). Its distribution is nevertheless highly affected by the process of biological washout of the induced activity, which must be corrected in order to compare predicted versus measured PT PET images (figure 1.6).

The remaining isotopes in table 1.1 are short lived. With the exception of ^{10}C, this means that their readout requires the application of the in-beam PET method further assisted by beam-on measuring techniques (i.e. acquisition of the PET signal during spill extraction (Crespo *et al* 2005)). Dendooven *et al* (2015) have studied the feasibility of utilizing the PET signal from ^{12}N, ^{38m}K, and ^{29}P, the latter two being only produced in bone tissue. The conclusions of that study are that these very-short-lived nuclei are produced in relevant amounts, thus opening new possibilities of using the beam-on in-beam PET method for monitoring proton therapy.

Using the in-beam PET method requires a scanner that takes data during patient irradiation. Its implementation can be accomplished by using a dual-head positron tomograph (Enghardt *et al* 2004, Nishio *et al* 2006). Nevertheless, Crespo *et al* (2006) have studied the induction of image artefacts produced by such a dual-head in-beam PET solution, if TOF PET is not implemented. A full-ring tilted PET scanner would allow these artefacts to be avoided. Although its realization is not trivial, a suitable design is being implemented by Tashima *et al* (2012) at the potential compromise of beam entrance portals. On the other

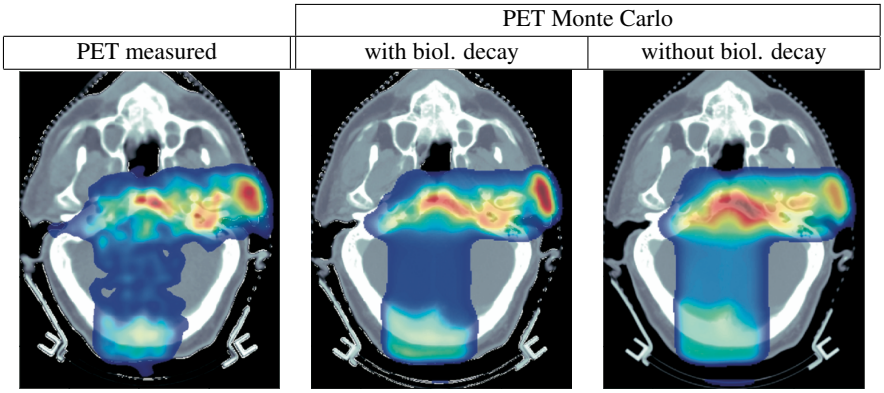

Figure 1.6: Clinical application of the offline PET method to monitor a two-field irradiation in proton therapy, after (Parodi *et al* 2007b). It can be seen that soft tissues are more affected by the process of biological washout than harder tissues like bone. In addition, poorly irrigated fat tissue (high-intensity PET signal in the face near beam entrance) reveals itself insensitive to biological washout.

Table 1.1: List of most-relevant positron emitters that can be produced by protons on the most abundant nuclei in human tissue (Beebe-Wang *et al* 2003, Fiedler *et al* 2012, Dendooven *et al* 2015). The different reaction channels for the production of the same radioisotope are listed in descending order of cross sections (Fiedler *et al* 2012).

Positron emitter	Half-life	Production channel
^{15}O	2.037 min	^{16}O(p,pn)^{15}O
^{11}C	20.385 min	^{12}C(p,pn)^{11}C; ^{14}N(p,2p2n)^{11}C$^{(a)}$; ^{16}O(p,3p3n)^{11}C$^{(b)}$
^{10}C	19.2 s	^{12}C(p,p2n)^{10}C; ^{14}N(p,nα)^{10}C; ^{16}O(p,3p4n)^{10}C
^{13}N	9.965 min	^{14}N(p,pn)^{13}N; ^{16}O(p,2p2n)^{13}N$^{(a)}$
^{12}N	11.00 ms	^{12}C(p,n)^{12}N
^{30}P	2.498 min	^{31}P(p,pn)^{30}P
^{29}P	4.1 s	^{31}P(p,p2n)^{29}P
^{38}K	7.636 min	^{40}Ca(p,2p2n)^{38}K
^{38m}K	0.925 s	^{40}Ca(p,2p2n)^{38m}K

(a): (p,2p2n) is inclusive of (p,α)
(b): (p,3p3n) is inclusive of (p, α pn)

hand, the aforementioned image artefacts are considerably reduced by including TOF information in the reconstruction, as shown by simulations of realistic clinical irradiations (Crespo *et al* 2007, Dendooven *et al* 2014) and phantom studies (Surti and Karp 2008, Surti *et al* 2011). Crespo *et al* (2007) has shown that a CRT of 200 ps FWHM or better is necessary for a dual-head tomograph with a coverage angle of 134° by 134°. For range estimation, it appears sufficient to have a CRT of 300 ps FWHM using a dual-head tomograph with a coverage angle of 90° by 90°, or a CRT of 600 ps FWHM and a larger coverage of 120° by 120° (Surti *et al* 2011).

1.2.2 Prompt gamma imaging

In the context of PET imaging, prompt gamma (PG) rays contribute to background (Parodi *et al* 2005a), thus dedicated random suppression techniques are required to realize beam-on PT PET (Crespo *et al* 2005). The idea to use the prompt gamma rays themselves for monitoring the proton range has been suggested and supported by simulations by Stichelbaut and Jongen (2003), while the first experimental evidence was reported by Min *et al* (2006). The main proton-induced characteristic PG lines emitted from elemental constituents of biological tissue (C, O, Ca, N) have been reviewed and supported by simulations (Polf *et al* 2009a, Verburg *et al* 2012) and measurements (Polf *et al* 2009b, 2013, Smeets *et al* 2012b, Verburg *et al* 2013, Verburg and Seco 2014). Characteristic PG emission was found proportional to the tissue density, while the relative intensity of the gamma lines scales with the respective atomic density and tissue composition (Polf *et al* 2009a). In particular, measurements of the 6.1 MeV gamma line from ^{16}O can be used to probe the oxygen concentration in tissues, as shown by Polf *et al* (2013). Various approaches have been suggested for imaging PGs, as described in the following sections.

1.2.2.1 Mechanical collimation

The principle of PG imaging by mechanical collimation is illustrated in figure 1.7. The collimator is made of a high-Z attenuating material that only accepts gamma rays impinging in certain directions, which in the case of the example shown corresponds to the direction perpendicular to the beam axis. Such a multi-slit or multi-slat collimator (Min *et al* 2010, 2012, Gueth *et al* 2013, Pinto *et al* 2014, chapter 6) is composed of parallel plates ('slats') regularly spaced, typically made of tungsten. The combination of the detection point of the gamma ray (r_γ) and the lateral position of the pencil beam (r_b) yields the position of gamma emission. The first experimental demonstrations of the correlation between PG collimated profiles and the dose distal falloff were demostrated by means of 90º angle projections with the beam axis through a collimator hole (Min *et al* 2006) or a slit (Testa *et al* 2008), measured by a single detector moved parallel to the beam. In the case of proton therapy, the particles that escape the patient are mostly neutrons, which contribute to background radiation (figure 1.7). Other collimator types have been suggested, such as a one-dimensional pinhole-like setup denoted as knife-edge slit (Peloso *et al* 2011, Bom *et al* 2012, Smeets *et al* 2012b) (chapter 4, figure 4.1).

Such collimators resemble to some extent those of typical gamma cameras used in nuclear medicine, viz. in scintigraphy or SPECT (single photon emission computed tomography). However, in PG imaging the ratio of occurence of Compton events (to the total interaction probability) is considerably higher than in nuclear medicine. This fact is attributed to the comparatively higher energies of PGs (viz. ~1-10 MeV versus a few 100 keV for typical radiotracers in nuclear medicine). In particular, the cross section for Compton scattering and the photoelectric effect for 5 MeV γ-rays in tungsten is 49% and 2.2%,

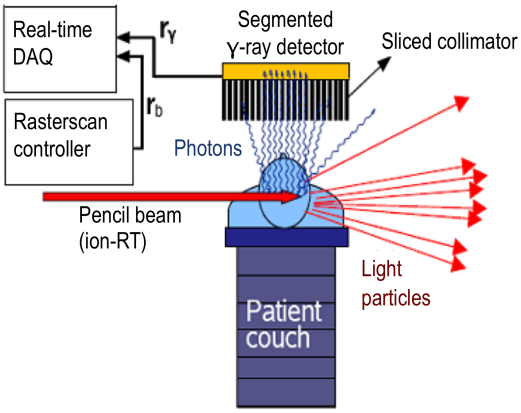

Figure 1.7: Possible prompt-gamma detector concept implementation at a proton therapy site. The 2D position of the pencil-beam (r_b) at each instant is delivered by the active-scan controller to the data acquisition (DAQ) electronics, which correlates it with each event collected in the gamma-ray detector. Due to the perfect azimuthal symmetry of each ejected photon with respect to the linear position of the beam, a 3D image with each beam position can be reconstructed if the detector provides only the axial coordinate of each event. For this reason, and in order to optimize counting statistics, it suffices that the collimator rejects only those photons that are tilted with respect to the beam direction.

respectively, of the total attenuation cross section. For 150 keV γ-rays in lead, these values are 5.0% and 95%, respectively (Berger and Hubbell 2010). Furthermore, the mean free path of 5 MeV γ-rays in tungsten is almost 30 times higher than for 150 keV γ-rays in lead. Different sizes and aspect ratios of the collimator geometries are therefore expected in comparison to a gamma camera, which has a typical collimator height of ~2.5 cm (Cherry *et al* 2003).

1.2.2.2 Compton camera

Different Compton camera concepts for PG imaging are currently being investigated (Kang and Kim 2009, Richard *et al* 2009, 2011, Llosá *et al* 2010, Peterson *et al* 2010, 2011, Kormoll *et al* 2011, Robertson *et al* 2011, Roellinghoff *et al* 2011). These concepts include multi-stage measurement devices capable of determining the initial energy and direction of a gamma photon as it undergoes Compton scattering within the different stages of the detectors that compose a Compton camera. Figure 1.8-left illustrates the principle of a single-layer Compton camera. The initial gamma ray ($E_{\gamma,i}$) must interact via Compton scattering in the scatterer, and undergo photoelectric effect in the absorber. Kinematic considerations implemented into an appropriate reconstruction algorithm allow a Compton cone to be defined in the image space. It is the overlap of Compton cones from several events that allows the original spatial distribution of gamma-ray emissions to be determined.

The detection efficiency of a Compton camera can be highly increased if several layers of position-sensitive tracking detectors are used to obtain the trajectory of the Compton-ejected electron (figure 1.8-right) (Thirolf *et al* 2014b). This allows the Compton cone to be restricted to an arc, hence improving the reconstruction efficiency since also incompletely absorbed photons can be used. This requires, however, the kinetic energy of the Compton electron to be large enough to penetrate at least one layer of the tracker array, which occurs

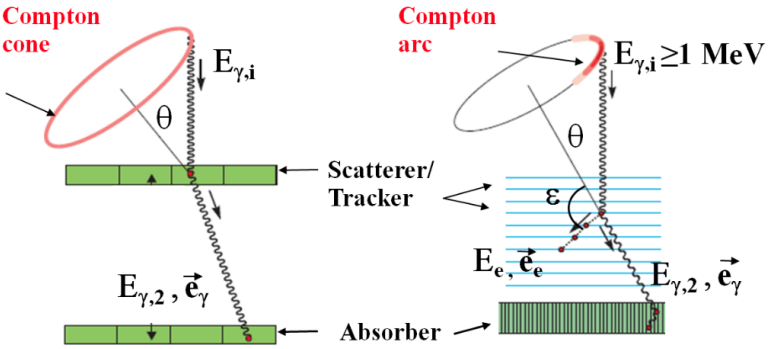

Figure 1.8: Illustration of the concepts of a single-layer 'γ−tracking' Compton camera (left) and an electron-tracking Compton camera (right). In γ−tracking mode, the position of Compton interaction and energy of the Compton electron (E_e) are detected in the scatterer, and both the (full) energy ($E_{\gamma,2}$) and the position of the scattered γ−ray are detected in the absorber, allowing for the determination of the direction of the scattered γ−ray ($\vec{e}_\gamma$), the initial γ−ray energy ($E_{\gamma,i}$) and the scattering angle θ. In electron-tracking mode also the direction of incidence of the initial γ−ray can be determined to some extent, using the additional information of the electron trajectory ($\vec{e}_e$) obtained by means of a scatterer made of multiple thin layers. From (Thirolf 2015).

for gamma rays with energies typically above 1 MeV.

Finally, an arrangement of, for e.g., four camera modules could even be used in a gamma-PET mode to detect delayed annihilation radiation from positron emitters in the irradiation interrupts (with improved performance in the presence of an additional third (prompt) photon (as in ^{10}C and ^{14}O) (Thirolf *et al* 2014a).

1.2.2.3 Prompt gamma-ray spectroscopy

Collimated, single-detector PG-ray spectroscopy has been proposed by Verburg and Seco (2014) as a method to determine (1) the absolute range of the proton beam and (2) the oxygen and carbon target concentrations at a position in the target close to the end-of-range of the beam (tested in targets of water and 'solid water', the latter containing carbon). Absolute ranges were determined with a standard deviation of 1.0 mm - 1.4 mm, based on five pencil-beam irradiations with different energies (thus Bragg peak locations) but same lateral location, each delivering 5×10^8 protons. In addition, the authors were able to detect a range shift (relative to an absolute pre-determined range) on the order of 1 mm for only one beam with a fluence of 5×10^8 protons. The method relies on the accurate knowledge of (1) the nuclear cross sections of the PG lines, (2) the distribution of proton energies along the beam path for a particular (initial) beam energy, (3) the transfer function of the collimator, representing the number of gamma rays impinging on the detector, and (4) the gamma-ray detection efficiency of the detector, which was based on a $LaBr_3$:Ce crystal surrounded by BGO crystals that served as an active anti-coincident shield. The detector is located at a fixed position, at an angle of 90º with respect to the beam axis. Prior RF-based, time-resolved measurements and optimization of differential cross sections for a set of discrete PG lines created on C and O are required as a function of a known set of proton energies. The method further relies on Monte Carlo modeling of the PG detection probability as a function of gamma-ray energy, proton energy, target element, and water

equivalent depth (i.e. the thickness of water that would cause the same Bragg peak shift as the material of interest). A mathematical function is then implemented that minimizes the square of the measured versus expected number of counts, yielding, for a given number of measured counts, the water equivalent depth and the concentrations of oxygen and carbon at the measurement point. The method was tested for beam energies corresponding to a range in water between 15.54 cm and 17.59 cm.

1.2.2.4 Prompt gamma-ray timing

A method based on the uncollimated, single-detector measurement of the cumulative distribution of PG arrival times originating from the whole proton path was proposed by Golnik *et al* (2014). The structure of the PG timing is determined by the ion transit time in the target, which in turn varies with energy (thus range) and can be affected by the presence of tissue heterogeneities in the traversed medium. The authors were able to describe the experimental findings with kinematic models and suggest the correlation of statistical moments with the proton range, such as the mean and sigma of the timing distribution (determined relative to the cyclotron RF). Hueso-González *et al* (2015) further showed experimentally that individual features in the spectrum shape can be identified in the presence of bone inserts or air cavities, provided that the proton bunch width is sufficiently low, viz. ~0.4 ns FWHM, which could be obtained for the highest proton energy of 230 MeV due to the absence of a degrader in the beam line. The method is able to determine range variations of the order of 2 mm in PMMA for a pencil-beam fluence of 10^{10} protons. Furthermore, the authors claim that 10^8 protons seem to be the threshold for determining a 5 mm shift of the falling edge in a single spot. Finally, kinematic considerations allowed depth-emission profiles to be reconstructed, providing the location of a 2-cm-thick bone insert within the beam path to some degree.

1.2.3 Role of Monte Carlo simulations

Monte Carlo (MC) plays a crucial role both in PT PET and PG techniques since it allows comparing measurements with the expected spatial distribution of β^+ emitters or PGs. Figure 1.6 shows such a clinical example for monitoring proton therapy, whereby the comparison is performed between calculated (MC) and measured (PT PET) β^+ distributions. Enghardt *et al* (2004) have shown for PT PET in the monitoring of carbon ion therapy that it is also possible and useful to compare β^+ distributions measured in different days of patient irradiation (i.e. different fractions). In addition, Enghardt *et al* (2004a) and Parodi (2004, 2012) have shown that deviations between the predicted and the measured β^+ distributions with PT PET may allow for conjecture on pertinent patient anatomy changes, which in turn serve as input for a dose recalculation: the first step towards adaptive PT based on PET. The same concept is also highly desired for PG imaging techniques. Indeed Freeman (2015) has reported that a PG device for monitoring proton therapy treatments has recently started clinical operation. It must be stated that the role of MC in PT monitoring is expected to increase should the implementation of hypo-fractionated treatments become a reality: in this case a comparison between images measured in different days would be reduced. For completeness, analytical models have been shown useful to predict PET emission data as a fast alternative to the MC approach (Attanasi *et al* 2011).

Finally, it is also known that treatment planning algorithms are mainly based on analytic calculations that incorporate more or less complex beam-delivery models adapted to the patient anatomy obtained via a planning CT. Detailed MC simulations are in many cases

avoided due to the long time required to converge to a dose distribution solution. Nevertheless, in more complicated cases the MC solution may indeed be sought, or otherwise further improvements in dose calculation algorithms should be implemented, as pointed out, for example, by Verburg and Seco (2013), whom have shown calculations of treatment plannings of chordoma patients with titanium implants (refer also to section 1.1.4.1).

1.2.4 Advantages and disadvantages of prompt versus delayed gamma radiation

The results shown in figure 1.9 summarize some of the advantages of imaging PGs versus β^+ emitters in PT. The images were obtained from a Geant4 simulation corresponding to a proton treatment in the dorsal region. The top-left image shows the dose distribution of the treatment, whereas the top-right one depicts the location of PG creation originated by the same treatment. The two bottom images correspond to the distribution of created β^+ emitters without (left) and with (right) biological washout for a measuring time complying to an in-room PET solution: 2 min delay time; 5 min acquisition time; and 30 second irradiation time, corresponding to a typical 2 Gy dose fraction. Distal extension of the PET distribution is smaller when compared to PG imaging, which in the case mentioned can be observed by a lack of PET signal in the irradiated abdominal aorta. This difference is due to the fact that the cross section for the production of β^+ emitters has a higher energy cutoff with respect to PG production. It can further be observed that a better correlation exists between CT and PG 2D distributions. This can be noticed for e.g. in the right kidney, vertebra, and in the proximal higher-density tissue corresponding to the ribs region. In addition, figure 1.6 shows that regions with poorly-irrigated fat tissue (carbon rich) present a high level of the PET signal that does not vanish with time. Since fat tissue does not present itself with high density, the PG signal is not enhanced in such region (not shown), again corroborating the verification that PG images are better correlated with CT information with respect to PT PET.

One strong advantage of PT PET over PG imaging is the fact that the former can be measured with beams delivered either by synchrotrons or cyclotrons. This is because the PET signal can be measured during the pauses of the spill, without neutron contamination. In fact, and with exception of the PG timing method operated with pencil beams, the neutron background constitutes one of the main challenges for PG imaging (Testa *et al* 2008, 2009, 2010, Biegun *et al* 2012 in chapter 3). Applying the TOF technique seems to be the best method to mitigate such neutron background. However, such TOF implementation requires that the proton accelerator delivers beams in microbunches with nanosecond to sub-nanosecond time widths.

Finally, the cross sections for the production of β^+ emitters are better established in present-day MC codes (Robert *et al* 2013), which makes the PET method more reliable when calculations are compared to measurements. With respect to PG yields, state-of-the-art experiments are being carried out in order to obtain the corresponding nuclear cross sections (Pinto *et al* 2015, Schumann *et al* 2015).

In conclusion, it is presently very difficult to compare the effectiveness of PET and PG imaging for monitoring proton therapy. On the one hand, PET is a mature technique that has already proven clinical value and shown great potential advantages; however, correlated with necessary technological advances (e.g., coincidence time resolution of whole system). On the other hand, PG imaging is in the early stage of development, with several competing approaches being proposed in the literature, in the form of proof-of-principle studies that highlight the promising capabilities of such PG technique(s). PG production in biological tissues show pertinent clinical correlations (to CT and proton range), but much demanding

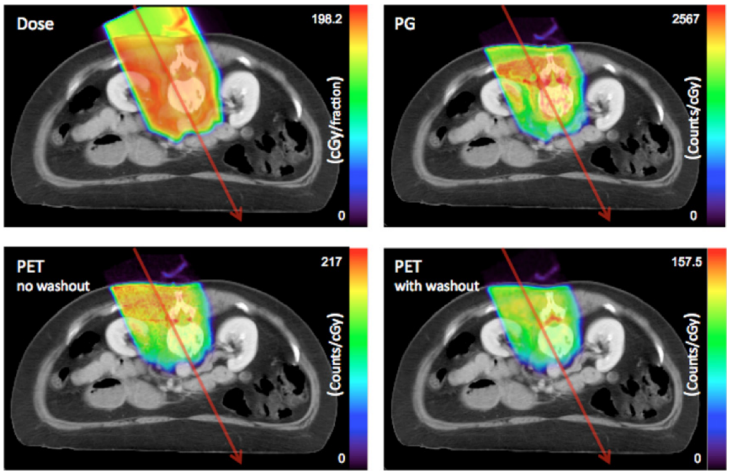

Figure 1.9: Geant4 simulation corresponding to a proton treatment in the dorsal region. The top-left image shows the dose distribution of the treatment, whereas the top-right one depicts the location of PG creation originated by the same treatment. The two bottom images correspond to the distribution of created β^+ emitters without (left) and with (right) biological washout for a measuring time complying to an in-room PET solution. From (Moteabbed *et al* 2011).

technology may be necessary in comparison to PET, before a working device is brought into operation. Only when PET and PG will be optimized at a full-system level can they be compared.

Furthermore, due to the different physics associated with the γ-radiation involved and the different imaging methodologies, they are likely to become complementary and their applicability and suitability may depend on the particular treatment circumstances (e.g., irradiation target, passive vs. active beam shaping) and on the particular treatment facility/infrastructure (affecting e.g., the beam time structure). For example, the amount of material used to shape the proton field in the widely applied, passive-scattering PT, produces a considerable amount of background (neutron, gamma) radiation, that might further hinder the useful PG signal measured with e.g. a collimated detector setup (Kurosawa *et al* 2012, Knopf and Lomax 2013), in comparison to active delivery techniques. As another example, PET imaging in situations where the irradiation field contains highly-perfused tissues might be ultimately hindered by the limited accuracy to model the biological washout of the radiation. Lastly, PG signal is not available during the beam pauses of synchrotron-delivered particle beams, in which case PET images with sufficient quality have been shown (Crespo *et al* 2006).

1.3 Scintillation γ-ray detectors

Scintillation-based gamma detectors have found wide-spread use in medical imaging applications, such as emission tomography. These detectors consist mainly of two components: the scintillation crystal and the photosensor. The scintillator converts the energy of the detected γ-ray into optical photons in the spectral region corresponding to the visible and/or ultraviolet. The scintillation photons further travel through the crystal and optical

coupling towards the photosensor, where they are converted into an electrical signal. The γ-ray may deposit all or part of its energy in the crystal, depending on the type of interaction(s) occurring, namely photoelectric effect, Compton scattering, and/or pair production. Full-energy deposition requires that a photoelectric interaction takes place alone or in combination with other interaction event(s). For example, if pair production occurs (for γ-rays with energies above 1.022 MeV), and one of the γ-rays emitted from positron/electron annihilation escapes the crystal while the second one is detected, a so-called single-escape event is observed, with an energy deposition equal to the original γ-ray minus the electron rest mass. Scintillators suitable for TOF applications (e.g., LYSO:Ce among others (Crespo *et al* 2007)) should produce a relatively high amount of scintillation photons in a short period of time, i.e. require a high light yield (number of photons emitted per unit energy deposited), and a short rise and decay times of the light pulse. The crystal size should be small enough to limit the transit time of the optical photons as well as light losses, at the same time large enough to ensure sufficient detection efficiency for the application.

1.3.1 Silicon photonmultiplier

Silicon photomultipliers (SiPMs) are increasingly interesting photosensors for fast readout of scintillation light. Their main advantages in comparison to typical photomultiplier tubes (PMT) are compactness, smaller timing jitter, and insensitivity to magnetic fields, opening up possibilities for e.g. integrating PET with magnetic resonance imaging (PET/MRI). SiPMs consist of arrays of many microcells operated in Geiger-mode, or single-photon avalanche photodiodes (SPADs), connected in parallel. Each microcell is capable of detecting a single photon, and the summation of signals from all fired microcells may produce a signal with amplitude proportional to the amount of incident light, provided that the number of cells is considerably higher than the number of incident photons (before saturation effects start to take place).

1.3.2 The digital photon counter

In the digital implementation of SiPMs (dSiPMs), first introduced by Philips Digital Photon Counting (PDPC) (Frach *et al* 2009, 2010, Degenhardt *et al* 2009), each microcell is equipped with active circuitry that quenches the discharge (avalanche) occurring after detection of a photon, as well as with a 1-bit cell memory or logical switch that stores the information of whether a discharge has occurred. Furthermore, each cell is connected to a balanced trigger network and a trigger level as low as the first photon can be set for the timestamp acquisition (Frach *et al* 2009). In these devices, light-pulse summation is done by simply counting the number of fired cells. This fact together with the unique feature of de-activating individual cells to reduce the dark-count rate, further reduces the electronic noise in comparison to analog SiPMs.

Such digital photon counters (DPCs) have been developed into a highly-compact, scalable modular design (figure 1.10-top) (Degenhardt *et al* 2012, Haemisch *et al* 2012). Its basic functional unit consists of an arrangement of 2×2 DPC-pixels (dSiPMs) at a 4-mm pitch, so-called DPC-chip, which incorporates two time-to-digital converters (TDCs) for time-stamp generation, and readout electronics. Each DPC-pixel contains 3200 microcells, with a fill factor (i.e. ratio of active to total sensor area) above 70% (Schaart *et al* 2016). The acquisition chain on the level of the chip, as depicted in figure 1.10-bottom, allows for a set of user-configurable thresholds (for triggering and validation) and delays (Frach *et al* 2009*,* 2010, Tabacchini *et al* 2014). Thresholds are satisfied when a (statistical) number of

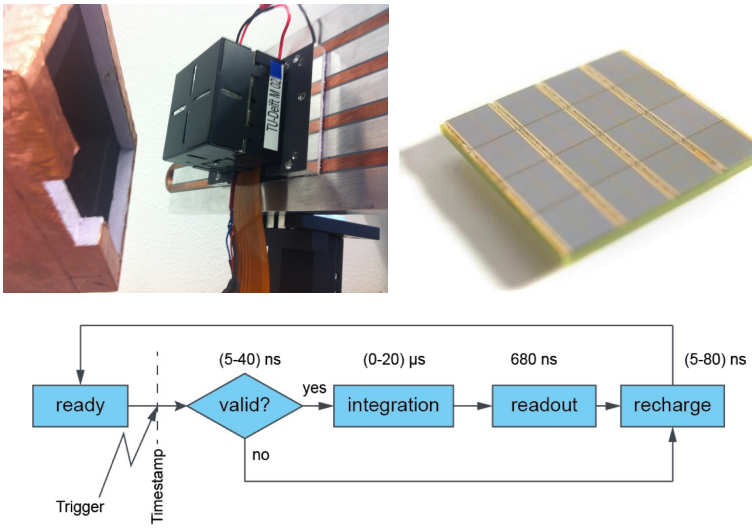

Figure 1.10: Top: Photographs of a DPC-MO-22-3200 detector module used in this thesis, with a total surface area measuring 68 mm × 68 mm (left), and a DPC3200-22-44 array of 8×8 digital photon counters or DPC-pixels, with a 4 mm pitch (right), from Philips Digital Photon Counting. Each module contains four DPC arrays, and each array is optically coupled to a stack of pixelated crystal matrixes, in a 1:1 coupling between the scintillator crystals and the DPC-pixels. The detector module shown is mounted on a cold plate being actively cooled by Peltier elements, which in turn are attached to a plate internally flushed with running tap water for heat dissipation. Also shown is the light-tight box used to enclose the detector and to prevent moisture by continuously flushing with dry nitrogen gas. Right image from (Degenhardt *et al* 2010). Bottom: Schematic representation of the data acquisition chain within a DPC-chip, which is composed of 2×2 DPC-pixels. From (Tabacchini *et al* 2014).

microcells fire in a given logic pattern (Tabacchini *et al* 2014). The trigger logic is implemented on pixel level, whereby the trigger threshold requires that a minimum number of sub-pixels (1, 2, 3, or 4) must be fired to create a time stamp. After triggering, the whole DPC-chip enters a validation phase, which is followed by an integration period (i.e. light pulse collection) if and only if the validation threshold is satisfied during the validation interval (chapters 2 and 4). Upon readout of a valid event, the DPC-chip outputs the (digital) number of fired cells on each of its four pixels, as well as one time-stamp. Low trigger thresholds are good for fast timing but may increase the sensor deadtime due to dark count triggers. For this reason, the sensors are preferably operated at low temperatures.

1.4 This thesis

It is too early to judge which of the two techniques, namely PET or PG imaging, will be the preferred instrument for *in vivo* proton therapy monitoring, as both show advantages and disadvantages for clinical implementation (section 1.2). For this reason, both PG and PET techniques are in the scope of this thesis, although most of the focus was put on PG imaging. The research conducted within this thesis aimed at the development and improvement of these techniques, by employing both simulation and experimental feasibility studies. Since

time-resolved detection of gamma radiation is considered to be important for both PT PET and PT PG imaging, the use of TOF information is a key aspect throughout the whole manuscript. The detector of choice for the experimental work was based on digital silicon photomultiplier arrays, so-called digital photon counters. These devices were chosen for the purpose of this work based on their fast timing performance and, in addition, their ease of use, in the sense that they are compact and provide integrated readout electronics.

The PET-related research focused on the application of such detectors to measure the proton-induced activity *in situ*. The very same detector technology, originally developed and tested for PET imaging, was used in the experimental studies regarding PG imaging. The PG-research related to this thesis focused on the development of methods for TOF rejection of background radiation, and their testing in the context of PG imaging with mechanical collimation. Here, the focus was on the use of 1D collimators (i.e. providing spatial resolution solely in the direction corresponding to the beam axis), such as presented in figure 1.7, which is intended to be applied in the case of pencil-beam-scanning proton therapy. An advantage of collimated PG-imaging over other PG-imaging approaches is the relative simplicity of implementation, i.e. it does not require the use of elaborate algorithms such as image reconstruction techniques, as image formation is based on simple projection of intensity profiles through the collimator. In particular, and as opposed to PG spectroscopy, it has the potential to resolve spatial information arising from the whole proton path, which may signal the presence of errors and complement the information on the proton range (spatial information such as marked variations in tissue densities correlated with CT, as highlighted from the PG production profiles reported by Moteabbed *et al* 2011).

1.4.1 Outline

Chapter 2 of this thesis reports on the first performance test of DPC detector modules to measure secondary gamma emission in the context of proton therapy. Activity distributions from β^+ emitters produced in phantoms were measured *in situ* with a dual-head TOF PET prototype (using pixelated LYSO:Ce scintillators) upon irradiation with a clinically-relevant synchrotron pencil beam. Furthermore, the influence of (1) the acquisition time protocol (beam-off in-beam versus post-beam), and (2) the phantom composition (with or without oxygen) on the relative contribution of different radionuclides, thus the total activity depth profiles (especially, on the activity range), is discussed and compared to MC simulations.

Chapter 3 presents a MC simulation study aiming at developing a method for neutron-related background rejection in PG imaging. This method explores the transit time of protons within the traversed medium and the different travel times of photon and neutrons between their emission point and the detector, and relies on the application of a shifting TOF window centered at the expected arrival time of prompt photons. The application of the TOF method in the context of collimated PG imaging at right angles with the beam axis is discussed, as well as its effectiveness depending on the influence of the beam time microstructure of typical clinical beams.

In chapter 4, the use of the DPC-based detectors in PG imaging is explored, using the fast LYSO:Ce scintillator (originally developed for TOF PET) in comparison to the slower BGO scintillator that is relatively less sensitive to neutrons. PG imaging was performed by means of a knife-edge slit collimator after pencil-beam irradiation. The PG profiles measured with and without TOF discrimination are presented in a comparative way, focusing on the signal-to-background ratio and the uncertainty in determining the profile falloff position for a realistic number of protons per spot. The necessary adjustments regarding the data acquisition settings, the synchronization with the cyclotron RF for applying TOF dis-

crimination, and the offline data processing, such as time-, energy-calibration, and multi-hit analysis are described in detail.

By using the same detector (LYSO:Ce only) and experimental methods as in chapter 4, albeit with a different collimator, viz. a single-parallel-slit collimator, it was possible to perform time-resolved measurements of PG-rays emitted at right angles with the beam axis, from several points close to the proton end-of-range. Based on these results, chapter 5 presents the necessary steps to implement the concept of a shifting time-of-flight (TOF) window introduced in chapter 3 for background rejection.

In order to image PGs at right angles with the beam axis emitted from the whole proton path, a multi-slat collimator designed for MeV gamma rays might be used. The detector should preferably be placed close to the collimator for improved spatial resolution. The presence of such a massive collimator in the vicinity of the detector may, however, contribute to considerable background due to neutron interactions that give rise to secondary, uncorrelated gamma rays, even using TOF discrimination. Chapter 6 presents a MC-simulation intended to study the feasibility of using multi-slat collimators in PG imaging for realistic irradiations of a patient-like, anthropomorphic phantom, where the influence of collimator spatial resolution may be relevant for resolving profile features arising from contrasted tissue densities. The influence of different collimator geometries and distances from the beam, on the visual correlation between PG profiles and the depth dose, are discussed in a comprehensive way, taking into account geometric performance of the collimators (i.e. effective resolution and efficiency). While the detector system was deliberately not simulated in order to give emphasis on the effect of the collimator itself, the results presented provide general guidelines on the geometrical properties of multi-slat collimators that are important to maximize the signal-to-background ratio.

Lastly, chapter 7 summarizes the most important findings of the research done within the scope of this thesis, and provides a discussion and outlook of this work.

Chapter 2

First *in situ* TOF-PET study using digital photon counters for proton range verification[1]

Positron emission tomography (PET) is the imaging modality most extensively tested for treatment monitoring in particle therapy. Optimal use of PET in proton therapy requires *in situ* acquisition of the relatively strong ^{15}O signal due to its relatively short half-life (~2 min) and high oxygen content in biological tissues, enabling shorter scans that are less sensitive to biological washout. This paper presents the first performance tests of a scaled-down *in situ* time-of-flight (TOF) PET system based on digital photon counters (DPCs) coupled to Cerium-doped Lutetium Yttrium Silicate (LYSO:Ce) crystals, providing quantitative results representative of a dual-head tomograph that complies with spatial constraints typically encountered in clinical practice ($2 \times 50°$, of $360°$, transaxial angular acceptance). The proton-induced activity inside polymethylmethacrylate (PMMA) and polyethylene (PE) phantoms was acquired within beam pauses (in-beam) and immediately after irradiation by an actively-delivered synchrotron pencil-beam, with clinically relevant 125.67 MeV/u, 4.6×10^8 protons/s, and 10^{10} total protons. Three-dimensional activity maps reconstructed with and without TOF information are compared to FLUKA simulations, demonstrating the benefit of TOF-PET to reduce limited-angle artefacts using a 382 ps full width at half maximum (FWHM) coincidence resolving time. The time-dependent contributions from different radionuclides to the total count-rate are investigated. We furthermore study the impact of the acquisition time window on the laterally integrated activity depth-profiles, with emphasis on 2-minute acquisitions starting at different time points. The results depend on phantom composition and reflect the differences in relative contributions from the radionuclides originating from carbon and oxygen. We observe very good agreement between the shapes of the simulated and measured activity depth-profiles for post-beam protocols. However, our results also suggest that available experimental cross sections underestimate the production of ^{10}C for in-beam acquisitions, which in PE results in an overestimation of the predicted activity range by 1.4 mm. The uncertainty in the activity range measured in PMMA using the DPC-based TOF-PET prototype setup equals 0.2 mm - 0.3 mm.

[1] P. Cambraia Lopes, J. Bauer, A. Salomon, I. Rinaldi, V. Tabacchini, T. Tessonnier, P. Crespo, K. Parodi and D. R. Schaart, Phys. Med. Biol. 61, 6203–30, 2016.

2.1 Introduction

At present, positron emission tomography (PET) is the imaging modality most extensively tested for treatment monitoring during or after irradiation in particle therapy (PT). This technique relies on the coincidence detection of delayed radiation, i.e. pairs of 511 keV annihilation gammas that are emitted in opposite directions as a result of the β^+ decay of irradiation-induced radioactive species produced in the target (by proton and heavy ion beams) and projectiles (heavy ions only). PET has been shown to provide valuable clinical information for quality assurance of the treatment delivery, such as: (1) on the positioning of the irradiated volume, (2) on morphology changes occurring during the course of the fractionated radiotherapy, and, very importantly, (3) on the finite particle range (Nishio *et al* 2006, Parodi *et al* 2007b, Fiedler *et al* 2010, Zhu *et al* 2011, Min *et al* 2013), which in turn is highly sensitive to the factors (1) and (2). These factors may not be sufficiently accounted for at the treatment planning stage or be subject to errors, thus giving rise to considerable range uncertainties (Engelsman *et al* 2013). Despite the rationale for treatment verification towards safer and more effective PT, and despite the clinical evidence of PET as a valuable instrument, it is not yet widely used in daily routine.

One reason for this is the complexity in translating measured activity into delivered dose. So far, the most accurate means for treatment verification has been implemented by comparing the PET activity to predicted activity distributions based on complex and time-consuming Monte Carlo (MC) simulations. Many efforts have been put into this direction, including the implementation into MC of (1) patient models based on computed tomography (CT) (Parodi *et al* 2007a), (2) functional models describing biologic decay (activity clearance/perfusion) (Parodi *et al* 2007b) and (3) experimental cross-section data of the main isotope production channels (Parodi *et al* 2007a, 2008); as well as (1) the fine-tuning of these cross-sections to better match simulated activity to PET measurements (Bauer *et al* 2013), (2) the comparison of different MC interaction models (Seravalli *et al* 2012), (3) development of methods to measure *in vivo* the ^{15}O production and clearance rates from dynamic PET data (Grogg *et al* 2015) and (4) the development of algorithms for automated detection of range deviations to increase the clinical throughput (Helmbrecht *et al* 2012, Frey *et al* 2014).

A main factor limiting the use of PET as a standard PT verification tool is the technological challenge of integrating it at the irradiation site. Optimal use of PET imaging requires the ability to acquire the signal from ^{15}O *in situ*, due to the relatively high abundance of oxygen in biological tissues and its relatively short half-life of ~ 2 min, requiring shorter scans that are less sensitive to blurring and biological distortion of the induced activity by physiologic mechanisms such as washout, wash-in, and transport. The implementation of a closed-ring PET at the beam nozzle has been argued to be feasible, collision-free with patient table and couch, using two separate heads and retractable arms in a rotating gantry (Kopf *et al* 2004, Crespo 2005). Alternative solutions have been proposed using two rings axially separated or a single ring cut at a slant angle (Tashima *et al* 2012), but all of these implementations cost a larger volume in the patient area and a larger axial field of view (Crespo *et al* 2006).

A possible compromise is a dual-head limited-angle tomograph having an opening angle that provides an input port for the therapeutic beam and an escape port for fragments leaving the patient, as well as easier access to the patient (Enghardt *et al* 1999, Nishio *et al* 2006, 2010). In addition, by using flat-panel detectors, the radius (thus, detection efficiency) can be adjusted depending on the irradiation site and spatial constraints (Nishio *et al* 2010). Drawbacks of this approach are the lower (solid angle) detection efficiency, and the presence of image artefacts due to limited-angle tomographic reconstruction (Crespo *et*

al 2006). Nevertheless, simulations have shown that image artefacts are significantly reduced in realistic clinical irradiations by including time-of-flight (TOF) information in the reconstruction (Crespo *et al* 2007, Dendooven *et al* 2014). Crespo *et al* (2007) has shown that a coincidence resolving time (CRT) of 200 ps (FWHM) or better is necessary for a dual-head tomograph with a $2 \times 134°$ (of 360°) transaxial angular acceptance. For range estimation, it appears sufficient to have a CRT of 300 ps using a dual-head tomograph with a $2 \times 90°$ (of 360°) transaxial angular acceptance, or 600 ps CRT and a larger, $2 \times 120°$ (of 360°) transaxial angular acceptance (Surti *et al* 2011). In addition to mitigating limited-angle image reconstruction artefacts, TOF information improves the image signal-to-noise ratio on a *per se* poor count-rate scenario, thus representing an important tool in PT PET.

Offline PET (post-therapeutic and outside treatment site, with a 5-10 min delay) has been implemented by means of commercial full-ring PET/CT solutions (Parodi *et al* 2007b, Parodi 2012), but have limited clinical applicability (Knopf *et al* 2009) and high impact on patient workflow (long scans). In-room full-ring solutions (nearby irradiation site, with few-minutes delay) were suggested as a good compromise between integration costs and quality (Shakirin *et al* 2011). Efforts have also been put in developing dedicated or custom-made PET tomographs. Examples are the dual-head *in situ* systems (Enghardt *et al* 1999, Iseki *et al* 2003, Nishio *et al* 2006) and in-room full-ring scanners-on-wheels for head-and-neck treatments (Zhu *et al* 2011). Technological developments are ongoing, including those recently reported by Tashima *et al* (2012), Shao *et al* (2014), and Sportelli *et al* (2014).

Here we present the first *in situ* performance test of PET modules based on digital photon counter (DPC) arrays as the photosensor, i.e. arrays of the digital silicon photomultipliers (dSiPMs) introduced and developed by Philips Digital Photon Counting (PDPC) (Frach *et al* 2009, 2010, Haemisch *et al* 2012). In contrast to the previous works referred to above, we have realized TOF-PET imaging thanks to the fast timing performance of the LYSO:Ce-coupled DPC detectors used (Degenhardt *et al* 2012). SiPMs are solid-state photosensors with high gain and fast time response, which function on the basis of single-photon detection in each of the (typically) several thousand microcells (single photon avalanche photodiodes, SPADs, operated in Geiger-mode), which are connected in parallel in an analog SiPM. Due to the local digitization of the SPAD signals in a digital SiPM (DPC-pixel) (Frach *et al* 2009), the electronic readout noise is much reduced and the sensor response is made even faster in comparison to analog SiPMs (Schaart *et al* 2016). The readout of a dSiPM is relatively simple due to the integration of logic circuitry for photon counting and time-to-digital conversion on the sensor chip, as well as the inclusion of further data acquisition and signal processing capability on the level of the dSiPM array (Frach *et al* 2010, Schaart *et al* 2016). Hence, detectors based on dSiPM arrays are very compact and scalable, making them particularly suitable for large-scale applications (Haemisch *et al* 2012) and applications with high space constraints.

In situ PET may include acquisitions during irradiation (in-beam) and/or after the end of the irradiation (post-beam). A post-beam acquisition with (ideally) zero delay (i.e. starting immediately after the end of irradiation) will be denoted here as an 'online' protocol, after (Nishio *et al* 2006). The term 'in-room' protocol will be used otherwise, generally referring to post-beam acquisitions with small, few-minute delays. In-beam acquisitions are easier to implement at synchrotron facilities, due to the periodic time-macrostructure of the beam delivery (beam-on/beam-off), allowing for background-free acquisitions (Parodi *et al* 2005a) during the beam pauses (beam-off) in between the spills (beam-on). The so-called 'in-beam' PET protocol used in the scope of this work corresponds solely to the case of beam-off in-beam PET. Nevertheless, implementation of in-beam PET during particle extraction at either synchrotron or continuous-wave cyclotron beams is possible with dedicated random suppression techniques that utilize the correlation of the random back-

ground structure with the sub-μs-microstructure of the beam (Crespo *et al* 2005). Inclusion of beam-on coincidence data has been shown advantageous and feasible (Crespo *et al* 2005, Parodi *et al* 2008, Sportelli *et al* 2014).

In this work we test a proof-of-concept *in situ* limited-angle PET setup comprising two DPC/LYSO:Ce modules operated in coincidence, under clinically relevant conditions (beam structure, beam current, and irradiation time). In addition, we investigate the influence on the PET reconstruction of different acquisition protocols (mostly based on two-minute acquisition windows with various starting times), focusing especially on the shape of the laterally integrated depth profiles and on the corresponding activity range. To this end, the contributions of the major proton-induced radionuclides to the detected coincidence rate are disentangled and the experimental results are compared to activity simulations using the MC particle transport and interaction code FLUKA (Ferrari *et al* 2005, Böhlen *et al* 2014).

2.2 Methods and materials

2.2.1 Experiment description

Figure 2.1 shows a photograph and a schematic overview of the measurement setup in the experimental room of the Heidelberg Ion-Beam Therapy Center (HIT). Two detectors with a surface area of 66 mm × 66 mm were positioned opposite to each other, such that the distance between the crystal front-surfaces was 121 mm. The setup forms a limited-angle, dual-head TOF-PET tomograph with an absolute transaxial angular acceptance of about 2 × 50° (of 360°, figure 2.1-bottom), resulting in about 9% relative solid-angle coverage, at the center of the field of view (FOV). Thus, the setup has an angular coverage comparable to that of a clinical limited-angle tomograph such as the pioneer BASTEI head scanner at GSI (Crespo *et al* 2006).

Homogeneous phantoms made of polymethylmethacrylate (PMMA, $C_5H_8O_2$, density 1.1845 g cm^{-3}) or polyethylene (PE, C_2H_4, density 0.95 g cm^{-3}) and with dimensions of 9 cm × 9 cm (lateral) and, at least, 30 cm (longitudinal) were irradiated along their longitudinal axis by a proton pencil beam with an energy of 125.67 MeV/u. The corresponding proton range, defined as the phantom depth at which the dose has decreased to 80% of the maximum value of the depth-dose profile, at the distal side of the Bragg peak, was 9.85 cm in PMMA and 11.69 cm in PE. These values were calculated on the basis of a FLUKA simulation of the depth-dose distribution in water and the water equivalent path lengths of PMMA and PE (viz. 1.165 and 0.982, respectively).

Table 2.1 summarizes the clinically relevant, synchrotron-delivered irradiation conditions that were used for all the measurements. A total of 10^{10} protons were delivered at an average beam intensity of 4.63×10^8 protons/s during extractions (spills), which is within the range of a typical single field of a head-and-neck treatment plan (Parodi *et al* 2007b, Bauer *et al* 2014). However, the beam was always pointing at the same spot, coinciding with the long axis of the phantoms, delivering a total dose of about 10 Gy in water at the Bragg peak, calculated considering the width of the beam envelope (focus). The irradiation lasted approximately 2.5 min, including 35 spills intercalated with pauses (table 2.1). The beam macro structure on average had a period of 4.42 s and a duty cycle (i.e. the spill duration as a percentage of the period) of 14%, which is favorable for realizing in-beam PET measurements during the 34 relatively long irradiation pauses. The relative differences between the mean pause durations of individual irradiations and the average value over all irradiations presented in table 2.1 were typically below 1%. For the mean spill duration and the total irradiation time these values were 5% and 2%, respectively. Within individual irradiations,

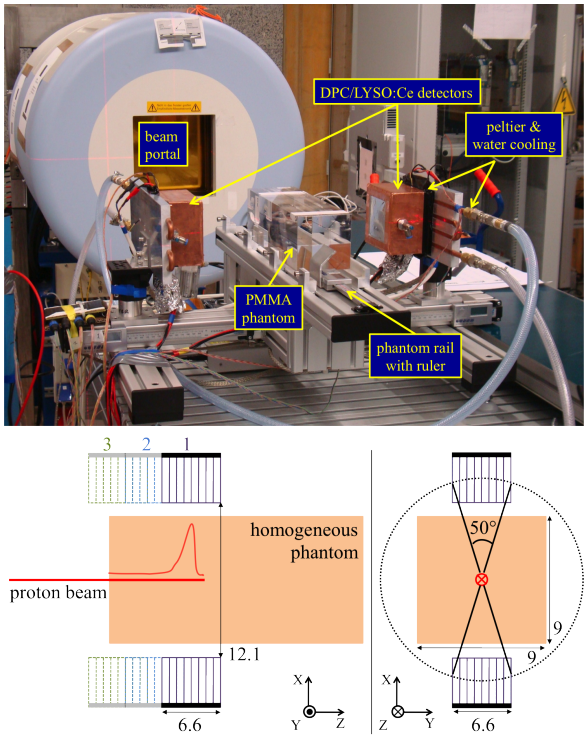

Figure 2.1: *Top:* photograph of the *in situ* TOF-PET setup at the HIT. The distance between the two detectors in the photograph is larger than in the actual measurement. *Bottom:* schematic overview of the measurement setup (not to scale), with distances displayed in centimeters. Three longitudinal detector positions with FOV overlap of 2.5 cm cover the full proton beam range. This was accomplished by translating the phantom over its support rail.

the root mean square (RMS) of the pause duration was typically 1%-3% (maximum 4%) of the mean value, while for the spill durations the RMS was 3%-5% of the mean value.

Coincidence data covering the entire proton range in both phantoms were acquired using three different detector positions, as indicated in figure 2.1-bottom. Detector position '1' was defined as follows: the center of the FOV was aligned with the laser crossing indicating the isocenter. Subsequently, the phantom was positioned such that the center of the detector FOV was located 8 mm proximal to the proton range. Positions '2' and '3' were defined by translating the phantom distally (+Z) along the beam direction on its support rail, by 41 mm and 82 mm, respectively, while the detectors were kept at a fixed position. The phantom length that was imaged by two adjacent detector positions corresponded to the total width of about 6 LYSO:Ce crystals (25 mm), so as to avoid areas of near-zero sensitivity when the detectors are operated in coincidence.

To characterize the sensitivity of the PET setup to deviations in the proton range, another series of experiments was performed in which the PMMA phantom was shifted by small increments along the beam axis, relative to position '1', in both the distal (+Z) and the proximal (-Z) directions. In this way, positron emitter distributions were measured for Bragg peak shifts of -4 mm, -2 mm, -1 mm, 0 mm, 1 mm, and 2 mm. A built-in digital

Table 2.1: Irradiation parameters: beam energy (E), average spill intensity ($< I >$), FWHM of the beam focal point at isocenter in air (focus), total number of delivered protons (N_p), total number of beam extractions (spills), average spill duration $< t_s >$, average pause duration $< t_p >$, and total irradiation time $< t_{irr} >$).

E (MeV/u)	$< I >$ (protons/s)	Focus (mm)	N_p	Spills	$< t_s >$ (s)	$< t_p >$ (s)	$< t_{irr} >$ (s)
125.67	4.63×10^8	12.9	1.00×10^{10}	35	0.62	3.80	151

ruler enabled the accurate longitudinal positioning of the phantom on its support rail with an accuracy of ~5 μm.

In all measurements, the activity generated by the protons inside the phantoms was continuously measured during irradiation and during a period of at least 15 min after irradiation. In order to avoid residual phantom activity from previous irradiations, four (PMMA) and three (PE) phantoms of equal dimensions were used alternatingly, allowing the activity in each phantom to decay to negligible levels before using it again.

2.2.2 Detector description and operation

We used DPC-MO-22-3200 detector modules developed by PDPC, which have been described elsewhere (Degenhardt *et al* 2012, Haemisch *et al* 2012, Schaart *et al* 2016). Each module contains a total of 256 polished $Lu_{1.8}Y_{0.2}SiO_5$:Ce (LYSO:Ce) crystals with dimensions of 3.8 mm × 3.8 mm × 22 mm, covering a total surface area of about 66 mm × 66 mm. The photosensor comprises 2 × 2 DPC3200-22-44 digital photon counter (DPC) arrays (figure 2.2-left). Each array is made of 4 × 4 independently read-out DPC chips, each chip comprising 2 × 2 DPC-pixels. The crystals are optically coupled to the DPC-pixels with UV-curable glue (DELO-PHOTOBOND 4436), in a 1:1 arrangement at a 4 mm pitch within each DPC-array, while a small gap (~2 mm) exists in between the DPC-arrays (figure 2.2-left, Degenhardt *et al* 2012). Each group of 2 × 2 LYSO:Ce crystals is thus coupled to a DPC-chip. These groups are optically isolated from each other by means of reflective foil (Vikuiti Enhanced Specular Reflector (ESR), by 3M), while some light sharing is allowed between crystals on the same DPC chip.

In order to minimize the sensor dark-count rate (DCR), the detectors were cooled using a combination of Peltier elements and a heat exchange plate with internal tap water flow, as in Cambraia Lopes *et al* (2015). The modules were kept inside a light-tight and moisture-free container, continuously flushed by dry nitrogen gas (figure 2.1-top). The temperature of operation was set as low as practically achievable, ranging from -10 °C to -9 °C for all of the DPC arrays. Cooling reduces sensor dead-time due to dark-count triggers, especially when using low trigger threshold settings (Frach *et al* 2009). The DCR was further reduced by inhibiting the 10% most noisy cells.

The acquisition settings used are within the range of typical values for PET applications (Somlai-Schweiger *et al* 2015): an excess voltage of 2.9 V, an integration time of 165 ns, a validation interval of 10 ns, an 8-OR validation threshold, and a trigger threshold on the 2nd registered photon. The principles of operation of DPCs have already been described and characterized (Frach *et al* 2009, 2010). The programmable thresholds and delays regulate the flow of the acquisition chain and they influence the sensor detection efficiency, gain, and dead time. Briefly, the trigger threshold is the condition necessary to start a validation cycle, which will be followed by an integration period (i.e. photon counting period) if and only if the validation threshold is satisfied during the validation interval. Thresholds are satisfied when a user-defined number of microcells fire in a given logic pattern (Tabacchini *et al*

2014). The trigger logic is implemented on pixel level, whereas the validation, integration, and readout are performed on chip level. Upon readout of a valid event, the DPC-chip outputs the (digital) number of fired cells on each of its four pixels, as well as one time-stamp. The time-stamp is defined as the moment when the trigger threshold is satisfied.

Data acquisition was done in coincidence mode, meaning that the DPC acquisition software made a pre-selection of events to be stored based on their time-stamp values, applying a paralyzable 'cluster window' (i.e. a coincidence window that acts on the level of a detector module) and a non-paralyzable 'coincidence window' between the two detector modules. Both windows were 10 ns long.

All PET acquisitions were synchronized with the beam macrostructure by using the so-called 'spill ON' signal, which reports the irradiation status, yielding a logical true or false depending on whether the beam is on (spill) or off (pause), respectively. This signal served as a trigger to generate a step-like logical signal using a gate/delay generator operating in flip-flop mode, which outputs a signal with a rising edge at the start of the first spill that remains at a logical true thereafter. The gate/delay generator output signal was fed into the DPC electronics as a gate 'enable' signal, such that the PET acquisition started at the same time as the irradiation. The PET measurements were acquired continuously using this configuration. By analyzing the beam record files offline, it was possible to relate the event time-stamps to the corresponding beam status.

Only in-beam data registered during the beam pauses were considered throughout the present work. It should be noted that the relatively high count rate during spills (due to prompt gamma rays (Parodi *et al* 2005a)) exceeded the bandwidth of the USB 2.0 interface of the PDPC technology demonstrator kit, which is not designed for high count rates, causing most of the time frames within spills to be dropped. This USB connection transfers the data (prior to coincidence sorting) between the DPC acquisition/control board and the computer.

The in-beam measurement time was about 120 s in total, which corresponded to 80% of the total irradiation time or 93% of the pause time (table 2.1). The in-beam measurement time did not include the last ~6% time of each pause, due to a small dead time in the beginning of the spills, between the start signal and the actual start of irradiation. It was not considered relevant to correct the acquisition time to include this small (~3% of counts) contribution.

2.2.3 Offline detector calibration and performance characterization

Time and energy calibrations were implemented offline based on measurements of the 511 keV gamma rays from ^{22}Na point sources with activities of about 0.5 MBq or 0.7 MBq.

2.2.3.1 Timing

Correcting for electronic time skews between DPC-chips is of utmost importance for obtaining good timing performance. Van Dam *et al* (2013) used a direct approach for determining these skews by irradiating the entire DPC-array simultaneously with a pulsed laser. Since this cannot be done after the detector modules have been assembled, we performed time calibration using a practical, indirect approach:

1. A coincidence measurement was done with the two modules facing each other and the ^{22}Na point source placed just in front of module 1 (M1) (about 1.5 cm away from the crystal front-surfaces) and far enough from module 2 (M2), such that all DPC chips in M2 could detect events in coincidence with M1.

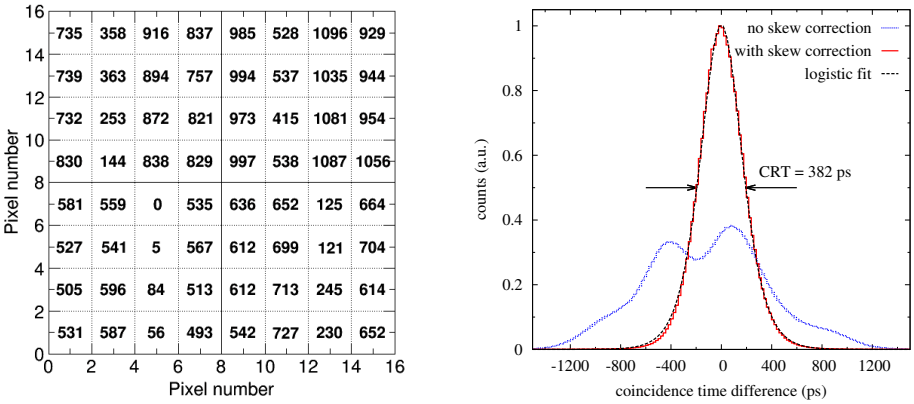

Figure 2.2: *Left:* electronic time skews (in picoseconds) of all DPC-chips within a detector module, relative to the chip with the earliest time stamp on average. The module is composed of 2 × 2 arrays of DPC-chips (separated by the solid lines in the figure, which in reality correspond to ~2 mm gaps). All chips (separated by dotted lines) are composed of 2 × 2 pixels. *Right:* coincidence time spectra obtained pre- (dotted line, blue) and post-skew correction (solid line, red), for a total of 3.8×10^6 coincidence events, as well as the logistic fit to the latter spectrum (dashed curve, black) obtained from a ^{22}Na point source measurement. The bin width is 20 ps.

2. The four central chips of M1, which were closest to the point source, were selected as reference chips, each one from a different DPC-array (note that the center of the detector front-surface where the point source was located coincides with the crossing between the four sensor arrays, figure 2.2-left).

3. For each DPC-array of M2, histograms were created with the time-stamp differences of coincidence events (within the 511 keV photo-peak) recorded between each of its constituting chips and the diametrically opposed reference chip of M1 (a different reference chip on M1 for each array on M2). The histogram peak positions were determined by fitting a logistic curve to each histogram.

4. As all chips of a certain array on M2 were operated in coincidence with a single reference chip on M1, the time skews between any two M2-chips on the same M2-array (intra-array skews) could be obtained by subtracting the corresponding peak positions calculated in 3..

5. Steps 1. to 4. were repeated after inverting the roles of M1 and M2, to determine the intra-array time skews of M1.

6. By selecting coincidences between an (arbitrary) reference M1-chip and each one of the reference M2-chips, the skews between the reference M2-chips can be determined relative to one another as in (4). Thus the skews of all chips within M2 can be determined, relative to an arbitrary M2 chip (and *vice-versa* for M1). The intra-module skews obtained for one of the detector modules are presented in figure 2.2-left.

7. Finally, the inter-module skew could be calculated from the peak position of the

coincidence time differences between the two modules, obtained in a measurement with a point source placed halfway between the modules.

The skews thus obtained (figure 2.2-left) are consistent with those reported by van Dam *et al* (2013) within DPC-arrays. Skews of up to 772 ps and 1096 ps were found between chips within an array and within a module, respectively. Figure 2.2-right shows the coincidence spectrum obtained with a point source, pre- and post-skew correction. The non-corrected spectrum is not only considerably broadened but also distorted and asymmetric, presenting multiple peaks and shoulders. This is attributed to the relatively-high inter-array skews (e.g., the lowest skew of the top-right array in figure 2.2-left is 415 ps relative to reference chip '0 skew' on the bottom-left array). The logistic distribution function was found to best reproduce the skew-corrected time difference histogram, which is very similar to a Gaussian except that the tails are slightly thicker. The system coincidence resolving time (CRT) was 382 ps, consistent with that reported by Degenhardt *et al* (2012) for identical detector modules, taking into account that the CRT degrades by about 100 ps when the 2nd registered photon instead of 1st one is used for triggering (Degenhardt *et al* 2009). In the present work 1st photon triggering was not used to limit the dead time caused by dark-count triggers.

Taking into account the small object size (i.e. the irradiation field) in these experiments, we used a coincidence time window of ±1 ns. Due to the broad coincidence pre-sorting window of 10 ns used by the acquisition software (section 2.2.2), it was possible to estimate the amount of random coincidences using a 5 ns delayed coincidence window. The random-to-true ratio thus obtained was negligible, i.e. always below 0.5% for in-beam (pauses) and post-beam acquisition protocols (as indicated in figure 2.10). The cluster window was also shortened in a post-processing step, to ±2 ns.

2.2.3.2 Energy

Energy calibration was performed using the 511 keV gamma line from a ^{22}Na point source. As in Cambraia Lopes *et al* (2015), the calibration was done on a per-pixel basis, although counts were summed on a per-chip basis to account for light sharing and the fact that the event processing on these sensors is done on chip level. Each chip-event was assigned to the pixel that registered the highest amount of fired cells. The measured number of fired microcells per pixel was corrected for saturation (total of 3200 SPADs per DPC-pixel) by applying a commonly used, logarithmic correction curve (Degenhardt *et al* 2009).

Figure 2.3 shows energy spectra measured by one of the detector modules. The global energy resolution was 12% (with a per-crystal mean resolution and standard deviation of 10.4% ± 0.7%). No major differences were observed between energy spectra from proton-induced activity acquired in-beam (pauses) and post-beam (post-beam protocols as indicated in figure 2.9; exemplary 'in-room(b)' protocol is shown in figure 2.3), except that the in-beam spectra exhibit a small broad pile-up component that peaks at about 0.72 MeV. The scatter fraction was about 22% within the energy window of 450 keV - 650 keV, obtained by fitting the proton-induced activity spectra with a Gaussian function (the full-energy peak) plus a linear baseline (the scatter pedestal). Event clustering was performed by summing the energies of multiple chip-events that had time-stamps spaced by less than 2 ns, in order to also detect 511 keV quanta undergoing multiple interactions within the detector. The average number of chips per (cluster) event used for image reconstruction was 1.3 in the energy range from 450 keV to 650 keV.

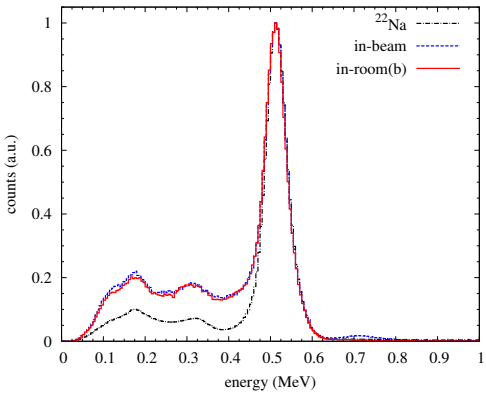

Figure 2.3: Energy spectra measured in coincidence for a ^{22}Na calibration point source (black curve) and for proton-induced β^+ activity in PMMA during irradiation pauses (2-minute duration – 'in-beam', blue curve) and after irradiation (2-minute delay and 2-minute duration – 'in-room(b)', red curve). The bin width is 5 keV.

2.2.4 Image reconstruction

Image reconstruction was performed using 11 iterations of the maximum-likelihood expectation maximisation (ML-EM) update scheme (Shepp and Vardi 1982):

$$\lambda_j^{(n+1)} = \lambda_j^{(n)} \cdot \frac{\sum_i c_{ij}^{TOF} \cdot \frac{y_i - \xi_i^{acc(n)}}{b_i^{(n)}}}{\sum_i c_{ij} a_i} \tag{2.1}$$

with the estimated non-attenuated activity:

$$b_i^{(n)} = \sum_k c_{ik}^{TOF} \lambda_k^{(n)}$$

and the estimated attenuation:

$$a_i = \exp\left(-\sum_k l_{ik} \mu_k^{(n)}\right),$$

where y_i is the measured number of coincidences in sinogram entry i and l_{ik} is the interaction length of the line-of-response (LOR) corresponding to sinogram entry i with voxel k. The entries of the system matrix c_{ij}^{TOF} denote the sensitivity of voxel j with respect to sinogram entry i and depend on the time-of-flight (TOF) information, while μ represents the attenuation coefficients for 511 keV photons and λ the estimated activity per voxel. The estimated number of accidental coincidences (scatter + randoms) is denoted as $\xi_i^{acc(n)}$ depending on both the estimated activity and the attenuation (details regarding activity reconstruction, scatter, and random correction have been reported by Salomon *et al* (2011)). Each entry of the geometric sensitivity matrix c_{ij} is calculated by the corresponding mean contribution of 128 single lines-of-response distributed between the corresponding crystal

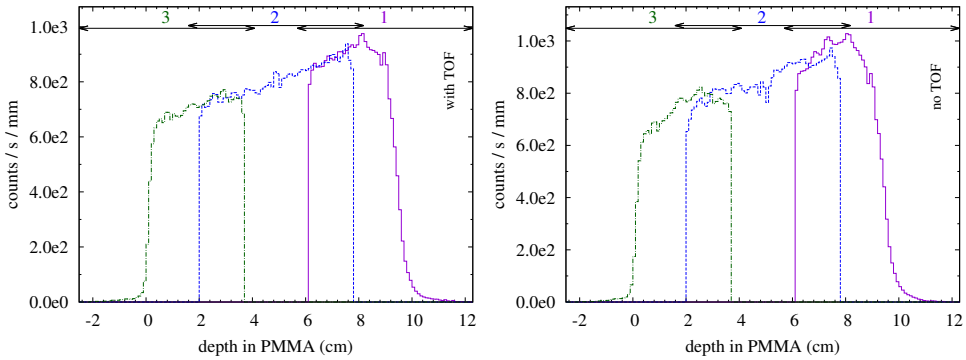

Figure 2.4: Laterally integrated activity depth-profiles (time-averaged counts) in PMMA, obtained from 15 min measurements starting right after irradiation, with the detectors placed at positions 1, 2, and 3 (figure 2.1-bottom). Better matching in FOV overlap regions is observed when TOF information is used (left) than in the non-TOF case (right). The last 4 mm (1 crystal) regions at both edges of the FOV were neglected as these had very low counting statistics.

pair.

Cubic voxels were used with a side dimension of 1 mm (1/4 of the detector-pixel pitch). For each coincidence event, the crystal with the highest photon count within the chip registering the highest deposited energy was selected for each of the two detectors ('winner-takes-all'). The flat-sinogram back-projection based sensitivity was well estimated over almost the entire field of view (FOV). This can be seen from the very good agreement, shown in figure 2.4-left, between longitudinal profiles obtained with the detector placed at different positions relative to the phantom axis (figure 2.1-bottom), in the regions where the different FOVs overlap. This is challenging in the present set-up due to the strong acolinearity between LORs and crystal main axis. If TOF information is not used, the agreement at the edges of the FOV is poor (figure 2.4-right). The reconstructed images and profiles covering the entire proton path that will be presented in the remainder of this work have been merged by doing pixel-by-pixel averaging of the counts in the regions of overlap.

A correction for the efficiency for each crystal was not implemented, so the reconstructed values are regarded as qualitative. The reconstructed images and profiles in this paper are plotted in units of time-averaged counts in order to be comparable to each other.

2.2.5 Dynamic count-rate modeling

To evaluate the count rate contributions from the main positron emitters, the detected coincidence count-rates were modeled using the mathematical formulation for pulsed beam delivery by Parodi *et al* (2002). The raw coincidence data registered in the energy window of the full-energy peak were analyzed as a function of time, without applying any correction for detection efficiency of the tomograph or in-phantom attenuation of annihilation photons. The modeling was done in two steps.

First, the function describing the exponential decay rates over time was fit to the coincidence rate registered during the 15 min immediately after the end of the irradiation ($t = t_0$), represented in steps of 0.05 s:

$$cps(t > t_0) = \sum_l \lambda_l N_l e^{-\lambda_l (t-t_0)} + C \tag{2.2}$$

where λ_l is the decay constant of isotope l, and C is a constant accounting for steady background and random coincidences. For PMMA, l = {1,...,4} (^{11}C, ^{10}C, ^{15}O, and ^{13}N) and for PE, l = {1,2} (^{11}C and ^{10}C). The N_l are fitting parameters which yield the relative amount of isotope species at the end of the irradiation.

In the second step, the relative (or absolute) amount of nuclei of species l present at the start of pause j can be calculated recursively from the corresponding amount present at the start of the previous pause j-1, by taking into account the isotope build-up and decay during the previous irradiation cycle. Assuming a constant beam intensity during particle extraction (thus, a constant isotope production rate, P_l), as well as fixed spill duration, t_s, and pause duration, t_p, the count-rate in the beginning of pause j ($cps_{j,l}$) can be calculated from the contributions of all previous cycles by the simple expression (Parodi *et al* 2002):

$$cps_{j,l} = P_l (1 - e^{-\lambda_l t_s}) \left\{ \sum_{i=1}^{j} e^{-\lambda_l (j-i)(t_s+t_p)} \right\}, \; j = 1, ..., 35 \tag{2.3}$$

where P_l is determined by the fitting parameter, by solving $cps_{35,l} = \lambda_l N_l$. Therefore, the average count rate of isotope l during pause j ('in-beam' $< cps_{j,l} >$) is given by:

$$< cps_{j,l} > = cps_{j,l} \frac{1 - e^{-\lambda_l t_p}}{\lambda_l \cdot t_p} \tag{2.4}$$

2.2.6 Calculation of average activity distributions from FLUKA simulations

Simulations of activity distributions were compared to experimental data for the following purposes: (1) to verify the qualitative agreement to the reconstructed activity distributions, obtained post-beam during a long acquisition of 15 min (low noise), in terms of the 2D images and laterally integrated depth profiles (section 2.3.2); (2) to assess the qualitative agreement to the laterally integrated depth-profiles obtained during short (mostly 2 min long) in-beam and post-beam acquisitions, trying to infer the main causes of discrepancies from the simulated, individual radionuclide contributions to the overall activity profiles (section 2.3.4); and (3) to compare the predicted activity range (depth in the phantom corresponding to the distal falloff of the longitudinal activity profile) to the ones resulting from fitting the reconstructed depth profiles obtained with different acquisition protocols (section 2.3.5).

The expected positron-emitter yields were simulated using the Monte Carlo (MC) particle transport and interaction code FLUKA used and further customized at HIT, in its most recent version 2011.2c. This code was found to very well reproduce the amount of proton-induced activity (to within a few percent) and the distal activity range (to within 0.6 mm) measured offline by means of a commercial PET/CT scanner in homogeneous and heterogeneous phantoms, after cross-section tuning of the main reaction channels leading to ^{11}C, ^{15}O, and ^{13}N (Bauer *et al* 2013).

The simulations took into account the phantom composition, proton energy, beam momentum spread, and irradiation time profile used in the experiments. The ionization potentials used for PMMA and PE were 74.8 eV and 57.0 eV, respectively, as in Bauer *et al* (2013), while the cross-sections tuned in that work were also applied. However, in contrast

with Bauer *et al* (2013), ^{10}C production is included in the present work. The cross-section data for ^{10}C production from proton interactions on ^{12}C was included in accordance with Parodi *et al* (2008), based on experimental cross-sections described elsewhere (Iljinov *et al* 1991, EXFOR/CSISRS 2007). The number of protons simulated was 5×10^6.

The outcome of the simulations is a spatial distribution of positron-emitter production yields per proton, R_l^{MC}, for each radionuclide species l. In the next step, we calculated the expected spatial distribution of the activity averaged over the PET measurement *duration*, starting with a *delay* since the end of the irradiation ($t_{\text{start}} = t_0 + delay$), as in (Bauer *et al* 2013):

$$< A >_l^{post-beam\,PET}(\overrightarrow{r}) = A_l(\overrightarrow{r};t_0)e^{-\lambda_l \cdot delay} \cdot \frac{1-e^{-\lambda_l \cdot duration}}{\lambda_l \cdot duration} \tag{2.5}$$

where $A_l(\overrightarrow{r};t_0)$ is the activity distribution immediately after the last spill. Similar to equation (2.3), this distribution can be derived by setting $j = 35$, and the isotope production rate as the product of the MC production yields per proton and the average spill intensity:

$$A_l(\overrightarrow{r};t_0) = < I > \cdot R_l^{MC}(\overrightarrow{r}) \cdot (1-e^{-\lambda_l t_s}) \left\{ \sum_{i=1}^{35} e^{-\lambda_l (35-i)(t_s+t_p)} \right\} \tag{2.6}$$

Although a more precise calculation of the activity is possible by using the individual spill intensity and duration values registered in the beam record files, the differences in total activity were found to be negligible due to the stable operation of the synchrotron.

Equation (2.5) is only valid for a PET acquisition starting after irradiation. The average activity per pause can be calculated in analogy to equation (2.4) and the average PET activity produced during the whole irradiation can be calculated as the mean value over the total of 34 beam pauses:

$$< A >_l^{in-beam\,PET}(\overrightarrow{r}) =$$

$$< I > \cdot R_l^{MC}(\overrightarrow{r}) \frac{(1-e^{-\lambda_l t_s})(1-e^{-\lambda_l t_p})}{\lambda_l \cdot t_p} \cdot \sum_{j=1}^{34} \left\{ \sum_{i=1}^{j} e^{-\lambda_l (j-i)(t_s+t_p)} \right\} \cdot 1/34 \tag{2.7}$$

Prior to the activity calculation, the simulated spatial distribution of positron-emitter production yields was convoluted with an isotropic Gaussian kernel with a standard deviation of 3.2 mm, as done by Bauer *et al* (2013) for a whole-body scanner, in order to more closely resemble the measured data that is subject to a finite spatial resolution. The voxel size used was 1 mm^3. Although it was impossible to determine the precise value of the spatial resolution of the dual-head PET tomograph on the basis of a single point-source measurement, the Gaussian kernel used seems a reasonable assumption taking into account the crystal size. Although Degenhardt *et al* (2012) reported a spatial resolution of 2.4 mm using identical detector modules mounted on a ring with a crystal-to-crystal distance of 20 cm, the resolution is likely to be worse in the present work due to parallax errors arising from the flat-panel geometry and the small distance between the detector modules.

2.3 Results and discussion

2.3.1 Count-rate and DCR measurements

The proton beam intensity of 4.63×10^8 protons/s was low enough that the transfer rate of events outside the spills (prior to coincidence sorting) between the DPC acquisition/control board and the computer did not exceed the bandwidth bottleneck imposed by the USB 2.0 connection from the PDPC technology demonstrator kit, which constituted the main count rate-limiting factor in our setup (see section 2.2.2). With the irradiation conditions used (table 2.1), we registered coincidence count-rates of up to about 8.6 kcps (no energy selection) without losses.

It is to be noted that the DPC sensor in principle can process much higher count-rates. The intrinsic maximum (validated) event rate of the DPC-chip when operated at a 200 MHz clock is 1.3 Mcps, even though in the current DPC-array this is limited to 120 kcps per chip by the available FPGA memory. In our measurements, single validated-event rates of only 1 kcps - 1.25 kcps per DPC-chip (averaged over the two detectors and a measurement time of about 15 min since the start of the irradiation) were registered on-chip. An event rate of 1.2 kcps/chip corresponded to 0.9 kcps/chip of single events recorded by the computer. Of these events, 0.04 kcps/chip were selected by the coincidence sorting algorithm. This resulted in a maximum (at the end of the last spill) total recorded coincidence rate of ~5.5 kcps, of which ~1.7 kcps fell within the energy selection window.

The vast majority of the trigger rate was dark-count related and corresponded to events that did not pass the validation threshold (section 2.2.2). After measuring the DCR per cell on every pixel, the trigger rate can be reduced by disabling the hottest cells on each DPC pixel. In the current experiments we inhibited the 10% noisiest cells, resulting in a DCR of 120 s^{-1} - 130 s^{-1} per cell, corresponding to about 75% - 80% reduction compared to the case where all cells are active. It should be noted that the DCR measurements were done with the LYSO:Ce crystals coupled to the sensors and that the intrinsic DCR per cell is expected to be about 3 times lower in the absence of the lutetium background.

Trigger rates of ~0.27 Mcps per chip were registered initially (after application of the inhibit map for DCR reduction). We observed a gradual increase by ~0.04 Mcps in every consecutive measurement/irradiation (10^{10} protons) performed on the same day, which could hint at some accumulation of radiation damage. The relative increase was small and dead-time losses were insignificant, as each DPC-chip on average had a 1% - 2% occupation time, i.e. the time that the sensor is busy with data acquisition, readout, and recharge (including both non-validated-trigger rates and validated-event rates). After a measurement cycle with a total of 7×10^{10} delivered protons, the DCR was re-measured and we observed an increase in the mean DCR per cell of ~2% and ~5% with and without applying the re-calculated inhibit map, respectively, compared to the initial DCR measurement. These results suggest that regular DCR measurement and inhibit calibration is advisable to maintain detector performance. It should be noted that the detectors were placed quite close to the beam, resulting in higher exposure to neutrons than expected in a realistic *in situ* PET setup. Further studies are required to assess the effect of long-term exposure to secondary radiation on the detector performance.

2.3.2 High-statistics post-beam PET images and depth-profiles: influence of TOF

To maximize counting statistics, the PET images presented in this section correspond to 15 min long acquisitions, starting immediately after irradiation. The in-beam PET data was excluded so that the results can be compared directly to simulation data tuned to well-

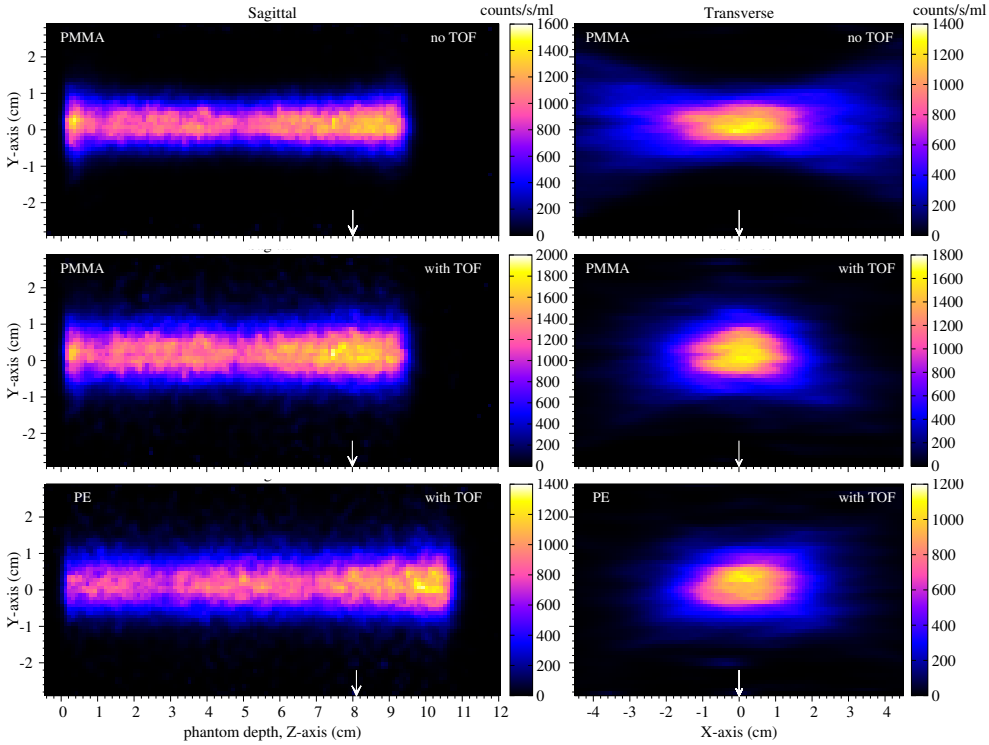

Figure 2.5: Measured images of proton-induced activity in PMMA, reconstructed without (top) and with (center) TOF information, and in PE (bottom), shown as 2 mm thick sagittal (left) and transverse (right) slices. The white arrows indicate the positions of the orthogonal slices. All images were acquired for 15 min, starting right after irradiation.

calibrated PET measurements performed post-beam with a commercial PET scanner (section 2.2.6) (Bauer *et al* 2013).

Figure 2.5 shows orthogonal slices of the 3D PET images obtained in PMMA and PE phantoms. Exemplarily results without and with TOF information are shown for PMMA, in the top and center row, respectively. If TOF information is used, limited-angle artefacts are significantly reduced, although not totally eliminated, as expected (Crespo *et al* 2007, Surti *et al* 2011). These artefacts cause the image to stretch along the X axis, i.e. the axis orthogonal to the detector planes (Crespo *et al* 2006). Even with TOF, the width of the activity distribution in the X direction still is about twice that in the Y direction (figure 2.5-center-right), while the relative difference in the FWHM of a line profile crossing the center of the beam in the Y direction, between measurement and simulation (the latter is not shown), appears to be only a few percent. The FWHM of the simulated activity in PMMA (not shown) in the same transverse slice as in figure 2.5-right (Z = phantom depth = 8.0 cm) is 1.5 cm along any direction due to circular symmetry. In case TOF information is not used, the distortion in the X direction is much worse than in the TOF case, while a considerable distortion is observed in the Y direction as well, in the form of a narrowing of the activity width that appears visible in both the sagittal and the transverse views.

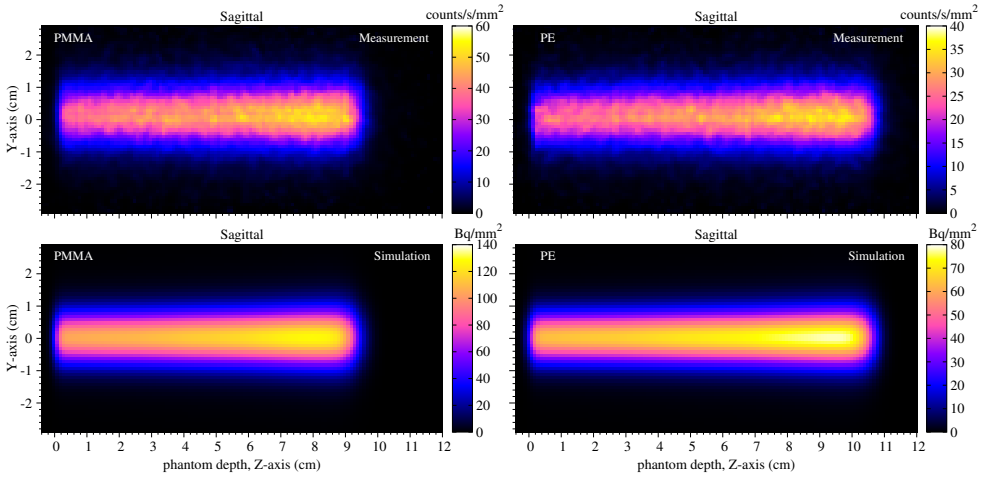

Figure 2.6: Sagittal views of measured projection images (reconstructed with TOF - top), and corresponding simulations of activity distributions (bottom) in PMMA (left) and PE (right). Images were acquired for 15 min, starting right after irradiation.

In the sagittal slices in figure 2.5, a slight reduction of intensity can be seen at the Z positions at which the centers of the field of views (FOVs) corresponding to the different detector positions (figure 2.1-bottom) are located, viz. at Z = 0.8 cm, 4.9 cm, and 9 cm for PMMA, and Z = 2.65 cm, 6.75 cm, and 10.85 cm (not visible) for PE. This may be the result of the small gaps (ca. 2 mm = ½ of the crystal pitch) between the 4 sensor arrays in each module (figure 2.2), in spite of the fact that these were taken into account in the reconstruction. Also noticeable is some intensity increase near the beam entrance position (Z = 0), which may be related to an imperfect correction of phantom attenuation. Iterative reconstruction algorithms typically are sensitive to sharp density transitions and because of the very atypical setup used (e.g., with a very small distance between the phantom and the detectors) these effects are difficult to correct for. No intensity overestimation near the beam entrance position is noticeable in the PE phantom, probably because it is closer to the edge of the FOV (i.e., ~ 6.5 mm vs 25 mm for PMMA). Interestingly, the phantom-entrance effect is not visible in the sagittal projection images, which are presented in figure 2.6.

Also shown in figure 2.6 are the simulated activity distributions projected in the Y direction, while figure 2.7 shows the laterally integrated depth-profiles. The qualitative agreement between the simulated and measured results is excellent in both figures. On the other hand, the shape of the laterally integrated depth-profiles obtained without TOF information (as shown in figure 2.4-right for PMMA) is distorted in comparison to the simulated case.

As the CRT of the current setup is not good enough to completely eliminate the limited-angle reconstruction artefacts in the X direction, there is a larger discrepancy between the total number of counts in the simulated and measured sagittal images if slices are considered instead of projection images (~1.2 higher ratio). The qualitative agreement between measurements and simulations thus is considerably better when projections are considered instead of slices. The simulated sagittal slices were not shown since they are qualitatively very similar to the corresponding projections presented in figure 2.6-bottom. For these reasons, only projection images and laterally integrated depth profiles reconstructed with TOF

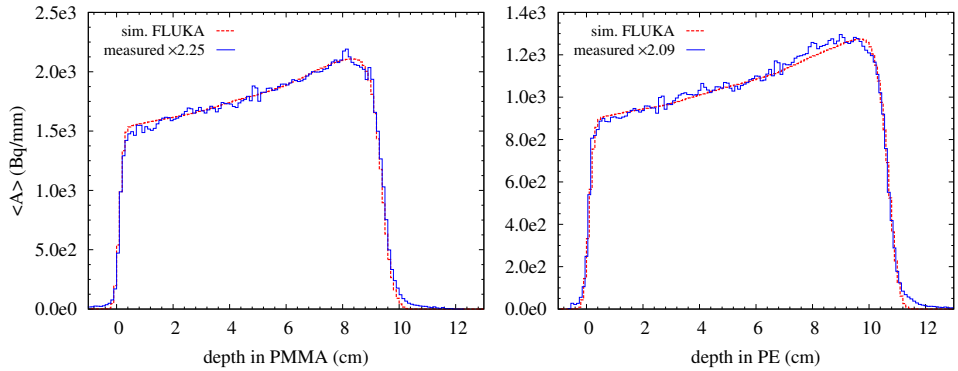

Figure 2.7: Measured (reconstructed with TOF - blue, solid) and simulated (red, dashed), laterally integrated depth-profiles of proton-induced activity in PMMA (left) and PE (right). All profiles correspond to 15 min acquisitions starting right after irradiation. The measured profiles have been normalized to the same total area as the simulated ones (scale factors are indicated in the legend, while the non-normalized measured profiles have units of counts / s / mm).

information are considered in the remainder of this work.

2.3.3 Time-dependent count-rate contributions from major radionuclides

Figure 2.8 presents the coincidence rate as a function of time, measured for PMMA (top) and PE (bottom) with the detector placed at position 1 (figure 2.1-bottom). Also shown in figure 2.8 are the total and radionuclide-specific coincidence rates calculated according to section 2.2.5. The constant baseline included in the fitting of the post-beam dynamic count-rate yielded a negligible background of about 5 cps, which corroborates the expected random coincidence rate.

Figure 2.9 presents the number of detected coincidences for different acquisition time windows. Four of the acquisition protocols considered have a duration of 2 min, with starting times corresponding to the beginning of irradiation ('in-beam'), the end of irradiation ('online'), or the end of irradiation plus a delay of 1 min ('in-room(a)') or 2 min ('in-room(b))'. Such 'in-room' protocol could represent an *in situ* PET solution, e.g., a dual-head dedicated system that would be kept distant from the irradiation area due to spatial constraints and/or to avoid radiation damage, and would be repositioned on-site after irradiation by robotic arms. For further reference, an 'in-room(c)' protocol was considered, having a delay of 2 min and a longer duration of 5 min. This protocol has been found by Min *et al* (2013) to yield results similar to a 20 min PET scan in terms of the average range differences between PET measurements and computed-tomography image-based MC predictions. However, it is to be noted that these authors reported results of clinical trials of much higher complexity, using passive-scattering irradiation fields and a full-ring in-room PET scanner on wheels.

In general, the 2-minute *in situ* acquisitions are comparable in terms of the total amount of coincidences detected, with the 'in-room(b)' protocol registering the least amount of counts, viz. about 37% less than the 'online' case that registered the highest amount. Furthermore, the 'in-room(c)' acquisition registers about 2-times more counts than 'in-room(b)' due to its longer duration (figure 2.9). Although offline PET imaging is outside

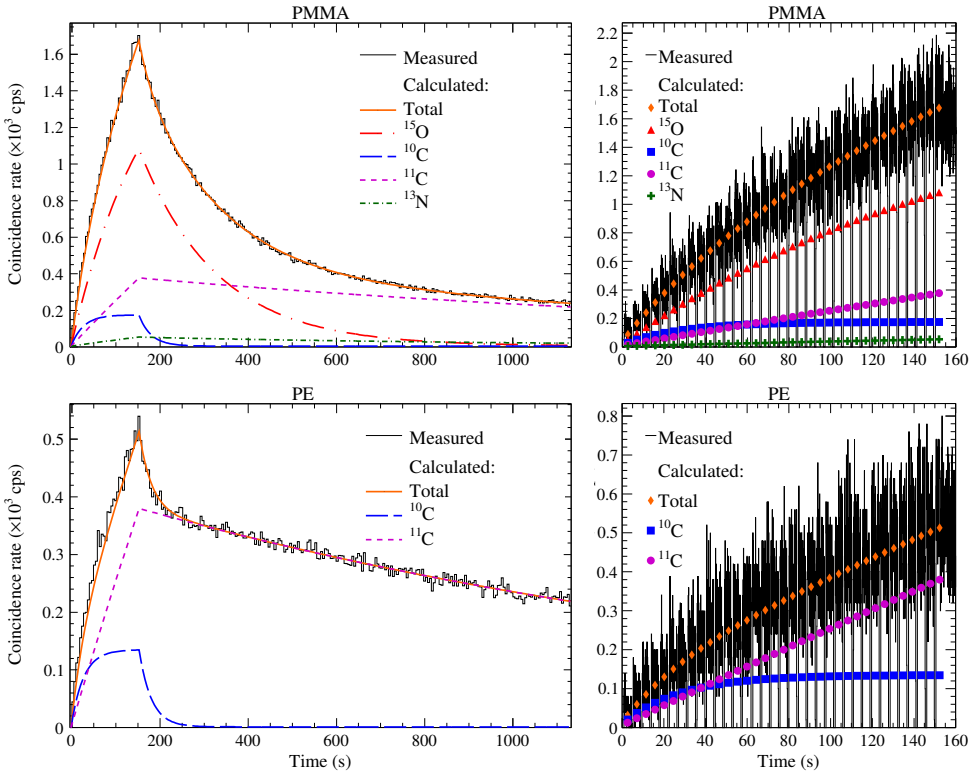

Figure 2.8: Comparison between measured and modeled coincidence count-rates (post energy selection) for PMMA (top) and PE (bottom). Also shown are the calculated individual contributions from each of the major nuclides. *Left:* measured data is presented with a bin size equal to one irradiation cycle (spill + pause), with each bin centered at the middle of the pause time, and with the count-rate per cycle approximated to the count-rate registered per pause. *Right:* zoom-in of the measured in-beam (pauses) coincidence count-rate, shown with a bin size of 0.05 sec, and the model prediction of the average rate per beam pause.

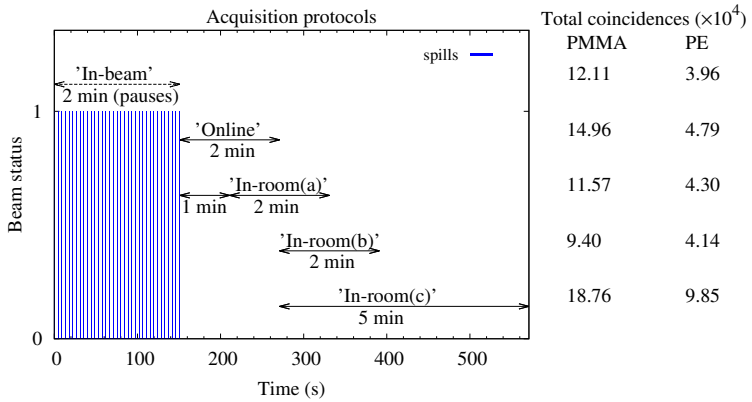

Figure 2.9: Definitions of acquisition protocols (left) and the corresponding measured total numbers of coincidences, post energy selection (displayed in-line on the right), from PMMA and PE phantoms. The coincidence counts were obtained with the detector placed at position 1 (figure 2.1-bottom). The 'in-beam' PET protocol corresponds to acquisitions during the beam pauses in between spills.

the scope of this paper, it is interesting to note that the amount of 43×10^4 registered coincidence counts from PMMA (not shown) for what is considered a best-case 'offline' delay of 5 min and a long scan duration of 30 min (Parodi *et al* 2008), is lower than the amount of 46×10^4 coincidences that would be obtained during the beam pauses and an extra *in situ* time of 7 min (i.e. 'in-beam' + 'online' + 'in-room(c)' protocols), if the detection efficiency is the same in both cases.

The total amount of modeled coincidences agreed with the detected coincidences shown in figure 2.9, to within < 1% for the 'online' and 'in-room(a), (b), and (c)' protocols, indicating the goodness of the fit. The amount of in-beam modeled coincidences summed over all pauses and for all isotopes, using equation (2.4), yielded ~4% higher amount of counts for PMMA and ~2% lower amount of counts for PE, compared to the detected counts listed in figure 2.9. It is to be noted that the full pause time was considered in equation (2.4), corresponding to a total in-beam time of 129 s, instead of the 120-second duration of the 'in-beam' measurement protocol considered, which in turn is expected to yield about 3% less counts compared to a measurement over the total pause time (section 2.2.2). Nevertheless, the agreement between the modeled and the measured in-beam count rate is satisfactory, as shown in figure 2.8.

Figure 2.10 shows the modeled relative amounts of coincidences from each of the main radionuclides produced in PMMA and PE, obtained with the *in situ* protocols, for detector position 1. Counts originating from ^{15}O surpass counts from other nuclides for all *in situ* protocols in PMMA, except for the 'in-room(c)' case in which ^{11}C disintegrations dominate. The fraction of ^{15}O counts for the 'offline' protocol is 8% only (not shown). Counts from ^{10}C, with a short half-life of 19.3 s, are found especially in the 'in-beam' acquisitions.

Changes can be noticed in the relative amount of coincidences from individual nuclides when the detectors are looking at the more proximal parts of the proton path (detector positions 2 and 3 in figure 2.1-bottom). Figure 2.11 shows the ratio of coincidences from carbon radionuclides (^{10}C plus ^{11}C) and ^{15}O (C/O ratio) for different detector positions and protocols. The C/O ratio is higher in general for detector positions 2 and 3 than for position

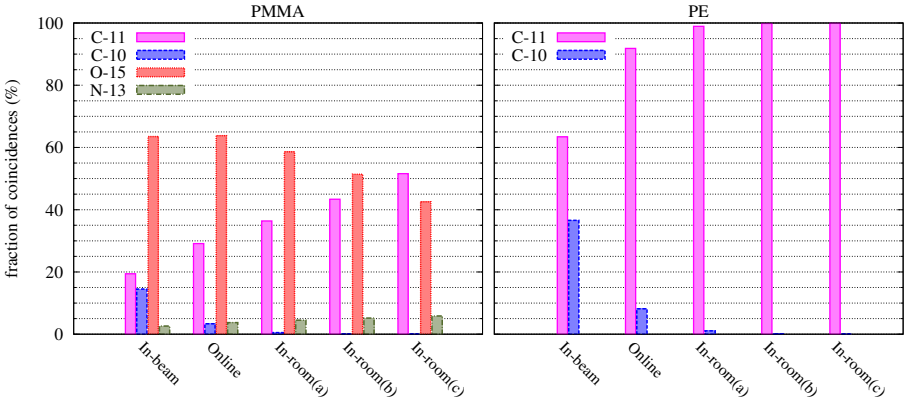

Figure 2.10: Modeled relative contributions of individual radionuclides to the count rate for PMMA (left) and PE (right), for different acquisition protocols (figure 2.9), obtained with the detector placed at position 1 (figure 2.1-bottom).

1. The maximum difference is observed for the 'in-beam' protocol, between positions 3 and 1, viz. a relative increase of 1.45. Overall, the C/O values in PMMA range from 0.5 to 1.3, consistent with previous values reported by Parodi *et al* (2005b). If weighted by stoichiometry, the C/O^{w} ratios range from 20% to 52%. Finally, the amount of ^{13}N counts is relatively low (< 7%) in all protocols.

The observed differences between detector positions are expected given the different energy dependency of the production cross-sections: the cross-section for the oxygen production channel, $^{16}O(p,pn)^{15}O$, is more peaked and higher for lower proton energies, compared to the main carbon production channel, $^{12}C(p,pn)^{11}C$, and the $^{16}O(p,3p3n)^{11}C$ channel (Bauer *et al* 2013). Therefore, a lower C/O is expected at the distal end of the proton path (position 1) compared to the more proximal phantom depths (positions 2 and 3). Likewise, the energy-dependent cross-section curve for the production channel $^{12}C(p,p2n)^{10}C$ is considerably shallower and has a higher energy threshold compared to that of the main channels leading to ^{15}O and ^{11}C (Iljinov *et al* 1991, EXFOR/CSISRS 2007). This may explain the larger differences in C/O ratio between detector position 1 and positions 2 and 3 for the 'in-beam' protocol compared to the other protocols.

2.3.4 Short PET acquisitions: activity distributions versus time window

Figure 2.12 shows the PET projection images obtained for the 'in-beam', 'online', and 'in-room(b)' protocols (figure 2.9). Figure 2.13-top shows the corresponding laterally integrated depth-profiles. Since protocols 'in-room(a), (b), and (c)' yielded qualitatively very similar results, only 'in-room(b)' is shown. The results present a hint of the crystal pattern (4 mm pitch), as the reconstruction algorithm becomes more sensitive to the detector

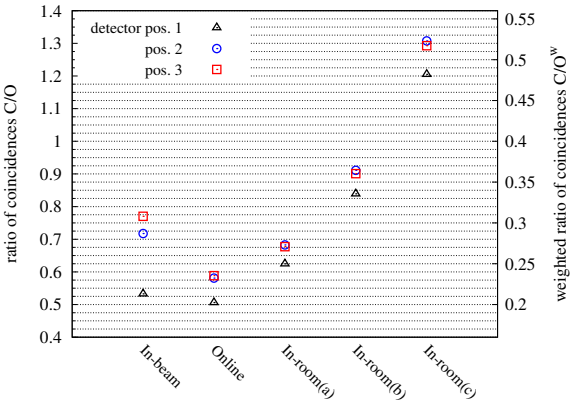

Figure 2.11: Carbon-to-oxygen (C/O) coincidence ratios in PMMA (modeled according to section 2.2.5), for different detector positions (figure 2.1-bottom) and acquisition protocols (figure 2.9). The carbon coincidences include contributions from ^{11}C and ^{10}C. The right axis displays the ratio of coincidences weighted by relative abundance of target nuclides (C/O^{w}).

discretization when the statistical fluctuations increase, compared to section 2.3.2.

The largest differences are observed between the 'in-beam' and post-beam protocols (both 'online' and 'in-room'), as the 'in-beam' depth-profiles are less peaked near the end of the proton range, especially for the PE phantom (figure 2.13-top). Based on the results of the previous section, these differences are probably due to the higher prevalence of ^{10}C decays (half-life of 19.2 s) in the 'in-beam' protocol (figure 2.10).

Figure 2.13 shows the activity depth-profiles simulated with FLUKA (bottom) in comparison to the measured ones (top). The simulated 'in-beam' profiles are shallower than the post-beam ones, especially in PE, in agreement with the measurements. To obtain further insight, the simulated 'in-beam' profiles were split into radionuclide-specific contributions, (figure 2.14). Indeed, the simulated ^{10}C profile is shallower than the others. Furthermore, due to the absence of ^{15}O activity in PE, the ^{10}C component is more prevalent than in PMMA. Finally, although in PMMA there is additional production of ^{11}C on oxygen, the ^{11}C activity is slightly higher in PE due to the molar ratio of carbon between PE and PMMA of 1.16.

The scale factors that normalize the measured activity depth-profiles to the same area as the simulated ones are not the same for all protocols. These values are presented in table 2.2. The scale factors appear to be consistent between the 'online' and 'in-room' protocols for PMMA, while for PE they are consistent between the 'in-room' cases. These results indicate that the total predicted activity in PMMA is underestimated by about 9% - 10% for the 'in-beam' protocol, while in PE the underestimation is about 18% for the 'in-beam' protocol and a few percent for the 'online' protocol. These differences might be due to an underestimation of the ^{10}C production, resulting from inaccuracies in the corresponding cross-section data. This hypothesis would also be consistent with the observed differences between the shapes of the simulated and measured 'in-beam' profiles in figure 2.13 (which are not observed for the other protocols).

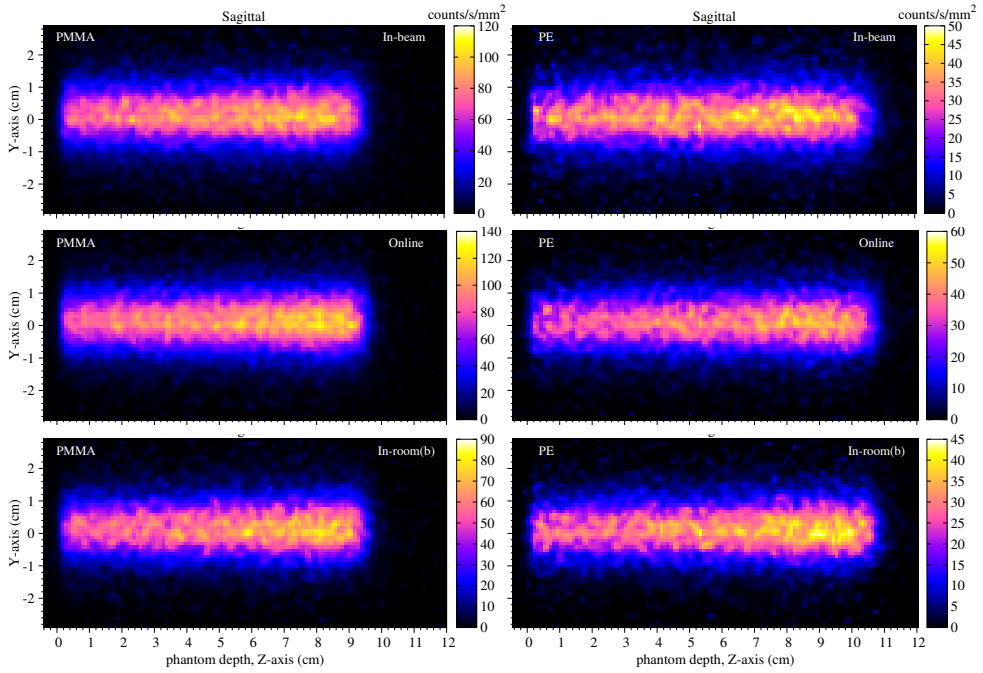

Figure 2.12: Sagittal views of measured projection images (reconstructed with TOF) of proton-induced activity in PMMA (left) and PE (right), obtained for 2-minute long *in situ* PET acquisitions (figure 2.9).

Table 2.2: Scale factors for normalization of the measured laterally-integrated depth profiles to the same area-under-the-curve as the simulated ones ($Norm_{area}$).

	$Norm_{area}$	
	PMMA	PE
In-beam	2.06	1.72
Online	2.27	2.05
In-room(a)	2.29	2.11
In-room(b)	2.29	2.11
In-room(c)	2.27	2.10

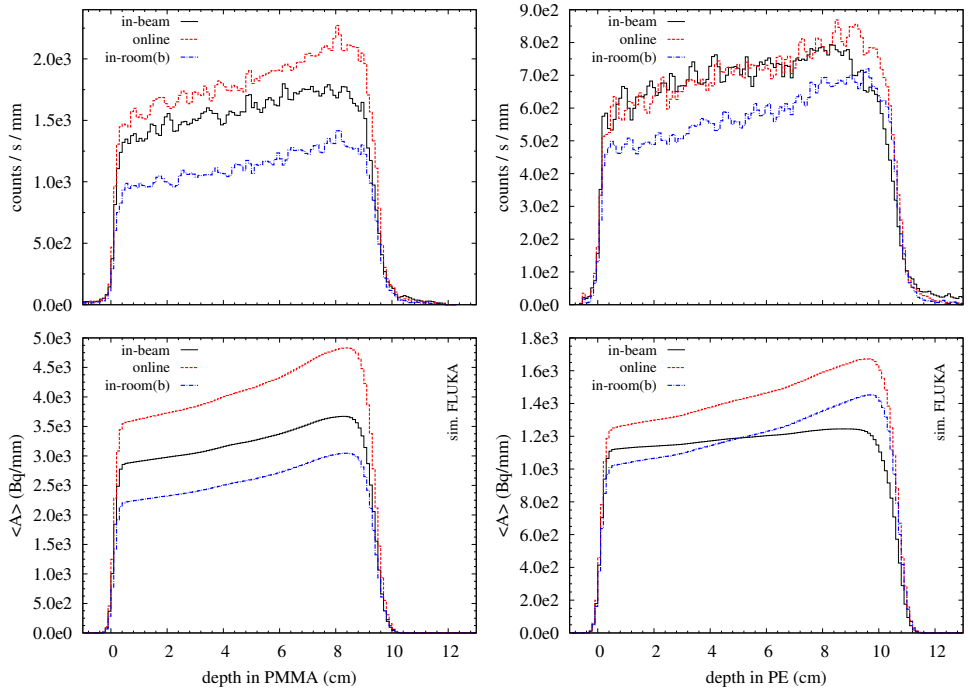

Figure 2.13: *Top*: laterally integrated measured depth-profiles (reconstructed with TOF) of proton-induced activity in PMMA (left) and PE (right), obtained during 2-minute long *in situ* PET acquisitions (figure 2.9). *Bottom:* corresponding simulated activity depth-profiles. Measured profiles are not calibrated to absolute activity.

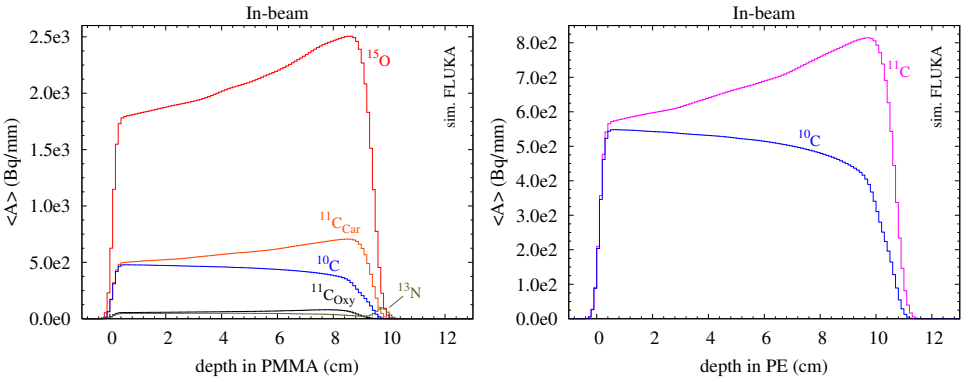

Figure 2.14: Simulated radionuclide-specific activity depth-profiles obtained during beam pauses, for PMMA (left) and PE (right). The ^{11}C activity is split between the two different production channels, viz. ^{12}C(p,pn)^{11}C (^{11}C$_{Car}$) and ^{16}O(p,3p3n)^{11}C (^{11}C$_{Oxy}$).

2.3.5 Range assessment: precision and bias for short PET acquisitions

The activity range was estimated by fitting a sigmoid curve to the distal end of the laterally integrated activity depth-profiles and determining the Z-position (phantom depth) of the inflexion point of the fitted curve. The 50% peak pickoff value is a typical way of determining activity range (e.g., Surti *et al* 2011, Shao *et al* 2014). For this purpose we used the four-parameter complementary error function previously described by Henriquet *et al* (2012). Figure 2.15 shows some examples obtained with the 'online' protocol.

The uncertainty in determining the activity range in PMMA was estimated as the standard deviation between six samples. Each profile was acquired with the proton range at a different location within the detector FOV, by shifting the phantom over known, small distances along the beam axis. The fitting range was between the profile mean and the distal end of the detector FOV, using a data set corresponding to one detector FOV of about 6 cm length along the beam path (figure 2.15). Phantom shifts of 1 mm are clearly distinguishable, see figure 2.15. The uncertainty in the activity range is represented by the error bars on the blue squares in figure 2.16-left and varies between ±0.2 and ±0.3 mm (one standard deviation).

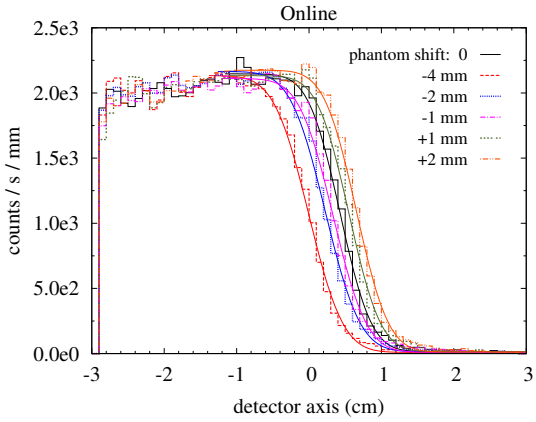

Figure 2.15: Laterally integrated measured depth-profiles (reconstructed with TOF) of proton-induced activity in PMMA, obtained from 2-minute long PET acquisitions, starting right after irradiation, with the phantom positioned such that the center of the field of view was located 8 mm proximal to the proton range (phantom shift = 0) and for various phantom shifts along the beam axis. The smooth curves correspond to sigmoid fits to the data.

The blue squares in left- and right-hand plots of figure 2.16 show the difference (bias) between the activity range and the proton range in PMMA and PE, respectively, where the proton range was determined from simulated depth-dose profiles (section 2.2.1). The differences between the various protocols are small, with the exception of the 'in-beam' measurement in PE, which differed by 1.6 mm and 1.9 mm relative to the 'online' and 'in-room(c)' protocols, respectively.

The bias in PE is more than 2 times larger than in PMMA for all protocols, which may be due to the absence of counts from ^{15}O and ^{13}N in PE. The energy threshold for the production channel ^{16}O(p,pn)^{15}O is lower than for the channel ^{12}C(p,pn)^{11}C (viz. 16.6 MeV vs 20.3 MeV), yielding a lower proton residual range in PMMA (Parodi *et al* 2000). Moreover,

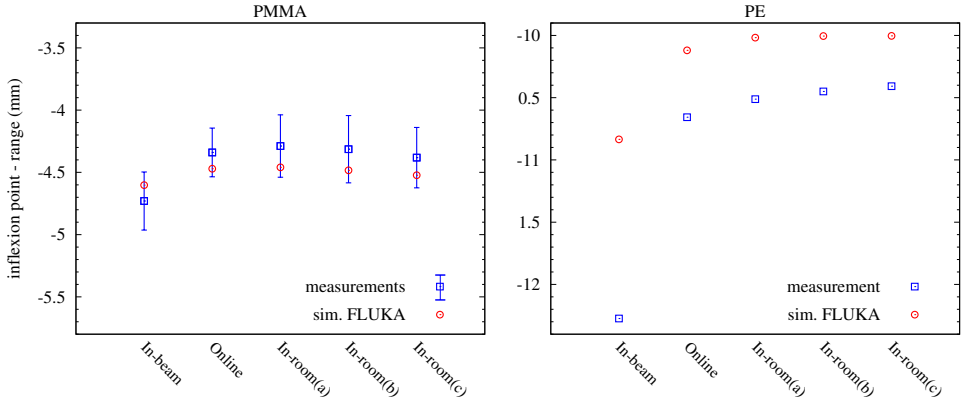

Figure 2.16: Differences (bias) between estimated activity range (inflexion point from sigmoid fit) and proton range, obtained from experimental (blue squares) and simulated (red circles) data, for PMMA (left) and PE (right). For PMMA, the mean and standard deviation (error bars) of six samples from the experimental data are shown.

despite the relatively small amount of nitrogen counts, the reaction ^{16}O(p,2p2n)^{13}N has a low threshold of 5.66 MeV (Beebe-Wang *et al* 2003) and the cross-section curve is strongly peaked at low proton energies (Bauer *et al* 2013), leading to a noticeable contribution at the very end of the activity profile in PMMA (figure 2.14).

The red circles in figure 2.16 represent the bias between the simulated activity range and proton range. The simulations are found to agree with the experimental results to within 0.2 mm for PMMA and to within 0.5 mm for PE, except for the 'in-beam' protocol in PE for which the discrepancy increases to 1.4 mm. These results corroborate the findings of section 2.3.4 regarding a presumable underestimation of ^{10}C counts in the simulation, taking into account that the ^{10}C production energy threshold (viz. 34.5 MeV (Beebe-Wang *et al* 2003)) is considerable higher than those of the other isotopes.

2.4 Conclusions

We have characterized, for the first time, the performance of TOF-PET detectors based on dSiPMs (viz. digital photon counters - DPCs) for imaging proton-induced β^+ activity *in situ*. PET acquisitions were done within beam pauses (in-beam) and immediately after irradiation of PMMA and PE phantoms by an actively-delivered synchrotron pencil beam, with a clinically relevant energy (125.67 MeV/u), intensity (4.6×10^8 protons/s), and total number of protons (10^{10}). The *in situ* TOF-PET prototype consisted of two detectors containing DPC arrays coupled in a 1-to-1 arrangement to LYSO:Ce crystal arrays with a 4 mm pitch. Coincidence count-rates of up to 8.6 kcps were registered (using a coincidence window of ±1 ns) while the crystal front-surfaces were placed at ~6 cm from the beam axis, representing a scaled-down version of a limited-angle dual-head PET system ($2 \times 50°$,

of 360°, transaxial angular acceptance). With this configuration, the scatter fraction was found to be 22%, while the energy resolution for 511 keV annihilation quanta equaled 12% FWHM and the random-to-true ratio was negligible (< 0.5%).

Fully 3D TOF-PET image reconstruction yielded distortion-free projection images in the mid-plane between the detectors, as well as laterally integrated depth-profiles of the activity distribution over nearly the entire detector FOV, which compare well with FLUKA simulations. Inspection of beam-transverse image slices reconstructed with and without TOF information demonstrate the benefit of TOF reconstruction for the reduction of limited-angle artefacts, although the full elimination of these artefacts requires a better coincidence resolving time than the 382 ps FWHM obtained with 2nd-photon triggering in the present setup.

The build-up of the in-beam coincidence rate as well as the post-beam decay were successfully modeled to disentangle the individual contributions from the major radionuclides involved. Differences in their relative contributions are observed at different phantom depths. The maximum variation in the C/O coincidence ratio is found for in-beam acquisitions (viz. C/O is 1.45-times higher when the detector is looking at the phantom-start region compared to the end-of-range region), which is attributed to the contribution from short-lived ^{10}C.

Laterally integrated activity depth-profiles from short (2-minute) in-beam and variable-delay post-beam PET acquisitions were compared with each other and with FLUKA simulations. The uncertainty in the activity range determined from sigmoid fits to the measured profiles in PMMA is 0.2 mm - 0.3 mm (SD out of six samples, between ~0.1M and ~0.15M crystal pairs reconstructed). Good agreement is observed between the simulated and measured profile shapes, as well as between the simulated and measured activity ranges (up to 0.5 mm difference in PE) for the post-beam protocols. However, a comparison of the areas under the simulated and measured activity curves suggests an underestimation by 9% - 10% (PMMA) and 18% (PE) of the total simulated activity in the case of in-beam acquisition. This is supported by the observed overestimation of the simulated activity range by 1.4 mm in PE, which is presumably due to an underestimation of ^{10}C counts in the simulated profiles.

In conclusion, this work provides a first demonstration of the feasibility of using DPC-based detectors for *in situ* TOF-PET imaging for proton therapy monitoring. The results presented are representative of a TOF-PET dual-panel tomograph that would comply with the spatial constraints typically encountered in clinical practice, thus providing information relevant to the development of clinical in-beam TOF-PET systems. Further studies will be necessary to understand the influence of radiation damage on the long-term performance of DPC-based detectors. Finally, our results indicate that further work is required to improve the prediction of proton-induced ^{10}C activity, which is relevant in particular for *in situ* PET systems that aim at measuring the activity in-beam.

Acknowledgments

This work was funded in part by the foundation for Fundamental Research on Matter (FOM), The Netherlands (grant no. 09NIG18), by the European Union Seventh Framework Program (grant agreement no. 241851), by the German Ministry for Education and Research (grant agreement no. 01IB13001G), and by the German Research Foundation DFG (KFO 214). P. Cambraia Lopes was supported by grant no. SFRH/BD/73705/2010 and P. Crespo by grant no. SFRH/BPD/39223/2007, both from FCT – Fundação para a Ciência e a Tecnologia, Lisbon, Portugal, co-funded by the European Social Fund and by

POPH – Programa Operacional Potencial Humano. P. Crespo is currently supported by QREN - FEDER under the Sistema de Incentivos à Investigação e Desenvolvimento Tecnológico (CENTRO-07-ST24-FEDER-002007, project 'Radiation for Life').

The authors would like to thank Philips Digital Photon Counting, in particular Carsten Degenhardt, York Haemisch, Ralf Schulze and Ben Zwaans, for fruitful discussions and help with the DPC hardware and software implementations. We acknowledge Jeroen Koning, Kees Langelaan and William van Goozen (DEMO, TU Delft) for technical support with the measurement setup, Stephan Brons (HIT, Heidelberg) for on-site technical support and advice on beam-related specifications, and Jan Huizenga (TU Delft) for support with the data acquisition and control electronics. We also thank Peter Dendooven (KVI, Groningen), Stefan Seifert (TU Delft), and Giacomo Borghi (TU Delft) for helpful discussions.

Chapter 3

Time-of-flight neutron rejection to improve prompt gamma imaging for proton range verification: a simulation study[1]

Therapeutic proton and heavier ion beams generate prompt gamma photons that may escape from the patient. In principle, this allows for real-time, *in situ* monitoring of the treatment delivery, in particular, the hadron range within the patient, by imaging the emitted prompt gamma rays. Unfortunately, the neutrons simultaneously created with the prompt photons create a background that may obscure the prompt gamma signal. To enhance the accuracy of proton dose verification by prompt gamma imaging, we therefore propose a time-of-flight (TOF) technique to reject this neutron background, involving a shifting time window to account for the propagation of the protons through the patient. Time-resolved Monte Carlo simulations of the generation and transport of prompt gamma photons and neutrons upon irradiation of a PMMA phantom with 100, 150 and 200 MeV protons were performed using Geant4 (version 9.2.p02) and MCNPX (version 2.7.D). The influence of angular collimation and TOF selection on the prompt gamma and neutron longitudinal profiles is studied. Furthermore, the implications of the proton beam microstructure (characterized by the proton bunch width and repetition period) are investigated. The application of a shifting TOF window having a width of ΔTOF_z = 1.0 ns appears to reduce the neutron background by more than 99%. Subsequent application of an energy threshold does not appear to sharpen the distal falloff of the prompt gamma profile but reduces the tail that is observed beyond the proton range. Investigations of the influence of the beam time structure show that TOF rejection of the neutron background is expected to be effective for typical therapeutic proton cyclotrons.

[1] A. K. Biegun, E. Seravalli, P. Cambraia Lopes, I. Rinaldi, M. Pinto, D. C. Oxley, P. Dendooven, F. Verhaegen, K. Parodi, P. Crespo and D. R. Schaart, Phys. Med. Biol. 57, 6429-44, 2012.

3.1 Introduction

Technological developments, such as intensity-modulated radiotherapy (IMRT, e.g., Cheung (2006) and Bortfeld (2006)), intensity-modulated proton therapy (IMPT, also studied by Bortfeld (2006), Lomax 2008a, 2008b, Pedroni *et al* 2004), or light ions delivered either with a raster-scanned beam (Haberer *et al* 1993, 2004), or passive shaped beams (Hiraoa *et al* 1992, Futami *et al* 1999), enable increased dose conformity and, therefore, higher tumor doses. The benefits of these recent technological improvements are now becoming measurable. One example is the dose escalation study by Schulz-Ertner *et al* (2004) for treating adenoid cystic carcinomas with carbon ions, which has been performed at the experimental ion therapy facility at the GSI Helmholtzzentrum für Schwerionenforschung, Darmstadt, Germany. Moreover, the same authors found that dose escalation in the tumor indeed correlates with higher local control rates for, e.g., skull-base chordomas (Schulz-Ertner *et al* 2007).

These new techniques have to be used with caution in order to ensure that high-dose exposure is restricted to the target volume only. Verification of the treatment delivery is particularly challenging in particle therapy since the primary radiation is fully stopped within the patient. However, a fraction of the particles in therapeutic proton and heavier ion beams undergo nuclear reactions within the body, generating positron emitters as well as prompt gamma photons that may escape from the patient. In principle, the prompt gamma emission allows for real-time, *in situ* monitoring of the treatment delivery, in particular the particle range within the patient, by imaging the emitted prompt gamma rays.

Prompt gamma imaging can be achieved in different ways. For example, a single, collimated detector can be moved parallel to the beam axis to measure the profile of perpendicularly emitted prompt gamma photons (Min *et al* 2006, Testa *et al* 2008, Polf *et al* 2009b). To enhance detection efficiency, one may use a planar or confocal multi-slit collimator (Krimmer *et al* 2012). In these approaches, the function of the collimators is to reject photons that are emitted from the patient in directions other than perpendicular to the beam axis. In another approach, a knife-edge slit collimator is used to project an image of the prompt gamma emission onto a gamma camera (Bom *et al* 2012, Peloso *et al* 2011, Prieels *et al* 2011, Roellinghof *et al* 2012, Smeets *et al* 2012a, 2012b). Collimator-free imaging of the prompt gamma emission is being investigated using several different Compton camera designs, i.e. multi-stage measurement devices capable of determining the initial energy and direction of a gamma photon as it undergoes the Compton scattering within the different stages of the detectors (Llosá *et al* 2010, 2011, Peterson *et al* 2010, Robertson *et al* 2011, Kormoll *et al* 2011, Roellinghoff *et al* 2011).

A preliminary Monte Carlo study on the use of prompt gamma emission as a method to verify the accuracy and efficacy of doses delivered with proton radiotherapy has been performed by Polf *et al* (2009a). The results showed that the prompt gamma spectra differ significantly for different types of tissue and that a strong spatial correlation exists between the delivered spread-out Bragg peak (SOBP) and the characteristic prompt gamma production. A comparison between treatment verification based on an idealized, simulated prompt gamma imaging scenario and a more realistic positron-emission tomography (PET) scenario for several anatomic locations has been modeled in a heterogeneous tissue environment by Moteabbed *et al* (2011). Prompt gamma imaging was found to be potentially advantageous especially for the verification of small tumor irradiations in the presence of highly heterogeneous tissues, provided that the emitted prompt gamma photons could efficiently be detected.

In all prompt gamma-based approaches, a considerable background signal resulting from the simultaneously created neutrons may obscure the prompt gamma image. This

background signal may result from direct interactions of the neutrons in the detectors and/or from gamma photons produced by the neutrons within the collimators and/or other structures surrounding the detectors. As the neutrons are strongly scattered within the body of the patient, their spatial and directional correlation with the dose profile is lost and their effect on the prompt gamma image can only be detrimental.

Inspired by the work of Testa *et al* (2008), we propose a method for neutron background rejection based on a shifting time-of-flight (TOF) acceptance window to enhance the accuracy of prompt-gamma-based range verification in pencil beam scanning proton radiotherapy. This method, which in principle is compatible with any of the previously outlined prompt gamma imaging approaches, is investigated by means of Monte Carlo simulations. As we observed relatively large discrepancies between the prompt photon and neutron production rates predicted by different codes, we present results obtained using Geant4 (version 9.2.p02) and MCNPX (version 2.7.D). We study the influences of angular collimation, TOF selection and energy discrimination on the prompt gamma and neutron longitudinal profiles. Furthermore, we investigate the implications of the accelerator-dependent proton beam microstructure (characterized by the proton bunch width and repetition period) on the proposed neutronrejection technique.

3.2 Materials and methods

The slowing down of protons within a PMMA phantom and the production of prompt photons and neutrons in the nuclear interactions undergone by some of these protons were simulated using two different Monte Carlo codes: Geant4 and MCNPX. In the following, we first summarize some specific features pertaining to each of these codes (sections 3.2.1 and 3.2.2) and then discuss the general simulation setup used for all calculations in this work (section 3.2.3).

3.2.1 Geant4

Geant4 (version 9.2.p02) is a C++ toolkit for simulating the transport and interactions of particles in matter, offering a comprehensive range of physics processes over a wide range of energies (Agostinelli *et al* 2003). In this work, two Geant4 physics lists were compared in order to check the proper choice of physics processes. Both sets are based on the Geant4 hadron therapy example (Cirrone *et al* 2009).

The models used in the first physics list (Physics List 1) are Decay, Photon-EPDL, Electron-EEDL, EMPositronStandard, Ion-LowE, EMMuonStandard and Proton-precompoundGEM. Low-energy packages for electromagnetic (EM) interactions and hadronic interactions were used, while the inelastic hadronic interactions were simulated-with the Binary Cascade model, in which the primary and secondary particles in a nucleus are propagated.

The second physics list (Physics List 2) contained the standard package for EM interactions combined with the G4Hadron-Elastic model for elastic hadronic interactions (Grevillot *et al* 2010). Physics List 2 was supplemented by a number of nuclear-reaction processes and finally contained Decay, EM-Photon-Standard, EMElectronStandard, EM-PositronStandard, EMHadronIonStandard, EMMuonStandard, HadronElastic-HadronIon-UElastic, HadronicInelastic-ProtonNeutron-Precompound, HadronicInelastic-Ion-LEP, HadronicInelastic-Pion-LEP and HadronicAtRest-MuonMinus-Capture.

The mean ionization potential for PMMA used by Geant4 is 74 eV. The production threshold of all secondary particles was fixed to 0.01 mm.

The type, position, momentum and time were registered for all proton-induced secondary particles when they crossed the surface of the detector. Angular selection of prompt gamma rays was performed offline.

3.2.2 MCNPX

MCNPX (version 2.7.D) is a radiation transport code developed at Los Alamos National Laboratory (LANL) and capable of tracking many particle types (electrons, photons, nucleons and ions) over a wide range of energies (MCNPX 2008). MCNPX uses (1) standard evaluated nuclear data tables for protons and neutrons up to 150 MeV, (2) physics models for additional particle types such as deuterons, tritons, alphas, pions, muons, etc. and (3) physics models for neutrons and protons when no tabular data are available. The proton transport algorithm takes into account energy straggling, multiple Coulomb scattering, elastic and inelastic scattering, and non-elastic nuclear interactions (MCNPX 2008). The use of the collision energy-loss model (maximum kinetic energy transfer model) leads to stopping powers in close agreement with ICRU data (ICRU 1984, MCNPX 2002). The implemented multiple-scattering model relies on Rossi's theory, assuming a Gaussian distribution of angular deflections (Herault *et al* 2005, MCNPX 2002, Sawakuchi *et al* 2010).

In this work, MCNPX 2.7D has been used, together with the LA150 evaluated nuclear data library (Chadwick *et al* 1999) whenever available for the transported particles, and the Cascade-Exciton model (Mashnik 2006) of nuclear reactions in all other cases, as suggested by the developers (Waters 2010).

The mean ionization potential for PMMA is 71 eV (Seravalli *et al* 2012). The energy cuts for all particles were left at their default values, which for protons equals 1 MeV (MCNPX 2008).

The surface current tally type (F1) was used for scoring prompt gamma photons and neutrons, combined with time and angular selection when required. The mesh tally type (F3) was used for scoring depth–dose profiles.

3.2.3 Simulation setup

The simulation setup is illustrated in figure 3.1. Mono-energetic proton pencil beams with energies E_p of 100, 150 and 200 MeV impinging on a polymethyl-methacrylate (PMMA) phantom (chemical composition $C_5O_2H_8$ and density ρ = 1.18 g cm^{-3}) were simulated to mimic a neutron-free proton beam delivered by an active scanning system. The energy deposition in the PMMA phantom was registered as a function of the longitudinal position z to determine the depth-dose profile for each simulation.

Prompt gamma photons and neutrons were detected in a cylindrical detector, coaxially surrounding the PMMA phantom and having the same length in the z direction. The detector was assumed to be 'perfect' in the sense that it had 100% detection efficiency as well as perfect position and time resolution. By using such an idealized detector we investigate the intrinsic properties of the prompt gamma fluence produced during proton therapy to deduce the potential of using these prompt gamma photons for treatment monitoring.

For each gamma photon or neutron arriving at the detector, the particle type, the energy, the position of detection along the z-axis, the angle of incidence in terms of the polar angle θ relative to the beam axis and the time of detection relative to the time at which the primary proton had been launched (at a distance d_0 of 1 cm from the PMMA target) were registered.

All calculations were performed with 2×10^7 primary protons. For comparison, during the delivery of a 2 Gy fraction in a typical spot-scanning scenario, the lowest dose spots

may receive less than 10^7 protons while the highest dose spots (typically the most distal spots) may receive more than 10^8 protons (Smeets *et al* 2012b).

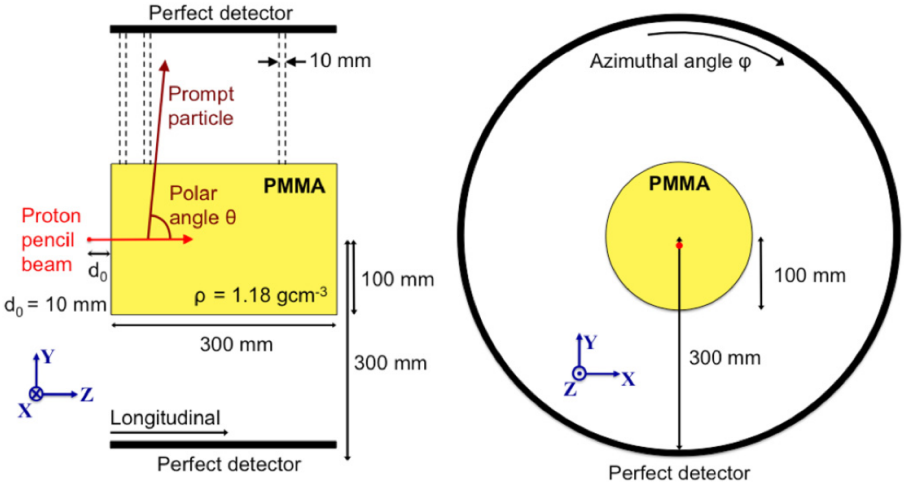

Figure 3.1: Longitudinal cross-section (left) and beam's eye view (right) of the simulation setup. The incident protons are assumed to be mono-energetic and the beam shape is pencil-like. The cylindrical PMMA phantom, placed in air, has a diameter of 20 cm and a length of 30 cm. The inner diameter of the detector is 60 cm, while its length is equal to that of the PMMA phantom.

3.3 Results and discussion

3.3.1 Geant4 physics list

The prompt gamma profiles computed with Physics List 1 and Physics List 2 (section 3.2.1) appeared to be the same, both in terms of the profile shape (including the distal falloff region near the location of the Bragg peak) and in terms of the integral prompt gamma yield, for all initial beam energies studied. Thus, one can conclude that both choices of the physics models are consistent in the prompt gamma studies presented. For the remainder of the studies presented here, models from Physics List 1 were used.

3.3.2 Prompt gamma, neutron and depth-dose profiles

To obtain the prompt gamma profiles, the effect of angular collimation was simulated by accepting only photons impinging on the detector within a certain range of polar angles θ around normal incidence, i.e. $\theta_\perp = 90^\text{o}$ (see figure 3.1 for the definition of the coordinates). Two angular acceptance windows were compared: a wide angular window $\Delta\theta_1$, corresponding to $87.0^\text{o} \leq \theta \leq 93.0^\text{o}$ and a narrow window $\Delta\theta_2$, corresponding to $89.3^\text{o} \leq \theta \leq 90.7^\text{o}$.

In contrast, neutron profiles were obtained by accepting all neutrons impinging on the detector. This reflects the assumption that neutrons will either not be stopped in a typical lead or tungsten collimator, or, if they are stopped, that they may create secondary gamma photons. Both scenarios may lead to background counts in the detector. Thus, the simulated neutron background may be seen as a worst-case scenario.

Figures 3.2(a) and (b) show the results obtained with Geant4 and MCNPX at proton energies of 100 and 200 MeV, respectively. These figures also show the corresponding proton depth–dose profiles in PMMA as calculated by Geant4. As in previous studies (Seravalli *et al* 2012), the depth–dose profiles calculated by MCNPX were found to be very similar and therefore are not shown. The prompt gamma yield predicted by MCNPX (red and blue dashed lines) is found to be lower by a factor of 2–5 (at different depths in PMMA and different proton beam energies) compared to Geant4 (red and blue solid lines). Conversely, MCNPX (dashed line) predicts a neutron yield about two times higher than Geant4 (solid line). These results indicate large discrepancies between the algorithms used by the two codes to simulate proton-induced nuclear reactions.

Nevertheless, both codes predict that for the narrow angular collimation window $\Delta\theta_2$, the prompt gamma profile shows a steep falloff that is well correlated with the Bragg peak. The wider collimation window $\Delta\theta_1$ allows for gamma spatial profiles to be detected that still show a falloff region correlating with the Bragg-peak position. It is evident that opening up the angular collimation window increases the number of detected photons and thereby improves the gamma-to-neutron (G/N) ratio, but also results in a shallower falloff of the measured prompt gamma profile. The uncertainty in the localization of the Bragg-peak position depends on both the G/N ratio and the slope of the gamma profile in the falloff region. Thus, when designing a collimator, a trade-off will have to be made between signal strength and profile shape.

The neutron yield, represented by the black curves in figures 3.2(a) and (b), is observed to be of the same order of magnitude or larger than the prompt gamma yield, depending on the proton energy and the Monte Carlo code used for the simulation. The correlation between the neutron profile and the dose distribution is found to be very weak. In a realistic prompt gamma imaging device, the neutrons may therefore give rise to a detrimental background signal via direct interactions in the detector and/or via gamma photons produced within the collimators and/or other structures surrounding the detector.

Consequently, some form of neutron background rejection should be implemented to preserve the accuracy of the proton range verification. Solutions such as TOF tagging (Testa *et al* 2008), pulse shape discrimination (Testa *et al* 2010) and neutron shielding (Min *et al* 2006) have been proposed. In this work, we investigate a neutron-rejection technique based on a shifting TOF window, described in more detail in section 3.3.3. In the remainder of this work, we focus mostly on the Geant4 simulations, since these were found to give the lowest gamma-to-neutron ratio and thus represent the worst possible starting scenario. All conclusions derived for the Geant4 code are therefore also assumed to be valid for the MCNPX simulations.

3.3.3 Prompt gamma and neutron TOF spectra

The total TOF measured for a given secondary particle (prompt photon or neutron), defined as the total elapsed time between the emission of the primary proton and the detection of the gamma (or neutron) in the detector, depends on the distance traveled by the primary proton in the phantom and the distance traveled by the gamma photon or neutron from the point of creation to the point of detection. In our simulation setup (figure 3.1), the TOF dispersion of the detected gamma photons therefore is correlated directly to the range of positions along the longitudinal z-axis at which prompt gamma photons are created. If one counts only gamma photons emitted in a short longitudinal segment of the phantom, a narrower TOF distribution is produced.

To investigate this in more detail, the detector was subdivided into 10 mm segments in the longitudinal direction, and for each segment, the TOF spectra of the prompt gamma

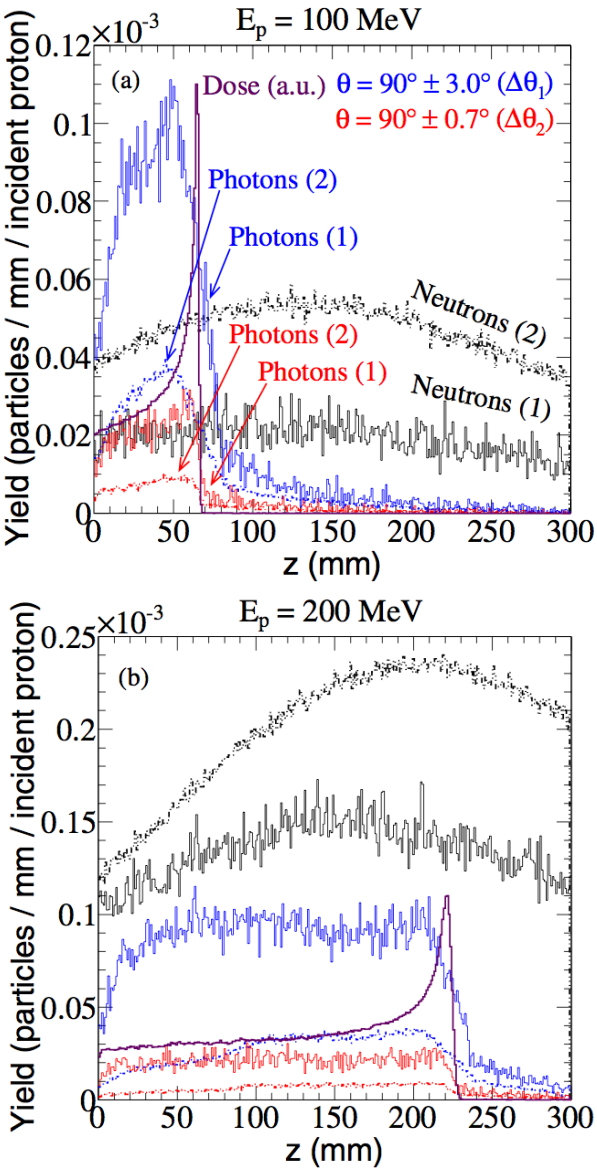

Figure 3.2: Prompt gamma yield (blue and red) and neutron yield (black) registered in the detector as a function of the longitudinal distance z, in comparison to the proton depth–dose profile in the PMMA phantom (purple), for mono-energetic proton pencil beams of (a) 100 and (b) 200 MeV. Simulated prompt gamma profiles are shown for the narrow angular collimation windows $\Delta\theta_2$ (red) and the wider one $\Delta\theta_1$ (blue). Data obtained with both Geant4, denoted as (1), and MCNPX, denoted as (2), are shown. The longitudinal bin width is 1 mm in all calculations and all results are normalized per incident proton, except for the proton depth-dose curve, which is given in arbitrary units (a.u.) and was calculated with Geant4.

photons detected within the angular collimation windows $\Delta\theta_1$ and $\Delta\theta_2$ were obtained. Figure 3.3(a) schematically shows two examples of such regions together with the depth-dose profile of 200 MeV protons in PMMA. The photon and neutron TOF spectra obtained with Geant4 for these two detector regions are shown in figures 3.3(b) and (c). It can be observed that the prompt gamma peak indeed occurs later for detector segments located at larger values of z.

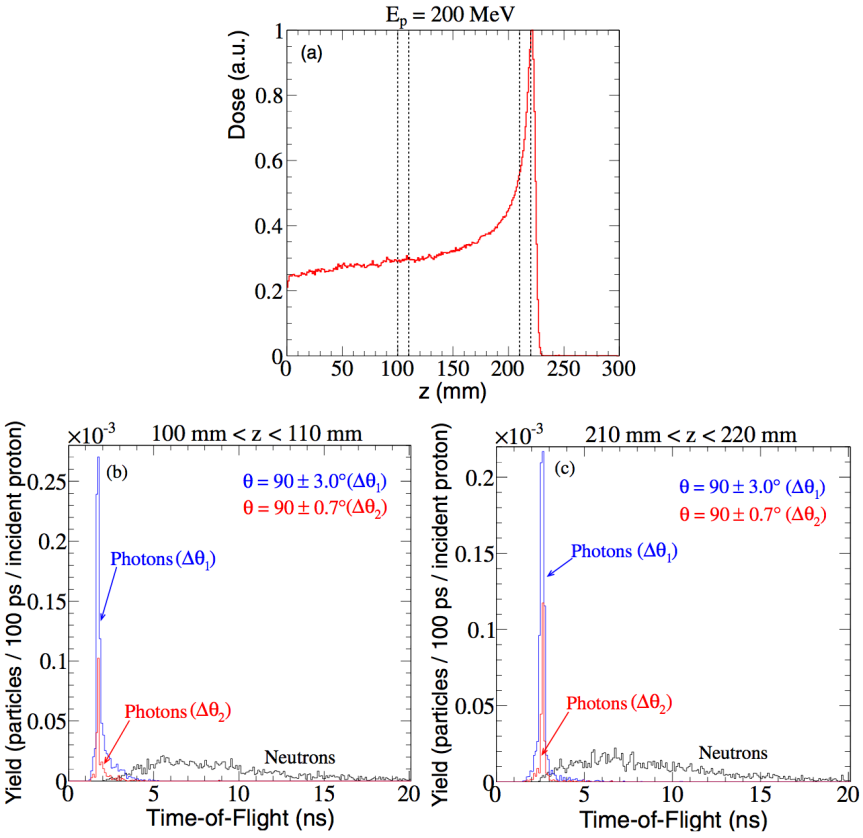

Figure 3.3: (a) Simulated depth–dose profile of 200 MeV protons in PMMA. Two examples of 10 mm wide regions along the proton beam path are indicated. (b), (c) The TOF spectra of the prompt gamma photons (blue and red) and neutrons (black) impinging onto the corresponding two detector regions (see also figure 3.1). Photon profiles are shown for the two angular collimation windows $\Delta\theta_1$ (blue) and $\Delta\theta_2$ (red). All results were simulated with Geant4.

For each segment, the prompt gamma TOF spectrum appears to form a relatively narrow peak that occurs earlier than the maximum of the much broader neutron TOF spectrum. This was found at all proton beam energies; however, the total yield as well as the overlap of the neutron and gamma TOF spectra was found to increase with increasing initial beam energy. In this respect, the results presented in figures 3.3(b) and (c) for 200 MeV protons may be seen as representative for the maximum overlap that may be expected within the range of typical clinical proton energies.

To investigate the rejection of the neutron contamination in the prompt gamma signal, the TOF information of the narrowly collimated gamma photons ($\Delta\theta_2$) is used. It is noted that TOF spectra similar to those shown in figures 3.3(b) and (c) were obtained with MCNPX, so the MCNPX results are not shown here for brevity. The prompt gamma TOF spectra obtained with both codes for the different detector segments each show a distinct, sharp peak. These peaks were fitted with Gaussian functions and their mean value μ and standard deviation σ were determined for all beam energies investigated in this study. The parameters μ (denoted as 'TOF shift') and σ are plotted as a function of the longitudinal position z in figure 3.4(a) (symbols with error bars). The data points obtained with Geant4 and MCNPX are very similar; they differ by less than 100 ps at all longitudinal positions.

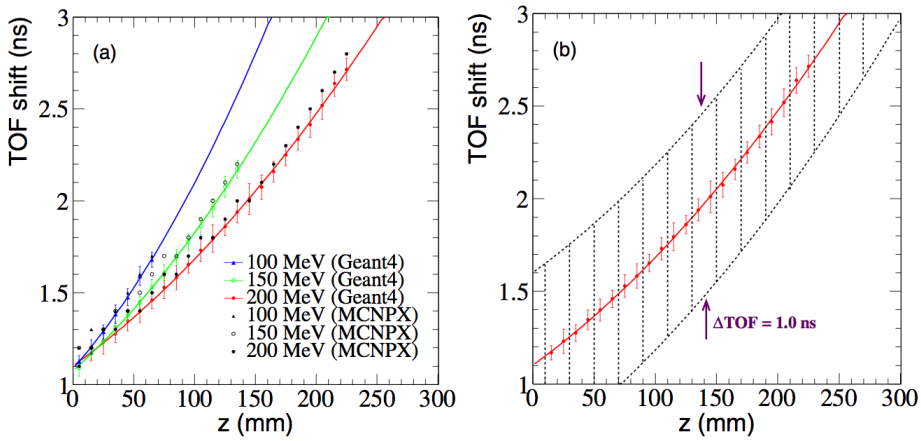

Figure 3.4: (a) TOF shifts obtained for each 10 mm detector segment along the z-axis for proton energies of 100, 150 and 200 MeV (symbols). Data were derived for narrowly collimated photons ($\Delta\theta_2$). Second-order polynomials were fitted to the data points (curves). (b) Example of the 1.0 ns wide TOF window used for 200 MeV protons.

3.3.4 Neutron rejection using a shifting TOF window

The data points of the Geant4 results in figure 3.4(a) were fitted with second-order polynomial functions (solid lines in the same figure). These fits were used to select events within a shifting TOF window ΔTOF_z, in order to discriminate the prompt gamma signal from the large neutron background. That is, at each longitudinal position of detection z, only photons and neutrons detected within a TOF window ΔTOF_z centered on the value of μ corresponding to z were accepted. An example of such a shifting TOF window, ΔTOF_z is indicated by the dashed lines in figure 3.4(b), for a proton beam energy of 200 MeV. Various ΔTOF_z windows, having widths ranging from ΔTOF_z = 0.4 ns up to ΔTOF_z = 2.0 ns, have been studied. The results show that TOF windows having a width of about 1.0 ns allow almost all prompt gamma photons to be detected while very few neutrons are accepted.

To illustrate this, prompt gamma and neutron profiles (Geant4 and MCNPX) obtained with a shifting time window of ΔTOF_z = 1.0 ns are presented in figures 3.5(a) and (b), for proton beam energies of 100 and 200 MeV, respectively. The prompt gamma profiles obtained with ΔTOF_z = 1.0 ns are similar to those in figure 3.2. For a proton energy of 100 MeV, Geant4 and MCNPX predict that in the region $0 \leq z \leq R$, where R = 68 mm is the proton range, they contain a total number of photons that is reduced by no more than

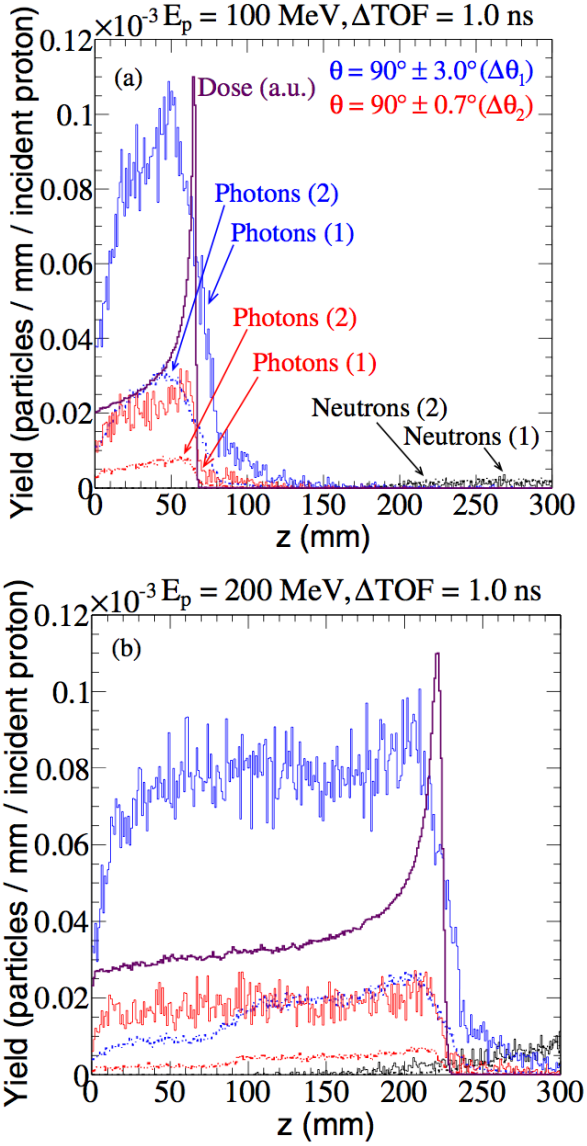

Figure 3.5: Prompt gamma yield (blue and red) and neutron yield (black) registered in the detector as a function of longitudinal distance z, in comparison with the depth–dose profile in the PMMA phantom (purple), for mono-energetic proton pencil beams of (a) 100 and (b) 200 MeV, upon application of the shifting time window shown in figure 3.3(b). Prompt gamma profiles are shown for the small angular collimation windows $\Delta\theta_2$ (red) and the larger one $\Delta\theta_1$ (blue). Data obtained with both Geant4, denoted as (1), and MCNPX, denoted as (2), are shown. The bin width is 1 mm in all calculations and all results are normalized per incident proton, except for the depth-dose curve, which is given in arbitrary units (a.u.) and was calculated with Geant4.

12% and 11%, respectively. At 200 MeV (R = 230 mm), these numbers are 15% and 32%, respectively.

In contrast, the neutron background is reduced much more strongly. Both codes predict that even at 200 MeV more than 99.6% of the neutrons are rejected in the region $0 \leq z \leq R$. The black curves in figures 3.5(a) and (b) indicate the small amount of neutrons remaining (Geant4 represented by a solid black line, MCNPX represented by a dashed black line). Most of these are found beyond the Bragg peak (i.e. at $z > R$). It can thus be concluded that the application of a shifting TOF window of an appropriate width can in principle eliminate almost all neutron background within the longitudinal region of interest.

3.3.5 Energy threshold

The influence of different energy thresholds on the prompt gamma profile has been studied. For example, figures 3.6(a) and (b) compare the prompt gamma profiles obtained for a proton energy of 200 MeVusing energy thresholds of 0.3 (red) and 1.0 MeV (blue) with those obtained without any energy threshold (black), for collimation windows $\Delta\theta_2$ and $\Delta\theta_1$, respectively.

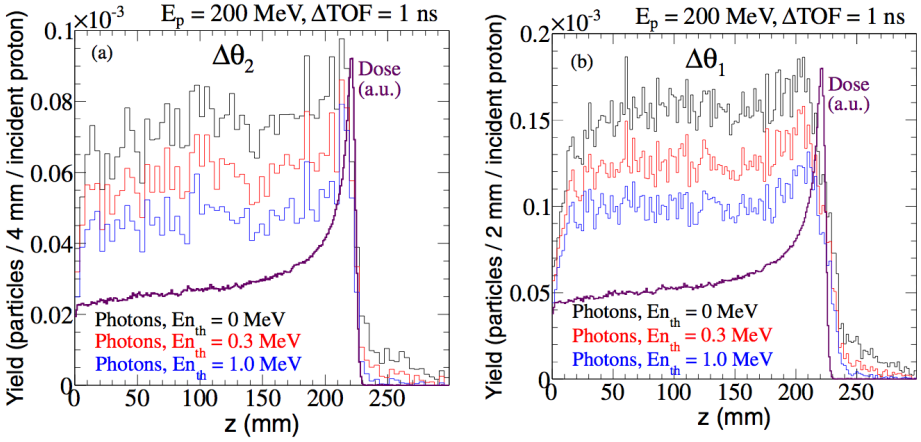

Figure 3.6: Prompt gamma profiles obtained with a proton energy of 200 MeV and the shifting TOF window indicated in figure 3.3(b), upon application of an energy threshold of 0.3 (red), 1.0 MeV (blue), or no threshold (black). Results are shown for both (a) the narrow angular collimation window $\Delta\theta_2$ and (b) the wide collimation window $\Delta\theta_1$. All results were simulated with Geant4.

Applying an energy threshold decreases the total number of prompt gamma photons detected but does not appear to influence the steepness of the distal falloff region. However, the energy threshold decreases the tail that can be observed beyond the Bragg-peak region, presumably by eliminating low-energy photons resulting from Compton scattering as well as neutron-induced reactions within the phantom. Interestingly, the application of an increasing energy threshold seems to progressively emphasize the peak in the prompt gamma profile that can be observed in the region just before the Bragg peak.

3.3.6 Beam time structure

Cyclotrons produce pulsed beams that can be characterized by their repetition period and bunch width. Proton cyclotrons typically operate at frequencies of 30–100 MHz, corresponding to repetition periods between 10 and 33 ns, and produce proton bunches with a Gaussian-like time profile having a width in the order of a nanosecond (Schippers 2009). In a few institutes, e.g., the Heidelberg Ion Therapy Centre (Ondreka and Weinrich 2008), a synchrotron is used to accelerate the protons (and/or other particles). In a typical therapy synchrotron, both the bunch width and the repetition period can be an order of magnitude larger than in a cyclotron. Furthermore, the beam time structure exhibit gaps of a few seconds, while particles are injected and accelerated; after this gap, the extraction (up to 10 s) takes place.

For typical cyclotron repetition rates, the neutrons generated by a given pulse may partially overlay themselves onto the next pulse. Figure 3.7(a) shows an example of the TOF spectra of the prompt gamma photons for $\Delta\theta_1$ (blue) and $\Delta\theta_2$ (red) registered in the detector region 210 mm $< z <$ 220 mm, i.e. in the Bragg peak area (figure 3.3(a)), for an incident proton energy of 200 MeV, simulated with Geant4. The black curve in this figure represents the corresponding TOF spectrum of the neutrons, for a repetition period of 20 ns. The inset shows a zoomed-in version of the initial part of the same plot. Compared to figure 3.3(c), the additional neutrons originating from the previous bunch are clearly visible. In synchrotrons, where the repetition period typically is an order of magnitude larger, this effect is accordingly smaller.

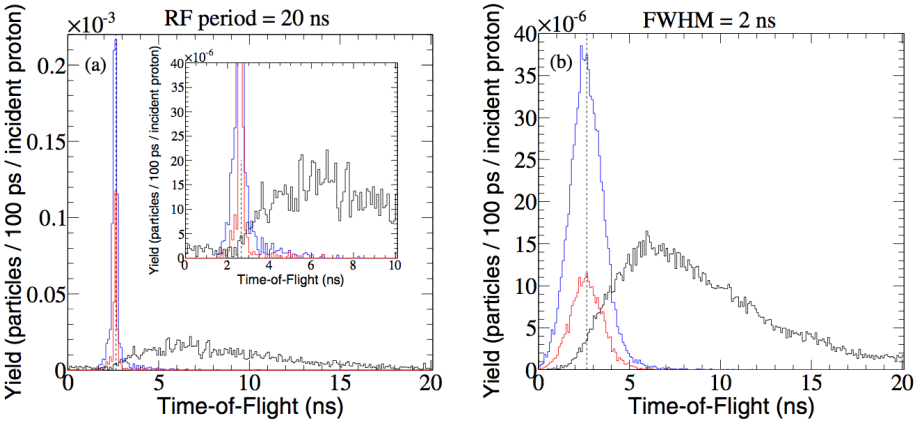

Figure 3.7: (a) Prompt gamma TOF spectra for angular collimation windows $\Delta\theta_1$ (blue) and $\Delta\theta_2$ (red) registered in the detector region 210 mm $< z <$ 220 mm (figure 3.3(a)), and neutron TOF spectrum (black) for a 20 ns repetition period (representative for cyclotrons). The inset shows a zoomed-in version of the initial part of the same plot. (b) TOF spectra convoluted with a Gaussian having a FWHM of 2 ns, representative of the bunch width of medical proton cyclotrons. All calculations were performed for a proton beam energy of 200 MeV.

Figure 3.7(b) provides an example of the influence of a finite bunch width. This figure shows the same photon and neutron TOF spectra (simulated with Geant4) as in figure 3.3(b), but convoluted with a Gaussian probability density function having a full-width at half-maximum (FWHM) of 2 ns. Although proton bunches may not exactly have a Gaussian shape in reality, this approximation is considered adequate for the present purpose. It can

be seen that a finite bunch width gives rise to an increased overlap between the photon and the neutron spectra.

To quantify the influence of the bunch width and repetition rate, the G/N ratio, averaged over the detector region $0 \leq z \leq R$ (i.e. over the entire proton range), is shown in figures 3.8(a) and (b) for various bunch widths (bunch FWHM) and for various repetition periods (1/RF), respectively. In addition, the total number of photons per incident proton registered in the same detector region is presented in figure 3.8(c) for various bunch widths. All calculations were performed for a proton energy of 200 MeV and for ΔTOF_z windows of 0.5 (black triangles), 1.0 (red squares) and 2.0 ns (blue circles).

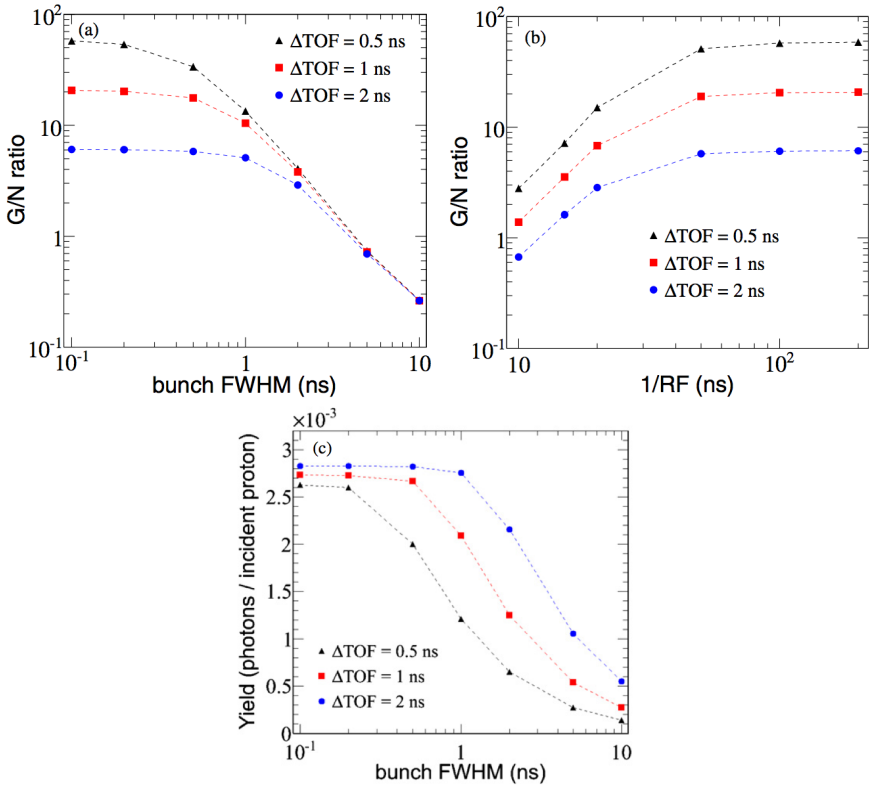

Figure 3.8: Gamma-to-neutron ratio (G/N ratio, see the text for explanation) as a function of (a) the proton bunch width (bunch FWHM) and (b) the accelerator repetition period (1/RF), as well as (c) the number of photons detected as a function of the bunch width, for TOF windows ΔTOF_z of 0.5 (black triangles), 1.0 (red squares) and 2.0 ns (blue circles). All calculations were performed for a proton energy of 200 MeV and are averaged over the detector region $0 \leq z \leq R$.

It appears that TOF neutron rejection is not expected to be effective for bunch widths larger than about 5 ns, which may typically be found in synchrotrons. Fortunately, for typical proton cyclotrons having a bunch width smaller than ∼2 ns and a repetition period larger than ∼10 ns, the TOF method is still expected to lead to significantly improved range verification, especially if the ΔTOF_z window is adapted appropriately to the beam time structure. As indicated in figures 3.8(a) and (c), larger bunch widths favor the use of larger

ΔTOF_z windows.

3.4 Conclusion

In this work, we investigate a method for neutron background rejection to enhance the accuracy of prompt gamma imaging for range verification in pencil beam scanning proton radiotherapy, based on a shifting TOF acceptance window that accounts for the propagation of the protons through the patient.

Significant neutron background rejection is achieved with the shifting TOF window even at the highest proton beam energy investigated (200 MeV), which gives rise to the highest neutron background and the largest temporal overlap between the photon and the neutron signals. Subsequent application of an energy threshold does not appear to sharpen the distal falloff of the prompt gamma profile but may still be beneficial as it reduces the tail that is observed at depths beyond the proton range.

To implement the proposed method in practice, one needs a start pulse for each proton bunch that enters the patient, as well as a stop pulse for each prompt gamma photon registered by the detector. The TOF value is then given by the time difference between the stop pulse and the start pulse. Since the TOF acceptance window should have a width in the order of a nanosecond, the timing uncertainty (jitter) on both the start and the stop pulses should be small in comparison.

The acquisition of start pulses with sub-nanosecond timing jitter is relatively straightforward as they can be derived from the cyclotron RF signal. Accurate stop pulses require that the prompt gamma detector has sufficiently good timing resolution. This is certainly achievable today. For example, current TOF-PET scanners offer coincidence resolving times in the order of $\sim$500 ps or better for pairs of 511 keV photons (Conti 2011, Daube-Witherspoon *et al* 2010), using fast scintillation detectors read out by photomultiplier tubes (PMTs). In the present context, it is interesting to note that the deposition of higher amounts of energy by (prompt) gamma photons is expected to improve the timing resolution achievable with scintillation detectors (Seifert *et al* 2012b). Furthermore, several groups are developing even faster scintillation detectors based on silicon photomultipliers (SiPMs), which have the added advantage that they are not affected by magnetic (stray) fields that might be found in a proton gantry (Degenhardt *et al* 2010, Del Guerra *et al* 2011, Gola *et al* 2012, Kim *et al* 2009, Powolny *et al* 2011, Seifert *et al* 2012a, Van der Lei *et al* 2011).

The time structure of the proton beam appears to be crucial for the effectiveness of the proposed TOF-based neutron-rejection technique. For typical proton cyclotron bunch widths smaller than 2 ns and repetition periods larger than 10 ns, the TOF method is expected to lead to significantly improved range verification, especially if the TOF window is adapted appropriately to the beam time structure.

Acknowledgments

The authors acknowledge the support from the teams of the high-performance computing clusters Millipede (Groningen University) and Milipeia (University of Coimbra). We also thank Professor Sytze Brandenburg (KVI, Groningen) for helpful discussions and Dr Mathias Schlett (FZD) for the initial support with Geant4. We equally acknowledge the initial support of Professor Eckart Grosse (FZD and Technische Universität Dresden), Professor Rui Marques (LIP and Physics Department, University of Coimbra, Portugal) and Professor Paulo Fonte (LIP and Instituto Superior de Engenharia de Coimbra, Portugal). The authors

are grateful to Julien Smeets (Service de Métrologie Nucléaire, Université Libre de Bruxelles) for his advice on the MCNPX simulations. We also thank João Silva (LIP) for his valuable help in solving several Linux-related issues. This research was supported in part by grant number 09NIG18 of the Foundation for Fundamental Research on Matter (FOM), The Netherlands, and by grant numbers SFRH/BD/73705/2010 and SFRH/BPD/39223/2007 of the Fundação para a Ciência e a Tecnologia (FCT), Portugal.

Chapter 4

Time-resolved imaging of prompt-gamma rays for proton range verification using a knife-edge slit camera based on digital photon counters[1]

Proton range monitoring may facilitate online adaptive proton therapy and improve treatment outcomes. Imaging of proton-induced prompt gamma (PG) rays using a knife-edge slit collimator is currently under investigation as a potential tool for real-time proton range monitoring. A major challenge in collimated PG imaging is the suppression of neutron-induced background counts. In this work, we present an initial performance test of two knife-edge slit camera prototypes based on arrays of digital photon counters (DPCs). PG profiles emitted from a PMMA target upon irradiation with a 160 MeV proton pencil beams (about 6.5×10^9 protons delivered in total) were measured using detector modules equipped with four DPC arrays coupled to BGO or LYSO:Ce crystal matrices. The knife-edge slit collimator and detector module were placed at 15 cm and 30 cm from the beam axis, respectively, in all cases. The use of LYSO:Ce enabled time-of-flight (TOF) rejection of background events, by synchronizing the DPC readout electronics with the 106 MHz radiofrequency signal of the cyclotron. The signal-to-background (S/B) ratio of 1.6 obtained with a 1.5 ns TOF window and a 3 MeV - 7 MeV energy window was about 3 times higher than that obtained with the same detector module without TOF discrimination and 2 times higher than the S/B ratio obtained with the BGO module. Even 1 mm shifts of the Bragg peak position translated into clear and consistent shifts of the PG profile if TOF discrimination was applied, for a total number of protons as low as about 6.5×10^8 and a detector surface of 6.6 cm × 6.6 cm.

[1] P. Cambraia Lopes, E. Clementel, P. Crespo, S. Henrotin, J. Huizenga, G. Janssens, K. Parodi, D. Prieels, F. Roellinghoff, J. Smeets, F. Stichelbaut and D. R. Schaart, Phys. Med. Biol. 60, 6063-85, 2015.

4.1 Introduction

Real-time particle range monitoring may facilitate online-adaptive particle therapy and improve treatment outcomes. Imaging of the prompt gamma (PG) rays emitted during proton irradiation has been suggested as a tool for range monitoring (Stichelbaut and Jongen 2003). Different PG imaging detectors are currently being investigated, including Compton cameras (Kang and Kim 2009, Richard *et al* 2009, 2011, Peterson *et al* 2010, Kormoll *et al* 2011) and various types of mechanically collimated cameras (Min *et al* 2010, 2012, Testa *et al* 2009, Testa *et al* 2010, Bom *et al* 2012, Cambraia Lopes *et al* 2012, Smeets *et al* 2012b, Gueth *et al* 2013, Roellinghoff *et al* 2014). The present work is focused on collimation with a knife-edge slit, as described by Smeets *et al* 2012b.

A major challenge in PG imaging is the suppression of background counts. Neutrons promptly emitted during proton irradiation give rise to uncorrelated events that degrade the signal-to-background ratio of the PG image. Even though scintillators exist that are relatively insensitive to neutrons, secondary gamma rays are often detected, which result from interactions of the neutrons with materials in the environment, the collimator especially, which is typically made from a dense material such as tungsten or lead.

Whereas neutron shielding is complicated by a number of technical and practical difficulties, previous studies have shown that time-of-flight (TOF) selection may efficiently reduce the neutron-induced gamma background in collimated cameras (Testa *et al* 2009, Testa *et al* 2010, Biegun *et al* 2012, Cambraia Lopes *et al* 2012, Roellinghoff *et al* 2014), provided that the proton-beam microstructure is favorable. That is, the proton bunch width should be sufficiently narrow and the bunch repetition rate sufficiently low, which tends to be the case for typical cyclotron-delivered proton beams. In addition, energy discrimination has experimentally been shown to successfully reject background events and increase the signal-to-noise ratio SNR (Min *et al* 2006, Smeets *et al* 2012b). It is therefore important that PG detectors offer a large enough dynamic range to enable appropriate energy selection.

Here we present an initial performance test of two gamma camera prototypes based on digital photon counter (DPC) arrays. The DPC is an implementation of the silicon photomultiplier (dSiPM) introduced by Philips Digital Photon Counting (PDPC) (Frach *et al* 2009, 2010, Degenhardt *et al* 2009). This photosensor technology has been developed into a modular design that can be used for diverse applications in medical imaging (Degenhardt *et al* 2012, Haemisch *et al* 2012). DPC arrays are rugged, compact, magnetic field insensitive, and exhibit low susceptibility to electronic noise, which makes them appealing for proton therapy monitoring. Furthermore, their good timing properties open up the possibility for TOF selection. We compare the performance of detector modules equipped with 4 DPC arrays coupled to either BGO or LYSO:Ce scintillator matrices in a prototype prompt gamma camera utilizing a knife-edge slit collimator. For the LYSO:Ce camera, profiles measured with and without TOF selection are evaluated.

4.2 Methods and materials

A knife-edge slit collimator was used to project prompt-gamma rays emitted from a phantom onto two prototype gamma cameras (section 4.2.1.1). The gamma cameras consisted of BGO or LYSO:Ce crystal matrices coupled to DPC arrays (section 4.2.1.2). The operating settings of the detectors were optimized and, in the case of the LYSO:Ce detector, time-of-flight (TOF) background discrimination was tested (section 4.2.1.3). Detector calibration and signal processing were performed offline (section 4.2.2). Finally, the measured prompt-gamma profiles were compared with MCNPX simulations (section 4.2.3).

4.2.1 Experimental

4.2.1.1 Measurement setup

The experimental set-up is similar to the one described by Smeets *et al* (2012b). A schematic representation of the setup is shown in figure 4.1-left. Figure 4.1-right shows a photograph of the actual setup installed in the gantry of treatment room 2 of the West German Proton Therapy Centre Essen (WPE), where all proton irradiations were performed. The LYSO:Ce and BGO detectors were mounted on a breadboard, at opposite sides of a cylindrical polymethylmethacrylate (PMMA) phantom. The knife-edge slit collimator was placed on a PMMA support rail in between the LYSO:Ce detector and the phantom. The PMMA phantom had dimensions of ∅15 cm × 20 cm and was irradiated with an 160 MeV proton pencil-beam. The Bragg peak position, defined as the distal position at which the depth-dose profile has reduced to 80% of the maximum height, was located at a depth of 15.2 cm into the phantom.

The knife-edge slit collimator was made of a tungsten alloy with a density of 16.96 g cm^{-3}. It had a thickness of 4 cm and a slit opening of 6 mm. The collimator was placed midway between the phantom axis and the mid-plane of the crystal matrix (figure 4.1-left), so as to project an inverse image of the prompt-gamma emission profile onto the detector with a magnification factor of 1. The distance between the beam axis (coinciding with the phantom axis) and the mid-plane of the scintillator matrix was 30 cm. The center of the slit was aligned with the expected Bragg peak position, as well as with the center of the detector. Additional measurements were made with the detector shifted by ±3.35 cm in parallel with the beam axis (corresponding to an overlap of 8 crystals), so as to enlarge the total field-of-view (FOV) to about 13.5 cm, still centered at the Bragg-peak position. In addition to the measurements performed with the knife-edge slit collimator, measurements were also done using a completely closed collimator (i.e. a tungsten slab with a uniform thickness of 4 cm), as well as without any collimator, for characterization purposes.

All acquisitions were done with a beam current at nozzle exit of about 10 pA or 6.24×10^7 protons/s. In most measurements, the administered dose was about 10 Gy per measurement, corresponding to about 6.5×10^9 protons delivered in total. A few measurements used for timing calibrations were acquired with a 5-times higher dose, using the same beam current. It is noted that this beam current is lower than those typically used in clinical treatments, which are of the order of 1 nA. The DPC data acquisition electronics used in the present measurements (section 4.2.1.2) is part of a technology demonstrator kit that is not designed for high count rates. In particular, it makes use of a USB 2.0 connection to the readout computer, which forms a bandwidth bottleneck. A higher-bandwidth connection would be required to obtain sufficient system bandwidth for clinical use of a DPC-based prompt gamma camera. The DPC detector is in principle capable of processing a much higher count rate than in the current experiment (section 4.2.1.3).

4.2.1.2 Detector description

The detectors were based on DPC modules manufactured by PDPC (DPC-MO-22-3200). Each DPC module has a total surface area of 68 mm × 68 mm and contains 2 × 2 DPC arrays (DPC3200-22-44). Each of the 4 DPC arrays measures 32 mm × 32 mm and comprises 8 × 8 DPC pixels at a pitch of 4 mm, each DPC pixel consisting of 3200 single-photon avalanche diodes (SPADs) or microcells (Frach *et al* 2009). A DPC array is assembled from 4 × 4 independent DPC-chips, each chip containing 2 × 2 pixels. It is equipped with readout electronics and a pair of 9-bit time-to-digital converters (TDCs). After light detection and readout, the DPC-chip outputs the total number of fired cells on each of its 4 pixels, as well

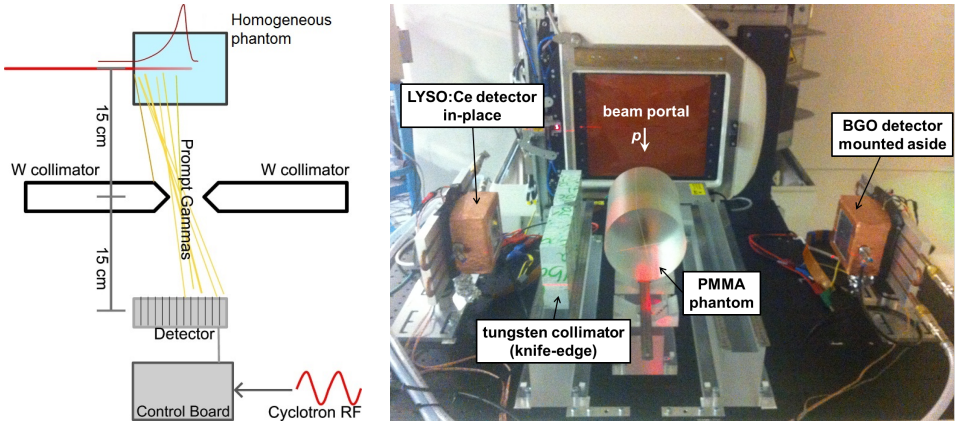

Figure 4.1: Schematic overview of the experimental setup (left) and photograph of the actual setup (right). Left: the detector center is aligned with the center of the slit and the Bragg-peak position. Right: the LYSO:Ce and BGO detectors are mounted on the breadboard; the collimator is placed in between the phantom and the LYSO:Ce detector on a PMMA support rail.

as a single time stamp. One of the modules was equipped with a matrix of 256 LYSO:Ce ($Lu_{1.8}Y_{0.2}SiO_5(Ce)$) crystals, each crystal having dimensions of 3.8 mm × 3.8 mm × 22 mm. The other detector had a matrix of 256 BGO ($Bi_4Ge_3O_{12}$) crystals of 3.8 mm × 3.8 mm × 20.5 mm each. The coupling between DPC-pixels and crystals was 1-to-1 in both cases. Each BGO crystal was optically isolated, whereas light sharing was allowed between each group of 4 LYSO:Ce crystals coupled to a same DPC-chip, so as to minimize saturation of the DPC-pixels. The detector modules were cooled by Peltier elements and attached to a heat exchange plate internally flushed with running tap water. The modules were enclosed in a light-tight and moisture-free box that was continuously flushed with dry nitrogen gas. The temperature of operation of the DPC arrays was -15°C.

The LYSO:Ce and BGO crystal matrices have comparable (i.e. within 4 % variation) total attenuation cross sections for photons between 1 MeV and 10 MeV (Berger and Hubbell 2010). Given the higher light output and lower decay time of LYSO:Ce (41 ns versus 300 ns for BGO), the LYSO:Ce detector was used for the time-of-flight (TOF) measurements. Due to technical reasons, one DPC array of the BGO detector was not operational.

4.2.1.3 Data acquisition settings

Data acquisition with DPCs is regulated by a programmable trigger and validation logic (Frach *et al* 2009, 2010). The trigger logic is implemented on pixel level, and the trigger threshold is defined as the number of sub-pixels (one-fourth of a pixel) that must be fired to create a time stamp. Triggering on the 1st or 2nd fired sub-pixel is best suited for fast timing applications. We used the 2nd sub-pixel threshold in all of the measurements performed in this work.

Upon triggering, the DPC-chip enters into the validation phase, i.e, it keeps counting during a certain validation interval, to check whether it reaches a given validation threshold. Upon validation, the DPC-chip continues acquiring for an additional time, the integration interval, after which it is read out and recharged/reset. If the validation threshold is not met, the integration and readout phases are skipped. Therefore, the optimum trigger and

validation settings depend on the application, measurement conditions, and crystal type, size, and coupling. The settings should reduce the dead-time due to system readout and/or resets of dark count-induced triggers, while maximizing the detection efficiency at the same time.

In the present work, the validation interval was set to 40 ns for the measurements with BGO, and to 10 ns for the LYSO:Ce measurements without RF synchronization. The validation threshold was set to a 2-OR validation pattern for the BGO measurements, and an 8-OR validation pattern for the LYSO:Ce measurements. This validation conditions only need to be satisfied by one sub-pixel (the four subpixels are connected through a logical OR), while each sub-pixel is subdivided into 8 logical validation regions. A 2-OR validation scheme requires that 2 mutually exclusive groups of 4 validation regions each have at least one fired microcell, whereas the 8-OR scheme requires one fired microcell per validation region (Tabacchini *et al* 2014). The expected number of fired cells on a pixel at the time of validation is 5.3±2.5 for the 2-OR validation pattern and 59±17 for the 8-OR validation pattern (Tabacchini *et al* 2014). Thus, stricter validation settings were used for LYSO:Ce than for BGO since LYSO:Ce has a higher light yield and a faster decay time. However, we expect that a validation threshold higher than 2-OR could be used with the BGO detector, without compromising the detection efficiency in the energy range of interest for prompt gamma imaging, since this validation threshold does not suppress counts at the energies above $\sim$ 1 MeV (figure 4.3). This may be beneficial for higher proton currents (higher event rate) than used in this study, to decrease dead time caused by unnecessary validated events with relatively low energies. The integration times used in our measurements were 1285 ns for BGO and 165 ns for LYSO:Ce without RF synchronization, so as to accumulate counts during approximately 4 decay time constants in each case. Finally, DPC saturation was reduced in the measurements with LYSO:Ce by using the lowest available excess voltage, viz. 2.2 V above tile breakdown voltage, whereas for BGO a typical excess voltage of 2.9 V was used.

For the measurements with TOF discrimination, the acquisition electronics of the LYSO:Ce detector module were synchronized with the cyclotron RF. This was done by converting the 106 MHz RF wave into a clock signal, which was then used as a reference clock by the acquisition electronics, instead of the 200 MHz internal DPC clock. In this way, the registration time of each event relative to the phase of the RF cycle could be obtained from the TDCs in the DPC-chip. The acquisition time settings used in this case were different from the ones used in the previous measurements, as the acquisition times are integer multiples of the reference clock. Specifically, the validation interval used in the experiments with RF synchronization was 18.9 ns and the integration interval was 160.4 ns. (As a result, the total measurement time changed by less than one percent.)

Finally, the DPCs were operated at a constant temperature (-15°C, section 4.2.1.2) to maintain stable detection efficiency throughout all measurements. Cooling reduces the dark-count rate and, therefore, the dead-time induced by triggers originating from dark counts. The dark-count rate was further reduced by switching off the 5% (160) cells with the highest dark-count rate (Frach *et al* 2009). The remaining average dark-count rate was about 50 s^{-1} per cell, measured with the BGO crystals coupled to the sensor tiles. It is noted that the temperature of operation was simply set as low as practically achievable; in this initial study we did not yet study or optimize the detector performance as a function of the operating temperature.

The average count rate obtained per DPC-chip was 0.88 kcps for LYSO:Ce and 0.42 kcps for BGO, in terms of overall validated events, as energy and time-of-flight selection was applied offline. In the case of LYSO:Ce, the chip count rate within the acceptance time-of-flight window (section 4.2.2.2) was 0.25 kcps. The total trigger rate (validated and

non-validated triggers) was 0.22 Mcps for both detectors, mainly due to dark counts.

The maximum (validated) event rate that the DPC-chips can process is 1.3 Mcps when operated at a 200 MHz clock, which scales with the clock frequency. However, the bandwidth of the DPC-sensor is artificially limited by the event storage available on the tile FPGA. Currently, the sensor can handle a maximum of about 120 kcps per chip when operating at the default 200 MHz clock frequency. Therefore, these detectors may be capable of acquiring an eventual 100 times higher validated-event count rate, which could be expected at a clinical beam current of 1 nA, provided that there are no bandwidth limitations on the interface between the acquisition electronics and the readout computer. With the present implementation, using the 106 MHz external clock for TOF discrimination, the bandwidth was reduced to about half of the 120 kcps per chip, due to the longer clock cycles. A possible way to increase the sensor bandwidth while ensuring synchronization to the cyclotron RF, would be to operate the sensors with a frequency double of that coming from the external clock. This would likely reduce the chip dead time and would increase FPGA bandwidth, eventually enabling to measure using typical clinical beam currents and cyclotron RF, with TOF discrimination.

4.2.2 Offline data processing

Each DPC-chip functions as an independent channel that processes an event and outputs the number of fired cells (hits) in each of its four DPC-pixels together with a single time-stamp. The data processing chain therefore consisted of the following steps: (1) saturation/crosstalk correction of the pixel hits; (2) energy conversion on a per-pixel basis; and, unless specified otherwise, (3) clustering of multiple-DPC-chip events, using a paralyzable 'coincidence window' that acts on the level of the detector. These steps are detailed in section 4.2.2.1. After these processing steps, an energy selection criterion was applied to the registered events. If time-of-flight (TOF) discrimination was applied, the time stamps were calibrated as explained in section 4.2.2.2.

After the processing of all events, a density map of crystal (pixel) counts was generated. One-dimensional PG profiles were subsequently obtained by summing the counts in each column of 16 crystals aligned parallel to the knife-edge slit. In the case of the BGO detector, only half of the crystals corresponding to the upper part of the detector were used to derive the 1D-profiles, since one of its DPC arrays was not functioning. The measured profiles presented in this work were subject to cluster processing, except for those presented in section 4.3.2.1. That is, for each event, the DPC-chip that registered the highest energy deposition was selected and the event was subsequently assigned to one of the corresponding 4 crystals according to the 'winner-takes-all' method (section 4.2.2.1).

4.2.2.1 Energy calibration and event clustering

Energy calibration was performed by measuring specific gamma lines from the following radioactive sources: ^{137}Cs (661.7 keV), ^{60}Co (1173 keV; 1333 keV), ^{22}Na (511 keV; 1275 keV), and ^{24}Na (1369 keV; 2754 keV; sum peak 4123 keV). The calibration was done on a per-pixel basis so as to normalize the response for each crystal. However, the counts were summed over each DPC-chip, since event acquisition is performed on a per-DPC-chip basis and since inter-crystal light sharing occurs within each DPC-chip, especially in the LYSO:Ce detector. Pixel assignment was done using the 'winner-takes-all' method, i.e. by selecting the brightest pixel within the DPC-chip.

Prior to energy calibration we corrected the measured number of fired microcells per pixel for saturation to improve linearity. Saturation occurs due to the limited number of

available cells, each of which can detect only one photon per scintillation event. A correction was implemented using the 'simple model' proposed by van Dam *et al* (2012), which takes into account optical crosstalk (Frach *et al* 2009) as well as dark count contributions over the total acquisition time. In the present case, we used a total crosstalk probability of 0.16, in accordance with Tabacchini *et al* (2014).

Upon saturation correction the LYSO:Ce detector presented good proportionality up to 1333 keV. In first instance we therefore used a linear energy calibration obtained from fitting the ^{22}Na and ^{60}Co peak positions, such that the ratios of saturation-corrected photon counts to energy equaled 4.3±0.4 keV^{-1} (mean ± standard deviation). With this calibration, which normalized the response of each crystal, the peak positions up to 4123 keV (^{24}Na sum peak) were re-calculated (energy$_{\text{extrapolated}}$) from the global spectra, i.e. the spectra obtained from all detector pixels. We thus derived a DPC-chip/pixel-independent energy correction function for the LYSO:Ce detector, by fitting a second-order polynomial to the true energy values, E, as a function of the extrapolated energy peak values, E_{extrap}. These values (E, E_{extrap}) and the energy correction curves are presented in figure 4.2.

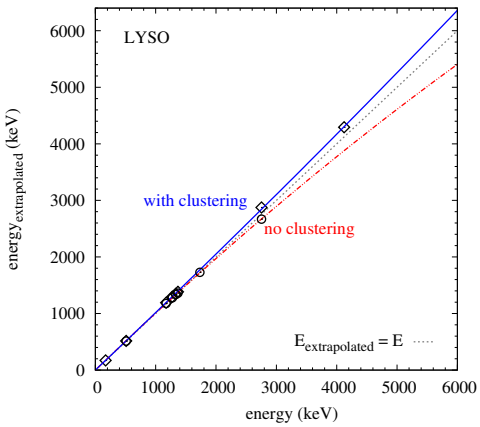

Figure 4.2: Crystal-independent energy correction curves used for the LYSO:Ce detector, and data points of the extrapolated energy peak values as a function of the true energy of gamma lines from the point sources Cs-137, Co-60, Na-22, and Na-24. Also the 170 keV backscatter peak from Na-22 and the 1732 keV double-escape peak of 2754 MeV peak (Na-24) were used, for the case with clustering and no clustering, respectively. The extrapolated values were obtained from point source spectra calibrated using crystal-specific linear curves, which only considered energy lines up to 1333 keV.

The energy correction functions obtained with and without cluster processing appear to be different, yielding: $E = 0.991E_{extrap} - 8{\times}10^{-6}E^2_{extrap}$, and $E = 0.969E_{extrap} + 2.3{\times}10^{-5}E^2_{extrap}$, respectively, where all energy values are expressed in units of keV. Event clustering was performed by summing up the energies of all DPC-chips with time-stamps spaced less than 5 ns apart, for the LYSO:Ce detector. Most probably these events originate from the same gamma quantum, which may undergo interactions in more than one DPC-chip. Omitting the clustering procedure results in a slight underestimation (~4%) of the extrapolated energy values at 2754 keV, which could be attributed to saturation. In contrast, if cluster processing is applied, there is an overestimation by about

4% at 2754 keV and 4123 keV, suggesting that energy overestimation outbalances saturation in this case. Presumably, this overestimation could be due to light sharing between neighbor DPC-chips. The per-pixel energy calibration may overestimate the energy in the presence of light sharing, because energy calibration curves have been derived from energy spectra of single-DPC-chip clusters (i.e. one DPC-chip validated per cluster window on whole detector).

In the case of the BGO detector we observed considerable inter-chip and inter-pixel response variations. Furthermore, lack of proportionality could be observed at 1275 keV already, with about 6% deviation of the saturation-corrected photon counts relative to the extrapolation from the 511 keV line. Possible reasons for this are the optical isolation between BGO crystals within a same DPC-chip and/or a (slight) mismatch between the crystal footprints and the DPC-pixels surfaces. For this detector, we therefore chose to apply a chip/pixel-dependent energy calibration curve, calculated by fitting a second-order polynomial to the positions of the five energy peaks from ^{137}Cs, ^{22}Na, and ^{24}Na, such that the curves of the saturation-corrected photon counts, c, as a function of energy, E, yielded: $c = p_0 + p_1 E + p_2 E^2$, with p_0 = 22±26, p_1 = 1.1±0.1 keV^{-1} and p_2 = (-4±1)×10^{-5} keV^{-2} (mean ± standard deviation). Since BGO has a lower timing resolution compared to LYSO:Ce, a longer clustering window of 20 ns was applied for that detector, which was sufficient to collect chip-events with energies as low as a few hundreds of keV.

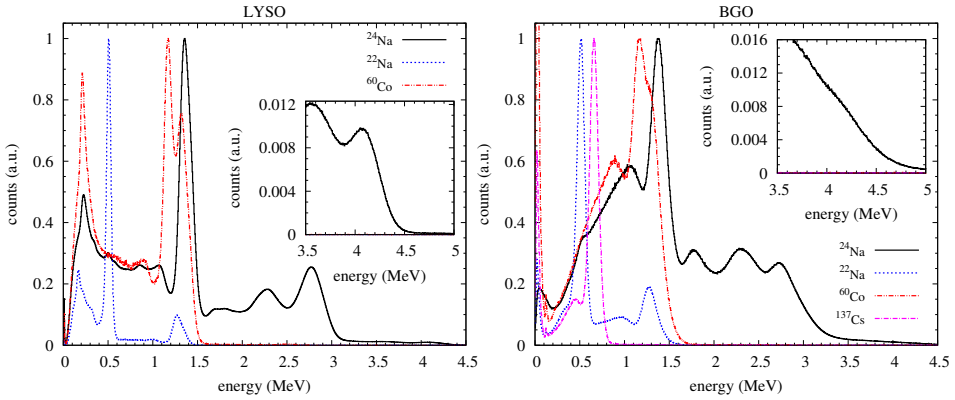

Figure 4.3: Energy spectra of point sources used for energy calibration, obtained with LYSO:Ce (left) and BGO (right). Intrinsic (Lu) background was subtracted from the LYSO:Ce spectra.

The resulting (global) energy spectra measured with point sources are shown in figure 4.3 for both detectors. Both here and in the remaining of this work, energy spectra are presented with cluster processing, except in section 4.3.1, figure 4.6, where specified. The insets in figure 4.3 show the position of the 4123 keV sum peak of ^{22}Na, which is clearly resolved for LYSO:Ce (figure 4.3-left) but hardly noticeable for BGO (figure 4.3-right). The FWHM of the gamma peaks at 511 keV, 1369 keV, 2754 keV, and 4123 keV was 12%, 11%, 10%, and 8%, for LYSO:Ce, respectively, and for BGO it was 19%, 14%, and 13% at 511 keV, 1275 keV, and 2754 keV, respectively. The BGO point-source spectra were obtained with a higher validation threshold than used in the prompt-gamma measurements (8-OR validation pattern instead of 2-OR), which lowered the detection efficiency for events up to $\sim$ 1 MeV, but did not affect the peak positions.

4.2.2.2 Time calibration

Time calibration of the LYSO:Ce detector was done to allow accurate time-of-flight (TOF) discrimination. The two TDCs on each DPC-chip run on half the system clock frequency, in opposition of phase, and have a resolution of 19.5 ps and a range that spans approximately 10 ns. In this particular case, the system clock of 200 MHz was replaced by a clock pulse derived from the 106 MHz cyclotron RF signal, resulting in nearly no overlap between the TDC time stamps, meaning the valid time stamps were given alternatively from TDC1 or TDC2. The TDC outputs provided a direct measure of the TOF of the detected events, relative to the arrival time of the proton bunch, due to the correlation of the proton arrival times with the phase of the RF signal (RF-pulsed beam delivery). It is noted that part of the 9.4 ns long RF wave period (not more than 30%) was not registered due to a firmware filter that rejected events with invalid combinations of TDC1 and TDC2 values, which had not been adapted to the 106 MHz operating clock by the time of the experiment. Nevertheless, the available TDC range was sufficient to apply the TOF discrimination, and the use of an adequate delay line ensured that the prompt signal fell within that range.

Figure 4.4 illustrates two exemplary time histograms derived from the TDC outputs of DPC-chips placed at two different locations that, upon projection through the slit, correspond to positions 13 mm proximal or distal to the proton range on the beam axis. In both cases, a peak can be observed between about 2 ns and 4 ns, which is attributed to the prompt gamma signal. The DPC-chip that looks at the region distal to the proton range registers fewer prompt counts, which are mainly attributed to prompt gammas that are scattered or that pass through the collimator without interacting. The prompt peaks are superimposed on a broad background, which is mainly attributed to neutron-induced gammas and neutrons. This slowly-increasing background peaks at time stamps posterior to the prompt arrival time and spans over the entire RF-range, most likely due to overlay of neutrons generated by a given proton bunch onto successive pulses (Biegun *et al* 2012).

TOF calibration was based on determining the prompt peak position for every DPC-chip. For this purpose, we fitted all time spectra (after applying a 3 MeV low-energy cutoff) by a Gaussian function plus a linear baseline in the range between -1.95 ns and +1.76 ns relative to the maximum of the histogram. Thus, the background is approximated by a linearly rising slope and the prompt gamma peak by a Gaussian curve. The solid curves in Figure 4.4 are examples of such fits. As illustrated by this figure, the prompt gamma peak position is chip-dependent, which is due to the clock skews between different chips of the DPC array (van Dam *et al* 2013). Furthermore, the sum of the proton travel time and the prompt gamma time-of-flight depends on the position within the phantom at which the prompt gamma quantum is created (Biegun *et al* 2012). These effects were corrected for by placing the TOF selection window symmetrically around the mean of the Gaussian fit of each DPC-chip.

The prompt gamma peak would be very narrow, in the order of 150 ps (Biegun *et al* 2012), if all protons would enter the phantom simultaneously. In practice, however, the prompt gamma peak is convoluted with the proton bunch width, i.e. the arrival time-spread of the protons within each RF cycle, as well as with the time resolution of the prompt gamma detector. In the present experiments, the (single-) detector time resolution is relatively small: viz. about 255 ps FWHM for 511 keV photons using 2^{nd} photon triggering (Degenhardt *et al* 2009, 2012). Moreover, it is expected to decrease with increasing prompt gamma energy (Seifert *et al* 2012b). Therefore, the width of the Gaussian fits is mostly determined by the proton bunch width and had an average value of 1.1 ns FWHM. Hence, TOF discrimination was implemented by rejecting events that did not fall within a time window of 1.5 ns width, centered at the calculated Gaussian mean for each DPC-chip. In

cases were clustering was performed, the TOF discrimination was applied post-clustering on the time stamp of the DPC-chip that registered the highest energy only.

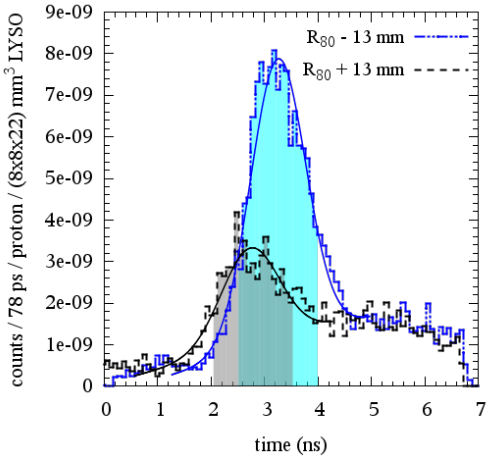

Figure 4.4: Measured time spectra (histograms) of events recorded by the LYSO:Ce detector, relative to an arbitrary phase of the cyclotron radiofrequency (RF) cycle, on two DPC-chips. The chip center positions upon projection through the slit onto the beam axis correspond to depths in the phantom that are 13 mm proximal (-) or distal (+) to the proton range (R80). A low energy threshold of 3 MeV was applied. The smooth curves overlaid on each measured histogram were obtained from fitting the data to a Gaussian function plus a linear baseline, while the shaded areas underneath each spectrum represent events accepted within a time-of-flight window of 1.5 ns width, centered at each Gaussian mean. These data were acquired for the highest amount of delivered protons.

4.2.3 MCNPX simulations

The measured profiles and corresponding count rates per proton were compared to Monte Carlo simulations performed with MCNPX version 2.5.0. This simulation code has been extensively used by Smeets *et al* (2012b) to characterize the collimator used in the present setup. The comparison was performed for a deposited energy ranging from 3 MeV to 6 MeV, which was previously found to yield the most favorable signal-to-background ratio (Smeets *et al* 2012b), to check consistency with those results.

A simplified version of our measurement setup was modeled, consisting of the PMMA target, the tungsten alloy collimator and one of the detector modules. The materials, dimensions and relative positions of these parts were modeled according to the descriptions given in section 4.2.1, except that the crystal dimensions were modeled as (4×4×22) mm^3 for LYSO:Ce and (4×4×20.5) mm^3 for BGO, for simplicity, and both densities were artificially scaled down to 6.4 g cm^{-3}, to compensate for the artificial increase in crystal volume, resulting from the increased footprint compared to the true footprint of 3.8 mm x 3.8 mm.

The proton beam was modeled as a perfect pencil beam with proton energy of 160 MeV, delivering a total of 1×10^9 protons. For simplicity, counts were scored independently for each pixel, assuming zero dead time and perfect energy resolution. Electrons were tracked inside the pixels. Therefore, in cases where measured profiles were compared with simulated ones, cluster processing was not applied to the measured profiles.

4.3 Results and discussion

4.3.1 Energy and time spectra

The energy spectra recorded with the LYSO:Ce and BGO detectors are presented in figure 4.5-top and -bottom, respectively. The measurements without a collimator were made with the detectors centered at the expected beam range. The energy spectra presented in figure 4.5 for the case of an open collimator were obtained with the detectors shifted by 3.35 cm in the beam direction, thus looking at the phantom region before the Bragg peak, where the amount of background counts relative to the total counts is smaller compared to '0 shift', thus the difference between the energy spectra from open and closed collimators is higher.

In general, the spectra present typical shoulders near the expected positions of strong prompt-gamma lines, such as the 2.2 MeV thermal-neutron-induced prompt gamma line, and the characteristic 4.4 MeV lines from C and O, and 6.1 MeV line from O, which have been interpreted elsewhere (Polf *et al* 2009a,b, Smeets *et al* 2012b, Kozlovzky *et al* 2002). Other spectral features may originate from single- and double-escape of the two previous gamma lines, as well as from the O line at 2.7 MeV and the C lines at 2 MeV and 1 MeV. The spectral features are better visible in the LYSO:Ce spectra due to the better energy resolution. Below 1 MeV, the LYSO:Ce spectra are dominated by the intrinsic activity of Lu, whereas in the BGO case a low-energy pedestal due to validated dark counts can be observed. This pedestal could be avoided by setting a stricter validation threshold, but should not affect the count rate in the present experiments considerably (section 4.3.2.1). The BGO detector presents better sensitivity at higher energies (i.e. above about 6 MeV). The prompt gamma lines are less evident in the closed-collimator spectra, as expected. These spectra are dominated by uncorrelated events, mainly scattered gammas, neutron-induced gammas, and neutrons, with an intensity that decreases monotonously with energy.

A key feature in the open-collimator spectra obtained with TOF discrimination (figure 4.5-top) is that it clearly resembles the shape of the no-collimator spectra, albeit with a difference in intensity of about a decade due to the presence of the collimator. In addition, this spectrum is close in shape and number of counts to the opening-difference spectrum obtained without TOF discrimination. These observations already indicate how effective TOF discrimination is in rejecting background gammas generated within the collimator by neutrons. By comparing the open-collimator spectra with and without TOF discrimination, we observe that the latter contains more events at energies below about 3.8 MeV. The same observation can be made between the opening-difference spectra with and without TOF discrimination. Also these results indicate that TOF discrimination improves the signal-to-background ratio, which is expected to lead to an improvement in contrast of the measured profiles.

The time-energy distributions of the events measured with the LYSO:Ce detector are illustrated in figure 4.6, from regions proximal (top row) and distal (bottom row) to the Bragg peak. The intensity of prompt events, with time stamps between about 2.2 ns and 3.2 ns, is very much decreased when the detector is looking beyond the Bragg peak, as expected. The time stamps of background events mostly lie posterior to the prompt time stamps, although they do spread over the entire RF range (section 4.2.2.2). The energy distribution of the correlated events ranges from approximately 1.2 MeV to 6-7 MeV, while the energy of the background events extends to higher values. As noted before, below 1 MeV (figure 4.6-left) prompt events are relatively scarce and the counts are peaked at a time posterior to the prompt peak, due to prevalence of the slower background.

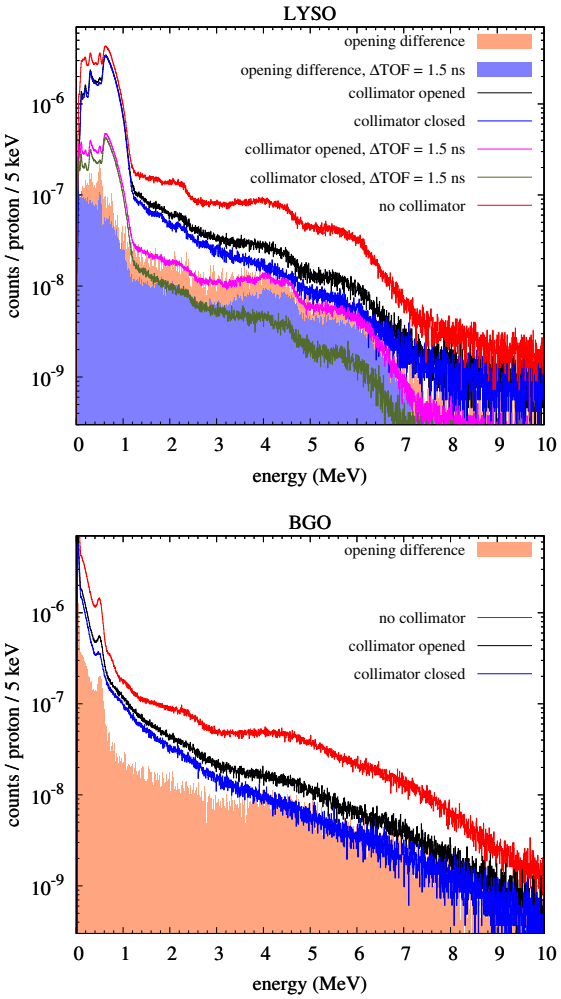

Figure 4.5: In-beam energy spectra measured using LYSO:Ce (top) or BGO (bottom), without a collimator, with the collimator closed, and with the knife-edge slit collimator (collimator opened). Also presented are the opening-difference spectra, i.e. the subtraction spectra of the collimator-opened case by the collimator-closed one. One-fourth of the LYSO:Ce detector surface was artificially not counted, to be comparable to the BGO case. The data with TOF discrimination was acquired with 5× higher statistics, in terms of total delivered protons.

Finally, figure 4.6-center shows the increase in detection efficiency in the range 3 MeV - 7 MeV by clustering multiple DPC-chip-events, in comparison to no clustering (figure 4.6-right). Without clustering, the spectrum exhibits local maxima at energy values of about 3.4 MeV and 3.9 MeV, corresponding with the double- and single-escape peaks of the prompt line at 4.4 MeV. As seen in figure 4.6-center, clustering processing considerably increases the chance of full-energy detection of the 4.4 MeV prompt gamma line and even of the 6.1 MeV line. Indeed, pair-production starts to compete with Compton scattering in this energy

range in LYSO:Ce (~36% versus ~62% of total cross-sections at about 4.5 MeV, and ~51% versus ~48% at 6 MeV, Berger and Hubbell 2010).

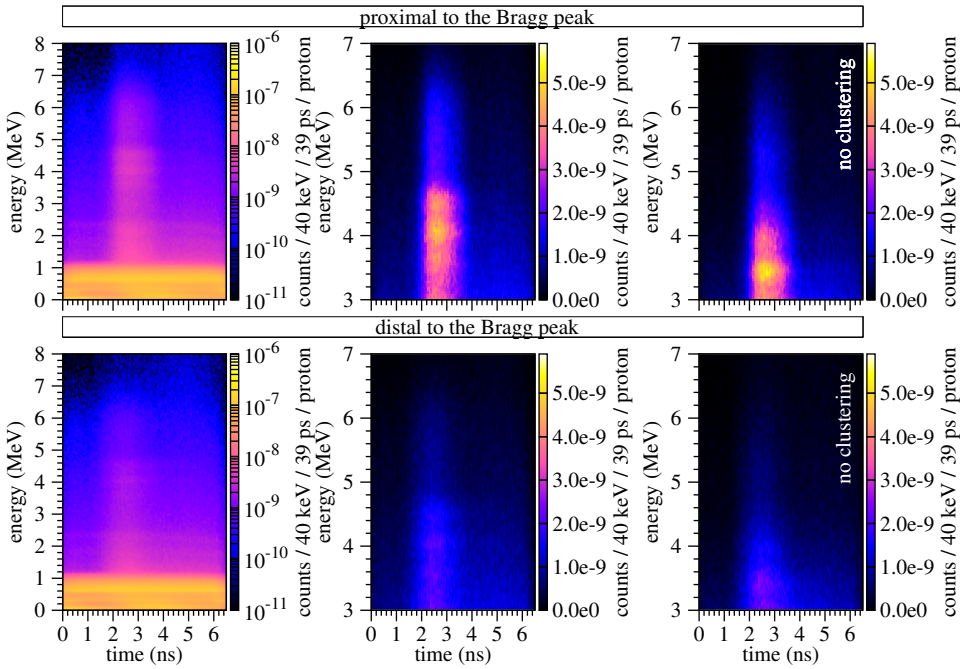

Figure 4.6: Time-energy intensity maps, measured over the whole LYSO:Ce detector area, having the detector center displaced 3.35 cm from the center of the slit in the beam direction, looking at the phantom region proximal (top row) or distal (bottom row) to the Bragg peak. The left and middle intensity maps were obtained with clustering of DPC-chip-events, whereas the right maps were not. These data were acquired for the highest amount of delivered protons.

4.3.2 Measured profiles

4.3.2.1 Comparison with simulations

Figure 4.7 shows a comparison of simulated and measured profiles, the latter without cluster processing, for both the LYSO:Ce and BGO detectors. The profiles measured with LYSO:Ce are shown taking into account only the upper half of the detector, in order to be directly comparable to the BGO case and to resemble more closely the simulation results, in terms of statistical fluctuations. Furthermore, the lower detector half of LYSO:Ce presents more background counts, presumably due to the presence of the treatment bed (section 4.3.2.2) that was not modeled in the simulations.

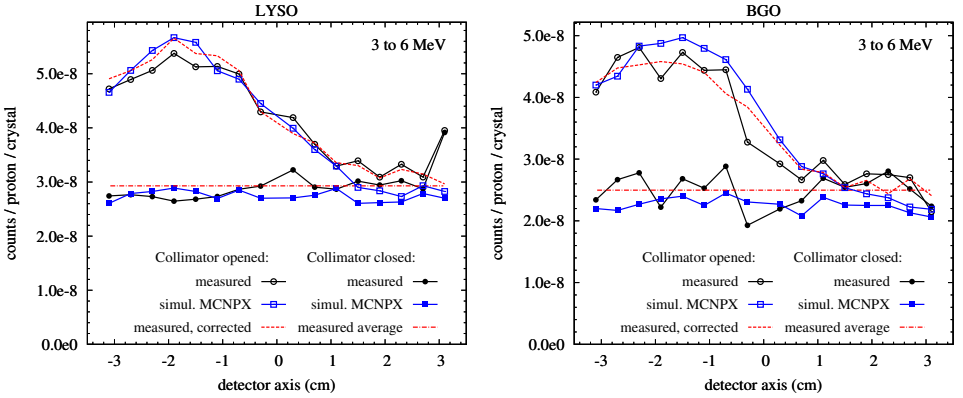

Figure 4.7: Comparison between measured and simulated profiles, for the LYSO:Ce (left) and BGO (right) detectors. Also presented are the open-collimator profiles corrected by subtracting the difference between the measured closed-collimator value and the corresponding average, for each pixel. The measured profiles were obtained without clustering of DPC-chip-events.

In general, both the experiments and the simulations indicate that the profiles obtained with LYSO:Ce and BGO are comparable in terms of the overall number of counts, but that the BGO profile contains slightly less background counts in comparison to the LYSO:Ce case, possibly due to a lower sensitivity of BGO to neutrons. By comparing the closed-collimator profiles and the open-collimator profiles beyond the Bragg peak, it seems that the simulations slightly underestimate the background, which is expected because the materials in the surroundings, such as the patient bed, are not taken into account in the simulations. However, the simulated open-collimator profile proximal to the Bragg peak is about 6% higher on average than the measured one, for both detectors.

It should be noted that an incoming particle that gives rise to multiple interactions on different pixels of a same DPC-chip was counted only once in the measured profiles, in contrast with the simulated profiles, in which each pixel was scored independently. This is not expected to have a major effect on the overall simulated counts, relative to the measurements. Taking into account the simplicity of the simulations, which do not take into account factors like additional background radiation and radiation scattering due to the materials in the vicinity of the detector, simulations and measurements are found to agree well. The agreement between simulation and measurements of closed collimator signal are in line with the recent results reported in Perali *et al* (2014) and in contradiction with the older ones reported in Smeets *et al* (2012b). This further indicates that MCNPX seems rather efficient at reproducing not only the prompt gamma signal, but also the closed collimator signal.

Furthermore, the profiles measured with BGO present remarkable fluctuations, larger than what would be expected on the basis of Poisson noise only. These fluctuations are similar in magnitude in both the open and closed collimator cases. Moreover, the pattern of these fluctuations is very similar in these two cases, suggesting that they may result from differences in the sensitivity of different BGO crystal columns aligned in parallel with the knife-edge slit. To further investigate this, a correction to the open-collimator profile was attempted, by subtracting the difference between the measured closed-collimator profile and the corresponding average. Indeed, the resulting profile is much smoother and shows a greater degree of similarity with the simulated BGO profile. A similar effect can be

observed for the LYSO:Ce case, although less pronounced.

One possible reason for the observed fluctuations in the uncorrected profiles could be the presence of systematic errors in the pixel assignment. Given that relatively large differences exist between the energy calibration curves of different BGO pixels especially, compared to the LYSO:Ce case, pixel assignment plays an important role in determining whether or not the detected event falls within the energy selection window. This effect is reduced when clustering processing is applied, as will be shown in the following section.

Overall, the agreement between simulations and measurements is quite satisfactory and reinforces that there are no important dead-time losses, as would be expected at the relatively low count rates under consideration. Given the present acquisitions settings and the measured count rate per DPC-chip, we expect that each DPC-chip is busy with event processing (acquisition, readout and recharge) for less than 2% of the time on average.

4.3.2.2 Signal-to-background ratio

Figure 4.8 and 4.9 show the measured profiles obtained with clustering of DPC-chip-events, decomposed into 1 MeV wide energy windows up to 8 MeV, for the LYSO:Ce and BGO detectors, respectively. In the interest of clarity, only profiles without uniformity correction are presented in these figures and in the remainder of this section. It should be noted that, without uniformity correction, the profiles obtained with cluster processing present less fluctuations compared to those without cluster processing (section 4.3.2.1). The highest correlation with the BP position, in terms of the slope of the distal falloff region, is observed for the energy range from about 3 MeV to about 7 MeV for LYSO:Ce, and from about 3 MeV to about 8 MeV for BGO. It is to be noted, however, that the number of counts per proton falls down by an order of magnitude above 6 MeV.

The falloff in the number of counts of the LYSO:Ce profile, relative to its maximum, is higher if TOF discrimination is applied, while the overall number of counts is reduced by a factor of 2.6, in the energy range from 3 MeV to 7 MeV.

As expected, the falloff steepness decreases below about 3 MeV in all cases studied, due to the prevalence of the background counts that result from neutron interactions in the collimator, as well as from scattered prompt gammas that are not efficiently discarded by TOF discrimination. Above 8 MeV, there is a prevalence of neutron counts and, therefore, there is little correlation between the detected profiles and the depth-dose distribution (Smeets *et al* 2012b).

The relation between the number of counts proximal and distal to the Bragg peak position can be used as a measure of the signal-to-background (S/B) ratio. Thus, the profiles measured with the detector centered at the expected beam range were interpolated with a sigmoid curve, by fitting them with the four-parameter complementary error function previously described by Henriquet *et al* (2012):

$$a + b \cdot \mathrm{erfc}\left\{c(z-d)\right\} \tag{4.1}$$

where z represents the depth into the phantom and a, b, c and d are fit variables. The profiles were corrected for non-uniformities using the corresponding closed-collimator profiles (section 4.3.2.1) prior to the fitting, and the first and last pixel columns were excluded from the fit. The signal-to-background ratio was estimated as the ratio of the difference between the two asymptotes of the curve to the lower asymptotic value. These values are presented in table 4.1, for different energy windows.

Table 4.1 confirms that the S/B ratio improves as the low-energy threshold is increased from 1 MeV to 3 MeV in all cases. Using an energy window from 3 MeV to 6 MeV, the BGO profiles have a S/B ratio of 0.8, about 60% higher than the value of 0.5 found for

the LYSO:Ce case without TOF discrimination. The use of TOF discrimination increases the S/B of the LYSO:Ce profiles to 1.6 using the same energy window. The TOF-resolved LYSO:Ce detection therefore presents a 2-fold increase in S/B, in regard to the BGO case. In what concerns the high-energy threshold, we did not observe important changes in S/B by increasing it from 6 MeV to 8 MeV. Nevertheless, the profile counts increase on average by 20% for BGO and by 11% for LYSO:Ce without/with TOF discrimination, respectively, and therefore it may be beneficial to increase the high-energy threshold if clustering is performed.

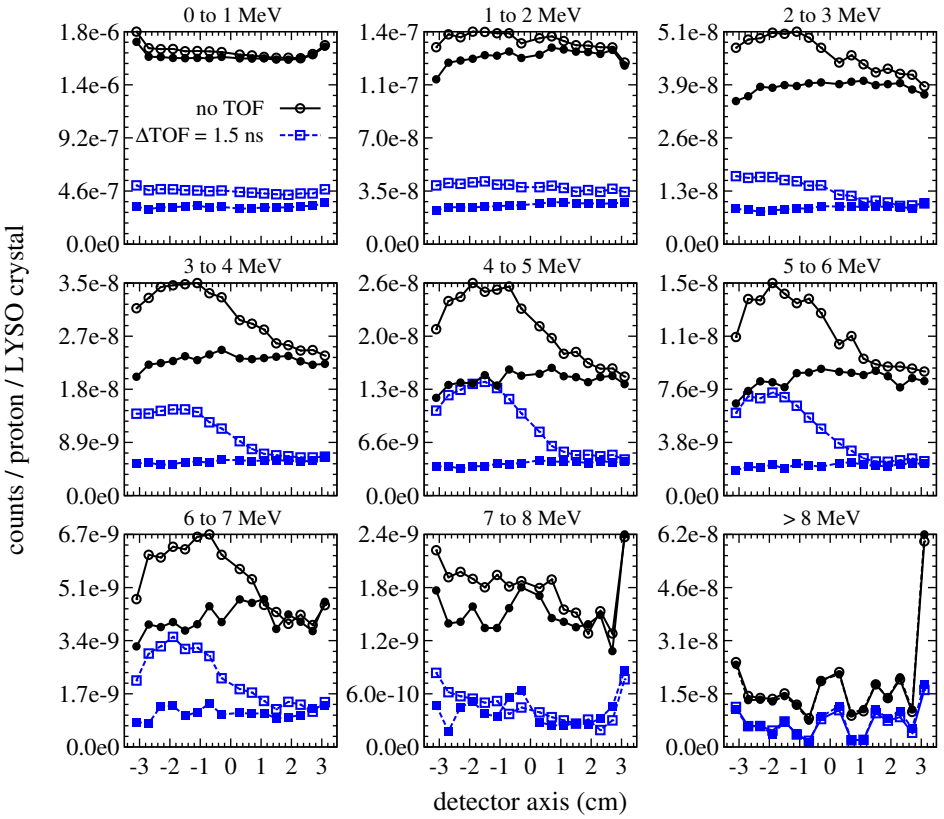

Figure 4.8: Decomposition into energy groups of the profiles measured with the LYSO:Ce detector centered at the expected beam range, with and without TOF discrimination, using an open (open symbols) or closed (closed symbols) collimator. The profiles obtained with a closed collimator and TOF discrimination were acquired with 5× higher number of protons. No uniformity correction was applied.

Maps of the count rate registered per crystal and the corresponding profiles are illustrated in figures 4.10 and 4.11, respectively, for the BGO detector and the LYSO:Ce detector with and without TOF discrimination, using an energy window of 3 MeV - 6 MeV in all cases. In figure 4.11, also the closed-collimator profiles are shown, as well as the profiles measured at two adjacent longitudinal detector positions that were added to increase

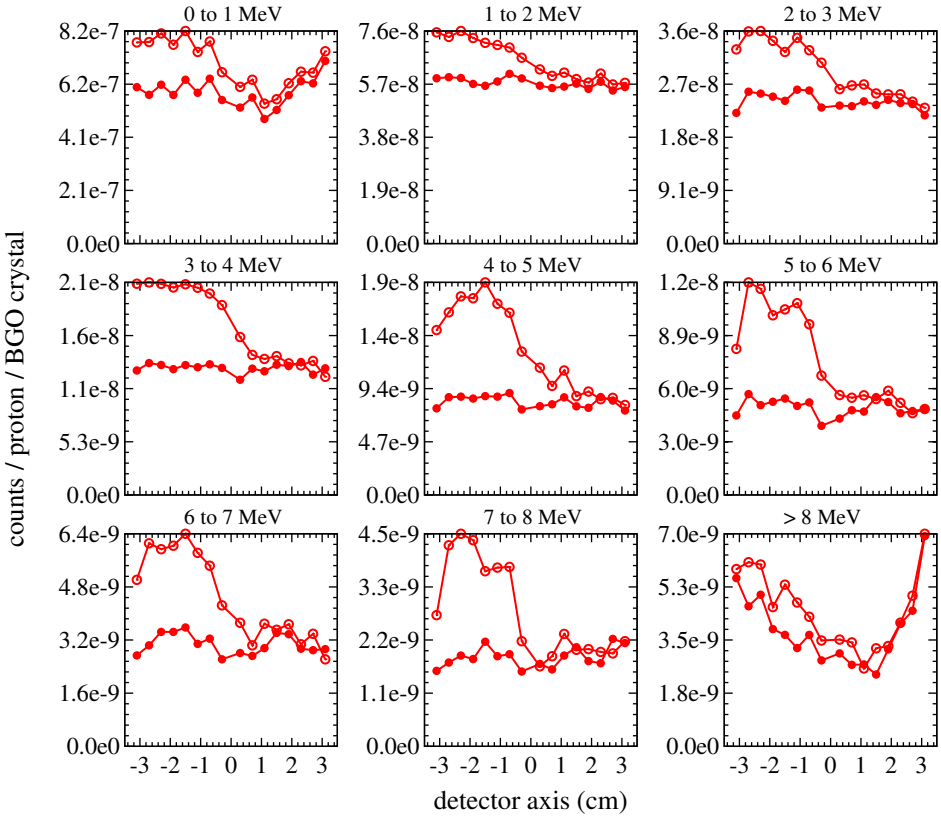

Figure 4.9: Decomposition into energy groups of the profiles measured with the BGO detector centered at the expected beam range, using an open (open symbols) or closed (closed symbols) collimator. No uniformity correction was applied.

Table 4.1: Signal-to-background ratios obtained with the BGO and the LYSO:Ce detectors from sigmoid fits to the measured PG profiles, for different energy windows and, for the latter detector, with/without time-of-flight (TOF) discrimination.

Energy window (MeV–MeV)	Signal-to-background ratio		
	BGO	LYSO:Ce	LYSO:Ce w/ TOF
1–6	0.40(2)	0.23(1)	0.64(2)
2–6	0.58(2)	0.39(2)	1.27(4)
3–6	0.79(4)	0.52(3)	1.61(7)
3–7	0.78(4)	0.52(2)	1.60(7)
3–8	0.80(3)	0.51(2)	1.58(6)

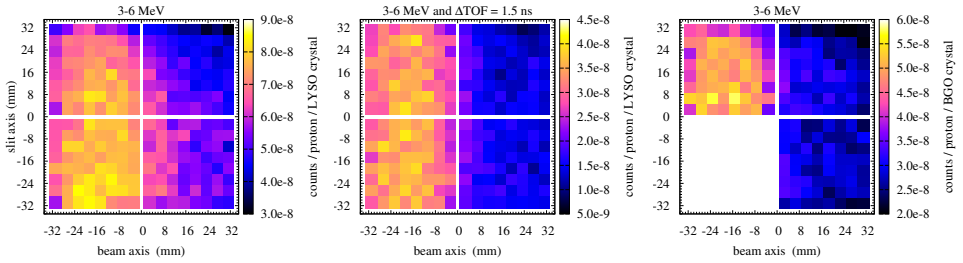

Figure 4.10: Intensity maps of crystal assignments of events registered in the energy window from 3 MeV to 6 MeV, using LYSO:Ce without TOF discrimination (left), LYSO:Ce with TOF discrimination (center), and BGO (right), having the detector centered at the expected beam range. No uniformity correction was applied.

the total field-of-view. In the latter profiles, the values of the edge pixel-columns were excluded to account for the observed systematic mismatches of the crystal count rates in the overlapping regions. Specifically, 2 pixel-columns were removed at each edge of the LYSO:Ce detector without TOF discrimination, 1 pixel-column for the same detector with TOF discrimination, and 2 pixel-columns on the left-most edge (on graph) for the BGO case.

The count-rate map obtained with LYSO:Ce (figure 4.10-left) shows a higher number of counts per proton in the lower half of the detector surface, compared to the upper part. This effect is reduced by applying TOF discrimination (figure 4.10-center), suggesting that the intensity offset is mostly due to background counts, for example gamma rays generated by neutrons interacting in the materials of the patient bed onto which the setup was placed.

By comparing the measured profiles shown in figure 4.11 to the ones presented in figure 4.7, we observe that cluster processing increases the detection efficiency of LYSO:Ce by 39% in the energy window between 3 MeV and 6 MeV, whereas for BGO this increase is 6-7% only. In case TOF discrimination is applied, the efficiency of LYSO:Ce increased by 30% with clustering. The higher efficiency increase in LYSO:Ce, compared to BGO, may be explained by the fact that the LYSO:Ce detector registers more DPC-chips per clustered event than the BGO one (specifically, 3.8 versus 3.3 chips per event for LYSO:Ce versus BGO, respectively, in the energy window between 3 MeV and 6 MeV), and that BGO presents higher efficiency. This is not unexpected given that the coefficient for photoelectric absorption of BGO is more than 1.5 times higher than that of LYSO:Ce in the energy range between 0.3 MeV and 6 MeV (Berger and Hubbell 2010). We did not observe relevant changes in the S/B ratios due to cluster processing.

Overall, our results indicate that BGO benefits from a higher gamma-to-neutron sensitivity compared to LYSO:Ce, resulting in a better S/B if no TOF discrimination is applied. Nevertheless, TOF selection appears to be the most effective way of rejecting background, rendering TOF-resolved LYSO:Ce detection the best option evaluated.

Given that TOF rejection of neutron-induced background relies on the difference in travel time between gammas and neutrons on their way to the collimator, the efficiency of TOF selection is expected to increase even further for larger distances between the beam

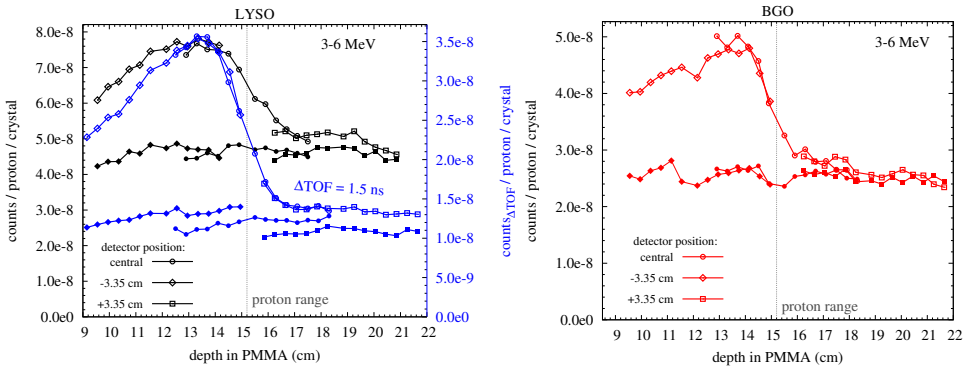

Figure 4.11: Measured profiles obtained with LYSO:Ce (left) and BGO (right) detectors, using an open (open symbols) or closed (closed symbols) collimator, at three detector positions along the beam axis (without uniformity correction). The dashed vertical line indicates the expected beam range. The profiles obtained with LYSO:Ce and TOF discrimination were acquired with 5× higher number of protons, except for the profile corresponding to the central detector position with the open collimator.

and the collimator. However, at large distances background reduction efficiency by a 1.5 ns TOF window may not exceed the limit of 84%, estimated by considering an homogeneous distribution of background time stamps over the 9.4 ns RF period, caused by the larger transit time spread of neutrons and the superposition of the background counts from consecutive proton bunches. Nevertheless, given that a 15 cm distance between the PG camera and the beam axis is close to the lower limit of what can be achieved in practice, the present efficiency of about 74% is very satisfactory.

4.3.3 Detection of proton range shifts

Figure 4.12 shows the profiles obtained at the reference phantom position, where the Bragg peak is aligned with the center of the detector, as well as with the phantom shifted along the beam axis by 1 mm, 2 mm, and 4 mm. The profiles were corrected for non-uniformities using the corresponding closed-collimator profiles (section 4.3.2.1), except for the cases where TOF discrimination was applied, in which the profile oscillations were irrelevant. The profiles are presented with energy windows corresponding to the highest S/B and efficiency (section 4.3.2.2), i.e. for event energies between 3 MeV and 7 MeV for LYSO:Ce and 3 MeV and 8 MeV for the BGO case. The left-side profiles were obtained with about 6.5×10^9 protons delivered in total, while the right-side profiles were obtained with reduced statistics, by randomly sampling 10% of the total amount of events for the LYSO:Ce and 20% for the BGO case, where the factor of two difference accounts for the fact that only half of the BGO detector surface was counted.

These results indicate that the improvement in the S/B ratio resulting from TOF discrimination directly translates into better possibilities to derive range position information. Visually, even the smallest steps, i.e. from the 0 position to +1 mm and from +1 mm to +2 mm, result in a clear and consistent shift of the PG profile over most of the distal falloff region if TOF discrimination is used, for the case of higher statistics (figure 4.12-left).

In order to quantitatively show this improvement in detectability of small shifts even for the case of reduced statistics presented, we used the technique of bootstrapping to randomly

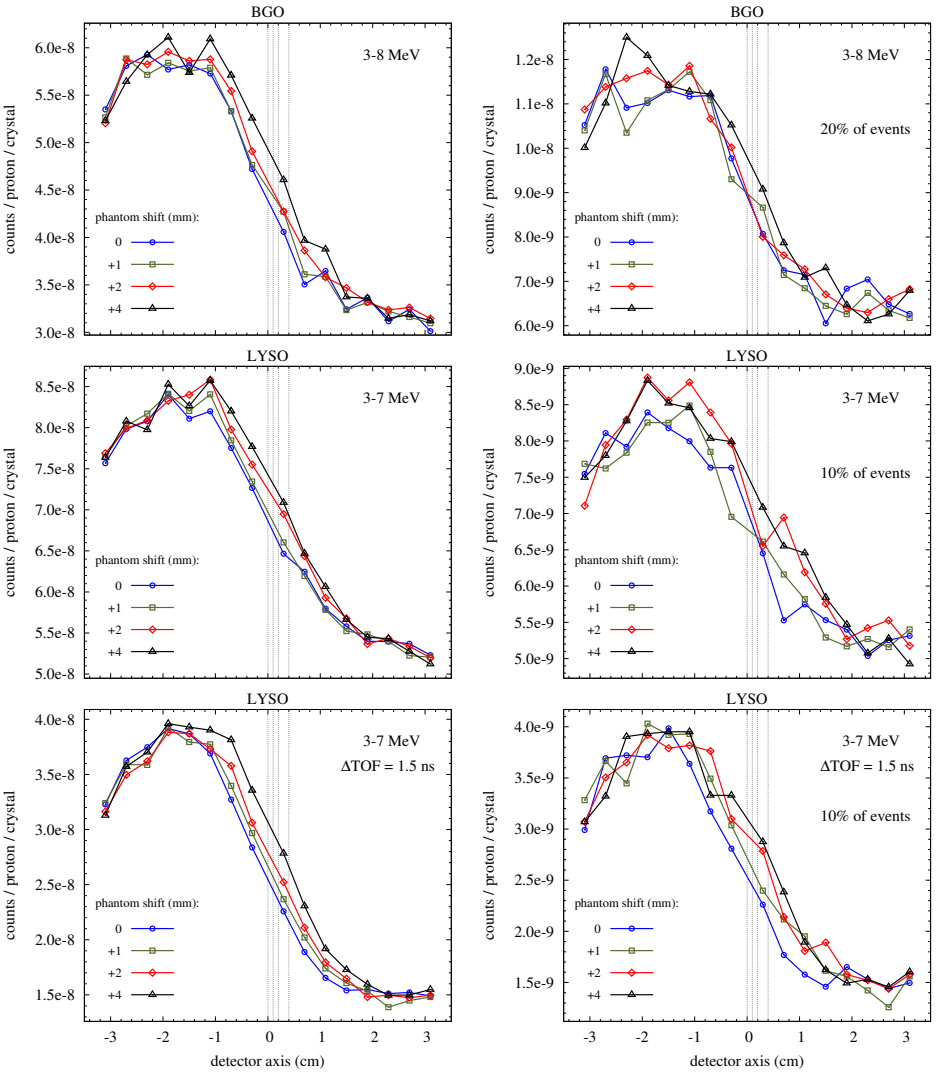

Figure 4.12: Profiles measured with about 6.5×10^9 protons delivered in total (left), and a lower-statistics scenario (right), having the detector centered at the expected beam range (phantom shift = 0) and for various phantom shifts along the beam axis. The vertical lines indicate the positions of the Bragg peaks corresponding to the different phantom shifts. The profiles of BGO and LYSO:Ce without TOF discrimination were corrected using the corresponding closed-collimator profiles (section 4.3.2.1). The lower-statistics scenario for the BGO case corresponds to 20% of the original detected events, in contrast to the LYSO:Ce case where a reduction to 10% of the original events was done, to compensate for the fact that only half of the BGO detector surface was used.

sample with replacement a set of 100 profiles from each of the profiles shown in figure 4.12-left. For each case studied, the sampled profiles were generated with the same number of counts as the original data, as well as with reduced statistics. A sigmoid curve was then fit to each profile, as explained in section 4.3.2.2, and similarly to Janssen *et al* (2014), the mean and standard deviation values of the inflexion points given by parameter *d* in equation (4.1) were obtained. These results are presented in figure 4.13.

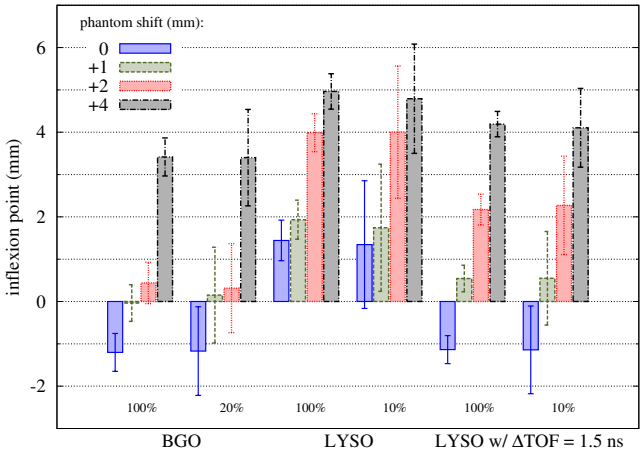

Figure 4.13: Mean and standard deviation (error bars) values of the inflexion points of sigmoid curves obtained by fitting 100 bootstrap samples from the profiles measured having the detector centered at the expected beam range (phantom shift = 0) and for various phantom shifts along the beam axis, applying energy windows between 3 MeV and 7 MeV for LYSO:Ce and 3 MeV and 8 MeV for BGO. Results are presented for bootstrap samples having the same size as the original data ('100%', i.e. total counts detected with about 6.5×10^9 protons delivered in total) and with lower statistics ('10%' for LYSO:Ce, and '20%' for the BGO case).

As it had been anticipated by visual inspection, figure 4.13 shows that the mean inflexion point positions corresponding to the different phantom shifts are more clearly and consistently separated for the case of LYSO:Ce detector with TOF discrimination, presenting no overlap (100% statistics) or less overlap (reduced statistics) between error bars from successive phantom shifts, compared to the other two cases (BGO, and LYSO:Ce without TOF). Moreover, in all the cases there is a good agreement between the mean inflexion point values derived from bootstrap samples with 100% statistics as well as with reduced statistics. This demonstrates the robustness and potential of this technique, which enables to derive statistical quantities (e.g., the mean value of a distribution) from a single measurement. The average difference between the mean inflexion points and the expected beam range for the various phantom shifts was -1.1 for BGO, 1.3 for LYSO:Ce, and -0.3 for LYSO:Ce with TOF. Finally, it should be noted that the size of the error bars (standard deviation) may be reduced by applying more sophisticated and robust fitting techniques that are less sensitive to noise.

Although the detection of small relative range shifts seems feasible using the present detection system and TOF discrimination, the detection of a range shift in the clinical case is certainly more challenging, especially if it relies on a single measurement. A possible way to detect range shifts in regard to a planned situation could be to carefully compare

measured profiles to reference ones, obtained by simulations. Future work is therefore desirable to fine-tune simulations to experimental data using highly heterogeneous phantoms and patient data. Additionally, it may be possible to provide absolute range assessment given the camera can be translated to detect the patient entry point in a similar way, by imaging prompt gamma rays from multiple proximal pencil beams with a common entry point.

4.4 Conclusions

We characterized the performance of DPC-based detector modules equipped with either BGO or LYSO:Ce scintillation crystals for the detection of prompt-gamma rays emitted from PMMA upon irradiation with 160 MeV proton beams. While the crystal matrices used were optimized primarily for the detection of 511 keV annihilation quanta in positron emission tomography (PET), consisting of arrays of high aspect-ratio crystals, it was possible to detect the main prompt gamma lines emitted in reactions involving H, C and O. Spectral characteristics were more clearly identified with the LYSO:Ce detector, due to its better energy resolution. The detection efficiency in the energy range between 3 MeV and 6 MeV could be increased by nearly 30% or 40% for LYSO:Ce with or without TOF discrimination, respectively, and by 6-7% for BGO, by using cluster processing, i.e. by applying a 'coincidence window' over the whole detector surface so as to find all crystals hit in a given event.

We used a knife-edge slit collimator to generate 1D-projection profiles that correlated with the expected proton range position. The measured profiles were in good agreement with MCNPX simulations. The signal-to-background ratio of 0.8 obtained with BGO was higher than the ratio of 0.5 found with LYSO:Ce if only energy discrimination was used to reject background counts. However, with the knife-edge slit collimator and detector placed at only 15 cm and 30 cm from the beam axis, respectively, the S/B ratio of the LYSO:Ce detector could be improved to 1.6 by synchronizing the DPC arrays with the 106 MHz cyclotron signal and applying a 1.5 ns wide TOF selection window centered around the prompt event peak.

Using only a single detector module with a total detection area of about 6.6 cm × 6.6 cm, equipped with 4 DPC arrays coupled to a total of 256 LYSO:Ce crystals of 4 mm × 4 mm × 22 mm each, the use of TOF discrimination enabled detection of Bragg peak shifts as small as 1 mm, for a single pencil beam delivering a total number of protons as low as about 6.5×10^8 in PMMA. Therefore, these results suggest that the proton range may be monitored precisely on a per-pencil beam basis, given a realistic detector size composed of multiple such detectors aligned along the slit axis (a factor of 10 approximately). In conclusion, this work shows the feasibility of using DPC-based detectors in prompt-gamma cameras for range monitoring in proton therapy and highlights the fact that TOF discrimination remarkably improves the detectability of small (~1 mm) range shifts even if the PG camera is placed at only 15 cm distance from the beam axis.

Acknowledgments

This work was funded in part by the foundation for Fundamental Research on Matter (FOM), The Netherlands (grant no. 09NIG18) and by the European Union Seventh Framework Program (grant agreement n. 241851 and 264552). P. Cambraia Lopes was supported by grant no. SFRH/BD/73705/2010 and P. Crespo was supported by grant no.

SFRH/BPD/39223/2007, both from FCT – Fundação para a Ciência e a Tecnologia, Lisbon, Portugal, co-funded by the European Social Fund and by POPH – Programa Operacional Potencial Humano. P. Crespo was further supported by QREN - FEDER under the Sistema de Incentivos à Investigação e Desenvolvimento Tecnológico (CENTRO-07-ST24-FEDER-002007, project 'Radiation for Life'). Enrico Clementel was funded by the Walloon Region of Belgium (convention no. 1017266).

The authors would like to thank Philips Digital Photon Counting, in particular Carsten Degenhardt, York Haemisch, Ralf Schulze and Ben Zwaans, for the fruitful discussions and help with the hardware and software implementations that made the synchronized measurements possible. Our thanks to the IBA team at WPE, in particular Andres Varga Sampedro and Pedro Vidal Caravaca, for their precious support, and to Jeroen Koning, Kees Langelaan and William van Goozen, from DEMO, TU Delft, for the technical support with the measurement setup. Our thanks to the colleagues at TU Delft, Stefan Seifert, Giacomo Borghi and Valerio Tabacchini, for the fruitful discussions, and to Mehmet Sarilar, from INAA lab., TU Delft, for preparing the Na-24 radioactive source.

Chapter 5

Background rejection in prompt gamma imaging using energy discrimination and a shifting time-of-flight window: experimental results with a scanning parallel-slit collimator[1]

Much attention is currently being paid to imaging prompt gamma (PG) emission for *in vivo* proton range monitoring in proton therapy. PG imaging using a collimator is affected by neutron-related background. We study the effectiveness of background reduction experimentally, using a scanning parallel-slit PG collimator as a simplified model of a multi-slat PG camera. The analysis is focused on the falloff region of the PG intensity profile near the Bragg peak, which is the typical region of interest for proton range estimation. Background reduction was studied for different energy windows, with and without a shifting time-of-flight (TOF) window that takes into account the proton velocity within the phantom (chapter 3). Practical methods are put forward that apply to cyclotron-based pencil beams. The parallel-slit collimator was placed in front of arrays of LYSO:Ce-coupled digital silicon photomultipliers, used to measure energy and time spectra together with intensity profiles of prompt events emitted from a PMMA phantom irradiated with a 160 MeV proton pencil beam. The best signal-to-background ratio of ~1.6 was similar to that obtained previously with a knife-edge-slit collimator, in the same experimental setup (chapter 4). However, the range-estimation performance, represented by the slope-over-noise ratio in the PG-profile falloff, was a factor ~1.2 higher for the present collimator, given its better resolution.

[1] Submitted for publication as: P. Cambraia Lopes, P. Crespo, J. Huizenga and D. R. Schaart, IEEE Trans. Rad. Pl. Med. Sci., 2017.

5.1 Introduction

In vivo monitoring of the proton range is currently a very active field of research in proton therapy, as most of the therapeutic effect of a proton beam is localized at its endpoint, where a maximum of energy (the Bragg peak) is imparted to the medium with nearly no dose deposited beyond that point. Much attention is currently being paid to the use of prompt gamma (PG) rays that are emitted along the beam path as a result of nuclear interactions between the protons and the irradiated medium. Due to the prompt nature of their emission, PGs can potentially provide valuable feedback on the treatment delivery in real-time and on a per-pencil-beam basis.

It is of great importance to suppress the large amount of background counts present in PG images, resulting directly and/or indirectly from the simultaneously created neutrons. Testa *et al* (2008) were the first to apply a time-of-flight (TOF) technique to reduce neutron-related background in PG imaging with a collimated detector, upon irradiation with 73 MeV/u carbon ions. Such TOF discrimination is based on the principle that neutrons travel slower than (massless) gamma quanta. Using time-resolved Monte Carlo (MC) simulations, Biegun *et al* (2012) (in chapter 3) proposed a general method to improve the effectiveness of TOF discrimination in PG detection, based on a shifting TOF acceptance window. The optimum TOF shift depends on the beam energy and the proton penetration depth, as it includes the travel time of the proton beam through the patient up to the PG emission-point being imaged. Golnik *et al* (2014) have further extrapolated these principles and have proposed a so-called prompt-gamma timing (PGT) method for range assessment, based on observables taken from the time-spectrum of PGs emitted along the entire particle path obtained from a single uncollimated point measurement.

This study focuses on PG imaging with (mechanical) collimation. PG images or intensity profiles can be obtained in a straightforward way by projection through a collimator, which only accepts rays emitted at certain angles, thus providing spatial information. In the context of proton therapy, experimental studies with collimator-based PG imaging systems have shown that TOF discrimination improves the signal-to-background ratio (S/B), even with a relatively broad time window (4 ns width, (Roellinghoff *et al* 2014)) or a relatively small (i.e. to what can be practically achieved) distance between the collimator and the beam (Cambraia Lopes *et al* 2015, in chapter 4). The S/B improvement directly translates into a reduced uncertainty in the estimated falloff position of the PG longitudinal profile, which is correlated to the proton range. First TOF-based studies have imaged PGs with a point detector coupled to a single-parallel-slit collimator, placed at 20 cm distance (front-surface) (Roellinghoff *et al* 2014) or 40 cm distance from the beam (Pinto *et al* 2014). Cambraia Lopes *et al* (2015) instead used a knife-edge slit collimator similar to Smeets *et al* (2012b), placed at only 13 cm from the beam, to image about 66 mm of the beam axis using a pixelated scintillation detector. In the latter work, TOF calibration was applied on a per-segment basis and a fine TOF window was used (viz. 1.5 ns width).

In all of the aforementioned experiments, the time stamps could be retrieved relative to a given phase of the cyclotron radiofrequency (RF) signal, due to the fact that bunches of protons are delivered synchronously to the RF cycle. This is also the case in the current work. The time spread of protons within the RF cycle (bunch width $\gtrsim 1$ ns FWHM) imposes a lower limit on the width of the TOF window and, therefore, on the achievable background reduction (Biegun *et al* 2012). The distance between the collimator and the beam also imposes a limit on the effectiveness of TOF background rejection, as it influences the degree of overlap between the arrival times of the PGs and the neutron-induced background.

In this work we quantify the degree of background reduction that can be achieved by applying energy discrimination and the shifting TOF window introduced by Biegun *et al*

(2012) to PG profiles measured with a parallel-slit collimator scanned along the beam axis. We focus on the falloff region of the PG intensity profile near the Bragg peak, which is the typical region of interest for estimating the proton range *in vivo*. The scanning parallel-slit collimator may be seen as a simple model of a multi-slat collimator (also named multi-slit (Min *et al* 2012)) in what concerns the timing information. Thus, the results of this work provide valuable information for the development of clinical PG imaging systems based on such collimators.

5.2 Experimental setup

The experiment was conducted at the West German Proton Therapy Center Essen (WPE), using a similar experimental setup as described in Cambraia Lopes *et al* (2015)[2], except that a parallel-slit collimator was used instead of a knife-edge slit collimator. A detector based on Philips digital photon counters (DPCs, Frach *et al* 2009, 2010, Degenhardt *et al* 2009) coupled to Cerium-doped Lutetium Yttrium Silicate (LYSO:Ce, $Lu_{1.8}Y_{0.2}SiO_5$(Ce)) crystals was used because of its good time resolution (coincidence resolving time $<$ 255 ps FWHM for $>$ 511 keV photons).

In brief, the detector module (DPC-MO-22-3200, Degenhardt *et al* 2012, Haemisch *et al* 2012) had a total surface area of 68 mm $\times$ 68 mm and contained 8×8 DPC pixels at a pitch of 4 mm, each pixel containing 3200 single-photon avalanche diodes (SPADs) or microcells. A total of 256 pixelated LYSO:Ce crystals, with dimensions of 3.8 mm $\times$ 3.8 mm $\times$ 22 mm, were optically coupled 1-to-1 to the pixels. The basic DPC functional unit consists of an arrangement of 2×2 DPC-pixels, the so-called DPC-chip, which incorporates two interleaved time-to-digital converters (TDCs) for time-stamp generation, and readout electronics (Frach *et al* 2009). The principles of operation and performance characteristics of DPCs have first been described and characterized by Frach *et al* (2009, 2010) and have been reviewed by Schaart *et al* (2016).

The detector acquisition electronics were synchronized with the cyclotron RF, i.e., instead of the internal 200 MHz clock an external reference clock was used, derived from the 106 MHz RF wave. In this way, the registration time of each event relative to the phase of the RF cycle could be obtained directly from the TDCs in the DPC-chip and time-of-flight discrimination could be applied offline.

A polymethylmethacrylate (PMMA) phantom with dimensions of $\varnothing$15 cm $\times$ 20 cm was irradiated using a proton pencil beam with 160 MeV energy, a beam current of ~10 pA, and ~6.5×10^9 protons delivered per measurement (~100 s long), corresponding to an administered dose of about 10 Gy. An additional two measurements of longer duration and equal beam current were performed in order to visualize the energy spectra and the per-pixel intensity maps with 5-times higher statistics.

Figure 5.1 presents the geometrical arrangement (left) and a photograph (right) of the experimental setup. We performed nine point measurements with the collimated camera accepting events emitted at right angles from various proton penetration depths spanning between 12.2 cm and 17.2 cm (the proton range R of 160 MeV protons in PMMA equals 15.2 cm, defined as the distal position at which the depth-dose profile has reduced to 80% of the maximum height). In order to measure at different depths, the phantom was translated longitudinally along the beam axis. The corresponding changes in proton travel time through air between measurements were corrected for, so that the experiment was equivalent to moving the detector + slit.

[2]Refer to section 4.2.1 in chapter 4 for details.

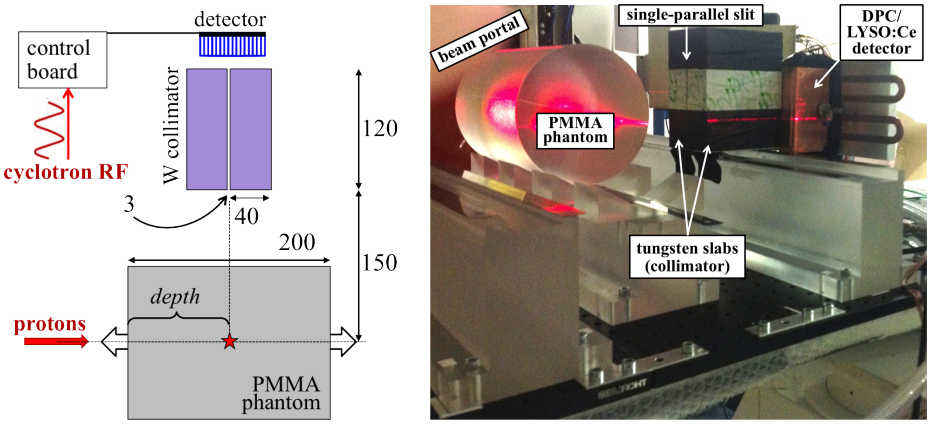

Figure 5.1: Left: Schematic representation of the measurement setup (top view), with distances displayed in millimeters. The distance between the collimator back-surface and the front-surface of the scintillators was about 12 mm. The intersection between the slit mid-plane and the beam axis ($\star$) gives the position of emission of the prompt gamma rays being imaged. Right: Photograph of the experimental setup. The LYSO:Ce detector was mounted on a breadboard; both the collimator and the phantom were placed on PMMA support rails.

The collimator was made of two tungsten slabs, each with dimensions of 12 cm $\times$ 4 cm $\times$ 15 cm. The collimator left uncovered a column of 8 DPC-chips with a total length of 6.6 cm. The slit width of 3 mm corresponded to a field of view (FOV) of 10.5 mm at the beam axis (excluding septa penetration), which upon projection onto the back-surface of the 22 mm long crystals yielded a width of 4.7 mm (figure 5.2). Since (1) the center of the slit was aligned with the center of the uncovered DPC-chips in the beam direction, and (2) each chip is subdivided into 2×2 pixels with a 4 mm pitch, with each pixel being coupled to a single crystal, the amount of crystals that were exposed to the collimated gamma rays was 2 (beam axis) $\times$ 16 (slit axis) $= 32$.

Although only one column of DPC-chips was left uncovered by the slit, the whole detector (with an area of 6.6 cm $\times$ 6.6 cm) was actively measuring. This enabled the clustering of multiple-chip events (arising due to inter-crystal Compton scattering) by means of a coincidence window acting on the detector level, so as to increase the detection efficiency (Cambraia Lopes *et al* 2015).

5.3 TOF-shift calibration curve

Time calibration was implemented offline by post-processing experimental in-beam time spectra. The clock skews between the DPC chips that were left uncovered by the collimator were accounted for, to ensure proper time alignment (van Dam *et al* 2013). These skews were derived from per-chip time-spectra previously measured in (Cambraia Lopes *et al* 2015) using the knife-edge slit collimator and a 5-times higher total amount of delivered protons, providing better statistics. The chips considered here for timing measurements were aligned with the (knife-edge) slit axis. The prompt peak position was determined for each chip as the time stamp (TS) corresponding to the maximum of the interpolated time

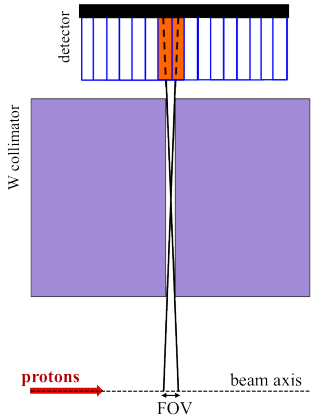

Figure 5.2: Zoom of figure 5.1-left (not to scale), showing that only the two rows of crystals represented in orange (corresponding to one row of DPC-chips) are directly exposed to the collimated gamma rays emitted from the field of view (FOV) in the beam axis.

histogram[3]. For inter-chip time calibration, considering chips in a given row exposed to the slit, a fixed beam energy was utilized, resulting in negligible influence of proton transit time on the time calibration. Hence, the time differences between the chips arise from the different inter-chip clock skews and from the different PG TOF arising from gamma rays impinging on the detector with different tilting angle (figure 5.3). These two effects result in a constant time difference between any two given chips, which was corrected for by aligning the peak positions of the per-chip time histograms.

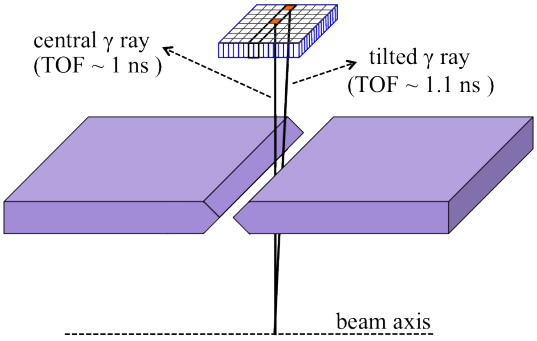

Figure 5.3: Schematic view of the experimental setup used for calculating the time skews between the sensors within the same row aligned with the slit axis. The maximum path difference between two detected gamma rays yields a TOF difference of about 100 ps.

The time spectra obtained at phantom depths proximal to the proton range are presented in figure 5.4, post time-skew correction. These time spectra show that the prompt peak sits on a slowly-rising slope of neutron-related background counts, which peak at time stamps posterior to the corresponding prompt peak. The intensity of this background shoulder

[3]Refer to section 4.2.2.2 in chapter 4 for details.

increases with increasing phantom depth, which is expected due to the fact that neutrons are mostly forward-projected. Background counts occurring before the PG peak are most likely originating from previous proton bunches (Biegun *et al* 2012), as the range of neutron arrival times is relatively large.

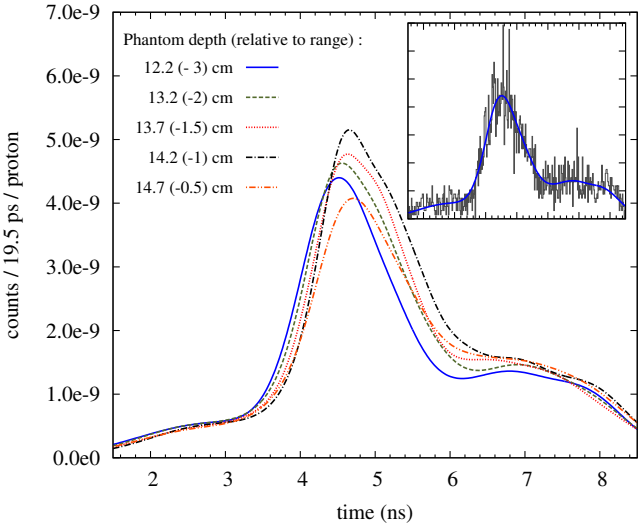

Figure 5.4: Time-spectra of DPC-chip-events registered over the entire detector segment uncovered by the single-parallel-slit (~66 mm length), relative to an arbitrary phase of the cyclotron radiofrequency (RF) cycle, post time-skew correction and with a low-energy cutoff of 3 MeV on chip level. The time spectra were measured at five different phantom depths (figure 5.1-left) proximal to the proton range. The differences in proton travel time in air between the various measurements were taken into consideration. The smooth curves correspond to kernel density estimation (KDE) results obtained from the measured data. The inset shows an exemplary data histogram obtained at 12.2 cm depth (gray) and the corresponding KDE curve (blue), plotted on the same horizontal/vertical axis as the main graph.

The prompt peak position is a function of the proton penetration depth, due to the finite proton velocity within the phantom. In order to accurately pinpoint the TOF shift value, the histograms of the time spectra were interpolated to reduce the influence of statistical noise. Fitting of the time spectra with pre-defined functions that model both the PG curve and the background, as previously done in (Cambraia Lopes *et al* 2015), was found to yield insufficiently accurate results. Possible reasons for this are: (1) the TS distribution of PGs is mostly determined by the proton-bunch time-width, which is approximately Gaussian-shaped but may not be completely symmetric (Parodi *et al* 2005a); (2) additional asymmetry in the PG-TS distribution may arise due to scattered PGs; and (3) the shape of the distribution of background TSs is not entirely known and difficult to model. Therefore, the time spectra were interpolated using the kernel density estimation (KDE) class available in the *ROOT Data Analysis Framework*, based on works by Scott (1992), Ben (2007), and Härdle *et al* (2004). KDE works on the raw TS data to estimate, in a non-parametric way, a probability density function of arbitrary shape. Default options and parameter *rho* (equal to 1.0) were used. The latter affects the kernel width and thus the degree of smoothing. KDE was also used to derive the time skews between the DPC-chips, from measurements

previously performed using a knife-edge slit collimator, as described above.

The inset in figure 5.4 shows a KDE result in comparison to the corresponding measured histogram. Note that the KDE function converges to zero at the edges. Also note that the counts at the edges of the original time spectra ($\lesssim$ 1 ns) were artificially reduced due to the facts that (1) there was a limit in the range of possible TS values output by the DPC-chips (the TS range was smaller than the 9.4 ns period of the RF-cycle (Cambraia Lopes *et al* 2015)), and (2) the time spectra from different chips were summed after being shifted relative to each other (to correct for the time skews).

The TOF shifts for the five phantom depths prior to the proton range were obtained from the TSs corresponding the maxima of the KDE curves. These TOF shifts are represented by the closed circles in figure 5.5-inset. They are compared to simulated TOF shifts in the main panel of figure 5.5 (open circles), which were obtained using Geant4 (version 9.3, package QGSP_BERT_HP) in a similar way as in Biegun *et al* (2012)[4]. The TOF shifts reported by Biegun *et al* (2012) are also shown. These correspond to proton energies above (200 MeV) and below (150 MeV) the energy of 160 MeV used in the current experiments.

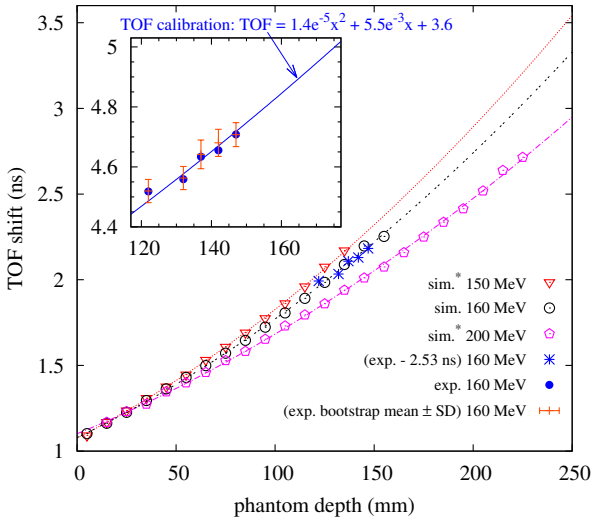

Figure 5.5: Simulated and measured TOF shifts, as a function of phantom depth, for the beam energy used in this experiment (160 MeV) and for higher and lower proton energies (simulations only, after (Biegun *et al* 2012)*). The simulated TOF shifts correspond to a start time when the proton is launched 1 cm before the phantom and a stop time at a detector located at 30 cm from the beam axis, while the measured ones (inset) were obtained relative to an arbitrary phase of the RF cycle and are displayed as in figure 5.4. Also shown are the curves fitted to the simulated TOF shifts and the TOF-shift calibration curve used to apply TOF discrimination (inset). The latter is equal to the double-dashed curve plus an arbitrary offset of 2.53 ns that minimized the square sum of the residuals relative to the experimental TOF shifts. The inset also shows the mean and standard deviation (SD) of the experimental TOF shifts, obtained by bootstrapping.

The simulated TOF shifts for proton penetration depths between zero and the proton range R = 15.2 cm were used to derive the overall shape of the TOF calibration curve. In

[4]Refer to chapter 3 and figure 3.1 for details.

a first step, a second-order polynomial function was fit to the simulated TOF shifts (as in (Biegun *et al* 2012)). Subsequently, the TOF-shift calibration curve was determined by fitting that polynomial function plus a constant offset to the experimental TOF shifts, with the offset as the only free parameter. Figure 5.5-inset shows this calibration curve in the range of phantom depths at which the measurements were done.

The uncertainty in TOF-shift determination was estimated using the technique of bootstrapping and the results are presented by the red error bars in figure 5.5-inset. From each time spectrum considered, a set of 100 time-spectra were generated, each of which was derived by randomly sampling, with replacement, the original data set of TS values, for a number of times equal to the original data size. The TOF-shift was subsequently derived for every bootstrap sample after interpolation by KDE, and the corresponding mean and standard deviation values were calculated.

5.4 Event processing

Energy calibration, cluster processing (using a 5 ns wide paralyzable coincidence window on detector level) and crystal assignment ('winner-takes-all') were applied as described in detail in Cambraia Lopes *et al* (2015)[5]. In cases where TOF discrimination was applied, only those events were accepted for which the TS on the DPC-chip that registered the highest energy was within a TOF window ΔTOF, which had a width of 1.5 ns and was centered at a TOF shift value given by the calibration curve in figure 5.5-inset.

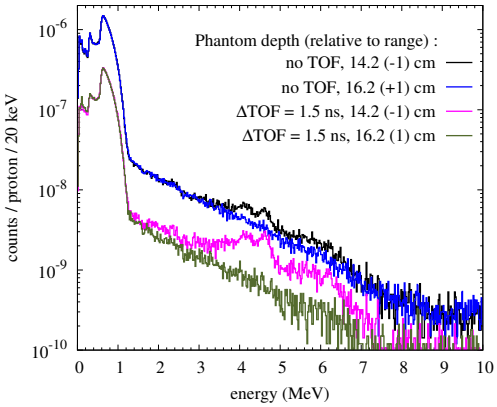

Figure 5.6: In-beam energy spectra measured with (pink and green) and without (black and blue) TOF discrimination, having the field-of-view of the single-parallel-slit collimator centered at phantom depths equal to $R - 1$ cm (pink and black) and $R + 1$ cm (green and blue), where $R = 15.2$ cm is the proton range in PMMA. The data were acquired for the highest amount of delivered protons.

The energy spectra from events originating at phantom depths proximal and distal to the proton range $R = 15.2$ cm, with and without TOF discrimination, are presented in figure 5.6. Figure 5.7-top shows the intensity maps of crystal assignment corresponding to the same measurements, for the case without TOF discrimination. Whereas figure 5.7 shows events

[5]Refer to section 4.2.2.1 in chapter 4 for details.

registered on the whole detector surface, the energy spectra (figure 5.6) include only events assigned to the 32 crystals that were exposed directly to the collimated radiation. Those crystals are indicated by the dashed rectangles in figure 5.7-top. The remaining crystals were located behind the collimator.

Figure 5.7 shows that a relatively high amount of background counts is registered at the detector pixels located most closely to the beam entrance point in the phantom. This can at least partly be attributed to the fact that PG rays emitted near the phantom entry point and traveling to crystals located at the upstream side may enter the collimator through its side surface instead of its front surface, resulting in a shorter path through the collimator material and, therefore, less efficient shielding of these PG rays. However, it is to be emphasized that such events are not expected to play a significant role in the analysis of prompt gamma profiles and background rejection presented in the next section, since only counts that are assigned to crystals uncovered by the collimator slit will be taken into account.

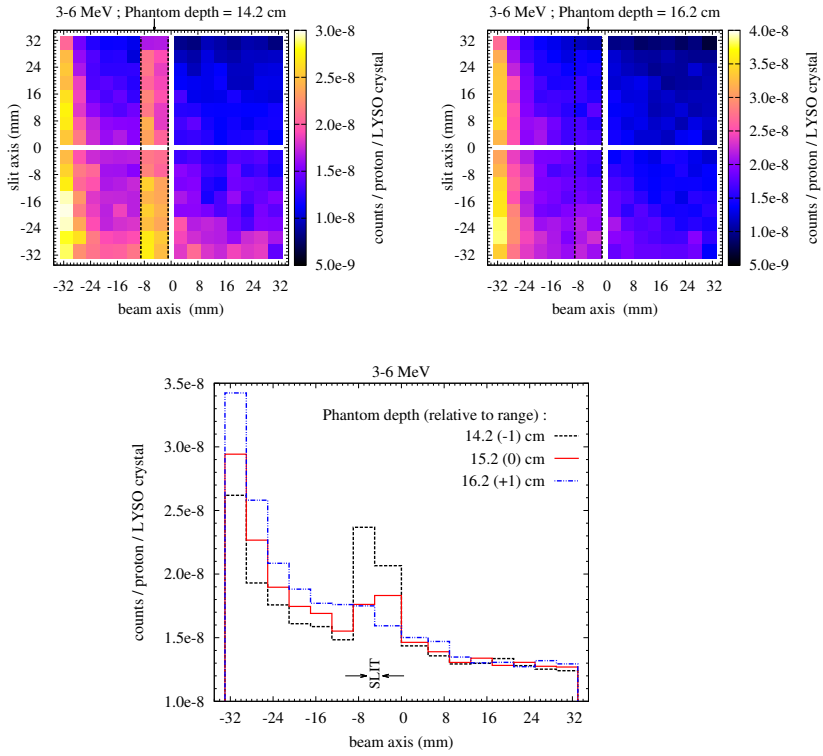

Figure 5.7: Intensity maps of crystal assignments (top) and projection profiles along crystal columns parallel to the slit (bottom), of events registered in the energy window between 3 MeV and 6 MeV without TOF discrimination, having the field-of-view of the single-parallel-slit collimator centered at phantom depths of $R - 1$ cm (black) and $R + 1$ cm (blue), as well as at R (projection profile only). The two crystal columns contained by the dashed line (top graphs) were exposed to the collimated radiation. The slit opening is indicated by the arrows on the bottom graph. The data corresponding to the 2D intensity maps were acquired with $5\times$ higher statistics, in terms of total delivered protons.

5.5 PG intensity profiles and background rejection

Prompt gamma intensity profiles with and without TOF discrimination were obtained by integrating the counts assigned to the 32 directly exposed crystals (figure 5.7), for each longitudinal position along the beam axis at which a measurement was done. As an example, Figure 5.8 shows the results obtained after applying an energy acceptance window ranging from 3 MeV to 7 MeV, with and without TOF.

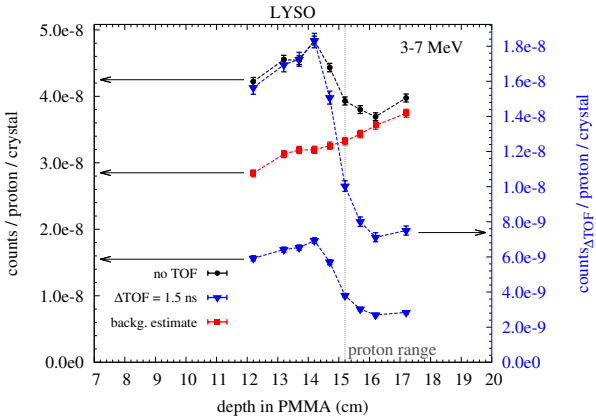

Figure 5.8: Profiles obtained without (back circles) and with (blue triangles) TOF discrimination, as well as the estimated background before TOF discrimination (red squares, see text for details). The profile with TOF discrimination is displayed on the same scale as the other profiles (left-axis), as well as on a separate scale (right-axis), chosen such that the maxima of the profiles with and without TOF coincide. The dashed vertical line indicates the proton range R. The error bars correspond to one standard deviation, as expected on the basis of Poisson statistics.

5.5.1 Signal-to-background ratio

The counts detected at phantom depths distal to the proton range are expected to be due to background, i.e. counts resulting from prompt neutrons (which may generate gamma rays in e.g. the collimator and detector materials), scattered gamma rays, and gamma rays penetrating through the tungsten parts of the collimator without being absorbed. Essentially the same can be said about counts assigned to detector pixels behind the collimator. Therefore, the background before TOF discrimination can be estimated by interpolation, i.e. by averaging the amount of counts assigned (without TOF selection) to the two columns of DPC-chips that are closest to the column of DPC-chips left uncovered by the collimator slit (as indicated in figure 5.7), namely left and right to it.

The resulting background intensity profile is represented by the red squares in figure 5.8. We observe an increase in background intensity with increasing phantom depth, which is attributed to the fact that the neutrons generated in proton-induced nuclear reactions are emitted mostly in the forward direction at the proton energies of interest. As expected, the background thus estimated accounts for almost all of the counts (black circles) registered beyond the falloff region (i.e. at depths $\geq R + 1$ cm). The small difference between the black circles and the red squares may primarily be due to gamma photons that are either

generated (by neutrons) or scattered in the distal part of the phantom and that subsequently travel through the collimator slit towards the detector.

Given the above, a pragmatic approach to compare the signal-to-background ratios (S/B) with and without TOF discrimination for different energy windows is to estimate them directly from the corresponding intensity profiles (i.e. from the blue triangles or black circles in figure 5.8, respectively), using the following equation:

$$\text{S/B} = \frac{C_{R-1\,cm} - C_{R+1\,cm}}{C_{R+1\,cm}} \tag{5.1}$$

where $C_{R-1\,cm}$ and $C_{R+1\,cm}$ represent the counts at R - 1 cm and R + 1 cm respectively, corresponding to the maximum and the minimum of the measured intensity profiles.

The method described in equation (5.1) is similar to the one previously used in (Cambraia Lopes *et al* 2015). Therefore, we will use this method in the present work to facilitate comparison of the results. Moreover, given that estimates of the proton range are typically derived from analysis of the falloff region of the PG intensity profile near the Bragg peak, equation (5.1) may be seen as an estimate of S/B relevant to the intended application. For completion, it should be noted that this definition assumes the same background level at R - 1 cm and R + 1 cm, whereas in reality the background intensity increases with increasing depth (red squares in figure 5.8). Hence, equation (5.1) can be seen as a conservative estimate of S/B in the region of interest.

5.5.2 Range estimation performance

As a figure of merit (FOM) for the performance of the collimator in estimating the proton range, we use the slope-over-noise ratio in the fall-off region of the PG profiles. This FOM takes into account the influence of both the signal-to-noise ratio in the measured PG profiles and the collimator resolution. For example, if we consider a simple estimator of the Bragg peak position, based on the depth ζ at which the PG falloff profile intersects a certain threshold level, then the uncertainty in ζ equals the ratio of the noise and the slope of the PG falloff profile at that point.

To determine the slope from the PG profiles measured with the single-parallel slit, we fitted a complementary error function (sigmoid curve) to the PG profiles obtained with the single-parallel slit. This procedure is similar to that used in Cambraia Lopes *et al* (2015), except that a linear baseline was used instead of a constant offset in addition to the sigmoid function, as this appeared to result in a better fit. The figure-of-merit was subsequently calculated as:

$$\text{FOM} = \left.\frac{\mathrm{d}n}{\sqrt{n}\mathrm{d}z}\right|_{\zeta=\text{inflexion point}} \tag{5.2}$$

where the noise is approximated by the square root of the number of counts at the inflection point of the sigmoid fit, n, z is the depth in the phantom, and $\mathrm{d}n/\mathrm{d}z$ is the slope evaluated at the inflection point ζ.

5.5.3 Performance optimization

Table 5.1 shows the S/B and FOM values for various energy acceptance windows and with/without TOF background rejection. TOF discrimination appears to improve the S/B ratio by a factor of ~6 for the energy window of 2 MeV - 6 MeV, and by a factor of ~5 for

Table 5.1: Estimated signal-to-background ratio (S/B, eq. (5.1)) and figure of merit (FOM, eq. (5.2)) for different energy windows and with/without time-of-flight (TOF) discrimination. The improvement factors obtained by using time-of-flight discrimination are displayed for both S/B and FOM as the ratio of the corresponding values with and without TOF.

Energy window	S/B		Improvement factor	FOM (mm^{-1})		Improvement factor
(MeV−MeV)	no TOF	TOF	$(S/B_{TOF}) / (S/B_{No\ TOF})$	no TOF	TOF	$FOM_{TOF} / FOM_{No\ TOF}$
1 – 6	0.04(1)	0.30(2)	8(2)	-0.53	-1.4	2.6
2 – 6	0.17(2)	1.02(5)	5.8(7)	-1.3	-2.8	2.2
3 – 6	0.33(3)	1.62(8)	5.0(5)	-1.7	-2.9	1.7
3 – 7	0.31(2)	1.57(8)	5.1(5)	-1.7	-3.1	1.8

the energy windows of 3 MeV - 6 MeV and 3 MeV - 7 MeV. In fact, these S/B improvements are somewhat underestimated, as some TOF selection is still present in the 'no-TOF' profiles due to the fact that events with time stamps at the edges of the 9.4 ns long RF wave period (not more than 30% of the total period) were not registered (Cambraia Lopes *et al* 2015[6]).

We also observe an improvement of the FOM by using TOF discrimination, namely by a factor of ~2.2, ~1.7, and ~1.8 for the energy window of 2 MeV - 6 MeV, 3 MeV - 6 MeV, and 3 MeV - 7 MeV, respectively. Interestingly, while there is no significant difference between the S/B ratios corresponding to the 3 MeV - 6 MeV and 3 MeV - 7 MeV energy windows with TOF discrimination, the FOM is slightly better for the latter window (3.1 mm^{-1} vs 2.9 mm^{-1}). This is attributed to the corresponding increase in the total number of counts by about 13%, which gives rise to a higher absolute slope and reduced statistical fluctuation.

5.6 Discussion and conclusions

In this work we have used a scanning parallel-slit collimator to measure time spectra, energy spectra, and intensity profiles of prompt gamma rays emitted at various depths along a 160 MeV proton pencil-beam in a PMMA phantom. The collimator was placed in front of a detector based on matrices of LYSO:Ce crystals read out by arrays of digital photon counters. The scanning parallel slit collimator may be seen as a simple model of a multi-slat collimator, especially in what concerns the timing information. We applied different energy windows and a shifting TOF window to the measured intensity profiles. Depending on the energy window used, TOF discrimination appeared to improve the signal-to-background ratio by a factor of ~5 to ~8. As a consequence, the range estimation performance, represented by a figure of merit based on the slope-over-noise ratio in the falloff region of the PG profile, improved by a factor of ~1.7 to ~2.6. The best FOM value was obtained for the energy window 3 – 7 MeV in combination with TOF discrimination.

From a comparison of the present results with those obtained in (Cambraia Lopes *et al* 2015), in which the same scintillation detector was used in combination with a knife-edge slit collimator made from the same material (tungsten) and in which essentially the same experimental setup was used for all tests, the following observations can be made.

[6]Refer to section 4.2.2.2 in chapter 4 for details.

1. The energy spectra obtained in the present work (figure 5.6) reveal more clearly marked spectral features in the energy range between ~3 MeV and ~7 MeV, such as the 4.4 MeV peak[7]. This suggests a lower relative contribution from gamma rays scattered within the collimator or phantom. This may indeed be expected because (a) the thickness of the collimator material between the beam and the detector is much larger in the present work, and (b) the collimator acceptance angle is much narrower, allowing fewer scattered photons to reach the detector.

2. The time spectra obtained in the present work (figure 5.4) show a somewhat lower ratio between the prompt peak intensity and the background baseline, suggesting a higher relative contribution from neutron-related background counts[8]. Also this is expected because the detector is placed much closer to the collimator, in which the neutrons may create gamma rays that can be detected. Here, it is to be noted that LYSO:Ce crystals are more sensitive to gamma rays than to neutrons.

3. Comparable S/B ratios of approximately ~1.6 can be achieved with both collimators, if a low-energy cutoff of 3 MeV is applied in combination with TOF discrimination in both cases (table 5.1 versus table 4.1). The fact that these optimal S/B values are comparable between the two collimators is somewhat expected as the beam-collimator distance is similar in both experiments, resulting in a similar exposure of the collimator to neutrons. However, poorer S/B ratios are observed in the present work for low-energy cutoffs < 3 MeV. Also, the relative differences between the S/B ratios obtained with and without TOF discrimination are larger in the present work for such energy thresholds. These observations are consistent with the hypothesis that a larger fraction of the background counts is due to gamma rays generated in the collimator by neutrons, taking into account that many of these gamma quanta may undergo Compton scattering in the collimator before reaching the detector. Hence, the selection of the low-energy cutoff appears to be more crucial for the case of the single-parallel-slit collimator.

4. Finally, figure 5.9 shows the effect of the improved spatial resolution obtained in the current experiment, compared to the knife-edge slit collimator (data from Cambraia Lopes *et al* 2015). Note that in the figure the two profiles are plotted with different scales (single-parallel slit in the left Y-axis, knife-edge slit in the right Y-axis) allowing for visual comparison of the relative slopes, which may be seen as a measure of the collimator resolution. By normalizing both profiles to a maximum intensity of 1, it can be shown that the relative slope of the parallel slit collimator is a factor of 1.8 better than that of the knife-edge slit. Interestingly, a simple geometrical calculation of the point-source resolution assuming infinitely-dense collimators indeed predicts a factor of 1.8 improvement in spatial resolution for the parallel-slit compared to the knife-edge slit (6.8 mm versus 12 mm, respectively). Such improved resolution may increase the capability to detect, among others, deviations in the shape of the distal falloff arising in the irradiation of highly-heterogeneous media. However, with the current single-parallel slit setup this comes at the expense of a reduction of the total number of counts by a factor of about two (figure 5.9).

To compare the range estimation performance of the two collimators, we can again use the FOM given in eq. (5.2). It appears that the FOM of the single-parallel slit is a factor ~1.2 better than that of the knife-edge slit, for all of the energy windows 2 MeV – 6 MeV, 3 MeV

[7] Refer to figure 4.5-top for comparison.
[8] Refer to figure 4.4 for comparison.

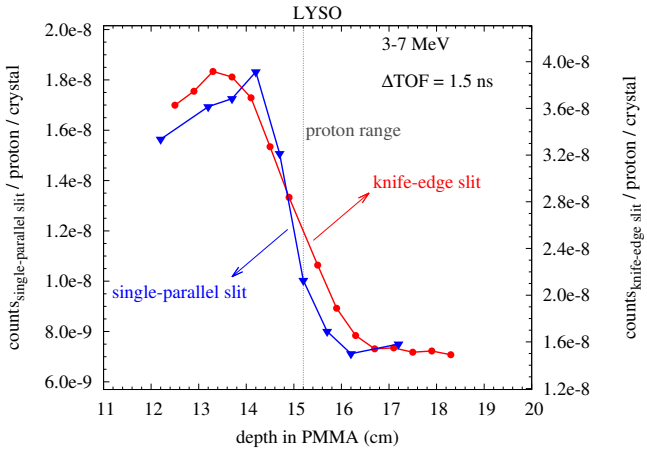

Figure 5.9: Comparison of intensity profiles measured in essentially identical experimental setups (including approximately the same distance between the beam axis and the detector front face, as well as between the beam and the collimator) with the current scanning single-parallel slit and the knife-edge-slit reported by Cambraia Lopes *et al* (2015). Only events falling within an energy window of 3 MeV to 7 MeV and ΔTOF = 1.5 ns were accepted in both cases.

– 6 MeV, and 3 MeV – 7 MeV, in combination with TOF discrimination. Specifically, the FOM values of the knife-edge slit are -2.3 mm^{-1}, -2.4 mm^{-1}, -2.5 mm^{-1}, respectively, while the FOM values for the single-parallel slit can be found in table 5.1. It is noted that these values were obtained for the same number of incident protons.

Finally, it is noted that, whereas the shifting TOF window can straightforwardly be applied to a multi-slat collimator, the results obtained in this work cannot be extrapolated to such a collimator directly. The multi-septa of a multi-slat collimator, interleaved by air slabs, would result in increased septa penetration by oblique gamma rays, which to some extent may degrade the effective spatial resolution with respect to the single parallel-slit case. On the other hand, the reduced amount of collimator material in the vicinity of the detector of a multi-slat configuration would reduce the amount of (n,γ) reactions, resulting in fewer background events. In addition, the total collimator volume would be considerably different, implying an overall different attenuation and scatter contribution. Nevertheless, the current results present insights that may be useful in the development and use of a PG camera based on a multi-slat collimator.

To conclude, our results indicate that the single parallel-slit collimator, when used in combination with optimized energy and TOF acceptance windows, yields PG profiles well correlated with the Bragg peak position, implying that it could be used to obtain important information on the accuracy of dose delivery in proton therapy. In comparison to a knife-edge slit collimator previously studied, the single-parallel slit shows potential advantages in the accuracy of determination of the Bragg peak position from the falloff of the PG profiles. Future studies are necessary to verify if these conclusions remain valid for a full-scale multi-slat collimator and to further optimize the collimator properties in order to achieve the best compromise between resolution, sensitivity, and signal-to-background ratio.

Acknowledgments

This work was funded in part by the foundation for Fundamental Research on Matter (FOM), The Netherlands (grant no. 09NIG18) and by the European Union Seventh Framework Program (grant agreement n. 241851 and 264552). P. Cambraia Lopes was supported by grant no. SFRH/BD/73705/2010 and P. Crespo was supported by grant no. SFRH/BPD/39223/2007, both from FCT – Fundação para a Ciência e a Tecnologia, Lisbon, Portugal, co-funded by the European Social Fund and by POPH – Programa Operacional Potencial Humano. P. Crespo was further supported by QREN - FEDER under the Sistema de Incentivos à Investigação e Desenvolvimento Tecnológico (CENTRO-07-ST24-FEDER-002007, project 'Radiation for Life').

The authors would like to acknowledge the team of IBA, namely S. Henrotin, G. Janssens, D. Prieels, F. Roellinghoff, J. Smeets, and F. Stichelbaut, as well as E. Clementel (iMagX Project, Université Catholique de Louvain), for assisting the measurements. The authors would also like to acknowledge Philips Digital Photon Counting, in particular C. Degenhardt, Y. Haemisch, R. Schulze and B. Zwaans, for the fruitful discussions and help with the hardware and software implementations that made the synchronized measurements possible. Our thanks to the IBA team at WPE, in particular A. Varga Sampedro and P. Vidal Caravaca, for their precious support, to J. Koning, K. Langelaan and W. van Goozen (DEMO, TU Delft) for the technical support with the measurement setup, and to the team of the high-performance computing Milipeia cluster (University of Coimbra). Finally, our thanks to S. Seifert, G. Borghi, and V. Tabacchini (TU Delft) for the fruitful discussions, and to M. Sarilar (INAA lab., TU Delft) for preparing the Na-24 radioactive source.

Chapter 6

Simulation of proton range monitoring in an anthropomorphic phantom using multi-slat collimators and time-of-flight detection of prompt-gamma quanta[1]

Prompt-gamma (PG) imaging has the potential for monitoring proton therapy delivery in real time. Different approaches are currently being investigated. In this work, we focus on developing multi-slat collimators to image PG quanta, aiming at optimizing collimator performance and sensitivity to deviations in treatment delivery. We first defined a number of multi-slat configurations by constraining either their resolution or their efficiency and optimizing the other, at various distances from the proton pencil-beam central axis. We then used Geant4 to simulate irradiations of the head (proton energy: 130 MeV) and pelvis (200 MeV) of the NCAT anthropomorphic phantom, with and without physiologic/morphologic or setup changes of clinical dosimetric relevance. The particles escaping the phantom were transported through each of these multi-slat configurations and the gamma count rate profiles were recorded at the collimator exit. Median filtering was applied to the registered PG profiles to mitigate the effects of septa shadowing and statistical fluctuations. Time-of-flight discrimination was used to enhance the signal-to-background ratio, which appeared crucial for the 200 MeV irradiations. The correlation between the obtained PG and depth-dose profiles enabled visual detection of the artificially introduced changes. Moreover, 2 mm proton range shifts could be detected in the head irradiation case using a simple linear regression fit to the falloff of the PG profile. The influence of changes in complex, patient-like dose distributions on the PG profiles post-collimation is first studied in this work, which further gives insight on multi-slat collimator design optimization and highlights its potential and simplicity for detecting proton treatment deviations.

[1]Part of this chapter is addressed in: P. Cambraia Lopes, M. Pinto, H. Simões, A. K. Biegun, P. Dendooven, D. C. Oxley, K. Parodi, D. R. Schaart and P. Crespo, "Optimization of collimator designs for real-time proton range verification by measuring prompt gamma rays", 2012 IEEE Nucl. Sci. Symp. and Med. Imag. Conf., Conference record, 3864-70, 2012. Part of this chapter is in preparation for publication.

6.1 Introduction

Proton therapy is a form of radiotherapy (RT) that uses proton beams to destroy solid tumors. The potential of proton RT over conventional (photon) RT is that it can deliver a high dose to the tumor with less overall dose to healthy-tissues, a factor very important to reduce the side effects of irradiation. This high dose conformity is enabled by the fact that protons release a large amount of their energy in a highly localized region, the Bragg peak (BP), just before they stop (Wilson 1946). This makes proton therapy well suited for treating e.g., deep-seated and pediatric tumors.

Despite these physical advantages, treatment plans in proton therapy are often suboptimal in clinical practice due to the relatively large uncertainty in the particle range *in vivo* (Engelsman *et al* 2013). Particle range strongly depends on tissue composition, density, and heterogeneities. The main causes of range uncertainty are related to: (1) the conversion of X-ray computed tomography (CT) data to proton interaction data (Schaffner and Pedroni 1998); and (2) patient morphological/anatomical and/or physiological changes occurring during the course of the therapy. Such changes may include, e.g., edema of the irradiated region (Cameron *et al* 1969), tumor regression (Nishio *et al* 2006), and filling of empty cavities due to inflammation and increased tissue permeability.

Prompt-gamma (PG) imaging has been suggested for *in vivo* monitoring of proton therapy delivery, range verification in particular (Stichelbaut and Jongen 2003, Min *et al* 2006). This technique is based on the detection of gamma quanta originating from proton-nuclear interactions within the body, which are emitted promptly and can escape from the patient. Compared to PET imaging of 511 keV gamma rays resulting from positron-emission decay of proton-induced radioactive nuclides (Enghardt *et al* 2004, Crespo *et al* 2006, Parodi *et al* 2007b, Nishio *et al* 2006, 2010), PG imaging does not rely on delayed emission and therefore is unaffected by biological processes (e.g., activity washout). Moreover, it may provide real-time feedback on the treatment delivery, on a pencil-beam basis.

PG rays are single photons, therefore Compton cameras (Kang and Kim 2009, Richard *et al* 2011, Peterson *et al* 2010, Kormoll *et al* 2011), mechanically collimated cameras, PG spectroscopy (Verburg and Seco 2014), and timing spectroscopy (Golnik *et al* 2014) are currently being investigated to resolve spatial information. The scope of this work is mechanical collimation, which has the advantages of relative simplicity of implementation and compactness, as well as the possibility to provide complementary information beyond the particle range. Prompt-gamma profiles can be obtained by simple projection of the object onto the image plane, without Compton reconstruction. Moreover, full-energy deposition is not required, unlike in spectroscopy measurements where only few energy-resolved lines are usually targeted (Polf *et al* 2009b,2013, Verburg *et al* 2013, Verburg and Seco 2014).

Different types of collimators have been investigated, such as the multi-slat collimator (Min *et al* 2010, 2012, Gueth *et al* 2013), the pinhole collimator (Kim *et al* 2009b), and a one-dimensional pinhole denoted as knife-edge slit (Peloso *et al* 2011, Bom *et al* 2012, Smeets *et al* 2012b). In pencil-beam scanning (PBS), the lateral position of the proton pencil beam is well known already, so obtaining information on the dose distribution along the beam direction is more important. Multi-slat collimators are made of multiple plates ('slats') made of a high-density material such as tungsten. The slats are typically placed perpendicular to the pencil-beam direction, although tapered configurations can also be used (Testa *et al* 2009).

Previous studies have shown that collimated PG profiles correlate well with the distal dose falloff, both in simulation (Biegun *et al* 2012, Bom *et al* 2012) and experiment (Testa *et al* 2010, Peloso *et al* 2011, Bom *et al* 2012, Min *et al* 2012, Smeets *et al* 2012b, Roellinghoff *et al* 2014). Although the results are encouraging, these works are proof-of-

principle studies focused mostly on comparing collimated PG profiles to pristine Bragg peak distributions in homogeneous phantoms and/or phantoms with simple artificial inserts of different materials.

The potential of multi-slat PG imaging can also be inferred to some extent from PG measurements using a single collimated detector scanned parallel to the beam axis (Testa *et al* 2010, Roellinghoff *et al* 2014, chapter 5). However, these studies give little insight into the signal-to-background ratio in a full-scale system. In conclusion, there is still little knowledge on the optimal properties of a multi-slat collimator for PG imaging. Min *et al* (2012) took a first step towards optimizing a multi-slat collimator based on Monte Carlo simulations, but considered a fixed distance between the phantom and the collimator only and did not apply time-of-flight (TOF) discrimination of neutron-induced background counts.

In this work, we focus on developing (parallel) multi-slat collimators that accept photons emitted at right angles from the beam axis, for proton therapy verification on a per-pencil-beam basis. Our goal is to optimize the collimator for detecting deviations from the treatment plan due to small errors, uncertainties, or unplanned changes in the patient and/or environment, which are likely to occur in clinical practice and may affect the treatment outcome.

As a first step, we perform a simple analytical study to define a set of multi-slat configurations for further study. Subsequently, Geant4 Monte Carlo simulations of the selected multi-slat configurations are performed, registering the PG profiles obtained upon proton pencil-beam irradiation of an NCAT (NURBS-based cardiac-torso) anthropomorphic phantom (Segars 2001). Several treatment-like case studies are performed: two head irradiations and one prostate case. In each study, simulations of the planned treatment and a compromised one are compared. In the latter case, we artificially introduced morphologic/physiologic or set-up changes in the simulation, leading to clinically relevant changes in the depth-dose profiles. The simulated PG profiles are analyzed to determine which collimator performs best. Furthermore, the influence of simple signal-processing options such as TOF discrimination, energy selection, and median filtering are studied. The detector system was not simulated on purpose, in order to give emphasis on the effect of the collimator itself, without compromising the different results that would be obtained by choosing one or other type of detector.

6.2 Methods

In the following section we describe how the multi-slat configurations for further study were selected. Section 6.2.2 subsequently describes the Monte Carlo simulation framework, section 6.2.3 the NCAT case studies, and section 6.2.4 the post-processing of the simulation data.

6.2.1 Definition of multi-slat collimator configurations

We first determined the optimum slat height, slat thickness, and slit aperture for a multi-slat collimator at different distances from the beam axis, by optimizing one performance parameter (either resolution or efficiency), while constraining the other one to that of a knife-edge slit collimator described by Bom *et al* (2012). These authors simulated a knife-edge slit with a slit aperture of 3 mm, a height of 8 cm, and a full opening angle of 30°, placed with its front-surface at a distance of 12 cm from the beam-axis in a head irradiation case, yielding a magnification factor of -4. Here we additionally study larger distances between

the otherwise equal collimator and the beam axis, which are required in the irradiation of other body sites such as the prostate.

The multi-slat parameters were derived at each distance based on simple geometric considerations. The resolution and efficiency were computed in the plane defined by the beam axis and the normal to the detector plane, as the spatial discrimination of the signal is performed in the direction of the beam axis only, whereas the signal is integrated in the beam-azimuthal planes along the length of the slit(s). Although the geometrical formulas used in principle apply to ideal collimators, i.e. they ignore septal penetration (Appendix), we used effective collimator heights (l_{eff}) and slit diameters (d_{eff}), calculated based on the linear attenuation coefficient $\mu = 7.9\times10^{-2}$ mm^{-1} of 5 MeV photons in tungsten (Hubbell and Seltzer 2004).

The resolution of the multi-slat collimator, in the beam axis direction, is equivalent to that of a parallel-hole collimator. Similar reasoning applies to the knife-edge slit and a pinhole collimator. The respective *effective point resolutions*, R_{eff}, of these collimators at the beam axis can therefore be written as follows (Cherry *et al* 2003):

$$R_{eff}^{multi-slat} \approx d \cdot \left(l_{eff}+b\right)/l_{eff}, \quad l_{eff} = l - 2/\mu \tag{6.1}$$

$$R_{eff}^{knife-edge\ slit} \approx d_{eff} \cdot \left(l'+b'\right)/l', \quad d_{eff} = \sqrt{d \cdot [d + 2\mu^{-1} tan(\varphi/2)]} \tag{6.2}$$

In equation (6.1), l is the slat height, d the slit aperture in the beam direction, and b the distance between the beam axis and the front surface of the multi-slat collimator. In equation (6.2), φ is the knife-edge full-opening angle, l' the distance from the slit-aperture to the detector, d the width of the slit aperture, and b' the distance from the slit-aperture to the beam-axis. Thus the magnification factor of the knife-edge slit collimator equals $M = -l'/b'$. $R_{eff}^{knife-edge\ slit}$ was calculated at the center of the FOV.

We now define the *effective 2D efficiencies*, g_{eff}, of the multi-slat collimator and the knife-edge slit collimator, respectively, as follows:

$$g_{eff}^{multi-slat} \approx d^2/\left[2\pi l_{eff} \cdot (d+t)\right], \quad t = [6d/\mu]/[l - (3/\mu)] \tag{6.3}$$

$$g_{eff}^{knife-edge\ slit} \approx d_{eff}/\left(2\pi b'\right) \tag{6.4}$$

where the slat thickness t is obtained assuming a penetration of 5% (Cherry *et al* 2003). The knife-edge slit efficiency was calculated for a point source in the center of the FOV, where it is maximum. The derivation of these equations is given in the Appendix, and the geometric parameters of the collimators are represented in figure 6.18.

Using equations (6.1) – (6.4), the multi-slat parameters for further study were selected as follows. First, for a given beam-to-collimator distance b, the 2D efficiency of the multi-slat collimator was set equal to that of the knife-edge slit ($g_{eff}^{multi-slat} = g_{eff}^{knife-edge\ slit}$). The resolution $R_{eff}^{multi-slat}$, the slat thickness t, and the slit aperture size d, can therefore all be calculated as a function of the slat height l, using equations (6.1) and (6.3). The parameter l was varied in steps of 2 cm. The value of l that resulted in the best resolution was selected, and the corresponding t and d values were derived. This procedure was performed for b = 15 cm, 25 cm, and 35 cm. In a similar way, the multi-slat parameters that maximize the multi-slat efficiency $g_{eff}^{multi-slat}$, given that $R_{eff}^{multi-slat} = R_{eff}^{knife-edge\ slit}$, were calculated at the same values of b (Cambraia Lopes *et al* 2012).

The resulting six sets of multi-slat parameters are listed in table 6.1. The values of

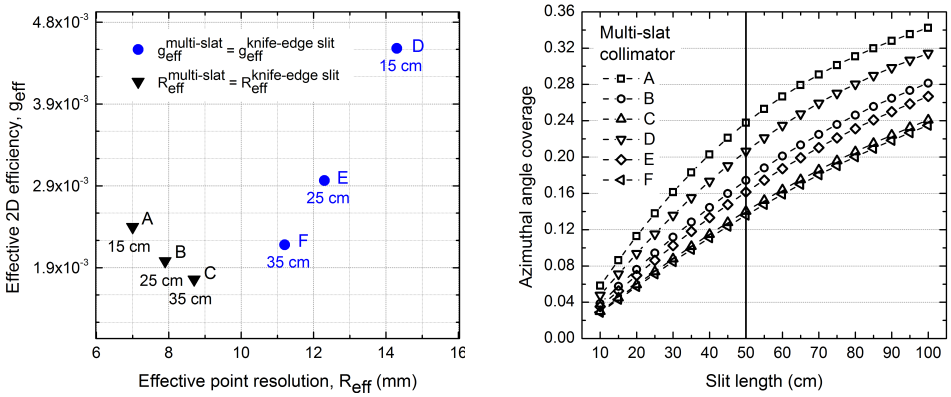

Figure 6.1: Left: Effective point resolution and 2D efficiency of the multi-slat collimators investigated. Right: (Beam-)Azimuthal angular coverage as a function of slit length. The slit length used in the simulations was 50 cm (figure 6.2), as indicated by the vertical line (right). The different multi-slat collimators either have equal resolution (A-C) or efficiency (D-F) to the knife-edge slit collimator from Bom *et al* (2012), placed at the same source-to-collimator distance as the multi-slat collimators (specified in cm, left).

b used are compatible with typical treatment scenarios. The corresponding performance characteristics, calculated using equations (6.1) and (6.3), as well as their azimuthal angle coverage, are shown in figure 6.1.

For completion it is noted that we did not consider the use of shifted multi-slats, which we have previously suggested to reduce the effect of septa shadowing (Cambraia Lopes *et al* 2012). That approach was found to be unpractical, since: (1) if an overlap septum is not added in the cleavage plane of the collimator, blurring occurs due to the crossing of oblique photons; (2) the overlap septum, however, reduces the azimuthal angle coverage; and (3) this coverage depends considerably on the beam spot position along the slit direction, for a static collimator.

6.2.2 Geant4 simulations

Monte Carlo (MC) simulations were performed using the Geant4 toolkit (Agostinelli *et al* 2003, Allison *et al* 2006). The simulations were done in two steps, to reduce computation time. First, the low-energy electromagnetic physics package QGSP_BERT_HP of Geant4, version 9.3, was used to simulate the irradiation of an anthropomorphic phantom by a proton pencil-beam. The range cuts were set to 700 μm for all particles. The absorbed dose in the phantom was stored in a cubic-millimeter grid covering the irradiated region. Furthermore, the properties of the particles escaping the phantom and crossing a surface fully containing the collimator field-of-view were registered in a phase-space file. The scored properties included the particle type, position, momentum, energy, and arrival time relative to the time of creation of the primary proton.

In a second step, the low-energy electromagnetic physics package QGSP_BERT_HP of Geant4 version 9.4 was used to simulate the propagation of the particles registered in the phase-space file through the collimator and towards an ideal flat-panel detector, located 1

Table 6.1: Characteristics of the multi-slat collimators used in Monte Carlo simulations. The weight was calculated for a pelvic collimator with length of 40 cm in the direction of the beam axis and a slit length of 50 cm (according to figure 6.2-right). The collimator weight for the case of a head irradiation equals half the value given here. The geometric parameters *b, l, d,* and *t* are illustrated in figure 6.18-left.

Multi-slat collimator	Collimator front-surface to beam distance, *b* (cm)	Collimator height, *l* (cm)	Slit aperture diameter, *d* (mm)	Slat/septa thickness, *t* (mm)	Weight (kg)
A	15	12	2.7	2.5	226
B	25	16	2.8	1.7	237
C	35	18	2.7	1.4	240
D	15	18	7.3	3.9	251
E	25	20	5.1	2.4	250
F	35	20	3.8	1.8	251

mm behind collimator exit. In this way, the phase-space file from each irradiation case-study could be used to test multiple collimator geometries. Only particles escaping the phantom with a momentum higher than 100 eV/c were considered in these simulations, corresponding to a kinetic energy of 100 eV for gammas and 5.34×10^{-6} eV for neutrons. The range cuts were set for all particles to 1 μm.

The particle type, position, momentum, energy, and time-of-flight were registered for each particle that hit the detector, post collimation. In addition, Compton scattering and the existence of a 'parent' particle (i.e. the detected particle is not the same as the one registered in the phase-space file) were tagged and stored for each particle detected. This information allowed distinguishing 'background' and 'direct' events, where direct events pertain to quanta that did not interact in the collimator. The time stamp (time-of-flight) of a detected particle was defined as the time difference between the launch of the proton and the arrival of the particle at the detector.

The anthropomorphic phantom was the NCAT phantom from Segars (2001), which was previously implemented in Geant4 using 4.68 mm cubic voxels (Crespo *et al* 2012). The incident proton energies were 130 MeV for the head irradiations and 200 MeV for the pelvis irradiation (no momentum spread). A single pencil-beam with a total of 10^8 protons was simulated in each case study, which is representative of the most distal pencil-beam in a typical treatment plan (Smeets *et al* 2012b). The pencil-beam had a lateral full-width-at-half-maximum (FWHM) of 9 mm, which is representative for presently-used PBS systems (Schwaab *et al* 2011, Parodi *et al* 2012).

The case studies were implemented as depicted in figure 6.2. The collimators were made of tungsten (density of 19.3 g cm^{-3}). The slit length was set to 50 cm. The total size of the collimator in the beam direction was 20 cm for the head irradiations and 40 cm for the pelvis case, so as to completely cover the irradiated region. The detector surface and collimator front- and back-surfaces were parallel to the phantom-axial plane behind the NCAT-head (figure 6.2-left), or to the phantom-coronal plane above the NCAT-phantom pelvis (figure 6.2-right), respectively.

The collimators listed in table 6.1 were used for the head irradiations. For the prostate case, only the collimators at distances of b = 25 cm and b = 35 cm were simulated. Additional simulations were performed with the collimator closed, to obtain a rough estimate (section 6.3.3) of the background level. The 'closed collimator' was implemented as a solid

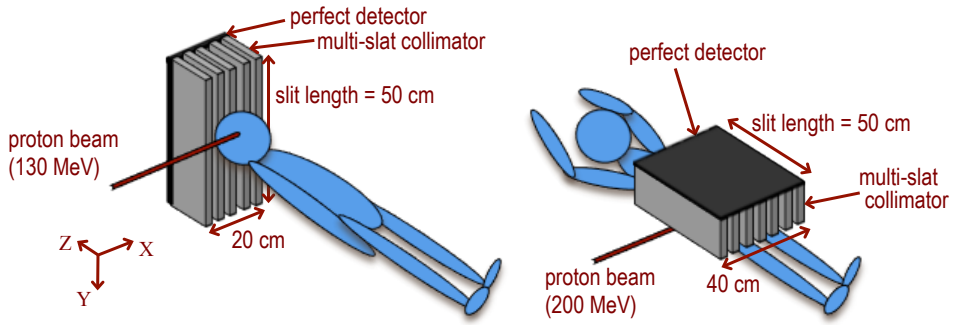

Figure 6.2: Schematic view (not to scale) of the simulation setups used for irradiation of the head (left) and pelvis (right). The perfect flat-panel detector was located 1 mm behind the collimator, and its dimension in the direction perpendicular to the beam axis was set fixed to 50 cm, as did the slit length.

tungsten block having the same outer dimensions as the corresponding multi-slat configuration.

To compare the secondary particle spectra obtained with the NCAT phantom to those obtained with a PMMA phantom, we additionally simulated a solid PMMA cylinder (20 cm diameter and 30 cm length; chemical composition $C_5H_8O_2$; density 1.18 g cm^{-3}) irradiated by a 200 MeV proton pencil beam.

Various studies have shown considerable overestimation of prompt gamma emission yields by Geant4, up to its version release 9.6, in comparison to other simulation codes (Biegun *et al* 2012, Verburg *et al* 2012, Robert *et al* 2013, Dedes *et al* 2014, Janssen *et al* 2014). Therefore, similar to a previous work (Biegun *et al* 2012), we adopted a conservative approach in which only 25% of the total gammas escaping the NCAT phantom are tracked through the collimator, thus affecting the post-collimation simulation results only (section 6.3.3 and thereafter). The gamma reduction factor of 4 thus applied followed from a comparison of the total gamma yields exiting a PMMA target (15 cm diameter and 20 cm length) obtained with our code, to that obtained by Smeets *et al* (2012b) with MCNPX 2.5, under the same circumstances: proton energy equal to 160 MeV, perfect detection system, and no modeling of the room geometry. The average ratios of the gamma (1 MeV to 10 MeV) and neutron (1 MeV to 160 MeV) counts found between Geant4 and MCNPX were 3.7 and 0.95, respectively.

6.2.3 Case studies

Three case studies were investigated: two head irradiations and one pelvis case. In each study, a reference ('planned') irradiation was compared to compromised irradiation(s), in which a phantom tissue property or set-up property was changed in a way that represents possible clinical inter-fractional changes with respect to the original treatment plan.

The first case study featured the irradiation of a head tumor located in the region of the sphenoid bone. A side irradiation was simulated with a horizontal (X-direction in figure 6.2-left) pencil beam, which enters the temple of the head, crosses the nasal cavity, and stops at the sphenoid bone part on the cavity wall. In the planned irradiation, the nasal cavity was empty. In the compromised case, the nasal cavity was filled with water tissue (density

1.02 g cm^{-3}). The compromised case could represent inter-fraction morphologic/physiologic changes such as the presence of mucus in response to a cold, edema or tissue swelling in response to irradiation injury, or tumor growth.

The second case study consisted of another irradiation of the head, aiming at the pituitary gland. A horizontal pencil beam also entered the head laterally (X-direction in figure 6.2-left), but posterior to the first case, towards the *sella turcica*, a depression in the sphenoid bone that houses the pituitary gland. The difference between the compromised irradiations and the planned one is in the density of the brain tissue traversed by the protons between the skull and the *sella turcica*, which in the planned case corresponds to $\rho = 1.040$ g cm^{-3} (figure 6.12). The brain density was changed to $\rho^* = \rho \cdot (1+4\%)$, for the 'over-dense' case and to $\rho^* = \rho \cdot (1-4\%)$, for the 'hypo-dense' case. These changes represent possible responses to radiation injury: the hypo-dense case could result from vascular permeability and edema formation, while the hyper-dense scenario could arise from local protein congregation, in an attempt to form scar tissue (Denham and Hauer-Jensen 2002).

The third case study concerned the irradiation of a prostate tumor. The beam is horizontal and laterally incident (X-direction in figure 6.2-right); the protons cross three pelvic bone structures before reaching the prostate. The proton energy required for this irradiation is among the highest used in clinical practice, thus constituting a worst-case scenario in terms of signal-to-background ratio (Biegun *et al* 2012). The compromised irradiation was implemented by shifting the phantom 1 cm in the ventral (-Y) direction. Such a misalignment could e.g., result from a positioning/setup error or patient weight change.

6.2.4 Post-processing of simulated data

Post-processing of the simulated data included time-of-flight and low-energy discrimination for background rejection. TOF selection was based on a shifting TOF acceptance window, with 1 ns width and centered on the prompt-gamma peak, following the method described in (Biegun *et al* 2012).

Subsequently, a median filter was applied to the registered gamma profiles to mitigate the periodic oscillations caused by the septa shadows, due to the proximity (1 mm) between the detector panel and the collimator back surface. Median filtering was implemented such that the median value of all data points lying within a given kernel width (span) was assigned to the point at the center of the kernel. In general, filtering the gamma profiles with a span covering at least two times the collimator pitch (i.e. the slit aperture plus slat thickness) was sufficient. However, for the profiles with the highest statistical fluctuations, a span of about four times the collimator pitch gave better results. In all cases, the span was kept as low as possible to avoid unnecessary degradation of resolution.

It is noted that the simulated PG-profiles are all represented in this work with a bin width of 2 mm, which is smaller than the slit apertures. In practice, this could be achieved by using segmented crystal arrays/slabs with a 2 mm pitch or by using a continuous detector with lateral position resolution of 2 mm.

6.3 Results and discussion

6.3.1 Multi-slat collimator configurations

Table 6.1 lists the geometry parameters of the multi-slat configurations studied in this work, derived as described in section 6.2.1. As can be seen from figure 6.1-left, the multi-slat collimator cannot have at the same time equally good geometrical efficiency and resolution

as the reference knife-edge slit at the beam-to-collimator distances b investigated in this work. If we set the resolution of the multi-slat equal to that of the reference knife-edge slit, the multi-slat efficiency was lower by a factor of 0.53, 0.68, and 0.81, for b = 15 cm (multi-slat A), 25 cm (B), and 35 cm (C), respectively. If, on the other hand, the geometric efficiency of the multi-slat is set equal to that of the knife-edge slit, the multi-slat resolution was worse by a factor of 2.0, 1.6, and 1.3 at b = 15 cm (multi-slat D), 25 cm (E), and 35 cm (F), respectively.

The geometric resolution and efficiency of the two collimators tend to converge as b increases. In particular, the overall geometric performance of the knife-edge slit worsens with increasing b. The performance of multi-slats A, B, and C also degrades with increasing b. For multi-slats D, E, and F, an increase in b decreases the efficiency but improves the resolution.

Figure 6.1-right, shows the (beam-)azimuthal angle coverage of the flat-panel detector for each multi-slat configuration, as a function of the slit length. The angular coverage hardly saturates for slit lengths up to 50 cm, which is considered a reasonable value for clinical application and thus is used in the remainder of this work.

It is to be noted that the performance of a collimator does not only depend on its geometric performance but also on factors such as the signal-to-background ratio. This ratio depends on the type and energy of radiation the collimator is exposed to, the energy acceptance window, the distance to the object, and collimator-specific parameters such as its size and geometry. In this regard, the knife-edge slit and the multi-slat are intrinsically different. In addition, the geometric performance of a knife-edge slit is optimal at the center of the FOV but degrades away from the center, whereas the geometric performance of a multi-slat collimator is constant throughout its FOV.

Interestingly, the two main knife-edge slit collimators that to our knowledge have been proposed to date have rather different geometric performances. Whereas Bom *et al* (2012) proposed a knife-edge slit with a relatively high resolution of 6.8 mm and an efficiency of 5.4×10^{-3}, Smeets *et al* (2012b) proposed a knife-edge slit concept with relatively high efficiency of 11.2×10^{-3} and a resolution of 21.2 mm (all values calculated with equations (6.2) and (6.4)). Nevertheless, the beam-to-collimator distances of both of these knife-edge slits are relatively small: 12 cm and 13 cm, respectively. This is advantageous in terms of geometric performance but results in a relatively small FOV (12.5 cm and 15 cm, respectively). Therefore, these collimators may need to be moved to remain aligned with the expected range of each layer of the treatment plan (Smeets *et al* 2012b). Unlike a knife-edge slit, the resolution of a multi-slat collimator does not affect the size of its FOV. Thus, a high-resolution multi-slat collimator may be advantageous to enable not only precise range monitoring, but also the detection of changes in the PG profile along the proton path.

Moreover, a small beam-to-collimator distance restricts the clinical applicability of the device. A distance of 12 cm - 13 cm between the collimator front-surface and the beam axis could be considered mainly appropriate for head irradiations. For e.g., pelvis or thorax irradiations, the minimum achievable value of b may be considerably higher, especially in situations where oblique beam incidence is preferable. For this reason, we investigated beam-to-collimator distances of up to 35 cm.

6.3.2 NCAT and PMMA escaping energy spectra

The energy spectra of photons and neutrons escaping the NCAT phantom upon irradiation with 200 MeV protons (pelvis irradiation) are shown in figure 6.3, together with those from the PMMA phantom for the same proton energy. The blue curves depict the spectra of photons with a momentum nearly perpendicular to the beam axis, i.e. within an acceptance

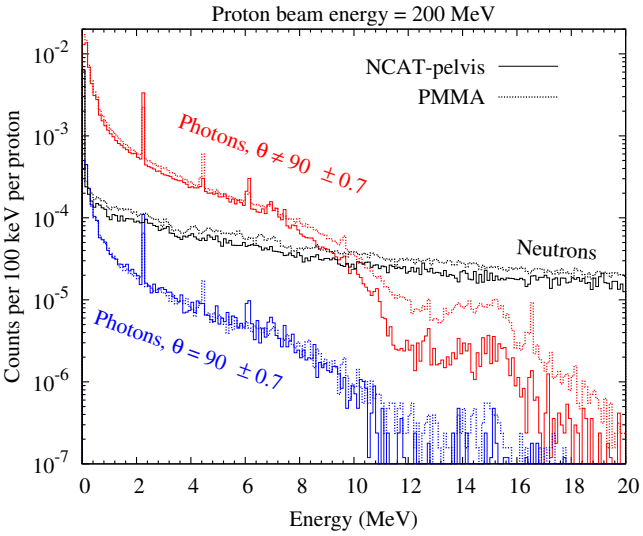

Figure 6.3: Comparison between simulated photon and neutron energy spectra escaping a cylindrical PMMA phantom (20 cm diameter and 30 cm length in the beam direction) and the NCAT phantom, upon irradiation with 200 MeV protons. The particle yields were registered in an ideal 50 cm × 50 cm planar detector positioned at 30 cm from the beam axis, in the -Y direction (figure 6.2) for the NCAT case. The detector surface is centered with the beam in the direction perpendicular to the beam axis, and is contained in the beam direction within the beam entrance point in the phantom, and a point 50 cm distal to it. Photons were discriminated according to their angle of incidence θ relative to the beam axis. The photons with a momentum nearly perpendicular to the beam axis ($\theta = 90°\pm0.7°$) are denoted as correlated photons, whereas the remaining photons ($\theta \neq 90°\pm0.7°$) can be interpreted as a measure of the uncorrelated (background) signal, as they hit the detector from arbitrary directions.

angle of 90°±0.7°. These photons hereafter are denominated as correlated photons. The remaining photons (red) can be interpreted as a measure of the uncorrelated (background) signal, as they hit the detector from arbitrary directions.

The PMMA and NCAT PG spectra show some differences. In particular, the oxygen lines show higher expression in the NCAT emission spectra compared to PMMA: the 6.92 MeV and 7.12 MeV lines are noticeable only in the NCAT spectra and the more intense line at 6.13 MeV has lower amplitude in the case of PMMA than NCAT. On the other hand, the 4.44 MeV line, which is mainly from carbon, is less visible for NCAT than for PMMA.

These differences are expected in view that the oxygen (O) and carbon (C) mass concentrations present in human tissues (Polf *et al* 2013) are different from those in PMMA. According to Polf *et al* (2013), the (background-subtracted) intensity of the 6.13 MeV line is expected to scale with the O concentration, while the intensity of the 4.44 MeV line depends on both C and O concentrations in the tissues, as it results from de-excitation of ^{12}C nuclei produced by both proton-carbon nuclei interactions and proton-oxygen nuclei interactions. In the present example of pelvis irradiation, about one half of the tissue traversed by the proton beam (~ 10 cm) is bone and the other half is soft tissue, the latter being represented mostly by muscle (density 1.06 g cm^{-3}, 71.0% of O by mass, 14.3% of C by mass). The three connecting bones irradiated (figure 6.14) are composed by a dense outer shell

(density 1.58 g cm^{-3}, 43.4% of O by mass, 23.5% of C by mass) and an inner trabecular part (bone marrow - density 1.16 g cm^{-3}, 36.7% of O by mass, 40.4% of C by mass). As a result, the oxygen mass concentrations in muscle, dense-bone tissue and bone marrow are a factor of 2.0, 1.81, and 1.13 higher than in PMMA, respectively. Conversely, the oxygen + carbon mass concentration in PMMA is 1.20 times higher than in muscle, 1.03 times higher than in dense-bone tissue, and 1.21 times higher than in the bone marrow. Therefore, the higher intensity of emission lines is consistent with a higher concentration of the corresponding elemental nuclide(s), although the exact quantification of these differences is outside of the scope of the present work.

In general, the uncorrelated photon yields are lower for NCAT compared to PMMA, by 10%-20% below 8 MeV and 70%-90% above ~11 MeV, relative to the PMMA yield. The differences in the correlated photon yields between PMMA and NCAT are lower for energies below 7 MeV, compared to the uncorrelated ones, and above ~11 MeV the photon yields are negligible for NCAT. These differences may be due to the fact that the NCAT phantom is more massive than the PMMA phantom (about 40-50 times, in the present case). The uncorrelated photons traverse on average more material, therefore they are more likely to be attenuated or scattered away from the detector, in the case of a bigger phantom. Furthermore, the attenuation may increase for higher-energy photons due to the increased cross sections for pair production. Finally, the global neutron yield for PMMA is a factor of 1.3 higher than for the NCAT phantom (black curves).

Consistent with these results, Polf *et al* (2014) observed that the simulated total PG emission decrease with distance at a much faster rate in the vicinity of a patient, compared to a water phantom. Although it is out of the scope of the current work to further address the differences between PMMA and NCAT, these results seem to suggest that experiments and simulations performed with small phantoms may overestimate the amount of background/uncorrelated events, in the presence of a collimator especially, which will also act as a scattering and attenuating object.

6.3.3 Energy and time spectra post-collimation: photon signal-to-background ratio

The simulated energy (top) and time (bottom) spectra of events scored at the perfect detector located just behind multi-slat E are shown in figure 6.4, for the NCAT head (left) and pelvis (right) irradiations. Photons that have interacted and/or were created in the collimator are denoted as 'background.' Otherwise, they are denoted as 'direct'. The time spectra (bottom) show that the direct photons arrive at the detector earlier than the neutrons, as expected due to that neutrons have mass. Since the time spectra were integrated over the entire detector area, the range of direct-photon time-of-flights is determined by the time needed by the protons to slow down inside the phantom, which is larger for 200 MeV protons than for 130 MeV protons. For this reason, there is a larger overlap between the direct-photon and neutron time spectra in the pelvis irradiation case.

The time spectra of the background photons (red curves in figure 6.4-bottom) exhibit a local maximum within the same time region as the direct photons (i.e. between about 2 ns and 4 ns). These background counts are attributed to secondary photons resulting from Compton interactions and/or electromagnetic cascades ('showers') initiated by the prompt gammas in the collimator material. The remaining background photons have a distribution of arrival times similar to that of the neutrons. These non-prompt background counts therefore are attributed to photons that are created in the collimator by neutron interactions.

In figure 6.4-bottom, it can be seen that the direct-photon yield is a factor of about 2 higher for the pelvis irradiation than for the head case. However, the neutron yield of the

200 MeV proton beam (pelvis) is about an order of magnitude higher than that of the 130 MeV proton beam (head). Since the neutron-induced background gamma yield is directly proportional to the neutron yield, this implies that the signal-to-background ratio will be considerably worse in irradiations of deep-seated tumors.

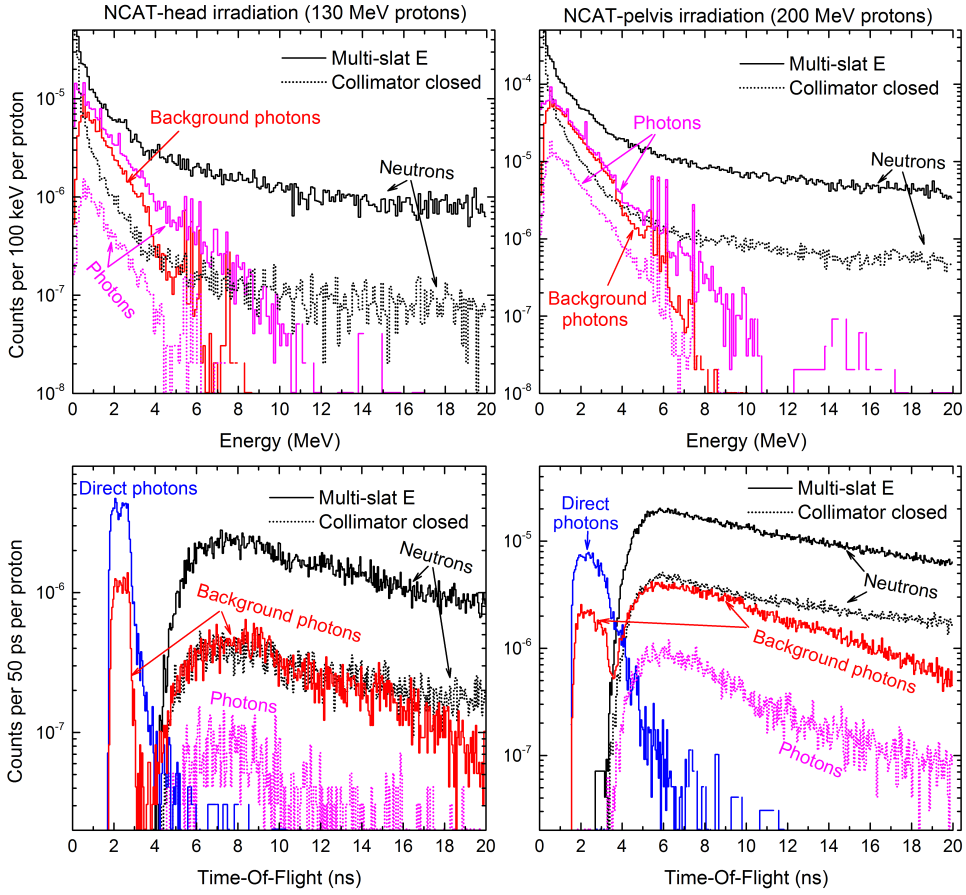

Figure 6.4: Simulated energy spectra (top) and time spectra (bottom) of photons and neutrons after passing through a multi-slat collimator or a tungsten block ('collimator closed') for proton irradiations of the NCAT-head (left) and -pelvis (right). Time-of-flight values are defined as the time difference between the creation of the proton and the arrival of a particle at the detector. Photons were assigned as 'background' if they interacted and/or were created in the collimator; otherwise, photons were assigned as 'direct'.

Peloso *et al* (2011) and Smeets *et al* (2012b) proposed to improve the signal-to-background ratio in their knife-edge slit experiments by subtracting a background profile measured with a closed collimator. The dashed curves in figure 6.4 represent the results obtained with this approach for multi-slat collimator E. The closed-collimator neutron and photon time and energy spectra appear similar in shape to the corresponding neutron (or background-photon) curves for the actual multi-slat collimator. However, the yields of both types of particle are

considerably lower. In contrast with a knife-edge slit collimator, the 'closed' equivalent of a multi-slat collimator constitutes a solid tungsten block with about 2-3 times more mass than the actual collimator. The majority of counts therefore is expected to arise from neutron interactions in the tungsten region nearby the detector. As a result, the closed-collimator signal does not accurately resemble the background signal of the multi-slat collimator. Different background suppression methods therefore are investigated in this work.

The energy spectra in figure 6.4-top indicate that some improvement of the signal-to-background ratio could be expected from the application of a low-energy threshold. The time spectra (bottom) indicate that further improvement should be possible by accepting counts within the time window in which the direct photons are detected only. Indeed, it has been shown that such time-of-flight background rejection can be quite effective if the uncertainty in the proton arrival time (i.e. proton bunch width) is of the order of a nanosecond (Testa *et al* 2009, Testa *et al* 2010, Biegun *et al* 2012, Verburg *et al* 2013, Roellinghoff *et al* 2014, Cambraia Lopes *et al* 2015).

To investigate these options in more detail, we assume that the detector behind the collimator can be made essentially insensitive to neutrons (e.g., by using a scintillator with low neutron cross section). We then investigate the ratio of direct-to-background photon counts, or photon signal-to-background ratio, S_γ/B_γ, for various combinations of low-energy cut and TOF acceptance window. The results are shown in figure 6.5 for irradiations of the brain and the prostate. It is noted that phantom scatter is not discriminated from either signal or background since only interactions in the collimator were tracked.

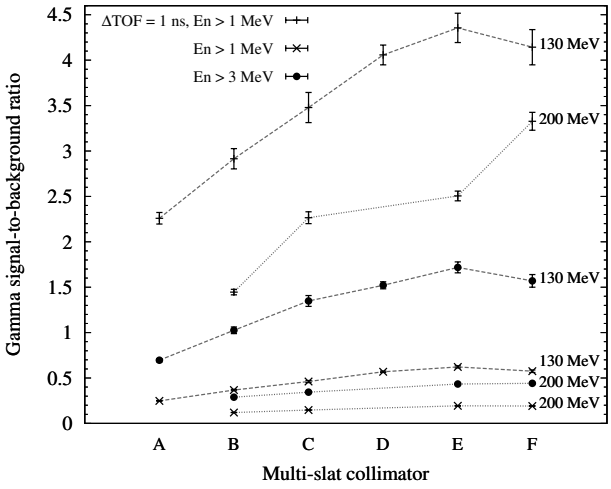

Figure 6.5: Gamma signal-to-background ratios simulated for different energy (En) discriminations and for energy and TOF discrimination, for each of the multi-slat collimators studied (A - F), and for different proton energies: 130 MeV protons (brain irradiation) and 200 MeV (prostate irradiation). The signal is defined as the number of prompt gammas that are detected without interacting in the collimator. The background represents the remaining number of gammas detected. The lines are present to aid visualization.

For all multi-slat configurations, S_γ/B_γ improves if the low-energy threshold is increased from 1 MeV to 3 MeV, namely by a factor of 2.7-2.9 for the 130 MeV proton beam and by a factor of 2.2-2.4 for the 200 MeV beam. Moreover, S_γ/B_γ increases by an order

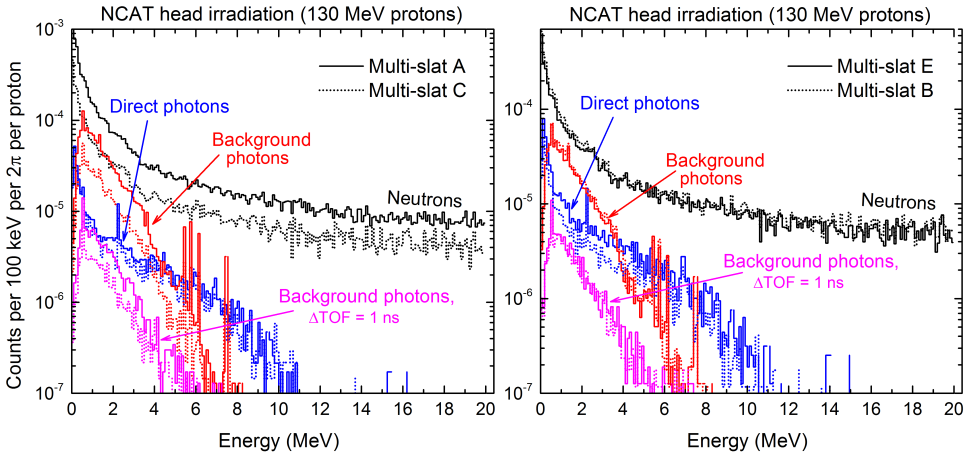

Figure 6.6: Comparison of simulated energy spectra of photons and neutrons emitted by the NCAT-phantom head after passing through multi-slat collimators A and C (left) and B and E (right). Photons were assigned as 'background' if they interacted and/or were created in the collimator; otherwise, photons were assigned as 'direct'. Background photon yields with and without TOF rejection are shown. For comparison purposes, the counts were normalized with respect to the beam-azimuthal angle of the collimators.

of magnitude if TOF discrimination is applied in combination with a low-energy threshold of 1 MeV, compared to a 1 MeV energy threshold only. Specifically, TOF discrimination improves S_γ/B_γ by a factor of 7-9 for 130 MeV protons and by a factor of 12-17 for 200 MeV protons. These results clearly favor the use of TOF discrimination in prompt-gamma imaging with multi-slat collimators.

We furthermore observe that the S_γ/B_γ increases from multi-slat configuration A up to E, regardless of the energy and TOF selection criteria applied. Multi-slat F has better S_γ/B_γ than multi-slat E for the case of prostate irradiation with energy and TOF discrimination, while the results are similar to those of multi-slat E in the other cases. Figure 6.1-left shows that the efficiency of multi-slat A is better than that of B, which in turn is better than that of C. The fact that the S_γ/B_γ improves in the opposite direction is attributed to the increasing distance to the beam, which results in a decreasing exposure of the collimator to neutrons and non-perpendicularly incident photons.

This is confirmed by figure 6.6-left, which shows the energy spectra of multi-slat collimators A and C. All particle yields are higher for multi-slat A than for C. However, the difference in background (and neutron) levels is higher than the difference in direct-photons counts, even when TOF discrimination is applied, and therefore C has the best S_γ/B_γ. Similar arguments apply for comparing multi-slats D, E, and F: the relative decrease in direct-photon counts as a result of a decrease of efficiency from D to F (figure 6.1-left) is accompanied by a decrease in background due to a higher distance from the beam, therefore the S_γ/B_γ increases only slightly for multi-slat E.

Finally, when comparing multi-slat collimators with different geometric performances placed at the same distance from the beam, as exemplified in figure 6.6-right for multi-slats B and E, we observe that the background levels are comparable, regardless of their resolution/sensitivity, as they emanate from the collimator at arbitrary directions. However,

the higher efficiency of multi-slat E improves its S_γ/B_γ compared to B, by increasing the amount of direct photons, at the expense of resolution.

6.3.4 Correlation between dose and collimated PG profiles

In this section, the collimated gamma profiles simulated with the various multi-slat configurations are compared with each other, in regard to the corresponding dose distributions. For each of the three NCAT case studies, the PG profiles of a 'compromised' treatment scenario are compared with those of the 'planned' reference situation.

6.3.4.1 Irradiation of the sphenoid region: morphological changes

The 2D dose distributions resulting from the irradiations of the sphenoid region are presented in figure 6.7, superimposed on a CT axial-slice of the phantom head. We observe that the filling of the nasal cavity causes the pencil beam to stop 14 mm proximal with respect to the treatment plan, which was made for an empty nasal cavity. This under-range implies considerable underdosage in the tumor located in the sphenoid bone, with the distal part of the tumor not receiving any dose from this spot irradiation.

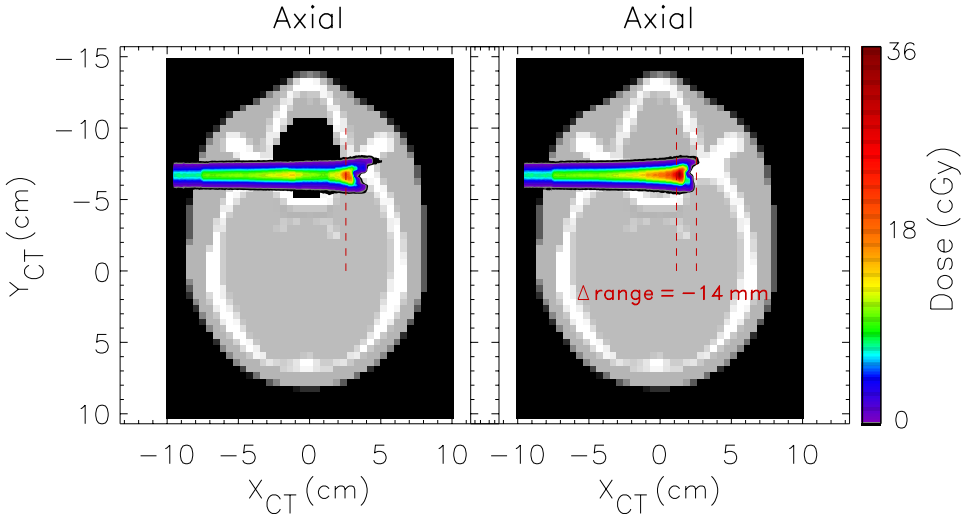

Figure 6.7: Dose distributions due to a 130 MeV proton pencil beam in the NCAT-head sphenoid region, superimposed on the corresponding CT axial slices (in gray scale). The proton range is reduced by 14 mm in the case of a filled nasal cavity (right) in comparison to the (planned) situation with an empty nasal cavity (left).

The collimated prompt gamma profiles obtained with a low-energy threshold of 3 MeV are shown in figures 6.8 and 6.9, whereas the ones obtained with a low-energy threshold of 1 MeV and TOF discrimination (ΔTOF = 1 ns) are presented in figures 6.10 and 6.11. To assist in visualization, the vertical dotted lines in these figures indicate the successive interfaces traversed by the protons in the 'empty nasal cavity' situation, i.e. soft-tissue/bone (X_{CT} = -5.1 cm), bone/nasal-cavity (X_{CT} = -1.6 cm), and nasal-cavity/bone (X_{CT} = 1.2 cm). Of course, these interfaces are not step-like but irregular across the beam diameter.

The longitudinal dose profiles are indicated by the red curves in figures 6.8-6.11. These profiles represent the integral of the 3D-dose distribution in the Y and Z directions for each X value (figure 6.2). The reference ('empty nasal cavity') BP position, defined as the position at which the dose has decreased to 80% of the maximum, is indicated by the dashed lines at X_{CT} = 2.55 cm.

If we look at the gamma profiles with discrimination by energy only (figures 6.8 and 6.9), we visually observe that the signal-to-background ratios increase from multi-slat A to E/F, in agreement with the analysis presented in section 6.3.3. Despite multi-slat A has the highest geometric resolution of all multi-slat collimators studied (figure 6.8), the ability to visually resolve the profile features is greatly hampered by the high background level. There are mainly two observables that corroborate that increase: the reduction in the closed-collimator counts, and the increase of the sharpness/contrast in the profile changes between the two irradiation scenarios. Such changes are especially apparent at (1) the patient entry point, (2) the BP position, and (3) the transitions between tissues with very different densities, in particular the boundaries of the air cavities and the bones, indicated by the dotted vertical lines.

The profiles obtained with simultaneous energy and TOF discrimination (figures 6.10 and 6.11) present better counting statistics than the ones with only energy discrimination, due to the lower energy threshold of 1 MeV that was possible to apply in the TOF-based profiles. More importantly, the addition of TOF discrimination considerably increases S_γ/B_γ and therefore enhances the correlation between the prompt gamma and depth-dose profiles. The profiles from multi-slat E and F in particular exhibit very sharp distal falloffs, which correspond to the depth-dose falloff within millimeter agreement. Furthermore, patient entry position and the boundaries of the air cavity are clearly visible in the 'empty nasal cavity' case.

The neutron-induced gamma background is negligible if TOF discrimination is applied, as indicated by the closed-collimator counts. Interestingly, the gamma profiles from multi-slat A present the air cavity less clearly compared to multi-slat E, while the overall number of counts are roughly the same and the geometric resolution of multi-slat A is considerably better. Similar 'resolution loss' is observed for multi-slat B. This finding indicates that the resolution of these collimators is compromised due to secondary gammas (e.g., scattering in the collimator material (section 6.3.3)), which is not rejected by TOF. Finally, the choice between collimator D, E, and F will ultimately depend on the number of counts obtained in practice, and is thus a compromise between resolution and efficiency.

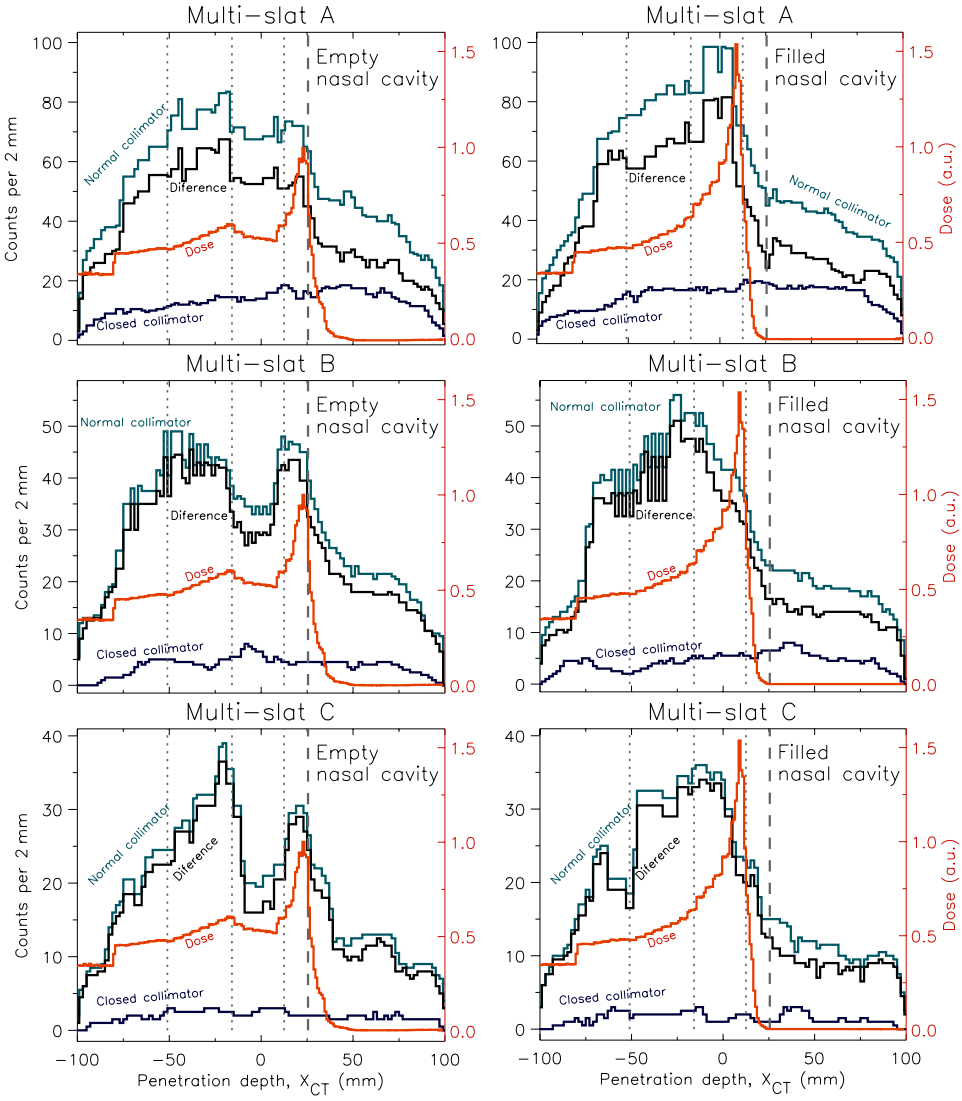

Figure 6.8: Collimated prompt gamma profiles simulated for the irradiation of the NCAT sphenoid region (figure 6.7) using multi-slat collimators A-C ('normal collimator'). Also shown are the laterally-integrated depth-dose profiles, the profiles from a closed collimator, and the 'normal collimator' profile after subtraction of the 'closed collimator' profile ('difference'). A low-energy threshold of 3 MeV was applied, together with a median filter with a span of 8, 10, or 8 bins, for multi-slat collimators A, B, and C, respectively (bin size = 2 mm). The vertical dashed lines correspond to the proton range in the planned, 'Empty nasal cavity' situation. The vertical dotted lines represent the soft-tissue/bone, bone/nasal-cavity, and nasal-cavity/bone interfaces traversed by the protons, from left to right, respectively.

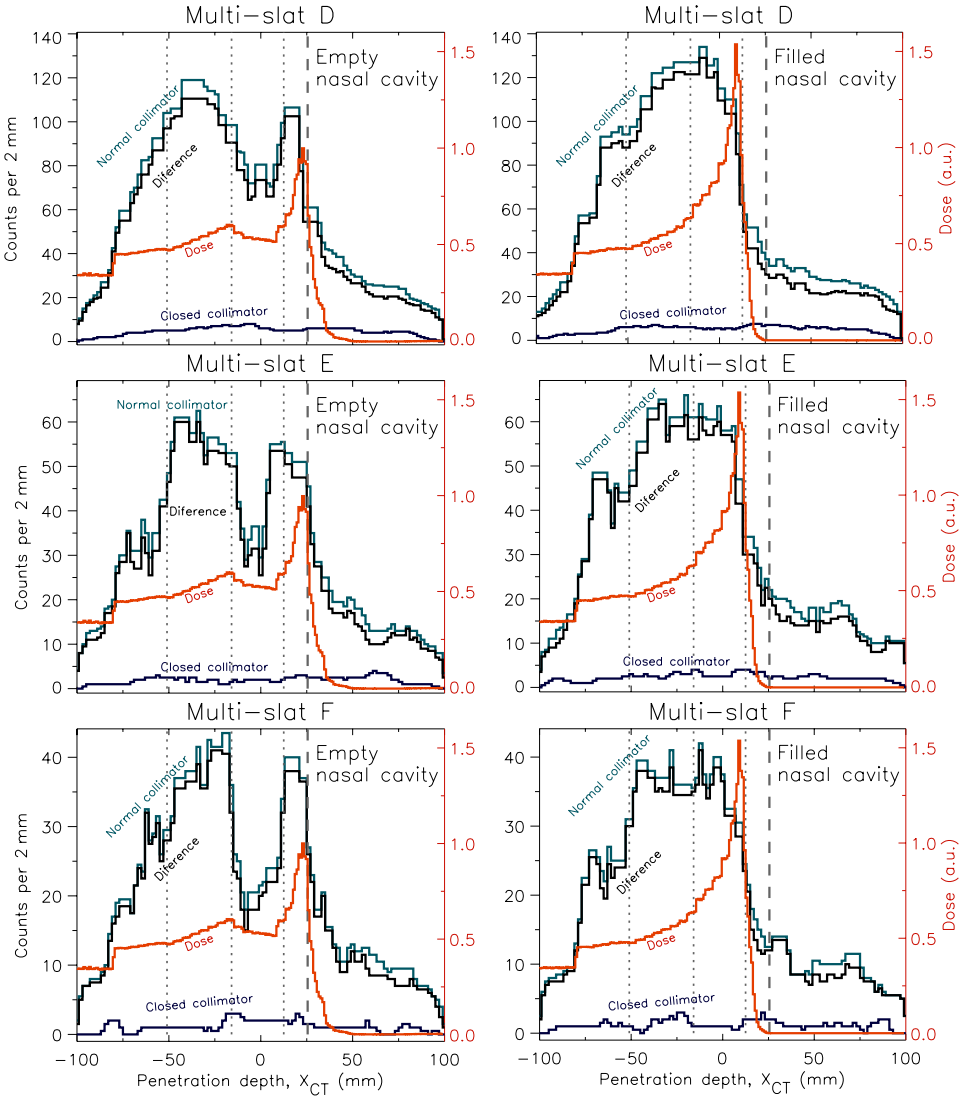

Figure 6.9: Collimated prompt gamma profiles simulated for the irradiation of the NCAT sphenoid region (figure 6.7), using the multi-slat collimators D-F ('normal collimator'). Also shown are the laterally-integrated depth-dose profiles, the profiles from a closed collimator, and the 'normal collimator' profile after subtraction of the 'closed collimator' profile ('difference'). A low-energy threshold of 3 MeV was applied, together with a median filter with a span of 12, 8, or 6 bins, for multi-slat collimators D, E, and F, respectively (bin size = 2 mm). The vertical dashed lines correspond to the proton range in the planned, 'Empty nasal cavity' situation. The vertical dotted lines represent the soft-tissue/bone, bone/nasal-cavity, and nasal-cavity/bone interfaces traversed by the protons, from left to right, respectively.

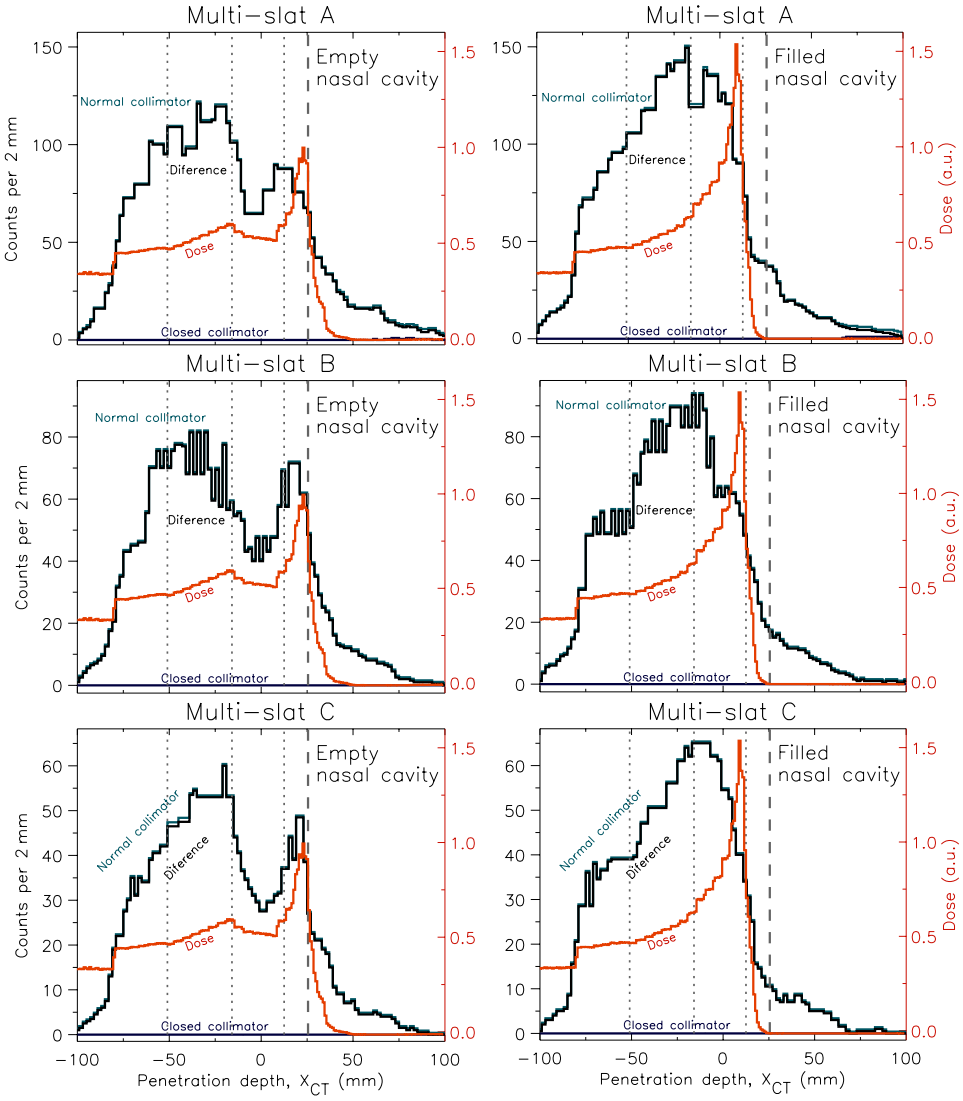

Figure 6.10: Collimated prompt gamma profiles simulated for the irradiation of the NCAT sphenoid region (figure 6.7), using the multi-slat collimators A-C ('normal collimator'). Also shown are the laterally-integrated depth-dose profiles, the profiles from a closed collimator, and the 'normal collimator' profile after subtraction of the 'closed collimator' profile ('difference'). A low-energy threshold of 1 MeV and a TOF acceptance window of 1 ns were applied, together with a median filter with a span of 8, 10, or 8 bins, for multi-slat collimators A, B, and C, respectively (bin size = 2 mm). The vertical dashed lines correspond to the proton range in the planned, 'Empty nasal cavity' situation. The vertical dotted lines represent the soft-tissue/bone, bone/nasal-cavity, and nasal-cavity/bone interfaces traversed by the protons, from left to right, respectively.

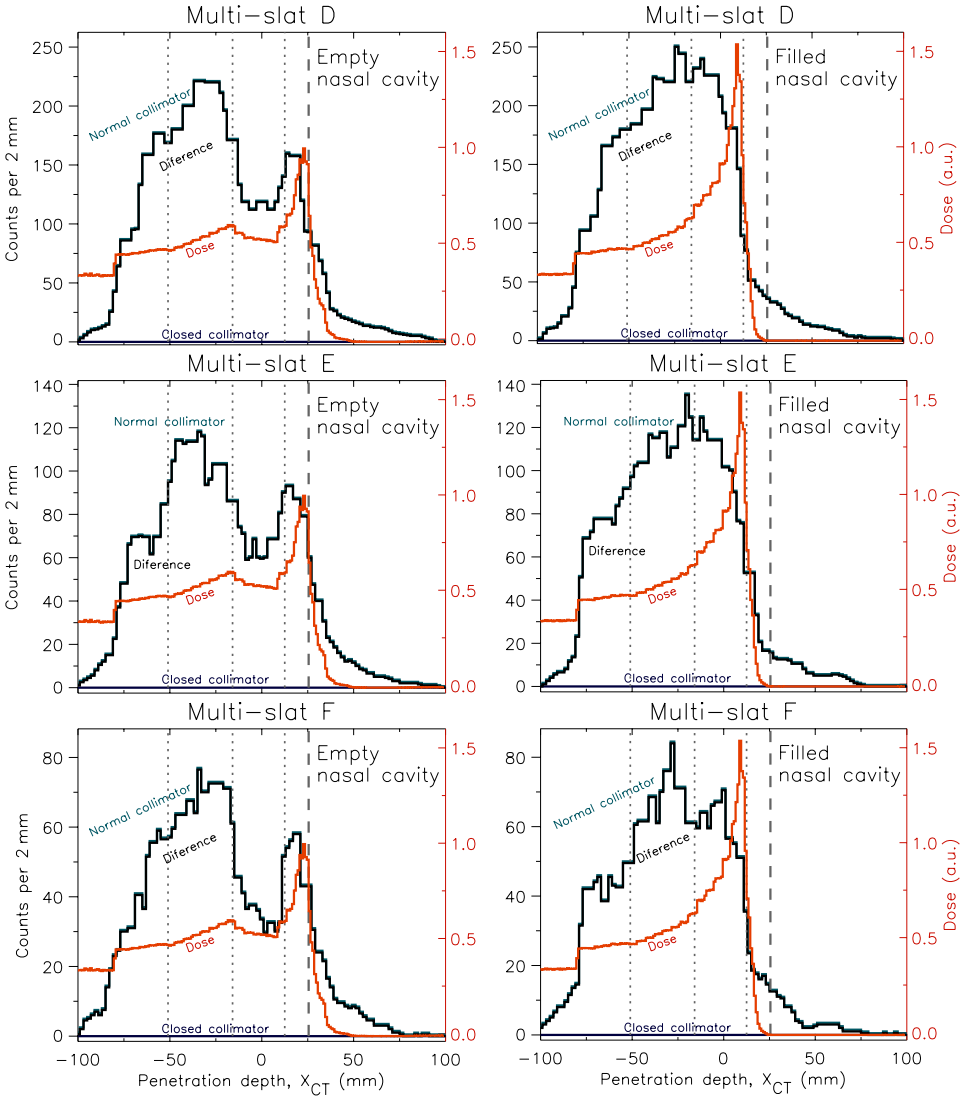

Figure 6.11: Collimated prompt gamma profiles simulated for the irradiation of the NCAT sphenoid region (figure 6.7), using the multi-slat collimators D-F ('normal collimator'). Also shown are the laterally-integrated depth-dose profiles, the profiles from a closed collimator, and the 'normal collimator' profile after subtraction of the 'closed collimator' profile ('difference'). A low-energy threshold of 1 MeV and a TOF acceptance window of 1 ns were applied, together with a median filter with a span of 12, 8, or 6 bins, for multi-slat collimators D, E, and F, respectively (bin size = 2 mm). The vertical dashed lines correspond to the proton range in the planned, 'Empty nasal cavity' situation. The vertical dotted lines represent soft-tissue/bone, bone/nasal-cavity, and nasal-cavity/bone interfaces traversed by the protons, from left to right, respectively.

6.3.4.2 Pituitary irradiation: small density changes

The planned 2D dose distribution for the irradiation of the pituitary gland, under the reference condition of normal brain tissue density, is presented in figure 6.12-top-right, superimposed on a CT axial-slice of the phantom head.

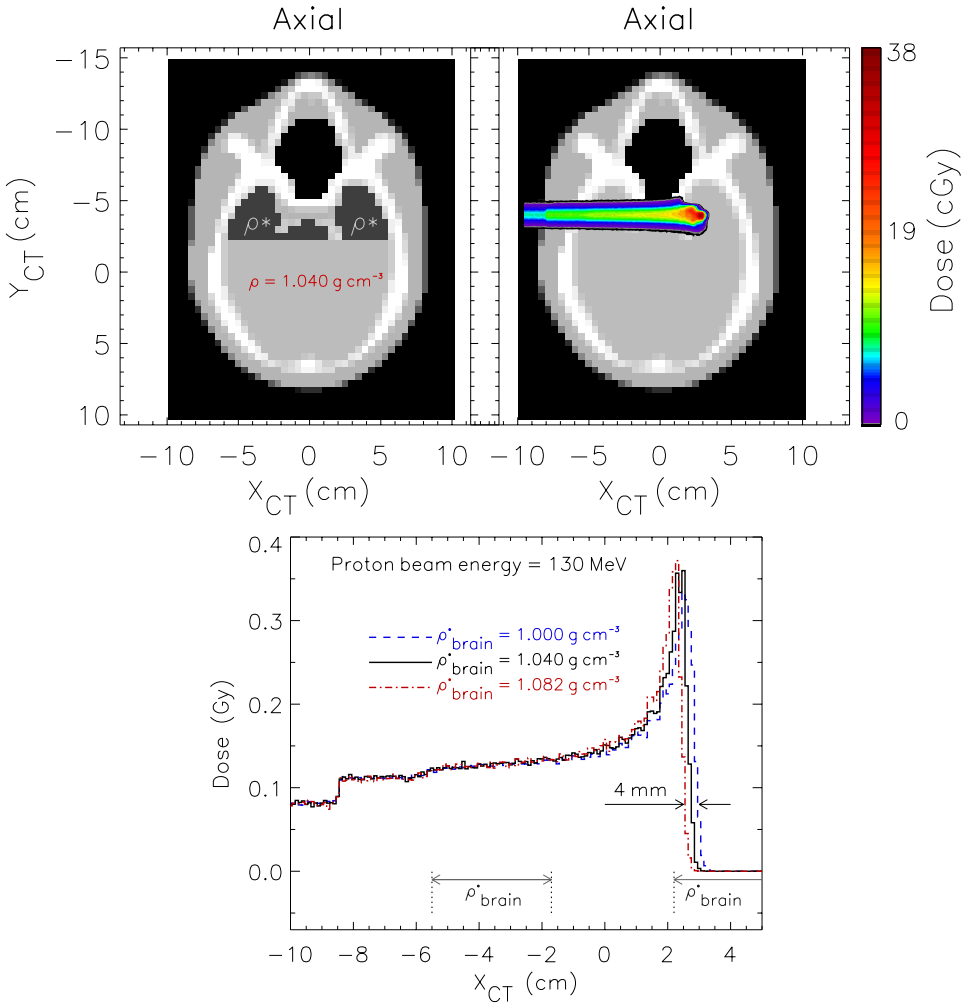

Figure 6.12: Top-left: NCAT-head axial slice showing the region in dark-grey color where the brain density was changed (ρ^*) by ±4% relative to the original value ($\rho = 1.040$ g cm^{-3}). Top-right: Dose distribution corresponding to 130 MeV proton irradiation of the pituitary gland (original brain density). Bottom: depth-dose profiles in the center of the pencil beam for the three brain-density cases studied.

In figure 6.12-bottom, we show the longitudinal dose profiles obtained for the three brain densities simulated. The brain region where the density was changed to ρ^* is colored dark-grey in figure 6.12-top-left. We observe that an increase or decrease in brain density

by 4% results in range shifts of -2 mm or +2 mm, respectively, in regard to the reference case. Such range shifts may have clinical importance, especially when the BP is located inside the tumor or in the vicinity of an organ at risk.

To assess the capability to resolve these small range changes, we study the profiles obtained with the multi-slat configuration and background rejection that yielded the best S_γ/B_γ ratio, i.e. with multi-slat E and simultaneous energy and TOF discrimination. These profiles are shown in figure 6.13-left, together with the normalized, longitudinal dose distribution in the reference situation. The range assessment was performed by a linear regression fit to the data points in the distal falloff region, between 20% and the 80% of each profile maximum (figure 6.13-right). The range was estimated as the position in depth (X_{CT} direction) corresponding to the 50% (E_{50}) level of the fitted curves; i.e. $E_{50} = (0.5 \cdot max - p_0)/p_1$, where p_1 is the slope, p_0 is the offset, and max is the profile maximum.

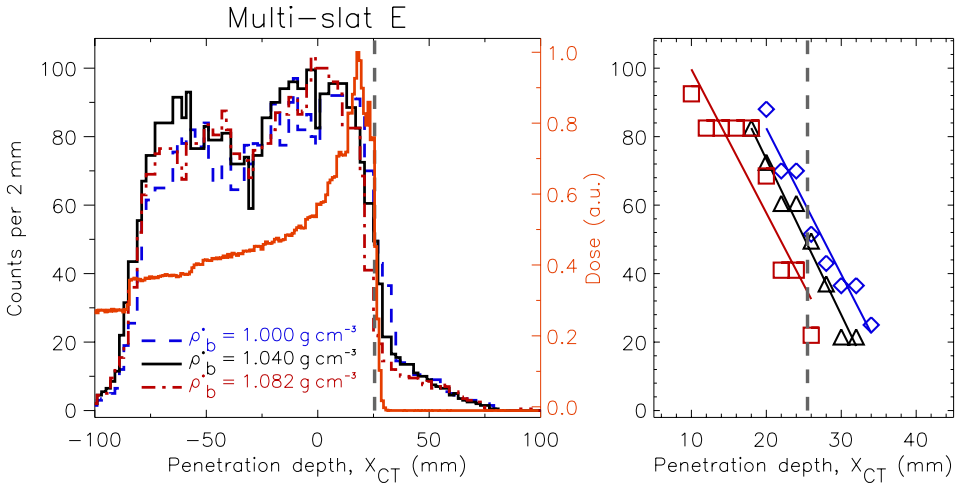

Figure 6.13: Left: Collimated prompt gamma profiles simulated for the irradiation of the NCAT pituitary region (figure 6.12), using multi-slat collimator E. Also shown is the laterally-integrated depth-dose profile in the case of original brain density ($\rho_b^* = 1.040$ g cm^{-3}). A low-energy threshold of 1 MeV and a TOF acceptance window of 1 ns were applied, together with a median filter with a span of 8 bins (bin size = 2 mm). Right: data points in the distal falloff region of each profile, between the 20% and the 80% of each profile maximum, for over-dense (red squares), normal (black triangles), and hypo-dense brain tissue (blue diamonds), together with the corresponding linear regression fits. The vertical dashed lines in both graphs indicate the proton range in the case of the original brain density.

These range estimations and their offsets in regard to the reference proton range are given in table 6.2. The reference proton range, for a normal brain density, is R_{70} = 110 mm (X_{CT} = 25.5 mm), and was defined as the phantom depth at which the dose has decreased to 70% of the depth-dose maximum. The 70% dose point was chosen instead of the usual 80% point for pencil beams, taking into account that the dose distribution presents azimuthal asymmetry, due to the fact that protons undergoing higher lateral spread traverse more bone tissue and therefore stop earlier than ballistic protons (figure 6.12-top-right). As a result, the value of the normalized laterally-integrated dose at the depth of the 3D dose maximum is about 0.8-0.9.

As shown in table 6.2, there is a clear difference between the E_{50} values obtained for

Table 6.2: Range estimation corresponding to the 50% (E_{50}) level of the gamma-profile maximum, using a linear regression fit to the distal falloff region between the 20% and the 80% levels of each profile maximum (figure 6.13). R_{70} = 110 mm is the range determined by the phantom depth at which the depth-dose profile of a normal density (planned) has decreased to 70% of the maximum. The range values corresponding to over- and hypo-brain density are 108 mm and 112 mm, respectively. The uncertainties correspond to one standard deviation and are obtained from propagation of the uncertainty in the fit results.

Brain density	Range estimation E_{50}(mm)	Offset to planned range E_{50}- R_{70}(mm)
Over-dense (+4%)	105.9 ± 3.0	-4.1
Normal	109.7 ± 2.5	-0.3
Hypo-dense (-4%)	112.5 ± 2.9	2.5

the three density cases. The use of improved algorithms for range estimation, which are less sensitive to statistical oscillations in the gamma profile, would probably reduce the differences between the estimated and true proton range, as well as the uncertainty associated to the range estimation. Nevertheless, the simple method presented here already shows encouraging range-resolving capabilities.

6.3.4.3 Prostate irradiation: patient setup error

The 2D dose distributions obtained from the irradiation of the prostate are presented in figure 6.14. We observe that the misalignment of 1 cm (patient to ventral) causes a proximal dose displacement and, consequently, tumor underdosage, in regard to the planned situation. Some protons traverse less bone tissue, contributing to an excess range and not to the correct, expected range. The 80% dose point from the laterally-integrated depth-dose profile in the compromised scenario is shifted by 11.8 mm in the proximal direction, in comparison to the reference irradiation. The prostate is situated between the bladder and the rectum, both of which are organs-at-risk. It can also be seen that the misalignment in this example causes higher dose deposition in the lining of the rectum.

Collimated gamma profiles are shown in figures 6.15-6.17. As before, in all graphs there are vertical dotted lines to assist in the visualization of the successive interfaces traversed by the protons, in this case soft-tissue/bone (X_{CT} = -14.5 cm), bone/soft-tissue (X_{CT} = -4.6 cm), soft-tissue/prostate (X_{CT} = -2.4 cm), and prostate/soft-tissue (X_{CT} = 1.5 cm). Again, these interfaces are not step-like, due to the tissue irregularities along the lateral span of the pencil beam. For instance, in figure 6.14-bottom, only about 1/3 of the lateral pencil-beam span at the ventral-most side passes through bone tissue. In each graph, the red curves indicate the longitudinal dose profiles, integrated over the Y and Z directions. The reference ('planned treatment') BP position is indicated in all graphs by the dashed lines at X_{CT} = 2.8 cm, and was defined as the traditionally used position at which the dose has decreased to 80% of its maximum.

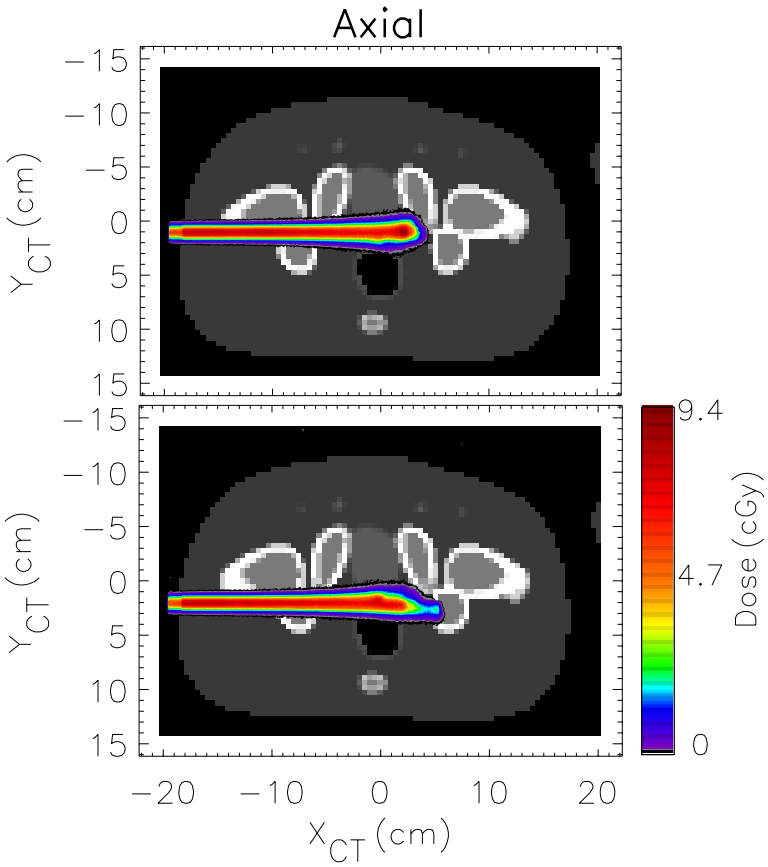

Figure 6.14: Dose distributions for 200 MeV proton pencil beam irradiation of the NCAT prostate region, superimposed on the corresponding CT axial slices (in gray scale, where windowing was done to improve visual contrast between soft tissues). Visual inspection reveals a proximal, longitudinal dose displacement, as well as tumor under-dosage in the case of a misalignment, where the patient is shifted 1 cm in the ventral direction (bottom), in comparison to the planned case (top).

The profiles obtained with energy discrimination only (3 MeV low-energy threshold) (figure 6.15) are more difficult to interpret than those obtained in the head irradiation cases because of the increased number of background gammas (figure 6.5). Not only do the more energetic protons generate more neutrons, also the collimator volume is twice as large as in the head irradiation cases, which may also contribute to higher amount of background. The effect of collimator geometry is consequently difficult to clearly visualize, thus exemplary profiles are shown in figure 6.15, only for multi-slat E. While the falloff of the gamma profile from the 'planned treatment' case in figure 6.15 visually correlates with the corresponding depth-dose distal falloff, it is less trivial to retrieve the BP position from the gamma profile in the 'misalignment' case. In the latter profile there can be seen 'bumps', which may be attributed to the bone/soft-tissue transition, the actual BP position, and the stopping of the higher-range protons that pass through the air cavity in the region of the rectum (figure 6.14-bottom). We furthermore observe that subtracting the 'closed collimator' profile does not improve the overall gamma profile shape by much. It thus appears that

background reduction by energy selection alone may not be sufficient to retrieve unambiguous information from PG multi-slat imaging in irradiations of the pelvic region.

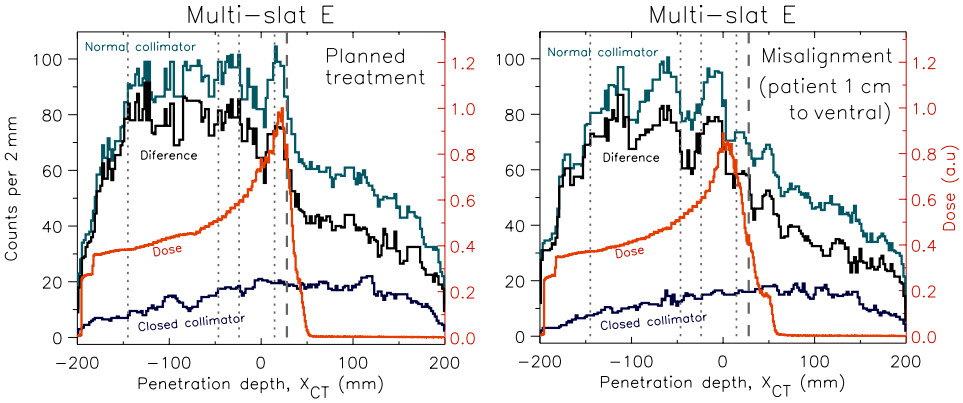

Figure 6.15: Collimated prompt gamma profiles simulated for the irradiation of the NCAT prostate (figure 6.14), using multi-slat collimator E ('normal collimator'). Also shown are the laterally-integrated depth-dose profiles, the profiles from a closed collimator, and the 'normal collimator' profile after subtraction of the 'closed collimator' profile ('difference'). A low-energy threshold of 3 MeV was applied, together with a median filter with a span of 8 bins (bin size = 2 mm). The vertical dashed lines correspond to the proton range in the 'planned treatment' situation. The vertical dotted lines represent the soft-tissue/bone, bone/soft-tissue, soft-tissue/prostate, and prostate/soft-tissue interfaces traversed by the protons, from left to right, respectively.

Fortunately, the gamma profiles obtained with simultaneous energy (1 MeV) and TOF discrimination (ΔTOF = 1 ns) (figures 6.16 and 6.17) present better S_γ/B_γ, resulting in less 'closed collimator' counts, an enhancement of the distal-falloff steepness, and better visibility of other profile features. It is to be noted that the background increases in the 10 cm long, most-distal FOV region, due to the increasing overlap between the time spectra of direct photons and neutrons (section 6.3.3). The magnitude of the distal background is higher for smaller beam-to-collimator distances. In particular, the profiles from multi-slat B are more affected due to the lower efficiency compared to multi-slat E. Nevertheless, in the present case, the distal background occurs after the BP position and therefore does not affect much the relevant profile features.

Without aiming at this point at a precise quantification, we visually observe that if TOF discrimination is applied (figures 6.16 and 6.17), there is in general a good agreement between about the 50% point of the PG distal-falloff, relative to a nearby local maximum, and the proton range in the 'planned treatment' cases, for all collimators studied. This was also noticeable in 6.13. Since the position of the local maximum may depend on the type of heterogeneities of the traversed tissue, this kind of assessment would most probably require user intervention. In addition, it appears feasible to retrieve the beam entry point from the PG profiles, but further work would be necessary to access the optimum profile pick-up point. For determining both the range and the entry point, it may be necessary to compare the PG profiles to reference, simulated and/or previously-measured ones. The use of automated methods for determining a shift relative to a reference profile may be a promising solution (Frey *et al* 2014). Furthermore, PG profiles show a correlation with certain anatomical features, such as the presence of bone tissue, comprehended between the 1st and 2nd dotted lines. This is particularly noticeable for multi-slats B, E, and F (figures 6.16

and 6.17).

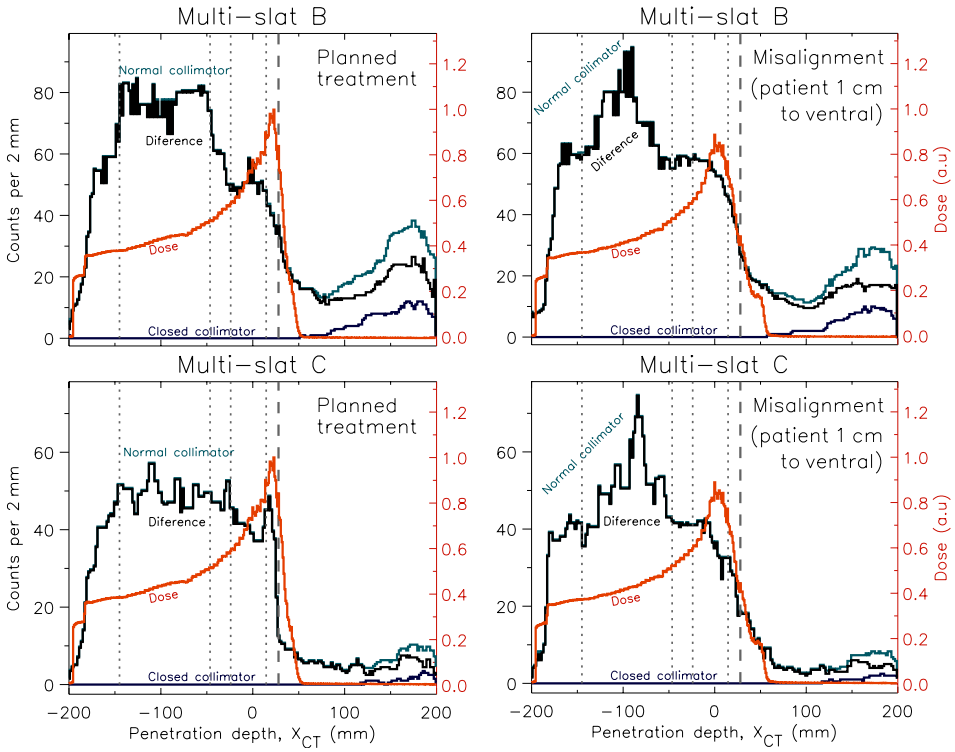

Figure 6.16: Collimated prompt gamma profiles simulated for the irradiation of the NCAT prostate (figure 6.14), using multi-slat collimators B and C ('normal collimator'). Also shown are the laterally-integrated depth-dose profiles, the profiles from a closed collimator, and the 'normal collimator' profile after subtraction of the 'closed collimator' profile ('difference'). A low-energy threshold of 1 MeV and a TOF acceptance window of 1 ns were applied, together with a median filter with a span of 12 or 8 bins, for multi-slat collimators B and C, respectively (bin size = 2 mm). The vertical dashed lines correspond to the proton range in the 'Planned treatment' situation. The vertical dotted lines represent the soft-tissue/bone, bone/soft-tissue, soft-tissue/prostate, and prostate/soft-tissue interfaces traversed by the protons, from left to right, respectively.

The profiles obtained with multi-slat E present the best overall visual correlation to the depth-dose and anatomy, in this study. Multi-slat F could be a good choice due to the higher resolution and S_γ/B_γ (figure 6.5), but in the present study the corresponding PG profiles are affected by statistical noise, which may give rise to artefacts after applying the median filter. Despite the low statistics, notice that the PG distal-falloff from multi-slats C and F, with TOF discrimination, are very sharp and agree well with the range position. In practice, one might add a second detector beneath the patient couch to increase the number of counts.

In particular, for multi-slat E (figure 6.17-top) we can detect about 40% reduction in the number of counts of the PG profile from the 'misalignment' case, at the expected proton range position, in regard to the 'planned treatment' case, corresponding to a 50% decrease of the depth-dose value. In addition, it seems feasible to identify other differences in the

PG profiles of the 'misalignment' case relative to the reference one, which could in practice complement the range information to confirm whether a change had occurred: for multi-slat E there is (1) a drop of counts at the distal end, just before the particles stop (comprehended between the 3rd and 4th dotted lines, from left); and (2) a shoulder of excess counts after the BP. These features may be attributed to (1) the protons traversing the rectum cavity; and (2) the excess proton range, visible in the depth-dose curve. In order to derive unambiguous information from these profile features, in practice the measured PG profiles may be compared with reference simulated ones, which would incorporate the volumetric density information of the patient (e.g., from a CT scan). In addition, measured PG profiles from a given fraction should be compared to those measured in the preceding treatment fractions, when available, to verify consistency or detect important deviations. The same applies for range verification.

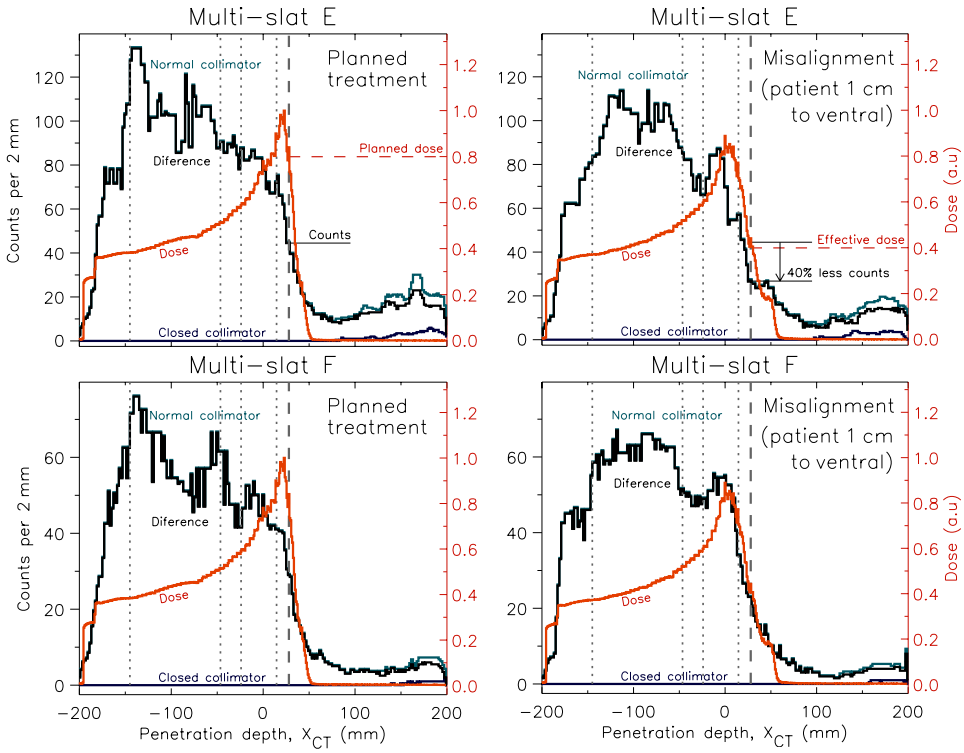

Figure 6.17: Collimated prompt gamma profiles simulated for the irradiation of the NCAT prostate (figure 6.14), using multi-slat collimators E and F ('normal collimator'). Also shown are the laterally-integrated depth-dose profiles, the profiles from a closed collimator, and the 'normal collimator' profile after subtraction of the 'closed collimator' profile ('difference'). A low-energy threshold of 1 MeV and a TOF acceptance window of 1 ns were applied, together with a median filter with a span of 8 or 12 bins, for multi-slat collimators E and F, respectively (bin size = 2 mm). The vertical dashed lines correspond to the proton range in the 'Planned treatment' situation. The vertical dotted lines represent the soft-tissue/bone, bone/soft-tissue, soft-tissue/prostate, and prostate/soft-tissue interfaces traversed by the protons, from left to right, respectively.

6.4 Conclusions and outlook

In this work, we simulated prompt-gamma imaging with various multi-slat collimator configurations placed at different distances from the beam axis, for realistic proton-therapy dose distributions in a human-like, voxelized phantom. We compared collimated prompt gamma profiles obtained from compromised treatment deliveries with those from reference (as-planned) irradiations and were able to visually detect relevant indicators of deviations in the delivered dose, in particular the depth-dose distal falloff position and the position of anatomic structures such as bone and air-cavities. In addition, the beam entrance point in the patient was well-resolved in all cases studied.

Different multi-slat configurations placed at various distances from the beam axis were compared in terms of photon signal-to-background ratio (S_γ/B_γ) and range- and heterogeneity-resolving power. Here, it is to be noted that the performance of a collimator does not only depend on its (intrinsic) geometric performance but also on the S_γ/B_γ. In all cases, a large amount of background counts (compared to the number of signal counts) was detected. The collimator is exposed to the highest fluence of neutrons (producing background gamma rays within the collimator material) if placed close to the patient. Additional 'uncorrelated' counts result from prompt gamma rays that undergo Compton scattering and/or trigger electromagnetic cascades in the collimator material. These results indicate that, due to the high total background level, a collimator with a relatively high geometric efficiency is preferable to a collimator with a relatively high intrinsic resolution, if the collimator is placed closer to the beam. If the same collimator is displaced further away from the beam, its intrinsic resolution deteriorates linearly with the distance (eq. (6.1)), while its efficiency remains essentially constant (eq. (6.3)). However, at larger distances from the beam the background level is lower, allowing for a different trade-off, namely a better resolution. A good spatial resolution is in principle desirable, especially in very heterogeneous targets, to detect changes in the longitudinal PG profile that contain important clues on the (causes of) deviations between the planned and delivered dose distribution. Therefore, it is necessary to optimize the trade-off between intrinsic collimator resolution and efficiency, as given by an optimal collimator design, depending on the type of irradiation performed (e.g., head vs. pelvis), on the beam energy and, importantly, on the distance between the collimator and the irradiation field.

It furthermore appears necessary to develop and optimize methods for the suppression of background counts. Background rejection by means of time-of-flight discrimination in combination with a 1 MeV low-energy threshold appeared remarkably more effective than using energy selection only (3 MeV threshold), for all collimator configurations and irradiation scenarios investigated. In fact, TOF discrimination appeared crucial to obtain a good S_γ/B_γ ratio in the pelvic irradiation with 200 MeV protons. Since the width of the TOF window is mainly determined by the proton bunch width, which can be of the order of 1 ns or lower for cyclotron beams, the analysis made in this work is realistic.

Compared to a knife-edge slit, a multi-slat collimator may have a larger weight. However, these collimators may not need to be moved to be aligned with the expected proton range of each layer of a treatment plan, as may be required with knife-edge slit collimators that intrinsically have a limited field-of-view (Smeets *et al* 2012b). Another potential advantage of a multi-slat collimator compared to a knife-edge slit is that the performance depends much less strongly on the distance between collimator and beam axis. Our results indicate that multi-slat PG imaging can be performed with all clinically used proton energies using a collimator placed at either a small or large distance from the target. This leaves flexibility to adapt the setup to practical and clinical considerations.

Gueth *et al* (2013) have suggested a different multi-slat configuration, made of 10 cm

high and 2 mm thick tungsten slats with a 2 mm slit aperture size and with a beam-to collimator distance b = 25 cm. In their concept, the detector is placed 25 cm behind the collimator back-surface in order to reduce septa shadowing. This requires that the distance between the detector front surface and the beam axis is kept constant, hence their detector has an annular shape in the azimuthal plane. In the present work we assume a simple flat-panel detector placed immediately behind the collimator, while the problem of septa shadowing is solved by applying a median filter to the recorded PG profile, at the same time preserving the main features of the gamma profiles. Advantages of this approach are improved resolution, simplicity of implementation and the fact that the collimator can be used at more than one distance from the beam axis. Indeed, in the optimized multi-slit designs obtained by Pinto *et al* (2014), the space between the collimator and the detector is kept as low as a few millimeters.

In conclusion, the results of this work provide several insights on the optimization of multi-slat collimator design for prompt-gamma imaging. The work highlights the relative simplicity and versatility of multi-slat PG imaging for *in situ* particle therapy treatment verification. In addition to enabling *in vivo* measurement of the proton range, multi-slat PG imaging potentially allows retrieving clues on the anatomical changes and patient setup errors that may occur relative to the treatment plan, thus enabling the detection of large as well as subtle deviations in the treatment delivery.

Appendix

In this appendix we derive equations (6.3) and (6.4) that give the geometrical efficiencies of a multi-slat and knife-edge slit collimator, respectively. Given the beam-azimuthal symmetry, we restrict this analysis to two dimensions, i.e. in the plane defined by the beam axis and the normal to the detector plane (figure 6.18). This is a special case of the classical 3-dimensional analysis of parallel-hole and pin-hole collimators that is described in (Cherry *et al* 2003, pp 239-247).

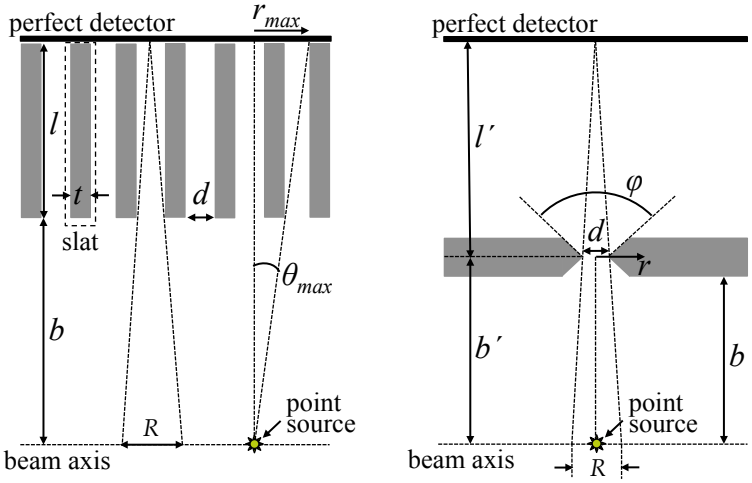

Figure 6.18: Schematic representation (not to scale) of the geometry of a multi-slat collimator (left) and a knife-edge slit collimator (right) (in gray), illustrating the parameters used to calculate the intrinsic resolution and efficiency of the collimators. R is the intrinsic point position resolution.

The fraction of gamma rays transmitted through the collimator from a point source on the beam axis is derived. We assume a perfect (i.e. infinitely dense) collimator. In case of a multi-slat collimator, the point source position on the beam axis is arbitrary, as the efficiency is constant throughout the collimator field-of-view. Let θ be the angle between the 2-dimensional photon momentum and the slat planes (figure 6.18-left). If $\theta = 0$, i.e. if the photon momentum is normal to the beam direction, the probability α for the photon to be transmitted depends only on the slit aperture size d and the slat/septum thickness t, according to equation (6.5):

$$\alpha = d/(d+t) \tag{6.5}$$

For obliquely incident photons (i.e. $\theta \neq 0$) the probability of transmission decreases as $|\theta|$ increases, and it equals zero for $|\theta| \geq \theta_{max}$, with θ_{max} defined by $\tan(\theta_{max}) = d/l$, in which l is the collimator height.

Let r be defined as the distance on the detector surface (in the beam-axis direction, figure 6.18-left) between the point of incidence of an oblique photon and a normally incident photon emitted by the same point source, such that:

$$\begin{cases} r & = (l+b)\cdot\tan(\theta) \\ r_{max} & = (l+b)\cdot(d/l) \end{cases} \tag{6.6}$$

where b is the source-to-collimator distance. The probability of transmission of a gamma ray incident at r can be approximated by a linear function, $f(r)$, where $f(0)=\alpha$ and $f(r_{max})=0$:

$$f_{m-s}(r) = \begin{cases} \alpha\cdot\left(1-\frac{r}{r_{max}}\right), & 0\le r\le r_{max} \\ 0, & r > r_{max} \end{cases} \tag{6.7}$$

Assuming symmetry around $r=0$, i.e. $f(-r)=f(r)$, the 2D geometric efficiency of the multi-slat collimator can now be written as:

$$g^{multi-slat} = 2\cdot\int_0^{r_{max}} \frac{f_{m-s}(r)}{2\pi\cdot(l+b)}\,\mathrm{d}r \tag{6.8}$$

where $(l+b)$ is the source-to-detector distance and $\mathrm{d}r/[2\pi\cdot(l+b)]$ is the elemental angular coverage for a direction of incidence with transmission probability $f_{m-s}(r)$. By substituting equations (6.5) and (6.7) in equation (6.8) and solving the integral function, we obtain:

$$\begin{aligned} g^{multi-slat} &= \frac{d}{(d+t)\cdot\pi\cdot(l+b)}\int_0^{r_{max}} 1-\frac{r}{r_{max}}\,\mathrm{d}r = \\ &= \frac{d}{(d+t)\cdot\pi\cdot(l+b)}\cdot\left[r-\frac{r^2}{2r_{max}}\right]_0^{r_{max}} = \frac{d}{(d+t)\cdot\pi\cdot(l+b)}\cdot\frac{r_{max}}{2} \end{aligned} \tag{6.9}$$

Finally, by substituting equation (6.6) for r_{max}, the 2D geometric efficiency of the multi-slat collimator is given by:

$$g^{multi-slat} = \frac{d}{(d+t)\cdot\pi\cdot(l+b)}\cdot\frac{(l+b)}{2}\cdot\frac{d}{l} = \frac{d^2}{2\pi l\cdot(d+t)} \tag{6.10}$$

The efficiency of a knife-edge slit collimator for a point source located on the beam axis and in the center of the field-of-view can be derived by assuming that the probability for collimator transmission equals:

$$f_{k-e}(r) = \begin{cases} 1, & -d/2\le r\le d/2 \\ 0, & |r| > d/2 \end{cases} \tag{6.11}$$

where d is the inner diameter of the slit aperture and r is now defined as a distance in the beam-axis direction contained in the middle plane of the collimator (figure 6.18-right). The 2D geometric efficiency of the knife-edge slit can thus be written as:

$$g^{knife-edge\ slit} = \int_{-d/2}^{d/2} \frac{1}{2\pi b'}\,\mathrm{d}r = \frac{1}{2\pi b'}\cdot\left[\frac{d}{2}-\left(-\frac{d}{2}\right)\right] = \frac{d}{2\pi b'} \tag{6.12}$$

where b' is the distance from the center of the slit-aperture to the point source.

Acknowledgments

This work was funded in part by the foundation for Fundamental Research on Matter (FOM), The Netherlands (grant no. 09NIG18). P. Cambraia Lopes was supported by grant no. SFRH/BD/73705/2010 and P. Crespo was supported by grant no. SFRH/BPD/39223/2007, both from FCT – Fundação para a Ciência e a Tecnologia, Lisbon, Portugal, co-funded by the European Social Fund and by POPH – Programa Operacional Potencial Humano. P. Crespo and H. Simões are now supported by QREN - FEDER under the Sistema de Incentivos à Investigação e Desenvolvimento Tecnológico (CENTRO-07-ST24-FEDER-002007, project 'Radiation for Life').

The authors like to thank Paul Segars (Johns Hopkins University) for providing the software-based anthropomorphic NCAT phantom, Marco Pinto (LIP-Coimbra) for the support given on the simulation code, Freek Beekman and Victor Bom (TU Delft) for helpful discussions on collimator design, Julien Smeets (Ion Beam Applications SA, Louvain-la-Neuve) for sharing the data simulated with MCNPX on neutron and gamma yields escaping PMMA, and Georgios Dedes (Ludwig Maximilian Universität, Muenchen) for helpful discussions on Geant4 models. Finally, thanks for the informatics support given by the staff of the Milipeia (University of Coimbra) and HPC11 (TU Delft) high-performance computer clusters.

Chapter 7

General discussion and outlook

Particle therapy (PT), including proton therapy, has important advantages compared to external beam photon therapy (section 1.1). This is because most of the therapeutic effect of a proton beam is localized at the endpoint, where most of its energy is imparted to the medium (Bragg peak), with nearly no dose deposited beyond that point. However, the highly localized dose deposition makes proton therapy more sensitive to (1) patient morphological alterations, including tumor progression / regression, (2) organ motion, (3) patient setup errors, (4) tissue lateral heterogeneities that render the results obtained with non-Monte-Carlo-based treatment planning algorithms unreliable to some degree, (5) beam characteristics utilized for treatment planning, and (6) the conversion of Hounsfield units (computed tomography data), to tissue density and stoichiometry. In addition, uncertainties in the mean excitation potential I, necessary to calculate the stopping power of the penetrating ions, further contribute to potential beam range inaccuracies.

Given the aforementioned sources of treatment error, an imaging technique capable of providing feedback proportional to the quality of the treatment being delivered is highly desired and a very active field of research in proton therapy (section 1.2). Specifically, it is of utmost importance to develop an imaging technique capable of providing feedback with respect to the *in vivo* beam range, especially when highly-heterogeneous beam paths are crossed by a pencil beam.

In this thesis, several such imaging techniques were put forward, viz. a dual-head time-of-flight positron emission tomograph (TOF-PET), a knife-edge-slit prompt-gamma (PG) camera, and a multi-slat PG camera, with both PG cameras assisted by TOF for background rejection. The following imaging techniques were tested experimentally for the first time (in prototype form) with innovative photon detectors (viz. digital photon counters, DPCs): TOF-PET (chapter 2), knife-edge-slit PG camera (chapter 4), and single-parallel-slit PG detector as a simplified prototype of a multi-slat PG camera (chapter 5). While the TOF-PET measurements were performed at a clinical synchrotron with a beam energy of about 126 MeV, the PG-based measurements were realized at a clinical proton cyclotron with a proton bunch width of about 1.1 ns full width at half maximum (FWHM) for a beam energy of 160 MeV. The fast timing performance of the DPC in combination with a fast, high light-output scintillator crystal (LYSO:Ce) enabled excellent detector time resolution, which has been demonstrated to be a very important parameter for all of the imaging techniques studied in this thesis.

In addition to experimental demonstrations of *in situ* PET- and PG-based imaging techniques for monitoring proton therapy, this thesis also explored, by means of Monte Carlo

(MC) simulations, methodologies enabling an improvement of the PG imaging technique: the concept of a shifting TOF window correlated with the transit time of the stopping ions in tissue was suggested (chapter 3), and the application of a multi-slat collimator system was analyzed for the first time in realistic treatment scenarios (anthropomorphic phantom), considering potential tissue morphological alterations, which gave rise to proton range shifts of a few cm and as low as 2 mm (chapter 6).

7.1 Dual-head TOF-PET

In proton therapy, nuclear reactions occurring between the projectile and target nuclei result in the production *in situ* of β^+ emitters that can be used for monitoring the irradiation procedure by using (1) specially adapted in-beam PET detectors (Parodi *et al* 2000, 2002) or (2) offline full-ring positron tomographs commonly utilized in nuclear medicine (Parodi *et al* 2007b). The latter can be implemented within the treatment room, thus avoiding to some extent the biological washout and physical decay mechanisms that decrease the measurable β^+ activity, complicating image evaluation. Another full-ring implementation may use a commercial PET scanner located outside the treatment room, although in this case the aforementioned mechanisms are further exacerbated. On the other hand a dual-head in-beam PET solution, despite providing more image statistics, suffers from limited-angle artefacts that strongly disturb image evaluation, especially when large tumors are being handled (Crespo *et al* 2006). While it is yet not clear which solution provides better treatment monitoring capability, simulations have shown that some of the artefacts arising with a dual-head in-beam PET scanner for monitoring proton therapy may be mitigated by applying the TOF information provided by modern PET scintillation detectors (Crespo *et al* 2007, Surti *et al* 2011).

In this work we have measured, for the first time, synchrotron-based, *in situ* β^+ activity deposited in homogeneous phantoms with modern PET detectors with a coincidence resolving time of 382 ps FWHM (chapter 2). The detectors consisted of arrays of DPCs coupled to finger-like LYSO:Ce crystals, with the two detectors forming a prototype dual-head positron camera with a transaxial coverage angle of $2 \times 50°$ (of 360°). As such, they enabled the aforementioned artefacts to be visualized if non-TOF reconstruction was applied to the measured data (figure 2.5-top). In contrast, TOF-based reconstruction resulted in a substantial reduction of these image-elongation artefacts (figure 2.5-middle).

The uncertainty in the activity range measured using this DPC-based TOF-PET prototype setup in PMMA equals 0.2 mm - 0.3 mm for a total spot fluence of 10^{10} protons and 2-minute-long acquisitions (in-beam or shortly after irradiation, with a maximum delay of 2 minutes). In addition, the obtained results also suggest, for the first time, that available experimental cross sections underestimate the simulated production of ^{10}C for in-beam acquisitions, which in PE resulted in an overestimation of the predicted activity range by 1.4 mm.

In regard to the stability of the detector performance with time, we have observed a gradual increase in the dark-count-related trigger rate, scaling with the number of protons delivered, within a day of measurements. This increase amounted to 40 kHz/10^{10} protons/chip on average for a detector operating temperature of -10 °C and a trigger setting on the 2$^{\text{nd}}$ photon, suggesting some amount of detector radiation damage. The dark-count-related trigger rate could be reset to within a few percent on a day-to-day basis. However, further studies are required to access the effect of long-term exposure to secondary radiation on the detector performance.

7.2 TOF in PG imaging

As mentioned in the previous section, an alternative approach to the imaging of β^+ emitters with PET for clinical proton therapy beam range monitoring is the readout of the larger amount of PGs via one of several single-photon imaging techniques (section 1.2.2). Despite the advantages of PG imaging, summarized in section 1.2.4, all PG imaging techniques may suffer from corruption by a neutron-related background. In chapter 3 a method was proposed that enables the reduction of such background by utilizing a so-called shifting TOF window that follows the ion transit time in the patient until the ion comes to rest. This method can be implemented in cyclotron-based clinical proton beams due to the relatively small bunch width delivered with such machines (indirectly measured to be about 1.1 ns FWHM for 160 MeV protons in chapter 4). Larger bunch widths of up to 2.1 ns FWHM have been measured by Hueso-González *et al* 2015 for beams of lower energy (100 MeV). However, neutron contamination at such low energies is of much less importance with respect to higher (and more utilized) beam energies. In addition, the most distal Bragg peak is typically irradiated by means of higher energy beams, with the bunch width being reduced to about 0.4 ns FWHM for a beam energy of 230 MeV, due in part to the absence of the energy degrader (Hueso-González *et al* 2015). It must be stated that the implementation of the shifting TOF method in synchrotron-based clinical facilities is highly compromised given the large bunch widths of such machines, which may e.g. reach tens of ns FWHM for carbon ions (Parodi *et al* 2005a).

7.3 Knife-edge-slit PG camera

The knife-edge-slit PG camera utilized in this work (chapter 4) constituted a prototype of a geometry previously proposed (Smeets *et al* 2012b). Here, it was shown experimentally for the first time that TOF-based background rejection improves the signal-to-background ratio (S/B) of the PG profiles obtained with this type of camera (by a factor of about 3). In addition, measurements were made with two types of scintillation crystals: LYSO:Ce and BGO. Although our results indicate that BGO benefits from a higher gamma-to-neutron sensitivity compared to LYSO:Ce, the best S/B was obtained for the measurements with LYSO:Ce crystals that made use of TOF-based background rejection.

One further advance established within this work was the use of DPC-based detectors for scintillation light readout in the context of PG imaging. Indeed, the readout system used in this work was not suitable to handle the count rates expected by a knife-edge-slit PG imaging device operating at clinical currents of the order of 1 nA, although the DPC sensors themselves have adequate rate capability. The total data rate acquired at such a beam current is the scope of the work by Perali *et al* (2014). These authors propose a knife-edge-slit PG camera based on LYSO:Ce crystals coupled to silicon photomultipliers, read out by 40 data acquisition systems working in parallel, and having the same pixel size of 4 mm in the beam direction as in the present work. No TOF is implemented in their work, resulting in an uncertainty in the estimated proton range in PMMA of 4 mm (2 sigma), for a single pencil beam containing 1.4×10^8 protons with an energy of 160 MeV, which may be compared to 3.3 mm obtained in this work by making use of the TOF technique. To obtain the value of 3.3 mm, the average standard deviation of 1.1 mm from the results shown in figure 4.13 (LYSO:Ce w/TOF, 10%) was used. This uncertainty was then corrected for the difference in efficiency resulting from the difference in total proton numbers (4.6-times higher proton fluence in this work, viz. 6.5×10^8 protons) and in azimutal angle coverage, considering that the uncertainty is proportional to the inverse of the square root of the number of counts.

The angle coverage in Perali *et al* (2014) was calculated for a slit length of 20 cm (vs 6.8 cm in this work) and a distance between the beam axis and the detector of 45 cm (vs 30 cm in this work).

The aforementioned facts allow to conclude that a knife-edge-slit PG camera can be implemented under clinical currents for monitoring the range of proton beams in homogeneous targets. Despite first steps towards the detection of range shifts in inhomogeneous targets (Priegnitz *et al* 2015), work remains to be done in order to prove the feasibility of a knife-edge-slit PG camera for monitoring the proton beam range in highly-heterogeneous clinical settings.

7.4 Single-parallel-slit PG detector

In order to analyze the viability of utilizing a multi-slat PG camera for monitoring the beam range in proton therapy, a single-parallel-slit PG detector experiment was carried out at the West German Proton Therapy Center Essen (WPE, chapter 5). In addition to obtaining PG profiles corrected with the shifting TOF method introduced in chapter 3, this work also served to put forward the methods necessary to implement such shifting TOF technique for the discrimination of neutron-induced events in cyclotron-based facilities. The experiment used a single-parallel-slit collimator to measure time spectra and intensity profiles of in-beam events emitted at various depths along a PMMA phantom upon irradiation with a 160 MeV proton pencil beam.

The experimental results allowed a PG profile to be reconstructed with the assistance of the shifting TOF technique. For the same experimental settings (including approximately the same distance between the beam axis and the detector front surface), the S/B obtained is of the same order as the one achieved with the knife-edge-slit camera provided that a low-energy cutoff of 3 MeV is applied in combination with TOF discrimination in both cases. This fact can be confirmed in figure 5.9, which, in addition, shows an improved spatial resolution obtained with the single-parallel-slit collimator, observable as a more pronounced falloff slope in the corresponding PG profile. Specifically, the relative slope in the falloff region of the PG intensity profile is larger by about a factor 1.8 in the single-parallel-slit experiment than in the knife-edge slit one, when both profiles are normalized to a maximum intensity of 1. Interestingly, a simple calculation that only accounts for the geometrical point resolution in an infinitely-dense collimator indeed predicts a factor of 1.8 improvement in spatial resolution for the single parallel-slit with respect to the knife-edge slit (viz., 6.8 mm versus 12 mm). In order to take into account also the statistical fluctuations in the falloff of the PG-profile, in the range-estimation performance, the slope-over-noise ratio in the PG-profile falloff was calculated, yielding a value ~1.2 higher for the single parallel-slit collimator.

The aforementioned results, including the results shown in figure 5.9, cannot be extrapolated directly to a multi-slat PG camera, mainly due to two factors. That is, the multi-septa of a multi-slat configuration, interleaved by air slabs, would result in increased septa penetration by oblique γ rays, which would blur the single-parallel-slit PG profile. On the other hand, the reduced amount of collimator material present in the vicinity of the detector in a multi-slat configuration would reduce the amount of (n,γ) reactions, which would reduce the measured background.

It must be stated for completeness that the improved spatial resolution obtained with the single-parallel-slit configuration results in potential increased capability to detect deviations in the shape of the entire PG profile in the irradiation of highly-heterogeneous media, deviations correlated to the dose distal falloff in particular. Such distal falloff shape deviations

can also be observed in the profiles simulated for multi-slat configuration in the irradiation case shown in figure 6.14, with the corresponding 1D dose and PG profiles shown in e.g. figure 6.17-top. The right image in the latter figure shows a concomitant dose underrange and overrange, which are visually correlated with the corresponding PG profile. The capabilities and limitations of a multi-slat PG camera were analyzed in more detail in chapter 6, with the corresponding conclusions and outlook presented in the next section.

7.5 Multi-slat PG camera

It is not yet clear if a knife-edge-slit collimator or a multi-slat collimator would perform best for monitoring proton beam range in proton therapy. On one hand, the knife-edge-slit collimator is attractive in that it can in principle combine relatively high sensitivity with high resolution, especially when a large magnification factor is applied. On the other hand, such implementation requires a large detector-collimator system positioned in close vicinity to the patient (tumor site), which represents a limitation in proton (particle) therapy: space occupied around the patient. One potential advantage of a multi-slat geometry is that it provides more compact devices if compared to a knife-edge-slit design with large magnification capability. In addition, the performance of the former in terms of sensitivity and resolution is less dependent on the (varying) distance to the beam axis. This represents an advantage as tumor locations vary within the body of the patient. Also of clinically relevance is the capability of maintaining performance at larger beam-to-detector distances in cases where vertical beams are being applied (e.g., irradiation of the abdomen, viz. liver (Bush *et al* 2011) and pancreatic tumors (Charles Nichols *et al* 2013)). Finally, the multi-slat design provides a much larger field of view (FOV) than the knife-edge slit. Indeed, the former allows monitoring the entire beam path - with constant performance - from its entrance into the patient to the Bragg peak location and beyond. To fully answer the question of which collimator performs best, both collimators need to be optimized and compared in realistic treatment scenarios. The Geant4 simulations of an anthropomorphic phantom presented in the current work (chapter 6) represent a step forward in the optimization of multi-slat collimators only, where particular emphasis was put on the use of irradiation conditions as similar as possible to clinical settings.

In this work, three irradiation scenarios were studied, two concerning head irradiation, and one for a pelvic treatment (prostate irradiation). For each study we investigated the effect of adding a density change or setup change that could be correlated to clinically relevant dosimetric changes. Here we have shown that a multi-slat PG camera using a shifting TOF window (window size of 1 ns) for background rejection could detect (1) anatomical changes, and (2) dose shifts in the Bragg peak region, based on a single pencil beam irradiation, with a fluence of 10^8 protons delivered with a 9 mm FWHM. By visual inspection of the longitudinal PG profiles we observed intensity changes that correlated to density changes along the beam path. This was so because the emission of PGs is highly correlated to tissue density. In particular, marked changes were observed corresponding to the presence or absence of an air cavity and to bone/soft tissue or bone/air interfaces. Also the presence of compact bone versus trabecular bone in the prostate case could be observed. Range shifts of the order of 2 mm were visually observed. This observation was further corroborated by a more robust method based on a linear regression analysis.

The results presented in chapter 6 for a multi-slat geometry were obtained with an ideal γ-ray detector having a longitudinal resolution of 2 mm. In practice this could possibly be achieved by using (1) segmented slabs of scintillator, or (2) finger-like scintillator crystals, coupled either to arrays of linear detectors or multi-pixel sensors forming a 2D matrix.

A monolithic scintillator might also be a solution provided modern methods for gamma photon interaction position determination are applied (van Dam *et al* 2011). In this case, however, it remains to be proven that the achievable spatial resolution does not become compromised due to the higher energy of PGs with respect to the 511 keV γ-rays in PET.

In a multi-slat implementation, multi-hit analysis may further improve the overall spatial resolution together with system sensitivity (e.g., (Rafecas *et al* 2003) for PET). Such multi-hit analysis may only work, however, if an event-by-event readout is possible. That is, piled-up PG events or PG events arriving in bunches would severely complicate the analysis. However, piled-up or bunched PG events do not seem likely in pencil-beam-based proton therapy. Indeed, a maximum fluence of about 5×10^8 protons per spot (Priegnitz *et al* 2015) delivered with a clinical beam current of ca. 5 nA (Perali *et al* 2014) can be assumed. This results in a count rate per detector slab of about 20 kHz (50 μs per event) resulting from ca. 320 γ-rays arriving on average at each slab of the multi-slat detector, provided that a 1 MeV low-energy threshold is implemented at the hardware level (simulated prostate irradiation, results not shown). This count rate already includes the detection of secondary γ-rays from reactions induced by neutron interactions in the patient or collimator, and excludes neutron-induced events in the detector. The 20-kHz event rate per slab results in a data acquisition rate of 4 MHz if a slab thickness of 2 mm is considered, together with a camera longitudinal length of 40 cm. Should this data acquisition rate be too high, the implementation of several segmented data acquisition systems working in parallel could be a solution.

Based on the above, it seems reasonable to assume that a multi-slat PG camera can be developed, yielding a number of benefits to the task of monitoring proton therapy, including the verification of the proton range.

7.6 Outlook

7.6.1 PT PET

In situ PET is a promising technique for the online *in vivo* monitoring of proton therapy. In particular, PET might be the more accurate approach for clinical synchrotron proton beams having a proton bunch width $>> 1\,ns$, which hampers the use of TOF information for background reduction in PG imaging. Furthermore, a recent study points in the direction of a PT PET technique possibly competitive with PG imaging. This method relies on PET nuclides with short half-life such as ^{12}N (half-life, $T_{1/2} = 11$ ms) and is called beam-on PET or prompt PET (Dendooven *et al* 2015). This approach might potentially enable PET imaging at nearly the same time scale as PG imaging, making it insensitive to biological washout.

Dual-head PET systems represent a practical and convenient *in situ* PT PET solution. We believe that TOF-PET detectors are a key element for future PT PET, in order to overcome limited-angle image artefacts and to compensate for the loss of geometrical efficiency with respect to a full-ring PET scanner (note that in the latter case also a certain loss of geometrical efficiency may be present due to the tilt or slant angles necessary in an *in situ* approach). TOF-PET further reduces random coincidences and opens up the possibility for fast image reconstruction and, therefore, fast feedback for therapy adaptation (Crespo *et al* 2007). The main limitation of the present study is that the image quality and the precision in detectability of small range shifts cannot be directly extrapolated from the small setup used to the case of a realistic scanner with a radius of about 40 cm positioned around a patient, since the influence of parallax error and gamma acolinearity would increase, just as the

fraction of scatter and random coincidences. Follow-up studies with scaled-up geometries are therefore warranted.

Based on the experimental results presented here and simulation studies available from literature (Crespo *et al* 2007, Dendooven *et al* 2014, Surti *et al* 2011) we believe that dual-head artefact-free TOF-PET may be a feasible solution. The solid angle coverage of the prototype tomograph used is on the conservative side, meaning that in practice, a larger coverage angle may be acceptable around the patient. As follow-up research, it would be interesting to experimentally study what would be the minimum solid angle coverage necessary to obtain artefact-free images of objects with the size of a typical irradiation field, and for the typical activity densities encountered in proton therapy, considering an acquisition time of the order of a few minutes. Similarly, it would be of interest to study the further reduction of limited angle artefacts when using detectors with even better TOF performance than the ones used in this thesis (Borghi *et al* 2016a, 2016b). Such results could then be used to make the step towards clinical implementation. An interesting assessment would be to balance the potential high costs associated with the use of demanding technology (in terms of fast timing resolution and segmented electronics to cope with high count rates) with the reduced costs resulting from an incomplete ring of detectors. Regarding the detector itself, monolithic scintillators appear as interesting candidates in this field. Such crystals are easy to produce, present an increased sensitive surface (hence detection efficiency) relative to pixelated detectors, and have the capability to provide depth-of-interaction (DOI) information (Borghi *et al* 2016a, 2016b). The latter is especially relevant if flat panel detectors are considered. Note that in the context of proton therapy, spatial resolution is somewhat less important than detection efficiency and time resolution, due to the broad nature of the spatial activity distributions.

7.6.2 PG imaging with mechanical collimation

In the context of PG imaging, the results presented in this work strongly encourage the further development of a collimated PG imaging device that would meet the following criteria: (1) an effective TOF rejection technique, preferably correlated to the proton transit time in the irradiated medium and having a time resolution for single gamma detection (for energies of a few MeV) lower than the expected proton bunch width (i.e. $\leq$ 1 ns) and (2) good detection efficiency for MeV γ-rays (at least comparable to that typically encountered in PET detectors). Preferably, the detectors would have the capability to sum up multiple energy depositions originating from the same incoming gamma ray, which otherwise might fall outside the lower energy threshold required to reject background radiation. These requirements are not difficult to meet with present-day technology. We further believe that a multi-slat collimator configuration might be a promising approach, amongst others because such collimators have a large field of view with constant performance characteristics. It remains a challenge to develop an affordable, realistically-sized camera, with an area of about $40\,\text{cm} \times 50\,\text{cm}$, covered with scintillator crystals and segmented detectors/readout so as to cope with the count rate during beam-on. This may be the subject of follow-up studies. One approach could be to segment the scintillator into detector slabs parallel to the direction of the collimator slits (Perali *et al* 2014).

Before making the step towards a clinical PG detector prototype, further feasibility tests are necessary. In particular, the concept of a multi-slat camera could be experimentally explored using a limited number of detectors under de following conditions: (1) a realistic collimator size, and (2) irradiation of a highly heterogeneous medium, preferably an anthropomorphic phantom. Condition (1) would allow measuring under actual background conditions while imaging an extended area. Condition (2) is very important to assess what

would be the necessary spatial resolution to achieve the desired detectability of range shifts and other types of error. The presence of inhomogeneities distorts the shape of the fall-off profile, making the detection of range shifts more challenging, compared to the ideal situation of homogeneous media.

Bottlenecks in PG imaging are the counting statistics available on a per-pencil-beam basis and the considerable amount of background radiation. Based on the results presented in this thesis, one can make some general recommendations on the collimator geometry for follow-up studies, which should be subject to further optimization. In chapter 4, PG profiles with sufficient statistics (extrapolating to a realistic-size detector) were obtained experimentally using a knife-edge slit collimator. The PG profiles obtained with a single parallel-slit collimator were subsequently compared to the ones with a knife-edge slit, revealing a similar signal-to-background ratio, S/B (chapter 5 and figure 5.9), and an improved slope-over-noise ratio (by a factor ~1.2) for the single parallel-slit, despite the relative decrease by a factor of two in the total number of counts. This single parallel-slit collimator has the same geometric properties as one of the multi-slat configurations investigated in chapter 6, configuration 'A', except for the fact that it has only one slit and two thick blocks of tungsten instead of septa. This last fact does not enable a direct comparison. However, it might be reasonable to assume that the sensitivity of a multi-slat collimator 'A' to PGs is at least equal to that of the single parallel-slit, but likely higher due to septa penetration. Based on this consideration one might expect sufficient counting statistics for multi-slat 'E', which had a slightly higher geometrical efficiency and worse spatial resolution (in fact, approximately equal to that of the knife-edge slit here studied, ~12 mm) compared to multi-slat 'A'. In fact, in that simulation study (chapter 6), multi-slat 'E' presented a better correlation between simulated PG profiles and the depth dose distribution, corroborated by a better gamma S/B. This fact was attributed to a slightly better efficiency and a lower exposure to background, as the collimator was placed further away from the beam axis (25 cm instead of 15 cm). Interestingly, such a multi-slat configuration is rather similar to an optimal multi-slat configuration found in an independent study by Pinto *et al* (2014), using complex mathematical algorithms to obtain the best precision on the fall-off position in an homogeneous target. As such, a simple and comprehensive analysis of geometrical collimator resolution and efficiencies as presented in chapter 6, section 6.2.1, may already provide first-order approximations of appropriate collimator geometries, which should be further supported by experimental evidence and simulation work.

References

Agostinelli S *et al* 2003 GEANT4: a simulation toolkit *Nucl. Instrum. Methods Phys. Res. A* **506(3)** 250–303

Allison J *et al* 2006 Geant4 developments and applications *IEEE Trans. Nucl. Sci.* **53(1)** 270–8

Attanasi F, Knopf A, Parodi K, Paganetti H, Bortfeld T, Rosso V and Del Guerra A 2011 Extension and validation of an analytical model for *in vivo* PET verification of proton therapy—a phantom and clinical study *Phys. Med. Biol.* **56** 5079–98

Battistoni G, Cerutti F, Fassò A, Ferrari A, Muraro S, Ranft J, Roesler S and Sala P R 2007 The FLUKA code: description and benchmarking *AIP Conf. Proc.* **896** 31–49

Bauer J, Sommerer F, Mairani A, Unholtz D, Farook R, Handrack J, Frey K, Marcelos T, Tessonnier T, Ecker S, Ackermann B, Ellerbrock M, Debus J and Parodi K 2014 Integration and evaluation of automated Monte Carlo simulations in the clinical practice of scanned proton and carbon ion beam therapy *Phys. Med. Biol.* **59** 4635-59

Bauer J, Unholtz D, Kurz C and Parodi K 2013 An experimental approach to improve the Monte Carlo modeling of offline PET/CT-imaging of positron emitters induced by scanned proton beams *Phys. Med. Biol.* **58** 5193-213

Beebe-Wang J, Vaska P, Dilmanian F A, Peggs S G and Schlyer D J 2003 Simulation of Proton Therapy Treatment Verification via PET Imaging of Induced Positron-Emitters *2003 IEEE Nuclear Science Symposium and Medical Imaging Conference Record* pp 2496-500

Ben J 2007 Univariate kernel density estimation (document for KDENS: Stata module for univariate kernel density estimation) *ETH Zurich, Switzerland.* Available from (`http://fmwww.bc.edu/repec/bocode/k/kdens.pdf`)

Berger M J and Hubbell J H 2010 XCOM: Photon cross sections database *National Institute of Standards and Technology (NIST) Physical Meas. Laboratory, NIST Standard Reference Database 8 (XGAM)* (`www.nist.gov`)

Bethe H 1930 Zur theorie des durchgangs schneller korpuskularstrahlen durch materie *Ann. Phys.* **5** 324–400

Bethe H A and Ashkin J 1953 Passage of Radiations through Matter, in Segré E (ed): Experimental Nuclear Physics vol. I*, Wiley, New York* p 176

Biegun A K, Seravalli E, Cambraia Lopes P, Rinaldi I, Pinto M, Oxley D C, Dendooven P, Verhaegen F, Parodi K, Crespo P and Schaart D R 2012 Time-of-flight neutron rejection to improve prompt gamma imaging for real-time proton range verification: a simulation study *Phys. Med. Biol.* **57** 6429-44

Bloch F 1933 Zur bremsung rasch bewegter teilchen beim durchgang durch materie *Ann. Phys.* **16** 285–320

Böhlen T T, Cerutti F, Chin M P W, Fassò A, Ferrari A, Ortega P G, Mairani A, Salad P R, Smirnov G and Vlachoudis V 2014 The FLUKA code: developments and challenges for high energy and medical applications *Nucl. Data Sheets* **120** 211-4

Bom V, Joulaeizadeh L and Beekman F 2012 Real-time prompt gamma monitoring in spot-scanning proton therapy using imaging through a knife-edge shaped slit *Phys. Med. Biol.* **57** 297–308

Boon S 1998 Dosimetry and quality control of scanning proton beams *PhD Thesis* University of Groningen, The Netherlands

Borghi G, Peet B J, Tabacchini V and Schaart D R 2016a A 32 mm × 32 mm × 22 mm monolithic LYSO:Ce detector with dual-sided digital photon counter readout for ultrahigh-performance TOF-PET and TOF-PET/MRI *Phys. Med. Biol.* **61** 4929-49

Borghi G, Tabacchini V and Schaart D R 2016b Towards monolithic scintillator based TOF-PET systems: practical methods for detector calibration and operation *Phys. Med. Biol.* **61** 4904-28

Bortfeld T 2006 IMRT: a review and preview *Phys. Med. Biol.* **51** R363–79

Bush D A, Kayali Z, Grove R and Slater J D 2011 The safety and efficacy of high-dose proton beam radiotherapy for hepatocellular carcinoma: a phase 2 prospective trial *Cancer* **117** 3053-9

Cambraia Lopes P, Clementel E, Crespo P, Henrotin S, Huizenga J, Janssens G, Parodi K, Prieels D, Roellinghoff F, Smeets J, Stichelbaut F and Schaart D R 2015 Time-resolved imaging of prompt-gamma rays for proton range verification using a knife-edge slit camera based on digital photon counters *Phys. Med. Biol.* **60** 6063–85

Cambraia Lopes P, Pinto M, Simões H, Biegun A K, Dendooven P, Oxley D C, Parodi K, Schaart D R and Crespo P 2012 Optimization of collimator designs for real-time proton range verification by measuring prompt gamma rays *2012 IEEE Nucl. Sci. Symp. Med. Imaging Conf. Record (NSS/MIC)* pp 3864-70

Cameron SJ, Grant IWB, Lutz W and Pearson JG 1969 The early effect of irradiation on ventilatory function in bronchial carcinoma *Clinical Radiology* **20:1** 12-8

Chadwick M B *et al* 1999 Cross-section evaluations to 150 MeV for accelerator-driven systems and implementation in MCNPX *Nucl. Sci. Eng.* **131** 293–328

Charles Nichols, Jr. R, George T J, Zaiden, Jr. R A, Awad Z T, Asbun H J, Huh S, Wei Ho M, Mendenhall N P, Morris C G and Hoppe B S 2013 Proton therapy with concomitant capecitabine for pancreatic and ampullary cancers is associated with a low incidence of gastrointestinal toxicity *Acta Oncol.* **52** 498–505

Cherry S R, Sorenson J A and Phelps M E 2003 Physics in Nuclear Medicine *Elsevier, PA: Saunders*

Cheung K Y 2006 Intensity modulated radiotherapy: advantages, limitations and future developments *Biomed. Imaging Interv. J.* **2** 19

Cirrone G A P *et al* 2009 Hadrontherapy: an Open Source, Geant4-based application for proton-ion therapy studies *2009 IEEE Nucl. Sci. Symp. Conf. Record* vol 1 pp 4186–9

Combs S E, Jäkel O, Haberer T and Debus J 2010 Particle therapy at the Heidelberg Ion Therapy Center (HIT) – Integrated research-driven university-hospital-based radiation oncology service in Heidelberg, Germany *Radiother. Oncol.* **95(1)** 41–4

Conti M 2011 Improving time resolution in time-of-flight PET *Nucl. Instrum. Methods Phys. Res. A* **648** S194–8

Crespo P 2005 Optimization of in-beam positron emission tomography for monitoring heavy ion tumor therapy, *Ph.D. Thesis, Technischen Universität Darmstadt*

Crespo P, Barthel T, Frais-Kölbl H, Griesmayer E, Heidel K, Parodi K, Pawelke J and Enghardt W 2005 Suppression of random coincidences during in-beam PET measurements at ion beam radiotherapy facilities *IEEE Trans. Nuc. Sci.* **52(4)** 980-7

Crespo P, Reis J, Couceiro M, Blanco A, Ferreira NC, Ferreira Marques R, Martins P, Fonte P 2012 Whole-body single-bed time-of-flight RPC-PET: simulation of axial and planar sensitivities with NEMA and anthropomorphic phantoms *IEEE Trans. Nucl. Sci.* **59(3)** 520-9

Crespo P, Shakirin G and Enghardt W 2006 On the detector arrangement for in-beam PET for hadron therapy monitoring *Phys. Med. Biol.* **51** 2143-63

Crespo P, Shakirin G, Fiedler F, Enghardt W and Wagner A 2007 Direct time-of-flight for quantitative, real-time in-beam PET: a concept and feasibility study *Phys. Med. Biol.* **52** 6795-811

Daube-Witherspoon M E, Surti S, Perkins A, Kyba C C M, Wiener R, Werner M E, Kulp R and Karp J S 2010 The imaging performance of a $LaBr_3$-based PET scanner *Phys. Med. Biol.* **55** 45–64

Dedes G, Pinto M, Dauvergne D, Freud N, Krimmer J, Létang J M, Ray C and Testa E 2014 Assessment and improvements of Geant4 hadronic models in the context of prompt-gamma hadrontherapy monitoring *Phys. Med. Biol.* **59** 1747-72

Degenhardt C, Prescher G, Frach Th, Thon A, de Gruyter R, Schmitz A and Ballizany R 2009 The digital silicon photomultiplier – a novel sensor for the detection of scintillation light *2009 IEEE Nuclear Science Symposium and Medical Imaging Conference Record* pp 2383-6

Degenhardt C, Rodrigues P, Trindade A, Zwaans B, Mülhens O, Dorscheid R, Thon A, Salomon A and Frach T 2012 Performance evaluation of a prototype positron emission tomography scanner using digital photon counters (DPC) *2012 IEEE Nuclear Science Symposium and Medical Imaging Conference Record* pp 2820-4

Degenhardt C, Zwaans B, Frach T and De Gruyter R 2010 Arrays of digital silicon photomultipliers—intrinsic performance and application to scintillator readout *2010 IEEE Nucl. Sci. Symp. Conf. Record* pp 1954–6

DeLaney T F 2011 Proton Therapy in the Clinic *Front. Radiat. Ther. Oncol.* **43** 465–85

Del Guerra A, Belcari N, Bisogni M G, Corsi F, Foresta M, Guerra P, Marcatili S, Santos A and Sportelli G 2011 Silicon Photomultipliers (SiPM) as novel photodetectors for PET *Nucl. Instrum. Methods Phys. Res. A* **648** Suppl 1 S232–5

Dendooven P, Biegun A K, Brandenburg S, Buitenhuis H J T, Cambraia Lopes P, Diblen F, Oxley D C, Schaart D R, van der Borden A J, van Goethem M-J, van der Schaaf A, Vandenberghe S, van 't Veld A A 2014 TOF-PET scanner configurations for quality assurance in proton therapy: a patient case study *Radiother. Oncol.* **110** (Suppl 1, 02/2014) S28-9

Dendooven P, Buitenhuis H J T, Diblen F, Heeres P N, Biegun A K, Fiedler F, van Goethem M-J, van der Graaf E R and Brandenburg S 2015 Short-lived positron emitters in beam-on PET imaging during proton therapy *Phys. Med. Biol.* **60** 8923–47

Denham J W, Hauer-Jensen M 2002 The radiotherapeutic injury – a complex 'wound' *Radiother. Oncol.* **63** 129-45

Durante M and Loeffler J S 2010 Charged particles in radiation oncology *Nat. Rev. Clin. Oncol.* **7** 37-43

Engelsman M, Schwarz M and Dong L 2013 Physics controversies in proton therapy *Semin. Radiat. Oncol.* **23** 88-96

Enghardt W, Crespo P, Fiedler F, Hinz R, Parodi K, Pawelke J and Pönisch F 2004 Charged hadron tumour therapy monitoring by means of PET *Nucl. Instrum. Meth. A* **525** 284-8

Enghardt W, Debus J, Haberer T, Hasch B G, Hinz R, Jäkel O, Krämer M, Lauckner K and Pawelke J 1999 The application of PET to quality assurance of heavy-ion tumor therapy *Strahlenther. Onkol.* **175** 33–6

Enghardt W, Parodi K, Crespo P, Fiedler F, Pawelke J and Pönisch F 2004a Dose quantification from in-beam positron emission tomography *Radiother. Oncol.* **73** Suppl 2 S96-S98

EXFOR/CSISRS 2007 Experimental nuclear reaction data (`http://www.nndc.bnl.gov/nndc/exfor/`). Accessed March 28 2007

Ferrari A, Sala P R, Fassò A and Ranft J 2005 *FLUKA: a multi-particle transport code* CERN-2005-10, INFN/TC_05/11, SLAC-R-773 Available from: `http://www.fluka.org/fluka.php?id=license&mm2=3`

Fiedler F, Shakirin G, Skowron J, Braess H, Crespo P, Kunath D, Pawelke J, Pönisch F and Enghardt W 2010 On the effectiveness of ion range determination from in-beam PET data *Phys. Med. Biol.* **55** 1989-98

Fiedler F, Kunath D, Priegnitz M and Enghardt W 2012 Online irradiation control by means of PET, in Linz U (ed): Ion Beam Therapy *Springer-Verlag Berlin Heidelberg* pp 527-43

Frach Th, Prescher G, Degenhardt C, de Gruyter R, Schmitz A and Ballizany R 2009 The digital silicon photomultiplier – principle of operation and intrinsic detector performance *2009 IEEE Nucl. Sci. Symp. Conf. Record* pp 1959-65

Frach Th, Prescher G, Degenhardt C and Zwaans B 2010 The digital silicon photomultiplier – system architecture and performance evaluation *2010 IEEE Nuclear Science Symposium Conference Record* pp 1722-7

Freeman T (ed) 2015 World's first proton therapy prompt gamma camera goes clinical *medicalphysicsweb.* Available from (`http://medicalphysicsweb.org/cws/article/newsfeed/62938`), Oct. 20, 2015

Frey K, Unholtz D, Bauer J, Debus J, Min C H, Bortfeld T, Paganetti H and Parodi K 2014 Automation and uncertainty analysis of a method for *in-vivo* range verification in particle therapy *Phys. Med. Biol.* **59** 5903-19

Futami Y, Kanai T, Fujita M, Tomura H, Higashi A, Matsufuji N, Miyahara N, Endo M and Kawachi K 1999 Broadbeam three-dimensional irradiation system for heavy-ion radiotherapy at HIMAC *Nucl. Instrum. Methods Phys. Res. A* **430** 143–53

GE Healthcare 2016 SIGNA PET/MR (`http://www3.gehealthcare.com/en/products/categories/magnetic_resonance_imaging/3-0t/signa_pet-mr`). Accessed October 9, 2016

Gola A, Piemonte C and Tarolli A 2012 The DLED algorithm for timing measurements on large area SiPMs coupled to scintillators *IEEE Trans. Nucl. Sci.* **59** 358–65

Golnik C, Hueso-González F, Müller A, Dendooven P, Enghardt W, Fiedler F, Kormoll T, Roemer K, Petzoldt J, Wagner A and Pausch G 2014 Range assessment in particle therapy based on prompt γ-ray timing measurements *Phys. Med. Biol.* **59** 5399-422

Gottschalk B 2012 Physics of proton interactions in matter, in Paganetti H (ed): Proton Therapy Physics *Boca Raton, CRC Press, Taylor & Francis Group* pp 19-59

Gottschalk B, Koehler A M, Schneider R J, Sisterson J M and Wagner M S 1993 Multiple Coulomb scattering of 160 MeV protons *Nucl. Instrum. Meth. B* **74** 467-90

Grevillot L, Frisson T, Zahra N, Bertrand D, Stichelbaut F, Freud N and Sarrut D 2010 Optimization of GEANT4 settings for proton pencil beam scanning simulations using GATE *Nucl. Instrum. Methods Phys. Res. B* **268** 3295–305

Grogg K, Alpert N M, Zhu X, Min C H, Testa M, Winey B, Normandin M D, Shih H A, Paganetti H, Bortfeld T and Fakhri G E 2015 Mapping ^{15}O production rate for proton therapy verification *Int. J. Radiation Oncol. Biol. Phys.* **92(2)** 453-9

Gueth P *et al* 2013 Machine learning-based patient specific prompt-gamma dose monitoring in proton therapy *Phys. Med. Biol.* **58** 4563-77

Haberer T, Becher W, Schardt D and Kraft G 1993 Magnetic scanning system for heavy ion therapy *Nucl. Instrum. Methods Phys. Res. A* **330** 296–305

Haberer T, Debus J, Eickhoff H, Jäkel O, Schultz-Ertner D and Weber U 2004 The Heidelberg ion therapy center *Radiother. Oncol.* **73** S186–90

Haemisch Y, Frach Th, Degenhardt C, Thon A 2012 Fully Digital Arrays of Silicon Photomultipliers (dSiPM) – a Scalable Alternative to Vacuum Photomultiplier Tubes (PMT) *Physics Procedia* **37** 1546-60

Härdle W, Müller M, Sperlich S and Werwatz A 2004 Nonparametric and Semiparametric Models *Springer*

Helmbrecht S, Santiago A, Enghardt W, Kuess P and Fiedler F 2012 On the feasibility of automatic detection of range deviations from in-beam PET data *Phys. Med. Biol.* **57** 1387-97

Henriquet P, Testa E, Chevallier M, Dauvergne D, Dedes G, Freud N, Krimmer J, Létang J M, Ray C, Richard M-H and Sauli F 2012 Interaction vertex imaging (IVI) for carbon ion therapy monitoring: a feasibility study *Phys. Med. Biol.* **57** 4655–69

Herault J, Iborra N, Serrano B and Chauvel P 2005 Monte Carlo simulation of a protontherapy platform devoted to ocular melanoma *Med. Phys.* **32** 910–9

Hiraoa Y *et al* 1992 Heavy ion synchrotron for medical use-HIMAC project at NIRS-Japan *Nucl. Phys. A* **538** 541–50

Hubbell J H and Seltzer S M 2004 X-Ray Attenuation and Absorption for materials of Dosimetric Interest *National Institute of Standards and Technology (NIST) Physical Meas. Laboratory, NIST Standard Reference Database 126* (`www.nist.gov`)

Hueso-González F, Enghardt W, Fiedler F, Golnik C, Janssens G, Petzoldt J, Prieels D, Priegnitz M, Römer K E, Smeets J, Stappen F V, Wagner A and Pausch G 2015 First test of the prompt gamma ray timing method with heterogeneous targets at a clinical proton therapy facility *Phys. Med. Biol.* **60** 6247-72

ICRU 1984 Stopping powers for electrons and positrons *ICRU Report 37* Bethesda, MD, USA

ICRU 1993 Stopping powers and ranges for protons and alpha particles *ICRU Report 49* Bethesda, MD, USA

Iljinov A S, Semenov V G and Semenova M P *et al* 1991 Production of radionuclides at intermediate energies. *Geneva: Springer-Verlag*

Iljinov A S, Semenov V G, Semenova M P, Sobolevsky N M and Udovenko L V 1991 *Production of radionuclides at intermediate energies* (Berlin: Springer) Landolt-Börnstein New Series Group I vol 13a

Iseki Y, Mizuno H, Futami Y, Tomitani T, Kanai T, Kanazawa M, Kitagawa A, Murakami T, Nishio T, Suda M, Urakabe E, Yunoki A, Sakai H 2003 Positron camera for range verification of heavy-ion radiotherapy *Nucl. Instr. Meth. Phys. Res. A* **515** 840–9

Janssen F M F C, Landry G, Cambraia Lopes P, Dedes G, Smeets J, Schaart D R, Parodi K and Verhaegen F 2014 Factors influencing the accuracy of beam range estimation in proton therapy using prompt gamma emission *Phys. Med. Biol.* **59** 4427-41

Kang B H and Kim J W 2009 Monte Carlo design study of a gamma detector system to locate distal dose falloff in proton therapy *IEEE Trans. Nucl. Sci.* **56** 46–50

Kim C L, Wang G-C and Dolinsky S 2009 Multi-pixel photon counters for TOF PET detector and its challenges *IEEE Trans. Nucl. Sci.* **56** 2580–5

Kim D, Yim H and Kim J-W 2009b Pinhole camera measurements of prompt gamma-rays for detection of beam range variation in proton therapy *J. Korean Phys. Soc.* **55(4)** 1673-76

Knopf A-C and Lomax A 2013 *In vivo* proton range verification: a review *Phys. Med. Biol.* **58** R131-R160

Knopf A, Parodi K, Bortfeld T, Shih H A and Paganetti H 2009 Systematic analysis of biological and physical limitations of proton beam range verification with offline PET/CT scans *Phys. Med. Biol.* **54** 4477-95

Kopf U, Heeg P, Emde P 2004 The gantry irradiation room at the Heidelberg irradiation facility *GSI Rep. 2004-1 (Ann. Rep. 2003)* p 183

Kormoll T, Fiedler F, Schöne S, Wüstemann J, Zuber K and Enghardt W 2011 A Compton imager for *in vivo* dosimetry of proton beams: a design study *Nucl. Instrum. Methods Phys. Res. A* **626–7** 114–9

Kozaki K, Ecker S, Habermehl D, Rieken S, Jäkel O, Herfarth K, Debus J and Combs S E 2012 Comparison of intensity modulated radiotherapy (IMRT) with intensity modulated particle therapy (IMPT) using fixed beams or an ion gantry for the treatment of patients with skull base meningiomas *Radiation Oncology* **7:44**

Kozlovsky B, Murphy R J and Ramaty R 2002 Nuclear deexcitation gamma-ray lines from accelerated particle interactions *Astrophys. J. Suppl. Ser.* **141** 523-41

Kraan A C, van de Water S, Teguh D N, Al-Mamgani A, Madden T, Kooy H M, Heijmen B J and Hoogeman M S 2013 Dose uncertainties in IMPT for oropharyngeal cancer in the presence of anatomical, range, and setup errors *Int. J. Radiat. Oncol. Biol. Phys.* **87(5)** 888-96

Kraft G 2000 Tumor therapy with heavy charged particles *Prog. Part. Nucl. Phys.* **45** 473-544

Kraft G, Scholz M, Bechthold U 1999 Tumor therapy and track structure *Radiat. Environ. Biophys.* **38(4)** 229237

Krämer M and Kraft G 1994 Calculations of heavy ion track structure *Radiat. Environ. Bioph.* **33(2)** 91109

Krimmer J *et al* 2012 Progress in using prompt gammas for ion range monitoring during hadrontherapy *Radiother. Oncol.* **102** (Suppl 1) S71–2

Kurosawa S *et al* 2012 Prompt gamma detection for range verification in proton therapy *Curr. Appl. Phys.* **12** 364-8

Llosá G, Barrio J, Cabello J, Crespo A, Lacasta C, Rafecas M, Callier S, de La Taille C and Raux L 2011 Detector characterization and first coincidence tests of a Compton telescope based on LaBr3 crystals and SiPMs *Nucl. Instrum. Methods Phys. Res. A* **695** 105-8

Llosá G, Barrio J, Lacasta C, Callier S, Raux L and Taille C L 2010 First tests in the application of silicon photomultiplier arrays to dose monitoring in hadron therapy *Nucl. Instrum. Methods Phys. Res. A* **648** S96–9

Lois C, Jakoby B W, Long M J, Hubner K F, Barker D W, Casey M E, Conti M, Panin V Y, Kadrmas D J and Townsend D W 2010 An assessment of the impact of incorporating time-of-flight information into clinical PET/CT imaging *J. Nucl. Med.* **51** 237-45

Lomax A J 2008a Intensity modulated proton therapy and its sensitivity to treatment uncertainties 1: the potential effects of calculational uncertainties *Phys. Med. Biol.* **53** 1027–42

Lomax A J 2008b Intensity modulated proton therapy and its sensitivity to treatment uncertainties 2: the potential effects of inter-fraction and inter-field motions *Phys. Med. Biol.* **53** 1043–56

Lomax A J, Bortfeld T, Goitein G, Debus J, Dykstra C, Tercier P-A, Coucke P-A and Mirimanoff R O 1999 A treatment planning inter-comparison of proton and intensity modulated photon radiotherapy *Radiother. Oncol.* **51** 257-71

Lu H-M and Flanz J 2011 Characteristics of clinical proton beams, in Paganetti H (ed): Proton Therapy Physics *Boca Raton, CRC Press* pp 103-24

Maccabee H D, Madhvanath U and Raju M R 1969 Tissue activation studies with alpha-particle beams *Phys. Med. Biol.* **14** 213-24

Mashnik S G 2006 Implementation of CEM03.01 into MCNP6 and its Verification and Validation Running Through MCNP6 CEM03.02 Upgrade Research Note X-3-RN(U)-07-03, Los Alamos National Laboratory

MCNPX 2002 MCNPX 2.3.0 User's Guide Report LA-UR-02-2607, Los Alamos National Laboratory

MCNPX 2008 MCNPX 2.6.0 Users's Guide Report LA-CP-07-1473, Los Alamos National Laboratory

Min C H, Lee H R, Kim C H and Lee S B 2012 Development of array-type prompt gamma measurement system for *in vivo* range verification in proton therapy *Med. Phys.* **39(5)** 2100-7

Min C H, Lee H R, Yeom Y S, Cho S and Kim C H 2010 Determination of the distal dose edge in a human phantom by measuring the prompt gamma distribution: a Monte Carlo study *J. Korean Phys. Soc.* **56(6)** 2059-62

Min C-H, Kim C H, Youn M-Y and Kim J-W 2006 Prompt gamma measurements for locating the dose fall-off region in the proton therapy *Appl. Phys. Lett.* **89** 183517

Min C H, Zhu X, Winey B A, Grogg K, Testa M, Fakhri G E, Bortfeld T R, Paganetti H and Shih H A 2013 Clinical application of in-room positron emission tomography for in vivo treatment monitoring in proton radiation therapy *Int. J. Radiation Oncol. Biol. Phys.* **86(1)** 183-9

Molière G 1948 Theorie der Streuung schneller geladener Teilchen II, Mehrfach- und Vielfachstreuung *Z. Naturforschung A* **3** 78-97

Moteabbed M, Espana S and Paganetti H 2011 Monte Carlo patient study on the comparison of prompt gamma and PET imaging for range verification in proton therapy *Phys. Med. Biol.* **56** 1063–82

Müller B S, Duma M N, Kampfer S, Nill S, Oelfke U, Geinitz H and Wilkens J J 2015 Impact of interfractional changes in head and neck cancer patients on the delivered dose in intensity modulated radiotherapy with protons and photons *Physica Medica* **31** 266-72

De Napoli M, Romano F, 'Urso D D, Licciardello T, Agodi C, Candiano G, Cappuzzello F, Cirrone G A P, Cuttone G, Musumarra A, Pandola L and Scuderi V 2014 Nuclear reaction measurements on tissue-equivalent materials and GEANT4 Monte Carlo simulations for hadrontherapy *Phys. Med. Biol.* **59** 7643–52

Newhauser W D and Zhang R 2015 The physics of proton therapy *Phys. Med. Biol.* **60** R155-R209

Nishio T, Miyatake A, Ogino T, Nakagawa K, Saijo N and Esumi H 2010 The development and clinical use of a beam on-line system mounted on a rotating gantry port in proton therapy *Int. J. Radiation Oncology Biol. Phys.* **76(1)** 277-86

Nishio T, Ogino T, Nomura K and Uchida H 2006 Dose-volume delivery guided proton therapy using beam on-line PET system *Med. Phys.* **33:11** 4190-7

Ondreka D and Weinrich U 2008 The Heidelberg Ion Therapy (HIT) acceleration coming into operation *Proc. Eur. Phys. Soc. Accelerator Group (Genoa, Italy)* vol 1 pp 979–81

Okada T, Kamada T, Tsuji H, Mizoe J, Baba M, Kato S, Yamada S, Sugahara S, Yasuda S, Yamamoto N, Imai R, Hasegawa A, Imada H, Kiyohara H, Jingu K, Shinoto M and Tsujii H 2010 Carbon Ion Radiotherapy: Clinical Experiences at National Institute of Radiological Science (NIRS) *J. Radiat. Res.* **51** 355–64

Paganetti H 2012 Range uncertainties in proton therapy and the role of Monte Carlo simulations *Phys. Med. Biol.* **57** R99-R117

Parodi K 2004 On the feasibility of dose quantification with in-beam PET data in radiotherapy with ^{12}C and proton beams *Ph.D. Thesis*, *Technischen Universität Dresden*

Parodi K 2012 PET monitoring of hadrontherapy *Nucl. Med. Rev.* **15** (Suppl. C) C37-42. Article available via: `http://www.nmr.viamedica.pl`, ISSN 1506–9680

Parodi K, Bortfeld T and Haberer T 2008 Comparison between in-beam and offline positron emission tomography imaging of proton and carbon ion therapeutic irradiation at synchrotron- and cyclotron-based facilities *Int. J. Radiation Oncol. Biol. Phys.* **71(3)** 945-56

Parodi K, Crespo P, Eickhoff H, Haberer T, Pawelke J, Schardt D and Enghardt W 2005a Random coincidences during in-beam PET measurements at microbunched therapeutic ion beams *Nucl. Instr. Meth. Phys. Res. A* **545** 446-58

Parodi K and Enghardt W 2000 Potential application of PET in quality assurance of proton therapy *Phys. Med. Biol.* **45** N151-6

Parodi K, Enghardt W and Haberer T 2002 In-beam PET measurements of β^+-radioactivity induced by proton beams *Phys. Med. Biol.* **47** 21-36

Parodi K, Ferrari A, Sommerer F and Paganetti H 2007a Clinical CT-based calculations of dose and positron emitter distributions in proton therapy using the FLUKA Monte Carlo code *Phys. Med. Biol.* **52** 3369-87

Parodi K, Mairani A, Brons S, Hasch B G, Sommerer F, Naumann J, Jäkel O, Haberer T and Debus J 2012 Monte Carlo simulations to support start-up and treatment planning of scanned proton and carbon ion therapy at a synchrotron-based facility *Phys. Med. Biol.* **57** 3759–84

Parodi K, Paganetti H, Shih HA, Michaud S, Loeffler JS, DeLaney TF, Liebsch NJ, Manzenrider JE, Fischman AJ, Knopf A and Bortfeld T 2007b Patient study of *in vivo* verification of beam delivery and range, using positron emission tomography and computed tomography imaging after proton therapy *Int. J. Radiat. Oncol. Biol. Phys.* **68(3)** 920-34. doi:10.1016/j.ijrobp.2007.01.063

Parodi K, Pönisch F and Enghardt W 2005b Experimental study on the feasibility of in-beam PET for accurate monitoring of proton therapy *IEEE Trans. Nuc. Sci.* **52(3)** 778-86

Pedroni E *et al* 2004 The PSI gantry 2: a second generation proton scanning gantry Z. *Med. Phys.* **14** 25–34

Peloso R, Busca P, Fiorini C, Basilavecchia M, Frizzi T, Smeets J, Roellinghoff F, Prieels D, Stichelbaut F and Benilov A 2011 Application of the HICAM camera for imaging of prompt gamma rays in measurements of proton beam range *IEEE Nucl. Sci. Symp. Conf. Record* vol 1 pp 2285–9

Perali I, Celani A, Bombelli L, Fiorini C, Camera F, Clementel E, Henrotin S, Janssens G, Prieels D, Roellinghoff F, Smeets J, Stichelbaut F and Vander Stappen F 2014 Prompt gamma imaging of proton pencil beams at clinical dose rate *Phys. Med. Biol.* **59** 5849-71

Peterson S W, Robertson D and Polf J 2010 Optimizing a three-stage Compton camera for measuring prompt gamma rays emitted during proton radiotherapy *Phys. Med. Biol.* **55** 6841–56

Philips-Healthcare 2015 Vereos PET/CT product brochure *Koninklijke Philips N.V., The Netherlands,* June 2015

Phillips M H, Pedroni E, Blattmann H, Boehringer T, Coray A and Scheib S 1992 Effects of respiratory motion on dose uniformity with a charged particle scanning method *Phys. Med. Biol.* **37(1)** 223-34

Pinto M, Bajard M, Brons S, Chevallier M, Dauvergne D, Dedes G, De Rydt M, Freud N, Krimmer J, La Tessa C, Létang J M, Parodi K, Pleskač R, Prieels D, Ray C, Rinaldi I, Roellinghoff F, Schardt D, Testa E and Testa M 2015 Absolute prompt-gamma yield measurements for ion beam therapy monitoring *Phys. Med. Biol.* **60** 565–94

Pinto M, Dauvergne D, Freud N, Krimmer J, Letang J M, Ray C, Roellinghoff F and Testa E 2014 Design optimisation of a TOF-based collimated camera prototype for online hadrontherapy monitoring *Phys. Med. Biol.* **59** 7653-74

Polf J C, Mackin D, Lee E, Avery S and Beddar S 2014 Detecting prompt gamma emission during proton therapy: the effects of detector size and distance from the patient *Phys. Med. Biol.* **59** 2325-40

Polf J C, Panthi R, Mackin D S, McCleskey M, Saastamoinen A, Roeder B T and Beddar S 2013 Measurement of characteristic prompt gamma rays emitted from oxygen and carbon in tissue-equivalent samples during proton beam irradiation *Phys. Med. Biol.* **58** 5821–31

Polf J C, Peterson S, Ciangaru G, Gillin M and Beddar S 2009a Prompt gamma-ray emission from biological tissues during proton irradiation: a preliminary study *Phys. Med. Biol.* **54** 731–43

Polf J C, Peterson S, McCleskey M, Roeder B T, Spiridon A, Beddar S and Trache L 2009b Measurement and calculation of characteristic prompt gamma ray spectra emitted during proton irradiation *Phys. Med. Biol.* **54** N519–27

Powolny F *et al* 2011 Time-based readout of a silicon photomultiplier (SiPM) for time of flight positron emission tomography (TOF-PET) *IEEE Trans. Nucl. Sci.* **58** 597–604

Prieels D, Smeets J, Stichelbaut F, Benilov A, Dehaes J C, Dubus A and Roellinghoff F 2011 Towards a practical solution for real-time measurement of the proton beam range in patients *50th Particle Therapy Co-Operative Group (PTCOG) Meeting (Philadelphia, PA, 8–14 May 2011)*

Priegnitz M, Helmbrecht S, Janssens G, Perali I, Smeets J, Vander Stappen F, Sterpin E and Fiedler F 2015 Measurement of prompt gamma profiles in inhomogeneous targets with a knife-edge slit camera during proton irradiation *Phys. Med. Biol.* **60** 4849-71

PTCOG 2014 PTCOG patient statistics of particle therapy centers per end of 2013

Rafecas M, Böning G, Pichler B J, Lorenz E, Schwaiger M and Ziegler S I 2003 Inter-crystal scatter in a dual layer, high resolution LSO-APD positron emission tomograph *Phys. Med. Biol.* **48** 821-48

Richard M H *et al* 2009 Design study of a Compton camera for prompt gamma imaging during ion beam therapy *2009 IEEE Nuclear Science Symp. Conf. Record (NSS/MIC)* pp 4172-75

Richard M H *et al* 2011 Design guidelines for a double scattering Compton camera for prompt gamma imaging during ion beam therapy: a Monte Carlo simulation study *IEEE Trans. Nucl. Sci.* **58** 87-94

Robert C, Dedes G, Battistoni G, Böhlen T T, Buvat I, Cerutti F, Chin M P W, Ferrari A, Gueth P, Kurz C, Lestand L, Mairani A, Montarou G, Nicolini R, Ortega P G, Parodi K, Prezado Y, Sala P R, Sarrut D and Testa E 2013 Distributions of secondary particles in proton and carbon-ion therapy: a comparison between GATE/Geant4 and FLUKA Monte Carlo codes *Phys. Med. Biol.* **58** 2879-99

Robertson D, Polf J C, Peterson S W, Gillin M T and Beddar S 2011 Material efficiency studies for a Compton camera designed to measure characteristic prompt gamma rays emitted during proton beam radiotherapy *Phys. Med. Biol.* **56** 3047–39

Roellinghoff F *et al* 2011 Design of Compton camera for 3D prompt-γ imaging during ion beam therapy *Nucl. Instrum. Methods Phys. Res. A* **648** S20–3

Roellinghoff F *et al* 2012 Real-time proton beam range monitoring by means of prompt-gamma detection with a collimated camera *Radiother. Oncol.* **102** Suppl 1 S120

Roellinghoff F, Benilov A, Dauvergne D, Dedes G, Freud N, Janssens G, Krimmer J, Létang J M, Pinto M, Prieels D, Ray C, Smeets J, Stichelbaut F and Testa E 2014 Real-time proton beam range monitoring by means of prompt-gamma detection with a collimated camera *Phys. Med. Biol.* **59** 1327-38

Salomon A, Goedicke A, Schweizer B, Aach T and Schulz V 2011 Simultaneous reconstruction of activity and attenuation for PET/MR *IEEE Trans. Med. Imaging* **30** 804-13

Sarrut D, Bardiès M, Boussion N, Freud N, Jan S, Létang J-M, Loudos G, Maigne L, Marcatili S, Mauxion T, Papadimitroulas P, Perrot Y, Pietrzyk U, Robert C, Schaart D R, Visvikis D and Buvat I 2014 A review of the use and potential of the GATE Monte Carlo simulation code for radiation therapy and dosimetry applications *Med. Phys.* **41** 064301

Sawakuchi G O, Mirkovic D, Perles L A, Sahoo N, Zhu X R, Ciangaru G, Suzuki K, Gillin M T, Mohan R and Titt U 2010 An MCNPX Monte Carlo model of a discrete spot scanning proton beam therapy nozzle *Med. Phys.* **37** 4960–70

Schaart D R, Charbon E, Frach T and Schulz V 2016 Advances in digital SiPMs and their application in biomedical imaging (invited), in special issue: Advances in detectors and applications for medicine *Nucl. Instrum. Methods Phys. Res. A* **809** 31–52

Schaart D R, Seifert S, Vinke R, van Dam H T, Dendooven P, Löhner H and Beekman F J 2010 LaBr(3):Ce and SiPMs for time-of-flight PET: achieving 100 ps coincidence resolving time *Phys. Med. Biol.* **55** N179–N189

Schaffner B and Pedroni E 1998 The precision of proton range calculations in proton radiotherapy treatment planning: experimental verification of the relation between CT-HU and proton stopping power *Phys. Med. Biol.* **43** 1579–92

Schardt D, Elsässer T and Schulz-Ertner D 2010 Heavy-ion tumor therapy: Physical and radiobiological benefits *Rev. Mod. Phys.* **82(1)** 383–425

Schippers J M 2009 Beam delivery systems for particle radiation therapy: current status and recent developments *Rev. Accel. Sci. Technol.* **2** 179–200

Schneider U and Pedroni E 1995 Proton radiography as a tool for quality control *Med. Phys.* **22** 353–63

Schulz-Ertner D, Karger C, Feurhake H, Nikoghosyan A, Combs S E, Jäkel O, Edler L, Scholz M and Debus J 2007 Effectiveness of carbon ion radiotherapy in the treatment of skull-base chordomas *Int. J. Radiat. Oncol. Biol. Phys.* **68** 449–57

Schulz-Ertner D, Nikoghosyan A, Muenter M, Jäkel O, Karger C and Debus J 2004 Optimized therapy strategies for locally advanced adenoid cystic carcinomas using modern radiation therapy techniques *Int. J. Radiat. Oncol. Biol. Phys.* **60** S504

Schumann A, Petzoldt J, Dendooven P, Enghardt W, Golnik C, Hueso-González F, Kormoll T, Pausch G, Roemer K and Fiedler F 2015 Simulation and experimental verification of prompt gamma-ray emissions during proton irradiation *Phys. Med. Biol.* **60** 4197–207

Schwaab J, Brons S, Fieres J and Parodi K 2011 Experimental characterization of lateral profiles of scanned proton and carbon ion pencil beams for improved beam models in ion therapy treatment planning *Phys. Med. Biol.* **56** 7813–27

Scott D W 1992 Multivariate Density Estimation: Theory, Practice, and Visualization *New York: Wiley*

Segars W P 2001 Development of a new dynamic NURBS-based cardiac-torso (NCAT) phantom *Ph.D. dissertation, The University of North Carolina*

Seifert S, Huizenga J, van Dam H T, Vinke R, Dendooven P, Löhner H, Beekman F J and Schaart D R 2012a Monolithic $LaBr_3$:Ce crystals on silicon photomultiplier arrays for time-of-flight positron emission tomography *Phys. Med. Biol.* **57** 2219–33

Seifert S, van Dam H T and Schaart D R 2012b The lower bound on the timing resolution of photon counting scintillation detectors *Phys. Med. Biol.* **57** 1797–814

Seravalli E, Robert C, Bauer J, Stichelbaut F, Kurz C, Smeets J, Van Ngoc Ty C, Schaart D R, Buvat I, Parodi K and Verhaegen 2012 Monte Carlo calculations of positron emitter yields in proton radiotherapy *Phys. Med. Biol.* **57** 1659-73

Shakirin G, Braess H, Fiedler F, Kunath D, Laube K, Parodi K, Priegnitz M and Enghardt W 2011 Implementation and workflow for PET monitoring of therapeutic ion irradiation: a comparison of in-beam, in-room, and off-line techniques *Phys. Med. Biol.* **56** 1281-98

Shao Y, Sun X, Lou K, Zhu X R, Mirkovic D, Poenisch F and Grosshans D 2014 In-beam PET imaging for on-line adaptive proton therapy: an initial phantom study *Phys. Med. Biol.* **59** 3373-88

Shepp L A and Vardi Y 1982 Maximum likelihood reconstruction for emission tomography *IEEE Transactions on Medical Imaging* **1** 113-22

Smeets J *et al* 2012a Prompt gamma imaging with a slit camera for real time range control in proton therapy *Radiother. Oncol.* **102** (Suppl 1) S32–3

Smeets J, Roellinghoff F, Prieels D, Stichelbaut F, Benilov A, Busca P, Fiorini C, Peloso R, Basilavecchia M, Frizzi T, Dehaes J C and Dubus A 2012b Prompt gamma imaging with a slit camera for real-time range control in proton therapy *Phys. Med. Biol.* **57** 3371–405

Smith A R 2009 Vision 20/20: Proton therapy *Med. Phys.* **36(2)** 556-68

Somlai-Schweiger I, Schneider F R and Ziegler S I 2015 Performance analysis of digital silicon photomultipliers for PET *JINST* **10** P05005

Sportelli G, Belcari N, Camarlinghi N, Cirrone G A P, Cuttone G, Ferretti S, Kraan A, Ortuño J E, Romano F, Santos A, Straub K, Tramontana A, Del Guerra A and Rosso V 2014 First full-beam PET acquisitions in proton therapy with a modular dual-head dedicated system *Phys. Med. Biol.* **59** 43-60

Stichelbaut F and Jongen Y 2003 Verification of the proton beam position in the patient by the detection of prompt gamma-rays emission 505 *39th Meeting of the Particle Therapy Co-Operative Group (San Francisco, CA)*

Surti S and Karp J S 2008 Design considerations for a limited angle, dedicated breast, TOF PET scanner *Phys. Med. Biol.* **53** 2911–21

Surti S, Zou W, Daube-Witherspoon M E, McDonough J and Karp J S 2011 Design study of an *in situ* PET scanner for use in proton beam therapy *Phys. Med. Biol.* **56** 2667-85

Tabacchini V, Westerwoudt V, Borghi G, Seifert S and Schaart D R 2014 Probabilities of triggering and validation in a digital silicon photomultiplier *JINST* **9** P06016

Tashima H, Yamaya T, Yoshida E, Kinouchi S, Watanabe M and Tanaka E 2012 A single-ring OpenPET enabling PET imaging during radiotherapy *Phys. Med. Biol.* **57** 4705-18

Testa M, Bajard M, Chevallier M, Dauvergne D, Freud N, Henriquet P, Karkar S, Le Foulher F, Létang J M, Plescak R, Ray C, Richard M-H, Schardt D and Testa E 2010 Real-time monitoring of the Bragg-peak position in ion therapy by means of single photon detection *Radiat. Environ. Biophys*. **49** 337–43

Testa E, Bajard M, Chevallier M, Dauvergne D, Le Foulher F, Freud N, Létang J-M, Poizat J-C, Ray C and Testa M 2008 Monitoring the Bragg peak location of 73 MeV/u carbon ions by means of prompt gamma-ray measurement *Appl. Phys. Lett.* **93** 093506

Testa E, Bajard M, Chevallier M, Dauvergne D, Le Foulher F, Freud N, Létang J M, Poizat J C, Ray C, Testa M 2009 Dose profile monitoring with carbon ions by means of prompt-gamma measurements *Nucl. Instr. Meth. Phys. Res. B* **267** 993-6

Thirolf P G 2015 Medical imaging: development of a Compton camera system as a versatile tool for position-sensitive photon detection (`http://www.ha.physik.uni-muenchen.de/research/new-detectors/index.html`). Accessed December 19, 2015

Thirolf P G, Aldawood S, Boehmer M, Bortfeldt J, Castelhano I, Gernhaeuser R, v.d. Kolff H, Lang C, Maier L, Schaart D R and Parodi K 2014a Development of a Compton camera prototype for online range verification of laser-accelerated proton beams *Med. Phys.* **41** 165

Thirolf P G, Lang C, Aldawood S, v.d. Kolff H, Maier L, Schaart D R and Parodi K 2014b Development of a Compton camera for online range monitoring of laser-accelerated proton beams via prompt-gamma detection *EPJ Web of Conferences* **66** 11036

Lewellen T and Karp J 2004 Pet systems, in Wernick M N and Aarsvold J N (eds): Emission tomography: the fundamentals of PET and SPECT *Elsevier Inc., San Diego / London*

van Dam H T, Borghi G, Seifert S and Schaart D R 2013 Sub-200 ps CRT in monolithic scintillator PET detectors using digital SiPM arrays and maximum likelihood interaction time estimation *Phys. Med. Biol.* **58** 3243-57

van Dam H T, Seifert S and Schaart D R 2012 The statistical distribution of the number of counted scintillation photons in digital silicon photomultipliers: model and validation *Phys. Med. Biol.* **57** 4885-903

van Dam H T, Seifert S, Vinke R, Dendooven P, Lohner H, Beekman F J and Schaart D R 2011 Improved nearest neighbor methods for gamma photon interaction position determination in monolithic scintillator PET detectors *IEEE Trans. Nucl. Sci.* **58** 2139–47

van der Laan H P, van de Water T A, van Herpt H E, Christianen M E M C, Bijl H P, Korevaar E W, Rasch C R, van 'T Veld A A, van der Schaaf A, Schilstra C, Langendijk J A and on behalf of the Rococo cooperative group 2013 The potential of intensity-modulated proton radiotherapy to reduce swallowing dysfunction in the treatment of head and neck cancer: A planning comparative study *Acta Oncologica* **52(3)** 561–9

van der Lei G J, Van Dam H T, Seifert S and Schaart D R 2011 First performance measurements of monolithic scintillators coupled to digital SiPM arrays for TOF-PET *2011 IEEE Nucl. Sci. Symp.Medical Imaging Conf.* MIC15. S-83

van de Water T A, Lomax A J, Bijl H P, de Jong M E, Schilstra C, Hug E B, Langendijk J A 2011 Potential benefits of scanned intensity-modulated proton therapy versus advanced photon therapy with regard to sparing of the salivary glands in oropharyngeal cancer *Int. J. Radiation Oncology Biol. Phys.* **79(4)** 1216–24

Verburg J M, Riley K, Bortfeld T and Seco J 2013 Energy- and time-resolved detection of prompt gamma-rays for proton range verification *Phys. Med. Biol.* **58** L37–L49

Verburg J M and Seco J 2012 CT metal artifact reduction method correcting for beam hardening and missing projections *Phys. Med. Biol.* **57** 2803–18

Verburg J M and Seco J 2013 Dosimetric accuracy of proton therapy for chordoma patients with titanium implants *Med. Phys.* **40** 071727

Verburg J M and Seco J 2014 Proton range verification through prompt gamma-ray spectroscopy *Phys. Med. Biol.* **59** 7089–106

Verburg J M, Shih H A and Seco J 2012 Simulation of prompt gamma-ray emission during proton radiotherapy *Phys. Med. Biol.* **57** 5459–72

Waters L S 2010 private communication, Los Alamos National Laboratory

Weyrather W K and Debus J 2003 Particle Beams for Cancer Therapy *Clin. Oncol.* **15** S23–8

Wilson R R 1946 Radiological use of fast protons *Radiology* **47(11)** 487–91

Yang M, Ronald Zhu X, Park P C, Titt U, Mohan R, Virshup G, Clayton J E and Dong L 2012 Comprehensive analysis of proton range uncertainties related to patient stopping-power-ratio estimation using the stoichiometric calibration *Phys. Med. Biol.* **57** 4095–115

Yang M, Virshup G, Clayton J, Zhu X R, Mohan R and Dong L 2010 Theoretical variance analysis of single- and dual-energy computed tomography methods for calculating proton stopping power ratios of biological tissues *Phys. Med. Biol.* **55** 1343–62

Zhu X, España S, Daartz J, Liebsch N, Ouyang J, Paganetti H, Bortfeld T R and El Fakhri G 2011 Monitoring proton radiation therapy with in-room PET imaging *Phys. Med. Biol.* **56** 4041-57

Summary

Particle therapy (PT), including proton therapy, has important advantages compared to external beam photon therapy (section 1.1). This is because most of the therapeutic effect of a proton beam is localized at the endpoint, where most of its energy is imparted to the medium (Bragg peak), with nearly no dose deposited beyond that point. However, the highly localized dose deposition makes proton therapy more sensitive to (1) patient morphological alterations, including tumor progression / regression, (2) organ motion, (3) patient setup errors, (4) tissue lateral heterogeneities that render the results obtained with non-Monte-Carlo-based treatment planning algorithms unreliable to some degree, (5) beam characteristics utilized for treatment planning, and (6) the conversion of Hounsfield units (computed tomography data), to tissue density and stoichiometry. In addition, uncertainties in the mean excitation potential I, necessary to calculate the stopping power of the penetrating ions, further contribute to potential beam range inaccuracies.

Given the aforementioned sources of treatment error, an imaging technique capable of providing feedback proportional to the quality of the treatment being delivered is highly desired and a very active field of research in proton therapy (section 1.2). Specifically, it is of utmost importance to develop an imaging technique capable of providing feedback with respect to the *in vivo* beam range, especially when highly-heterogeneous beam paths are crossed by a pencil beam. Such a imaging technique can make use of secondary gamma (γ) radiation emitted by the patient, as a result of nuclear interactions between the projectiles and the nuclei of the irradiated medium. These techniques are mainly divided into two categories, according to the type of secondary γ rays probed: (1) positron emission tomography (PET), which makes use of delayed emission, namely pairs of 511 keV annihilation photons, resulting from β^+-decay; and (2) prompt gamma (PG) imaging, which makes use of the emission of single photons typically on a sub-nanosecond timescale.

In this thesis, several such imaging techniques were put forward, viz. a dual-head time-of-flight positron emission tomograph (TOF-PET), a knife-edge-slit prompt-gamma camera, and a multi-slat PG camera, with both PG cameras assisted by TOF for background rejection. The following imaging techniques were tested experimentally for the first time (in prototype form) with innovative photon detectors (viz. digital photon counters, DPCs): TOF-PET (chapter 2), knife-edge-slit PG camera (chapter 4), and single-parallel-slit PG detector as a simplified prototype of a multi-slat PG camera (chapter 5). While the TOF-PET measurements were performed at a clinical synchrotron with a beam energy of about 126 MeV, the PG-based measurements were realized at a clinical proton cyclotron with a proton bunch width of about 1.1 ns full width at half maximum (FWHM) for a beam energy of 160 MeV. The fast timing performance of the DPC in combination with a fast, high light-output scintillator crystal (Cerium-doped Lutetium Yttrium Silicate, LYSO:Ce) enabled excellent detector time resolution, which has been demonstrated to be a very important parameter for all of the imaging techniques studied in this thesis.

In addition to experimental demonstrations of *in situ* PET- and PG-based imaging techniques for monitoring proton therapy, this thesis also explored, by means of Monte Carlo (MC) simulations, methodologies enabling an improvement of the PG imaging technique: (1) the concept of a shifting TOF window correlated with the transit time of the stopping ions in tissue was suggested (chapter 3), and (2) the application of a multi-slat collimator system was analyzed for the first time in realistic treatment scenarios (anthropomorphic phantom), considering potential tissue morphological alterations, which gave rise to proton range shifts of a few cm and as low as 2 mm (chapter 6).

TOF-PET

PET is the imaging modality most extensively tested for treatment monitoring in PT. Optimal use of PET in proton therapy requires *in situ* acquisition of the relatively strong ^{15}O signal due to its relatively short half-life (~2 min) and high oxygen content in biological tissues, enabling shorter scans that are less sensitive to biological washout.

Chapter 2 presents the first performance tests of a scaled-down *in situ* TOF-PET system based on DPCs coupled to LYSO:Ce crystals, providing quantitative results representative of a dual-head tomograph that complies with spatial constraints typically encountered in clinical practice ($2 \times 50°$, of 360°, transaxial angular acceptance). The proton-induced activity inside polymethylmethacrylate (PMMA) and polyethylene (PE) phantoms was acquired within beam pauses (in-beam) and immediately after irradiation by an actively-delivered synchrotron pencil beam, with clinically relevant 125.67 MeV/u, 4.6×10^8 protons/s, and 10^{10} total protons. Three-dimensional activity maps reconstructed with and without TOF information were compared to FLUKA simulations, demonstrating the benefit of TOF-PET to reduce limited-angle artefacts using a 382 ps FWHM coincidence resolving time.

The time-dependent contributions from different radionuclides to the total count-rate were investigated. We furthermore studied the impact of the acquisition time window on the laterally integrated activity depth-profiles, with emphasis on 2-minute acquisitions starting at different time points. The results depended on phantom composition and reflected the differences in relative contributions from the radionuclides originating from carbon and oxygen. We observed very good agreement between the shapes of the simulated and measured activity depth-profiles for post-beam protocols. However, our results also suggested that available experimental cross sections underestimate the production of ^{10}C for in-beam acquisitions, which in PE resulted in an overestimation of the predicted activity range by 1.4 mm. The uncertainty in the activity range measured in PMMA using the DPC-based TOF-PET prototype setup equaled 0.2 mm - 0.3 mm for 10^{10} delivered protons.

Prompt gamma imaging

Therapeutic proton and heavier ion beams generate prompt gamma photons that may escape from the patient. In principle, this allows for real-time, *in situ* monitoring of the treatment delivery, in particular, the hadron range within the patient, by imaging the emitted prompt gamma rays. Unfortunately, the neutrons simultaneously created with the prompt photons create a background that may obscure the prompt gamma signal. To enhance the accuracy of proton dose verification by prompt gamma imaging, chapter 3 proposes a TOF technique to reject this neutron background, involving a shifting time-of-flight window to account for the propagation of the protons through the patient.

Time-resolved MC simulations of the generation and transport of prompt gamma photons and neutrons upon irradiation of a PMMA phantom with 100, 150 and 200 MeV protons were performed using Geant4 and MCNPX. The influence of angular collimation and TOF selection on the prompt gamma and neutron longitudinal profiles was studied. Furthermore, the implications of the proton beam microstructure (characterized by the proton bunch width and repetition period) were investigated. The application of a shifting TOF window having a width of ΔTOF_z = 1.0 ns appeared to reduce the neutron background by more than 99% for proton bunch widths smaller than ΔTOF_z, if we neglect the overlay of neutrons generated within a given pulse onto subsequent pulses. The additional application of an energy threshold did not appear to sharpen the distal falloff of the prompt gamma

profile but reduces the tail that is observed beyond the proton range. Investigations of the influence of the beam time structure showed that TOF rejection of the neutron background is expected to be effective for typical therapeutic proton cyclotrons.

Experimental evidence of the effectiveness of TOF background rejection in PG imaging with mechanical collimation is presented in chapter 4, which reports on the initial performance testing of two knife-edge slit camera prototypes based on arrays of DPCs. PG profiles emitted from a PMMA target upon irradiation with a 160 MeV proton pencil beam (about 6.5×10^9 protons delivered in total) were measured using detector modules equipped with four DPC arrays coupled to Bismuth Germanate (BGO) or LYSO:Ce crystal matrices. The knife-edge slit collimator and detector module were placed at 15 cm and 30 cm from the beam axis, respectively, in all measurements. The use of LYSO:Ce enabled TOF rejection of background events, by synchronizing the DPC readout electronics with the 106 MHz radiofrequency signal of the cyclotron. The signal-to-background (S/B) ratio of 1.6 obtained with a 1.5 ns TOF window and a 3 MeV - 7 MeV energy window was about 3 times higher than that obtained with the same detector module without TOF discrimination and 2 times higher than the S/B ratio obtained with the BGO module. Even 1 mm shifts of the Bragg peak position translated into clear and consistent shifts of the PG profile if TOF discrimination was applied, for a total number of protons as low as about 6.5×10^8 and a detector surface of 6.6 cm × 6.6 cm.

A different type of collimator is the so-called multi-slat, which consists of alternating slats of a high-density material and air slits, aligned perpendicularly to the beam direction. To analyze the viability of utilizing a multi-slat PG camera to monitor the beam range in proton therapy a single-parallel-slit PG detector experiment was carried out (chapter 5). In addition to obtaining PG profiles corrected with the shifting TOF method introduced in chapter 3, this work also served to put forward the methods necessary to implement such shifting TOF technique for the discrimination of neutron-induced events in cyclotron-based facilities. The experiment used a single-parallel-slit collimator to measure time spectra and intensity profiles of in-beam events emitted at various depths along a PMMA phantom upon irradiation with a 160 MeV proton pencil beam. For the same experimental settings (including approximately the same distance between the beam axis and the detector front surface), the S/B obtained is of the same order as the one achieved with the knife-edge-slit camera provided that a low-energy cutoff of 3 MeV is applied in combination with TOF discrimination in both cases. In addition, an improved spatial resolution obtained with the single-parallel-slit collimator experiment was observed in the PG longitudinal profile around the Bragg peak (a factor of ~2 larger PG falloff slope).

In chapter 6, we simulated potential multi-slat collimator designs in PG imaging, aiming at optimizing collimator performance and sensitivity to deviations in treatment delivery. We first defined a number of multi-slat configurations by constraining either their resolution or their efficiency and optimizing the other, at various distances from the proton pencil beam central axis. We then used Geant4 to simulate irradiations of the head (proton energy: 130 MeV) and pelvis (200 MeV) of the NCAT anthropomorphic phantom, with and without physiologic/morphologic or setup changes of clinical dosimetric relevance. The particles escaping the phantom were transported through each of these multi-slat configurations and the gamma count rate profiles were recorded at the collimator exit. Median filtering was applied to the registered PG profiles to mitigate the effects of septa shadowing and statistical fluctuations. TOF discrimination was used to enhance the gamma signal-to-background ratio, which appeared crucial for the 200 MeV irradiations. The correlation between the obtained PG and depth-dose profiles enabled visual detection of the artificially introduced changes. Moreover, 2 mm proton range shifts could be detected in the head irradiation case using a simple linear regression fit to the falloff of the PG profile. The influence of changes

in complex, patient-like dose distributions on the PG profiles post-collimation is first studied in this work, which further gives insight on multi-slat collimator design optimization and highlights its potential and simplicity for detecting proton treatment deviations.

Conclusion

The experimental results presented in this work show that, using either PT PG or PT PET, it is possible to monitor the range in proton-irradiated homogeneous phantoms to within a few millimeters. Moreover, MC simulations in an anthropomorphic phantom indicate that similar results could be feasible in patients. The use of modern multi-pixel detectors capable of providing TOF information appeared crucial, either to minimize artefacts in dual-head TOF-PET images and profiles, or to reject neutron-induced background in PG profiles obtained via mechanical collimation. Such neutron rejection increases the corresponding S/B, resulting in improved estimation of the falloff of the PG profile.

This work does not yet show which imaging modality will perform better at the task of proton range monitoring in clinical practice. It nevertheless provides important building blocks towards a clinical solution for *in vivo* proton therapy monitoring.

Samenvatting

Deeltjestherapie, waaronder protonentherapie (PT), heeft belangrijke voordelen ten opzichte van externe radiotherapie met fotonen (sectie 1.1). Dit komt doordat de hoogste dosis wordt afgeven rond het distale eind van de protonenbundel (Bragg-piek), terwijl er vrijwel geen dosis wordt afgeven na dit punt. Echter, de sterk gelokaliseerde dosisafgifte maakt de effectiviteit van protonentherapie extra gevoelig voor (1) morfologische veranderingen in de patiënt, waaronder groei of krimp van de tumor, (2) orgaanbeweging, (3) afwijkingen in de positionering van de patiënt, (4) laterale heterogeniteit van het weefsel, (5) onzekerheden in de bundeleigenschappen die worden gebruikt in de planning van de behandeling, en (6) het omrekenen van Hounsfield eenheden (computer tomografische data) naar de massadichtheid en stoichiometrie van het weefsel. Bovendien dragen onzekerheden in de gemiddelde excitatiepotentiaal (I), nodig om het energieverlies van de protonen te berekenen, bij aan de onzekerheid in de dracht van de bundel.

Gezien de bovengenoemde oorzaken van mogelijke afwijkingen in de behandeling is een beeldvormende techniek die informatie kan geven over de kwaliteit van de toegediende behandeling zeer gewenst. Dit is dan ook een zeer actief onderzoeksterrein binnen de deeltjestherapie (sectie 1.2). In het bijzonder is het van belang een techniek te ontwikkelen die bij iedere fractie de *in vivo* dracht van de deeltjes kan bepalen, met name in situaties waarbij de deeltjesbundel door een zeer heterogeen gebied gaat. Een dergelijke imaging techniek kan gebruik maken van de uit de patiënt gezonden secondaire gammastraling (γ), ten gevolge van nucleaire wisselwerking tussen de deeltjes en de kernen in het bestraalde weefsel. Deze technieken kunnen worden onderverdeeld in twee categorieën, volgens het type secundaire γ-straal die wordt gemeten: (1) positronemissietomografie (PET), die gebruik maakt van vertraagd uitgezonden straling; en (2) prompte gamma (PG) imaging, die gebruik maakt van fotonen die worden uitgezonden op een sub-nanoseconde tijdschaal.

In dit proefschrift worden verschillende beeldvormende technieken besproken die dit in potentie mogelijk maken: *time-of-flight* positronemissietomografie (TOF-PET), een *knife-edge-slit* prompte gamma camera en een *multi-slat* PG camera; in beide PG camera's wordt ook TOF gebruikt, in dit geval om het achtergrondsignaal ten gevolge van neutronen te onderdrukken. Deze technieken werden voor het eerst experimenteel getest met scintillatiedetectoren gebaseerd op een nieuw type fotosensor (de zogenaamde *digital photon counter* of DPC). Specifiek zijn experimenten gedaan met een TOF-PET opstelling (hoofdstuk 2), een *knife-edge-slit* PG camera (hoofdstuk 4) en een *single-parallel-slit* PG detector als een eenvoudig prototype van een *multi-slat* PG camera (hoofdstuk 5). De TOF-PET metingen werden uitgevoerd met 126 MeV protonen uit een klinisch synchrotron. De PG metingen werden uitgevoerd met protonenbundels uit een klinisch cyclotron met een protonenpulsbreedte van ongeveer 1,1 ns *full-width-at-half-maximum* (FWHM) en een protonenenergie van 160 MeV. De snelle tijdsresolutie van de DPC in combinatie met de snelle en hoge lichtopbrengst van de gebruikte scintillatiekristallen (cerium-gedoteerd lutetium-yttrium-orthosilicaat, LYSO:Ce) zorgen voor een uitstekend tijdsresolutie van de detector. Dit proefschrift laat zien dat dit een belangrijke factor is voor alle onderzochte beeldvormingstechnieken.

Naast experimentele demonstraties van *in situ* PET- en PG-gebaseerde beeldvormingstechnieken voor de bewaking van protonentherapie worden er in dit proefschrift, door middel van Monte Carlo (MC) simulaties, methoden onderzocht die zorgen voor een verbetering van de PG beeldvormingstechniek. In hoofdstuk 3 wordt het concept van een verschuivend TOF venster, gerelateerd aan de snelheid van de in het weefsel afremmende

therapeutische deeltjes, onderzocht. In hoofdstuk 6 wordt voor het eerst de toepassing van een *multi-slat* collimator systeem geanalyseerd voor realistische behandelscenario's (antropomorfisch fantoom), waarbij potentiele morfologische veranderingen in het weefsel leiden tot variaties in de protonendracht van 2 mm tot enkele centimeters.

TOF-PET

PET is de tot op heden meest diepgaand geteste beeldvormingsmodaliteit voor kwaliteitsbewaking van de behandeling in PT. Optimaal gebruik van PET in PT vereist *in situ* detectie van het relatief sterke ^{15}O signaal. Vanwege de relatief korte halveringstijd (~2 min) en het hoge zuurstofgehalte in biologisch weefsel maakt dit kortere scans mogelijk die minder gevoelig zijn voor het "uitwassen" van de activiteit ten gevolge van biologische processen.

In hoofdstuk 2 worden de eerste testen besproken van een vereenvoudigd *in situ* TOF-PET systeem gebaseerd op DPCs gekoppeld aan LYSO:Ce kristallen. De kwantitatieve resultaten zijn representatief voor een *dual head* tomografiesysteem ($2 \times 50°$, van 360°, transaxiale dekkingshoek) dat past bij de typische ruimtebeperkingen die in de klinische praktijk van toepassing zijn. De door protonen opgewekte activiteit in fantomen van polymethylmethacrylaat (PMMA) en polyethyleen (PE) is gemeten tijdens (*in beam*) en onmiddellijk na bestraling (*post beam*) met een door een synchrotron geproduceerde *pencil beam* met klinisch relevante eigenschappen: protonenenergie 125,67 MeV/u, $4{,}6\times10^8$ protonen/s, and 10^{10} protonen per bestraling. De driedimensionale activiteitsverdelingen zijn vervolgens gereconstrueerd met en zonder TOF informatie en deze zijn vergeleken met FLUKA simulaties. Deze vergelijking liet duidelijk het voordeel van TOF-PET zien met betrekking tot het verminderen van *limited-angle* artefacten wanneer er gebruik wordt gemaakt van een tijdresolutie (*coincidence resolving time*) van 382 ps FWHM.

De individuele bijdragen van verschillende radionucliden aan het totale teltempo zijn in detail onderzocht. Verder bestudeerden we de invloed van de meettijd op de lateraal geïntegreerde activiteitsprofielen, waarbij vooral is gekeken naar metingen van 2 minuten met verschillende startmomenten ten opzichte van de bestraling. De resultaten hingen af van het fantoommateriaal en gaven de verschillen weer in de relatieve bijdragen van de uit koolstof en zuurstof geproduceerde radionucliden. Voor de *post-beam* protocollen vonden we een zeer goede overeenstemming tussen de vormen van de gesimuleerde en gemeten activiteitprofielen als functie van de diepte. Echter, onze resultaten suggereren ook dat de in de literatuur beschikbare werkzame doorsneden voor de productie van ^{10}C de werkelijke waarden onderschatten, wat in PE resulteert in een overschatting van de activeringsdiepte met 1,4 mm. De gemeten onzekerheid in de activeringsdiepte in PMMA, gebruikmakend van de op DPCs gebaseerde TOF-PET prototype opstelling, was gelijk aan 0,2 mm - 0,3 mm voor 10^{10} afgeleverde protonen.

Prompt gamma imaging

Therapeutische bundels van protonen en zwaardere ionen wekken prompte gammafotonen op die vervolgens uit de patiënt kunnen ontsnappen. In principe staat dit *real-time, in situ* kwaliteitscontrole van de geleverde behandeling toe. In het bijzonder kan het detecteren van de prompte gammafotonen ons in staat stellen de hadrondracht binnen de patiënt te bepalen. De neutronen die tegelijk met de prompte gammafotonen worden opgewekt creëren helaas een achtergrondsignaal dat het prompte gammasignaal verdoezelt. Om protondosisverificatie door middel van *prompt gamma imaging* (PGI) nauwkeuriger te maken, stelt hoofdstuk

3 een TOF techniek voor om deze neutronenachtergrond te onderdrukken. Hierbij wordt gebruik gemaakt van een verschuivend TOF venster dat rekening houdt met de beweging van de protonen door de patiënt.

MC simulaties van de productie en het transport van prompte gammafotonen en neutronen als functie van de tijd ten gevolge van de bestraling van een PMMA fantoom met 100, 150 en 200 MeV protonen werden uitgevoerd met Geant4 en MCNPX. De invloed op de longitudinale prompte gamma- en neutronenprofielen van collimatie (op basis van invalshoek) en TOF selectie werden bestudeerd. Ook werden de implicaties van de temporele microstructuur van de protonenbundels (gekarakteriseerd door de protonenpulsbreedte en herhaalperiode) onderzocht. De toepassing van een verschuivend TOF venster met een breedte van ΔTOF_z = 1,0 ns bleek de neutronenachtergrond met meer dan 99% te verminderen, voor protonenpulsbreedtes van minder dan ΔTOF_z, mits we de superpositie van het neutronensignaal dat binnen een bepaalde protonenpuls wordt gegenereerd op de navolgende protonenpulsen negeren. Het toepassen van een energiedrempel bleek de distale *fall off* van het prompte gammaprofiel niet scherper te maken, maar verminderde wel de "staart" die voorbij de Bragg-piek optreedt. Onderzoek naar de invloed van de tijdstructuur van de protonenbundel toonde aan dat het uitsluiten van de neutronenachtergrond door middel van de TOF techniek naar verwachting effectief zal zijn voor therapeutische protonencyclotrons.

Experimenteel bewijs van de effectiviteit van neutronenachtergrondonderdrukking door middel van TOF bij PGI met mechanische collimatie wordt gegeven in hoofdstuk 4. In dit hoofdstuk beschrijven we de eerste testen van twee *knife-edge slit* cameraprototypen die gebruik maken van DPCs. PG-profielen uitgezonden door een PMMA fantoom tijdens bestraling met een 160 MeV protonen *pencil beam* (ongeveer $6{,}5 \times 10^9$ protonen in totaal) werden gemeten met behulp van detectormodules uitgerust met vier matrices van DPCs gekoppeld aan bismut germanaat (BGO) of LYSO:Ce kristallen. De collimator en de detectormodule werden geplaatst op respectievelijk 15 cm en 30 cm van de bundel-as. Het gebruik van LYSO:Ce maakte onderdrukking van het neutronenachtergrondsignaal door middel van TOF mogelijk, door de DPC uitleeselektronica te synchroniseren met het 106 MHz radiofrequente signaal van het cyclotron. De signaal-achtergrond (S/B) verhouding van 1,6 verkregen met een 1,5 ns TOF-venster en een 3 MeV - 7 MeV energievenster was ongeveer 3 keer beter dan de verhouding die werd verkregen met dezelfde detectormodule zonder TOF discriminatie. Dit resultaat was ook 2 keer hoger dan de S/B-verhouding die werd verkregen met de BGO module. Verschuivingen van de Bragg-piekpositie van 1 mm vertaalden zich in duidelijk waarneembare en consistente verschuivingen van het PG profiel indien TOF discriminatie werd toegepast, voor een totaal aantal protonen van $6{,}5 \times 10^8$ en een detectoroppervlak van slechts 6,6 cm × 6,6 cm.

Een ander soort collimator is de zogenaamde *multi-slat*, die bestaat uit lamellen van een materiaal met hoge dichtheid met luchtspleten daartussen, met het vlak van de lamellen loodrecht op de bundel-as. Om de haalbaarheid te analyseren van het gebruik van een *multi-slat* PG camera voor het monitoren van de protonendracht, hebben we een experiment uitgevoerd met een *single-parallel-slit* PG detector (hoofdstuk 5). Naast het verkrijgen van PG-profielen welke zijn gecorrigeerd met de TOF methode die in hoofdstuk 3 werd geïntroduceerd, diende dit werk ook om de methodiek te beschrijven die noodzakelijk is om het verschuivende TOF venster toe te passen wanneer de deeltjesversneller een cyclotron is. In dit experiment is een *single-parallel-slit* collimator gebruikt om de tijdspectra en de intensiteiten te meten van de prompte gammastraling die wordt uitgezonden vanaf verschillende posities in een PMMA-fantoom als gevolg van bestraling met een proton *pencil beam* van 160 MeV. Voor dezelfde experimentele opzet (inclusief ongeveer dezelfde afstand tussen de bundel-as en het vooroppervlak van de detector) is de verkregen S/B ratio bij benadering

hetzelfde als met de *knife-edge-slit* camera, als in beide gevallen een energiedrempel van 3 MeV wordt toegepast in combinatie met TOF discriminatie. Daarnaast werd een betere spatiele resolutie verkregen in het experiment met de *single-parallel-slit* collimator, zoals te zien is in het longitudinale PG-profiel rondom de Bragg-piek (helling van de *fall off* van het PG-profiel ~2 keer zo groot).

Hoofdstuk 6 beschrijft een simulatiestudie van potentiële ontwerpen van *multi-slat* collimatoren voor PGI met als hoofddoelen het optimaliseren van de collimator in termen van resolutie en sensitiviteit en van de detectiegevoeligheid voor afwijkingen in de afgeleverde behandeling. Allereerst zijn er een aantal *multi-slat* configuraties gekozen door het vastleggen van ofwel de resolutie ofwel de sensitiviteit en het optimaliseren van de andere parameter, met verschillende afstanden tussen de collimator en de centrale as van de *pencil beam*. Vervolgens hebben we Geant4 gebruikt om bestralingen van het hoofd (proton energie: 130 MeV) en het bekken (200 MeV) van het antropomorfische NCAT fantoom te simuleren, met en zonder fysiologische/morfologische veranderingen of setup wijzigingen van klinisch dosimetrisch belang. De ontstane deeltjes die aan het fantoom ontsnapten werden door de verschillende *multi-slat* configuraties getransporteerd en de teltempi ten gevolge van gammafotonen werden geregistreerd in het vlak aan de uitgang van de collimator. Een mediaanfilter werd toegepast op de geregistreerde PG-profielen om schaduwen ten gevolge van de lamellen en statistische fluctuaties te verminderen. TOF discriminatie werd gebruikt om de S/B verhouding te verhogen, hetgeen met name cruciaal bleek voor de bestralingen bij een energie van 200 MeV. Detectie van kunstmatig geïntroduceerde veranderingen in de protonendracht bleek mogelijk door het bekijken van de correlatie tussen de verkregen PG- en dosisprofielen. In het geval van de hoofdbestraling konden verschuivingen van 2 mm in de protonendracht worden gedetecteerd door gebruik te maken van eenvoudige lineaire regressie in het *fall off* gebied van het PG-profiel. De invloed van afwijkingen in een complex, antropomorfisch fantoom op de PG-profielen na collimatie werd in dit werk voor de eerste keer uitgezocht. Daarnaast geven de resultaten inzicht in factoren die van belang zijn voor het optimaliseren van het ontwerp van *multi-slat* collimatoren. Ook brengt dit werk het potentieel van dit eenvoudige type collimator naar voren voor wat betreft het opsporen van afwijkingen in de afgegeven protonenbehandeling.

Conclusie

Uit de experimentele resultaten van dit werk blijkt dat zowel PGI als *in situ* PET het mogelijk maken om variaties in de protonendracht in de orde van een millimeter te detecteren in met protonenbundels bestraalde homogene fantomen. Bovendien laten Monte Carlo simulaties in een antropomorfisch fantoom zien dat dergelijke resultaten ook haalbaar zouden moeten zijn in patiënten. Het gebruik van scintillatiedetectoren die in staat zijn om TOF-informatie te bepalen bleek essentieel, zowel om artefacten in *dual-head* TOF-PET afbeeldingen te minimaliseren, als om de door neutronen gegenereerde achtergrondsignalen in PGI acquisities te onderdrukken. Dergelijke neutronenachtergrondreductie verhoogt de bijbehorende S/B, wat weer resulteert in een betere inschatting van de *fall off* positie in het PG-profiel.

Uit het huidige werk kan nog niet worden geconcludeerd welke beeldvormende modaliteit het meest geschikt is voor kwaliteitsbewaking van PT in de klinische praktijk. Het draagt desalniettemin belangrijke bouwstenen aan voor de ontwikkeling van een klinische oplossing voor de *in vivo* kwaliteitsbewaking van protonentherapie.

Acronyms and abbreviations

1D/2D/3D	one-/two-/three-dimension(al)
BGO	Bismuth Germanate, $Bi_4Ge_3O_{12}$
BP	Bragg peak
C/O	ratio of coincidences from carbon and oxygen radionuclides
CRT	coincidence resolving time
CT	computed tomography
DCR	dark-count rate
DNA	deoxyribonucleic acid
DPC	(Philips) digital photon counter
dSiPM	digital silicon photomultiplier
FOM	figure of merit
FOV	field of view
FPGA	field-programmable gate array
FWHM	full width at half maximum
G/N	gamma-to-neutron ratio
HIT	Heidelberg Ion-Beam Therapy Center
ICRU	International Commission on Radiation Units & Measurements
IGRT	image-guided radiation therapy
IMPT	intensity-modulated particle therapy
IMRT	intensity-modulated radiation therapy
LET	linear energy transfer
LOR	line of response
Lu	lutetium
LYSO:Ce	Cerium-doped Lutetium and Yttrium Oxyorthosilicate, $Lu_{1.8}Y_{0.2}SiO_5$:Ce
MC	Monte Carlo
MCS	multiple Coulomb scattering
MRI	magnetic resonance imaging

NCAT	NURBS-based cardiac-torso (phantom)
NIST	(USA) National Institute of Standards and Technology
NURBS	non-uniform rational basis spline
OAR	organ at risk
PBS	pencil beam scanning
PET	positron emission tomography
PE	polyethylene, C_2H_4
PG	prompt gamma
PMMA	polymethylmethacrylate, $C_5H_8O_2$
PMT	photomultiplier tube
PT	particle therapy
PTCOG	Particle Therapy Co-Operative Group
RBE	relative biological effectiveness
RF	particle accelerator radiofrequency
RT	radiation therapy or radiotherapy
S/B	signal-to-background ratio
S_γ/B_γ	gamma signal-to-background ratio
SD	standard deviation
SI	International System of Units
SiPM	silicon photomultiplier
SNR	signal-to-noise ratio
SOBP	spread-out Bragg peak
SPAD	single-photon avalanche diode
TDC	time-to-digital converter
TOF	time of flight
TS	time stamp
WPE	West German Proton Therapy Centre Essen

Acknowledgments / Agradecimentos

Here I would like to say some words of acknowledgements, as far as possible in chronological order.

Não poderia deixar de começar por agradecer, do coração, à minha mãezinha Laura e ao meu avô Lopinhos. Sem eles, eu não teria iniciado e muito menos completado esta longa caminhada. Obrigada pelo vosso apoio incondicional.

Aos meus primos Toninho e Graça, o meu muito obrigada por toda a amizade, apoio e carinho que me deram.

I would like to express my gratitude to my direct supervisors, Paulo, Dennis, and Katia, for giving me this opportunity and for your continuous support during my PhD work; and to my promotor Harry van der Graaf, thank you for your engagement. Obrigada Paulo por me teres aberto as portas e os horizontes. Contigo aprendi muita ciência e também muitos valores pessoais. Mais do que orientador, és um Amigo. Thank you Dennis for your enthusiasm and for all your support, even *in situ,* during our experimental adventures, which bring me very nice memories. And thank you Katia, you always had something constructive to give, it has been a pleasure to work with you.

I wish to express my acknowledgement to FCT, FOM, and the European Union taxpayers, for financing me and my PhD project.

Jure, thank you for making this period of my life full of joy, and for being always there when I needed you. You made this possible. *More than this... there is nothing...*

A big thanks to all my colleagues, I cannot name you all, for the nice working environment, all your help and discussions, and very importantly, all the *gezelligheid*. A special thanks to my office mates in Delft: Ola, Victor, Valerio, Giacomo, Stefan Seifert, Stefan Brunner; and in Coimbra: Hugo, Paulo Martins, Sharif. A special thanks also to the secretaries José Buurman, Thea Miedema, and Anouk Nieuwesteeg, for your precious help and, of course, the *gezelligheid*. A big thank you to Jan Huizenga for all the engagement in the work and key technical support. I also could not leave unmentioned the international parties that provided me with technical assistance, supervision and a lot of enthusiasm. Especially, thank you York Haemisch, Ralf Schulze and Ben Zwaans, from Philips; thank you Ilaria, Julia, and Stephan, from HIT, and thank you Enrico, Julien, and Damian, from IBA.

A special thanks to my friends in Delft for making The Netherlands really feel like home: Astrid, Neven, Albert, Damian, Luís, Stella and Dimitris, and Bob and Lisanne.

O meu profundo agradecimento à Alcinda e ao Dr. Sousa Martins, pela ajuda imensurável e incondicional que me deram.

Finally, thank you Marieke Smit and Eelco Lens for helping me with the difficult task of writing the *samenvatting*. And my thanks to Ben for styling my thesis cover.

Curriculum Vitæ

Patrícia Cambraia Lopes was born in Figueira da Foz, Portugal, on May 10, 1986. In 2004, she concluded the science track of secondary school in Cooperativa de Ensino de Coimbra, Coimbra, Portugal. From 2004 to 2008 she studied Physics at the University of Coimbra, Portugal, where she obtained the degree of Bachelor of Science in Physics, during which she received an annual award attributed to the 3% best students in 2004/2005. During the last academic year she performed extra-curricular studies on the topic "Study of THGEM (Thick Gaseous Electron Multiplier) operation within rare gases under low and high pressures" at the Instrumentation Center-University of Coimbra, where she was the recipient of a Scientific Initiation Fellowship supported by Fundação para a Ciência e a Tecnologia (FCT), Lisbon, Portugal. She developed early in her studies an interest for the application of fundamental sciences on health care, which drove her to start a master course in Medical Physics at the University of Porto in 2008. During her master thesis project, she performed spectroscopic studies using near-infrared micro-Raman on *ex vivo* human colonic tissue samples, normal and affected by adenocarcinoma, for diagnostic application. The experiments were carried out during a short internship in March 2010, at the Institute of Physics of the Academy of Sciences of the Czech Republic, Prague. While finishing her master studies she applied in September 2010 for an FCT individual doctoral grant, in the framework of a joint collaboration between three institutions: Delft University of Technology (TU Delft), Delft, The Netherlands, the Laboratório de Instrumentação e Física Experimental de Partículas, Coimbra (LIP-Coimbra), Portugal, and the Heidelberg Ion-Beam Therapy Center (HIT), Heidelberg University Clinic, Heidelberg, Germany, and under the supervision of Dr. Ir. Dennis R. Schaart, Dr. Paulo Crespo and Prof. Dr. Katia Parodi, respectively. In December 20, 2010, she concluded her master studies and in January 2011 she was awarded a doctoral grant. She then started in April 2011 her doctoral track as PhD student at TU Delft, Faculty of Applied Sciences, department of Radiation Science and Technology, co-hosted by LIP and HIT. At the 2013 IEEE Medical Imaging Conference in Seoul, Republic of Korea, she received the first place student paper award, for the paper "First performance tests of digital SiPMs in prompt gamma imaging with a knife-edge slit camera for proton range verification". Since the motivation to become a medical physicist persisted with her, she started in February 2016 as a medical physicist in training, radiotherapy (nl. *klinisch fysicus in opleiding, radiotherapie*), at Erasmus Medical Center (Erasmus MC) Cancer Institute, Rotterdam, The Netherlands.

Publications

Peer-reviewed journal papers

- P. Cambraia Lopes, J. Bauer, A. Salomon, I. Rinaldi, V. Tabacchini, T. Tessonnier, P. Crespo, K. Parodi and D. R. Schaart, "First *in-situ* TOF-PET study using digital photon counters for proton range verification", Phys. Med. Biol. 61, 6203–30, 2016.

- P. Cambraia Lopes, E. Clementel, P. Crespo, S. Henrotin, J. Huizenga, G. Janssens, K. Parodi, D. Prieels, F. Roellinghoff, J. Smeets, F. Stichelbaut and D. R. Schaart, "Time-resolved imaging of prompt-gamma rays for proton range verification using a knife-edge slit camera based on digital photon counters", Phys. Med. Biol., 60 6063–85, 2015.

- F. M. F. C. Janssen, G. Landry, P. Cambraia Lopes, G. Dedes, J. Smeets, D. R. Schaart, K. Parodi and F. Verhaegen, "Factors influencing the accuracy of beam range estimation in proton therapy using prompt gamma emission", Phys. Med. Biol. 59, 4427-41, 2014.

- A. K. Biegun, E. Seravalli, P. Cambraia Lopes, I. Rinaldi, M. Pinto, D. C. Oxley, P. Dendooven, F. Verhaegen, K. Parodi, P. Crespo and D. R. Schaart, "Time-of-flight neutron rejection to improve prompt gamma imaging for proton range verification: a simulation study", Phys. Med. Biol. 57, 6429–44, 2012.

- P. Cambraia Lopes, J. Agostinho Moreira, A. Almeida, A. Esteves, I. Gregora, M. Ledinsky, J. Machado Lopes, R. Henrique and A. Oliveira, "Discriminating adenocarcinoma from normal colonic mucosa through deconvolution of Raman spectra", J. Biomed. Opt. 16(12), 127001, 2011.

Conference proceedings

- P. Dendooven, A. K. Biegun, S. Brandenburg, H. J. T. Buitenhuis, P. Cambraia Lopes, F. Diblen, D. C. Oxley, D. R. Schaart, A. J. van der Borden, M.-J. van Goethem, A. van der Schaaf, S. Vandenberghe, A. A. van 't Veld, "TOF-PET scanner configurations for quality assurance in proton therapy: a patient case study", Radiother. Oncol. 110 (Suppl 1, 02/2014), S28-9, 2014.

- P. Cambraia Lopes, M. Pinto, H. Simões, A. K. Biegun, P. Dendooven, D. C. Oxley, K. Parodi, D. R. Schaart and P. Crespo, "Optimization of Collimator Designs for Real-Time Proton Range Verification by Measuring Prompt Gamma Rays", 2012 IEEE Nucl. Sci. Symp. and Med. Imag. Conf. (Anaheim, CA USA), Conf. Record, 3864-70, 2012.

- A. K. Biegun, P. Cambraia Lopes, I. Rinaldi, D. C. Oxley, E. Seravalli, F. Verhaegen, P. Dendooven, K. Parodi, D. R. Schaart and P. Crespo, "Time-Of-Flight method for neutron rejection in prompt gamma imaging of beam range and density changes in proton therapy", Radiother. Oncol. 102 (Suppl 1, 03/2012), S135-6, 2012.

- D. Oxley, A. K. Biegun, A. van der Borden, S. Brandenburg, P. Cambraia Lopes, F. Diblen, S. Vandenberghe, A. Van't Velt, D. R. Schaart and P. Dendooven, "Verifying proton therapy irradiations with time-of-flight positron emission tomography" Radiother. Oncol. 102 (Suppl 1, 03/2012), S90-1, 2012.

- A. K. Biegun, P. Cambraia Lopes, P. Dendooven, D. C. Oxley, K. Parodi, M. Pinto, I. Rinaldi, D. R. Schaart, E. Seravalli, F. Verhaegen and P. Crespo, "Range and density variations monitoring during proton therapy based on time-of-flight detection of prompt gamma radiation", 2011 IEEE Nucl. Sci. Symp. and Med. Imag. Conf. (Valencia, Spain), Conf. Record., 3492-95, 2011.

TU Delft